Title

Design of BCC-B2 Precipitation Strengthened Nb Alloys

Permalink

https://escholarship.org/uc/item/0s61w6sk

Author

Frey, Carolina Hennig

Publication Date

2024

Peer reviewed|Thesis/dissertation

University of California
Santa Barbara

Design of BCC-B2 Precipitation Strengthened Nb Alloys

A dissertation submitted in partial satisfaction
of the requirements for the degree

in
Materials Science and Engineering

by

Carolina Hennig Frey

Committee in charge:

Tresa Pollock, Chair
Samantha Daly
Daniel Gianola
Carlos Levi

June 2024

The Dissertation of Carolina Hennig Frey is approved.

Samantha Daly

Daniel Gianola

Carlos Levi

Tresa Pollock, Committee Chair

June 2024

Design of BCC-B2 Precipitation Strengthened Nb Alloys

by

Carolina Hennig Frey

To everyone who helped me grow

Acknowledgements

In many ways, I feel like I have had an incredibly fortunate six years. Moving to California to pursue a PhD in metallurgy, something I knew very little about before I started, was a great gamble and yet, somehow, it turned out alright. However, none of it would have been possible without the generous support and love of my friends and family, or without the support of an excellent group of undergraduate students, graduate students, post-doctoral researchers, and other scholars at UCSB and elsewhere. The road has been long but I am glad I could travel it with all of you.

To begin, I must start by thanking my advisor, Tresa Pollock. Tresa has been one of my greatest advocates and her constant, unwavering support kept me going through my early years of doubt and confusion. It takes great patience to let students pursue their own intellecutal rabbits and to guide them without judgement or rancor. Tresa, thank you for taking a chance on me and giving me so much room to grow.

Navigating the great highs, terrible lows, and dreadful doubts of graduate school would not have been the same without the other seven women in my cohort. Victoria Christensen, Lauren Fey, Emily Foley, Leah Mills, Kira Pusch, Colleen Reynolds, and Muna Saber, thank you for some of the most social and active years of my life. Our weekly book club was a silver lining of the COVID-19 shutdowns and I am glad that returning to the hustle of our lives didn't slow us down. I had the additional luck to work with Leah and Kira everyday. Leah, my laboratory partner-in-crime, thank you for listening to even my most foolish ideas. Kira, thank you for always reminding me to look up and remember the greater community. I also had the honor of getting to live with Colleen for five years and could not imagine what this experience would have been like without her daily support. Colleen, you were a rock for me. Thank you for everything, especially all the times you drove me to the airport at 4 am.

Thank you to everyone in the Pollock Group for their intellectual and emotional support. I am proud to be apart of such a cheerful and collaborative group of scientists. While everyone who has passed through has shaped me in some way, there are a few members to single out. I am especially grateful to have had Sean Murray and Joe Wendorf as mentors when I arrived. Their patience, calm, and meaningful interest in everyone's work taught me to take this experience one step at a time. I can only hope that I have lived up to their example. My long sessions on the SEM would not have been the same without Kaitlyn Mullin, who always seemed happy to receive random screenshots of my microstructures at all hours and who also sent me many beautiful images of her own materials. Her excellent TEM work is featured in Chapters 3 and 5 of this dissertation. I deeply appreciate all of the contributions made by my undergraduate interns, Anthony Botros, Benjamin Neuman, and Haojun You, and thank them for all of their cheerful hard work. I would also like to thank Chris Torbet for being an incredible group manager. Without him the Pollock Group would grind to a halt.

Academic research can sometimes be an isolating experience, with input from many great scholars but with a lack of perspective from outside the academic community. In that respect, I must thank Noah Philips from ATI for taking the time to discuss my work on numerous occasions and giving me an opportunity to broaden my thinking. After Tresa, Noah has been my biggest mentor and he gave me a perspective on my work that I deeply appreciate. I also have to thank Benjamin Eick, Matthew Carl, Megan McCormick, Randy Hickman, and all the other technicians and engineers at ATI for graciously welcoming me and patiently mentoring me over the course of my four month internship. It can be very difficult for a PhD student have an internship in the last years of their program and Noah and Ben put in great effort to give me the opportunity. It was a very special experience for me. Thank you for everything.

None of my research would have been possible without Kirk Fields, Aidan Taylor, Claire Chisholm, Ravit Silverstein, Youli Li, Deryck Stave, and Dano Pagenkopf and their incredible efforts to maintain the shared experimental facilities. Thank you for all your hard work, both visible and invisible.

As someone who had not heard of materials science and engineering until midway through my undergraduate degree, there are a number of serendipitous moments and chance encounters that led me to the path I am on today. To recognize those who placed the largest signposts, I must thank: Mary Fredell, my high school chemistry teacher who inspired me to pursue chemistry; Catherine Haslam and Emily Durisin, two friends who first made the leap to materials science and encouraged me to follow; Professor Wynarsky, who taught my introduction to materials course with great passion; Rachel Wallace, my graduate student mentor, who made me feel at home in a research group even as I broke far too many AFM tips; and finally, Professor Halloran, who was the first person to recommend the University of California, Santa Barbara to me and without whom I may never have looked up Tresa's name. I could not have known then how much I would fall in love with metallurgy and I would not have gotten the chance without all of them.

To my parents, my mother Adriana and my father David, thank you for all your sacrifices and your willingness to let me go so far away. To my brother Chris, your unconditional love and support has meant the world to me. I look forward to coming to visit more often.

Finally, to Ryan. You have cheered me on at every high and buffered my every doubt. This would not have been the same without you. I love you.

Curriculum Vitæ
Carolina Hennig Frey

Education

2024	Ph.D. in Materials Science and Engineering, University of California, Santa Barbara.
2018	B.S. in Materials Science and Engineering, University of Michigan, Ann Arbor.

Publications

1. **Frey, C.**, Neuman, B., Mullin, K., Botros, A., Lamb, J., Holgate, C., Kube, S. A., Pollock, T.M. "On the stability of coherent HfRu- and ZrRu-B2 precipitates in Nb-based Alloys". *In preparation.* (2024).
2. **Frey, C.**, Neuman, B., Botros, A., Kube, S. A., Pollock, T.M. "Refractory multi-principal element alloys with solution and aged HfRu-B2 precipitates". *In preparation.* (2024).
3. **Frey, C.**, You, H., Kube, S., Balbus, G. H., Mullin, K., Oppenheimer, S., Holgate, C. S., Pollock, T.M. "High temperature B2 precipitation in Ru-containing refractory multi-principal element alloys". *Metall. Mater. Trans. A* (2024). [doi].
4. S. A. Kube, **C. Frey**, C. Mcmullin, B. Neuman, K. M. Mullin, and T. M. Pollock. "Navigating the BCC-B2 refractory alloy space: Stability and thermal processing with Ru-B2 precipitates". *Acta Materialia* **265**, 119628 (2024). [doi].
5. D. B. Miracle, O. N. Senkov, **C. Frey**, S. Rao, and T. M. Pollock. "Strength vs temperature for refractory complex concentrated alloys (RCCAs): A critical comparison with refractory BCC elements and dilute alloys". *Acta Materialia* **266**, 119692 (2024). [doi].
6. K. M. Mullin, **C. Frey**, J. Lamb, S. K. Wu, M. P. Echlin, and T. M. Pollock. "Rapid screening of single phase refractory alloys under laser melting conditions". *Materials & Design* **238**, 112726 (2024). [doi].
7. L. H. Mills, M. G. Emigh, **C. Frey**, N. R. Philips, S. P. Murray, J. Shin, D. S. Gianola, and T. M. Pollock. "Temperature-dependent tensile behavior of the HfNbTaTiZr multi-principal element alloy". *Acta Materialia* **245**, 118618 (2023). [doi].
8. S. P. Murray, E. B. Raeker, K. M. Pusch, **C. Frey**, C. J. Torbet, N. Zhou, S. A. J. Forsik, A. D. Dicus, G. A. Colombo, M. M. Kirka, and T. M. Pollock. "Microstructure Evolution and Tensile Properties of a Selectively Laser Melted CoNi-Base Superalloy". *Metallurgical and Materials Transactions A* **53**, 2943-2960 (2022). [doi].

9. J. Rossin, P. Leser, K. Pusch, **C. Frey**, S. C. Vogel, A. I. Saville, C. Torbet, A. J. Clarke, S. Daly and T. M. Pollock. ”Single crystal elastic constants of additively manufactured components determined by resonant ultrasound spectroscopy”. *Materials Characterization* **192**, 112244 (2022). [doi].
10. H. Samadian, R. L. Merzel, J. M. Merzel, J. Chen, **C. Frey**, A. Jones, M. Vartanian, B. B. Ward, M. M. Banaszak Holl. ”Anti-tumor Effect of Folate-Binding Protein: In Vitro and in Vivo Studies”. *Molecular Pharmaceutics* **19**, 843-852 (2022). [doi].
11. M. Zhang, Q. Yu, **C. Frey**, F. Walsh, M. I. Payne, P. Kumar, D. Liu, T. M. Pollock, M. D. Asta, R. O. Ritchie, and A. M. Minor. ”Determination of peak ordering in the CrCoNi medium-entropy alloy via nanoindentation”. *Acta Materialia* **2022**, 118380 (2022). [doi].
12. **C. Frey**, R. Silverstein, and T. M. Pollock. ”A high stability B2-containing refractory multi-principal element alloy”. *Acta Materialia* **229**, 117767 (2022). [doi].
13. J. Rossin, P. Leser, K. Pusch, **C. Frey**, S. P. Murray, C. J. Torbet, S. Smith, S. Daly, and T. M. Pollock. ”Bayesian inference of elastic constants and texture coefficients in additively manufactured cobalt-nickel superalloys using resonant ultrasound spectroscopy”. *Acta Materialia* **220**, 117287 (2021). [doi].
14. C. K. H. Borg, **C. Frey**, J. Moh, T. M. Pollock, S. Gorsse, D. B. Miracle, O. N. Senkov, B. Meredig, and J. E. Saal. ”Expanded dataset of mechanical properties and observed phases of multi-principal element alloys”. *Scientific Data* **7**, 1-6 (2020). [doi].
15. M. A. Charpagne, K. V. Vamsi, Y. M. Eggler, S. P. Murray, **C. Frey**, S. K. Kolli, and T. M. Pollock. ”Design of Nickel-Cobalt-Ruthenium Multi-Principal Element Alloys”. *Acta Materialia* **194**, 16013 (2020). [doi].
16. R.L. Merzel, **C. Frey**, J. Chen, R. Garn, M. Van Dongen, C. A. Dougherty, A. K. Kandaluru, P. S. Low, E. N. G. Marsh, and M. M. Banaszak Holl. ”Conjugation Dependent Interaction of Folic Acid with Folate Binding Protein”. *Bioconjugate Chemistry* **28**, 2350-2360 (2017). [doi].
17. R.L. Merzel, S. M. Boutom, J. Chen, **C. Frey**, K. Shedden, E. N. G. Marsh, and M. M. Banaszak Holl. ”Folate binding protein: therapeutic natural nanotechnology for folic acid, methotrexate, and leucovorin”. *Nanoscale* **9**, 2603-2615 (2017). [doi].

Abstract

Design of BCC-B2 Precipitation Strengthened Nb Alloys

by

Carolina Hennig Frey

High temperature structural materials are critical for many applications that underpin modern civilization, including commercial aviation, spaceflight, and chemical processing. These materials must be able to function within extreme conditions, including severely corrosive and oxidative environments, for extended periods, and improvements in mechanical and environmental properties must be balanced with the ability to tolerate damage without catastrophic failure. The materials of choice for many extreme environments have been the Ni-based superalloys. Developed continuously from the mid-nineteenth century, and most recognizable for their role in the hot sections of jet turbine engines, Ni-based superalloys exhibit an excellent balance of properties, including high temperature creep and fatigue strength, intrinsic resistance to oxidation, and reasonable fracture toughness and cost. Their properties are derived from their two-phase microstructres, where a high volume fraction of coherent intermetallic $L1_2$ (γ') precipitates are embedded in a solid solution strengthened FCC (γ) matrix. However, further improvements to the temperatures capabilities of Ni-based superalloys are unlikely due to their level of technological maturity. Increasing temperature demands for turbine engines and other applications motivate the search for new materials that can surpass the temperature limits of Ni-based superalloys. Nb-based alloys are one promising group of candidate materials, where the principal element Nb has a high melting temperature of 2477 °C, a density lower than Ni at $\rho = 8.582$ g/cm^3, and excellent room temperature fabricability.

Of the Nb-based alloys that have been investigated, precipitation strengthened alloys are the closest to achieving the balance of properties required of high temperature materials for critical components. The most promising design strategy is strengthening by a large volume fraction of coherent intermetallic precipitates. This approach attempts to replicate the enormous success of the Ni-based superalloys, only within refractory alloys at higher temperatures. The refractory metals are body-centered cubic (BCC, β) materials at high temperature and therefore, alloys designed with this strategy are β + β' alloys, where the β' phase is an ordered derivative of the BCC crystal structure. To be successful, β + β' alloys must contain coherent precipitates that are morphologically and thermodynamically stable at temperatures above 1200 °C.

The β' phase is ideally the B2 (CsCl) phase. A B2 former of particular interest is Ru, a platinum group metal that forms a variety of B2 phases with the refractory metals. The binary Ru-B2 phases are thermodyanmically stable to much higher temperatures compared to the other candidate strengthening phases in the literature, which dissolve at temperatures below 1200 °C. For example, the binary BCC + B2 phase field in the Hf-Ru binary extends up to 1610 °C. While most of the Ru-based B2 phases have lattice parameters that are significantly smaller than the lattice parameter of pure Nb (a_{Nb} = 3.301 Å), Nb can theoretically be alloyed to be coherent with the largest of the B2 phases, HfRu (a_{HfRu} = 3.225 Å) and ZrRu (a_{ZrRu} = 3.253 Å). Therefore, Ru presents an opportunity to form both coherent and thermally stable precipitates.

In this dissertation, the first comprehensive investigations into the potential of Ru-B2 precipitates to strengthen Nb-based alloys are investigated. Due to their lower lattice misfit with Nb, alloys were designed to contain HfRu- and ZrRu-B2 phases. Initial investigations focused on equiatomic Hf-, Zr-, and Ru-containing alloys, where the B2 phases were stable to the melting point and alloys demonstrated complex solidification pathways. The insights gained from these preliminary investigations are used to successfully

design solution and age hardenable alloys with controllable B2 solvus temperatures from 1000-1900 °C. When the matrix compositions are tailored to reduce the lattice misfit between the B2 and BCC phases to below 1%, a homogeneous distribution of spherical precipitates is achieved. HfRu is found to be more stable than ZrRu, exhibiting higher B2 soluvs temperatures and fewer deleterious phases at equivalent Ru concentrations. An initial investigation of dislocation behavior in these systems is provided by post-mortem transmission electron microscopy of microcompression pillars, revealing the presence of paired dislocations and dislocation loops around precipitates. Preliminary investigations of high temperature mechanical properties show promise compared to current commercial refractory alloys. Implications for further development of Nb-based alloys by Ru-B2 precipitates are discussed, including strategies to mitigate deleterious phase formation and increase B2 volume fractions. While many fundamental questions remain regarding Nb-BCC + Ru-B2 systems, they offer a promising path forward for developing new high temperature materials.

Contents

Chapter 1

Introduction

1.1 Considerations for high temperature structural materials

The ability of structural materials to survive in extreme environments underpins many of the features of modern industrial society[1, 2]. These materials protect the exteriors of spacecraft from the heat of re-entry, enable rocket propulsion systems, and line the inside of nuclear reactor cores that provide our civilizations with power and which will be necessary to transition us to a more sustainable future[3]. Successful functioning in these environments requires an exceptional combination of properties, including resistance to deformation at high homologous temperatures, sufficient toughness to prevent catastrophic failure in the the event of damage, and the ability to tolerate contact with corrosive or oxidative environments for extended periods[4]. Even as temperature demands increase, materials improvements must always be balanced with constraints on density, element scarcity, cost, and fabricability[5].

The materials considerations and engineering complexity that is required of high temperature structural materials is best exemplified by the Ni-based superalloys. The ability of Ni-based superalloys to function at $\geq$ 85% of their melting point in highly corrosive environments for thousands of hours has enabled the modern era of commercial aviation [2, 4]. The efficiency of a turbine engine is directly related to the turbine entry temperature, which translates into an incentive to develop materials that can withstand ever increasing temperatures. Ni-based superalloys were developed to meet this need and are located in the hot sections of turbine engines that power jet aircraft, where temperatures today range from 850 °C (in the compression section) to 1500 °C (in the high pressure turbine)[1, 4, 6]. Since the beginning of superalloy development in 1929[7], the temperature capabilities of these alloys have increased by 300 °C[4] (Figure 1.1). The most advanced Ni-based superalloy components can now operate in temperatures above the incipient melting temperature of the metallic substrate, protected by parallel developments in manufacturing that allow for complex cooling channels and the addition of low-conductivity thermal barrier coatings to the surface[4, 8].

Ni-based superalloys typically contain at least ten alloying components and have complex, multi-phase microstructures. Their mechanical properties derive primarily from their precipitation strengthened γ/γ' microstructures, where a high volume fraction ($\approx$ 70 %) of the ordered $L1_2$ intermetallic Ni_3Al (γ') is embedded in thin channels of a solid solution strengthened Ni (γ) matrix (Figure 1.2). The disordered γ matrix provides ductility and toughness, while strength is conferred by the less ductile, high strength γ' and its interfaces with γ. These microstructures are produced by sequential annealing steps, where the γ' formers are dissolved into the matrix at temperatures above the γ' solvus temperature and then aged below the γ' solvus to produced a homogeneous dispersion of sub-micron particles.

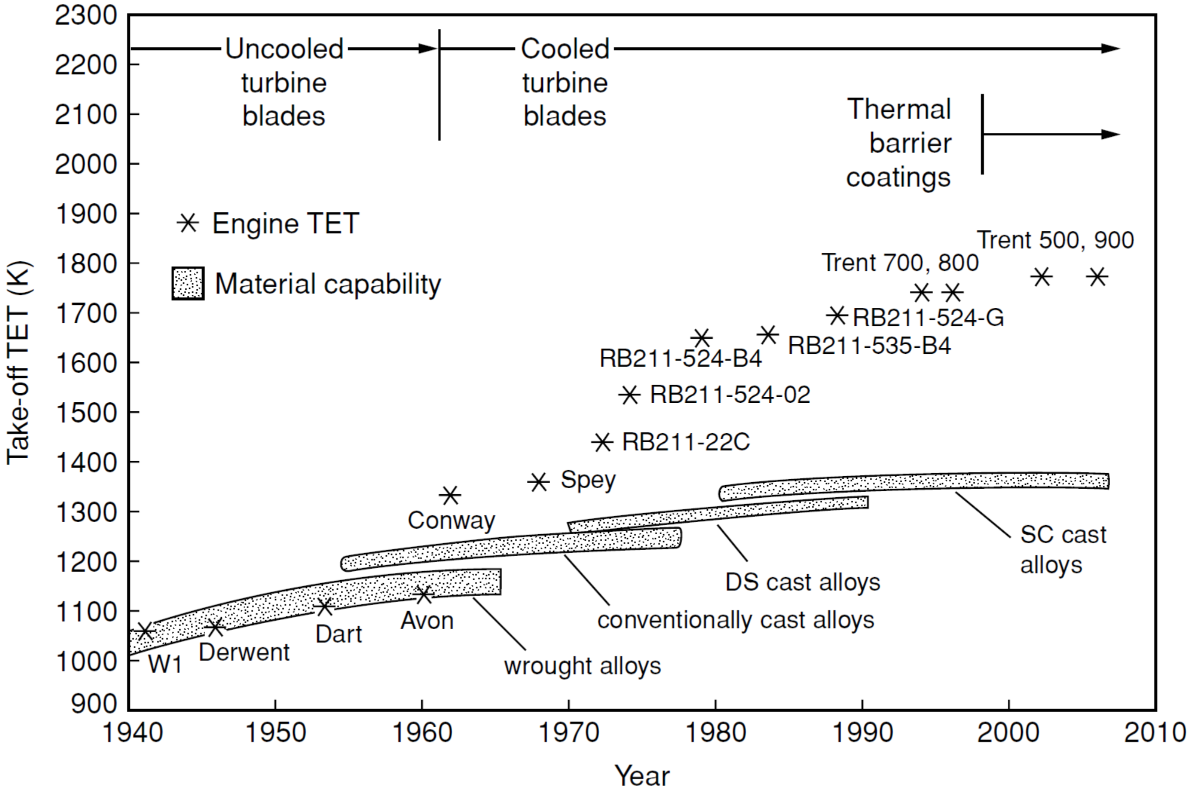

Figure 1.1: Improvements in the turbine entry temperature capability of the Rolls-Royce civil aeroengines, from 1940 to the present day. Reproduced from "The Superalloys: Fundamentals and Applications" by R. Reed, 2006, pg. 5. Copyright by Cambridge University Press. Reproduced with permission [4].

Both the γ and γ' phases possess face-centered cubic crystal structures and can align with a cube-cube orientation relationship when their lattice misfit is sufficiently small. The lattice misfit (δ) between the γ and γ' phases is a critical design property that is related to both microstructural stability and high temperature strength and is defined as:

$$\delta = 2 * \frac{a_{\gamma'} - a_{\gamma}}{a_{\gamma'} + a_{\gamma}} \tag{1.1}$$

and a_{γ} is the lattice parameter of γ, and $a_{\gamma'}$ is the lattice parameter of γ'. Precipitate coarsening is driven by the reduction in interfacial energy that occurs when larger particles grow at the expense of smaller ones, reducing the total interfacial surface area[9]. The interfacial energy, and therefore the driving force for coarsening, is reduced when δ is decreased below 1%, making the precipitate coherent and allowing for continuity of the atomic planes from one phase to the other. This low interfacial energy also facilitates homogeneous nucleation of precipitates, without preferential precipitation on microstructural defects[10, 11]. During deformation, dislocation interactions with the coherent γ/γ' interfaces and the resistance to dislocation shearing of γ' controls strength[12, 13].

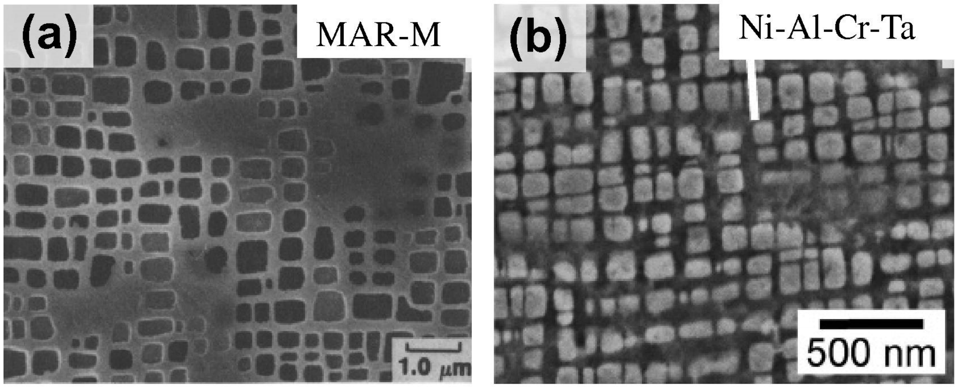

2.8W·11.4Al·1.7Ti·9.9Cr·9.9Co·0.4Mo 10Al·8.5Cr·2Ta

Figure 1.2: Example microstructures of two different Ni-based superalloys. Reprinted from Sluytman and Pollock, *Optimal precipitate shapes in nickel-base γ–γ' alloys, Acta Materialia* **60** (2012) 1771-1783 [14]. Reproduced with permission from Elsevier.

Beyond the composite relationship between γ and γ', each phase is individually alloyed to improve its properties. Alloying additions are selected to, for example, decrease the rate of diffusion in γ by the addition of refractory elements[15] or tailor the antiphase boundary energy of γ' to effect its resistance to dislocation shear[16]. Alloying agents are classified on their partitioning behavior between the γ and γ' phases, with Al, Nb, Pt, Ta, and Ti generally partitioning to γ' and Co, Cr, Mo, Re, and W partitioning to γ[15]. However, the partitioning behavior is strongly dependant on the overall alloy composition and design decisions must consider the complex interactions between different elements[17]. Compositions must also be tailored to prevent the formation of deleterious topologically close-packed (TCP) phases, which deplete the the matrix of elements that improve creep strength[15, 4]. Interstitial additions like C and B are added as grain boundary strengtheners, often resulting in boride or carbide formation, except in single crystal alloys where specific manufacturing techniques are used to eliminate grain boundaries[18].

In service, Ni-based superalloys also need to be resistant to environmental degradation from oxidation and hot corrosion. The engine components are exposed to extremely hot combustion gases, which results in reactions with O and N, as well as other debris present in the atmosphere, such as volcanic ash[19]. Environmental resistance at the highest temperatures is provided by the formation of an external, continuous scale of alumina (Al_2O_3) on the surface of the alloy after exposure to oxygen[20]. The oxide scale must be slow-growing and adherent to ensure it is resistant to spallation[21]. At the highest temperatures, the protective capabilities of the Al_2O_3 scale are insufficient and additional protective coatings are applied to the surface; however, intrinsic oxidation resistance is still necessary to prevent catastrophic failure in case of coating damage. The need for thermal and mechanical compatibility with these coatings introduces additional constraints for material development[22, 23].

Ni-based superalloys are exceptional materials that have overcome numerous challenges to become indispensable materials for high temperature applications[7]. They represent the very cutting edge of materials engineering. However, the melting temperature of Ni ($T_{m,Ni} = 1455$ °C) presents a fundamental limit to their temperature capabilities and future improvements will be difficult to achieve. Coupled with the continued demand for higher operating temperatures in air- and land-based turbines is the rising need for materials that can also protect the leading edges of advanced aircraft and serve the needs of the emerging private space industry[24]. These challenges motivate the search for materials that can surpass the temperature capabilities of Ni-based superalloys. Many materials have been investigated, including ceramic matrix composites[25], intermetallic alloys like RuAl[26], and Co-based superalloys[27], though only a few have made it into commercial service[28]. One potential class of materials are alloys based on the refractory metals, which were investigated extensively in the mid-20th century and which have recently experienced a resurgence of interest.

1.2 Historical development of refractory alloys

Refractory metals as a class of materials are loosely defined but are frequently taken to be metals with melting temperatures $\geq$ 2000 °C. This category always includes Mo, Nb[1], Ta, and W, which are the most commercially significant of the refractory metals, and may also include their typical alloying elements (Cr, Hf, Ti, V, Zr) and certain platinum group elements (Re, Rh, and Ru)[31, 32, 33, 34]. Their much higher melting points make them candidate materials for increasing operating temperatures beyond those allowable by Ni-based superalloys (Figure 1.3).

Serious commercial development of the refractory metals began in the 1950's. Driven initially by increasing temperature demands for turbine engines, refractory metals were also key materials of interest for space-based nuclear reactors[33] and as protective materials for re-entry vehicles[31]. With considerable support from the United States government and close government-commercial partnerships, rapid advancements in refractory

---

[1] Niobium (Nb) is frequently referred to as columbium (Cb) in the historical literature of the United States. Charles Hatchett first isolated Nb oxide from a mineral sample in 1801; the sample was sourced from the North American continent and he proposed to name it *columbium* and the ore *columbite*, which derived from the poetic name for the Americas, Columbia. This became the name of choice in the United States. In 1802, Anders Ekeberg discovered tantalum and named it for Tantalus, a mythical king of Phrygia in Greek mythology. Tantalum and columbium were mistakenly thought to be the same element until 1844, when Heinrich Rose definitively identified two elements within columbite, tantalum and a second element he named niobium, after Niobe, the daughter of Tantalus. Niobium therefore become the name of choice in Europe. In 1950, the International Union of Pure Applied Chemistry formally adopted the name niobium, after the European tradition; in exchange, they adopted the name tungsten for element 74, after the North American tradition, instead of wolfram, which was used in Europe[29, 30].

metallurgy occurred. Only one commercial structural refractory alloy (Mo-0.5 wt% Ti) was available in 1957[32]; by 1965, at least 35 alloys were in development and achieving property targets[35]. This progress was related in part to concerted alloy development, but also to significant investments in manufacturing. A key breakthrough was the invention of vacuum arc melting and electron-beam melting, which allowed for high purity material to be produced at scale[36, 35]. However, decreased interest in space-based power generation and the selection of ceramic materials for the Space Shuttle resulted in a rapid decline in refractory alloy development in the 1970's in the United States[33, 37], though development continued in the Soviet Union[38, 39, 40, 41]. A brief period of interest occurred in the 1980's, driven by the SP-100 program (focused on space-based nuclear power)[33] and the National Aerospace Plane program (focused on hypersonic vehicles)[42]. However, these programs were short lived and terminated in the mid-1990's. Research has continued for specific systems, such as the continued improvement of zirconium cladding alloys for nuclear reactors[43] or development of Nb silicide alloys as a part of a national research thrust on intermetallics[44, 45], but otherwise the field is largely unchanged from where it was left in the 1970's.

Many excellent reviews covering the metallurgical research of the 1950-1970's have been published[46, 47, 33, 48, 49, 34, 50]. The research of this time period, due to large programs within national laboratories and manufacturing companies specializing in refractory metals, was characterized by wide compositional sweeps and rigorous mechanical testing of fully processed material[51, 46, 52, 53]. The general behaviors of the core refractory metals (Mo, Nb, Ta and W) is summarized as follows: they all possess a body centered cubic (BCC) crystal structure at all temperatures. Therefore, their deformation behaviors are characterized by three regimes, which are related to mobility of thermally activated screw dislocations. The thermal activation of screw dislocations results in a steep decline in yield strength from low to intermediate temperatures as the

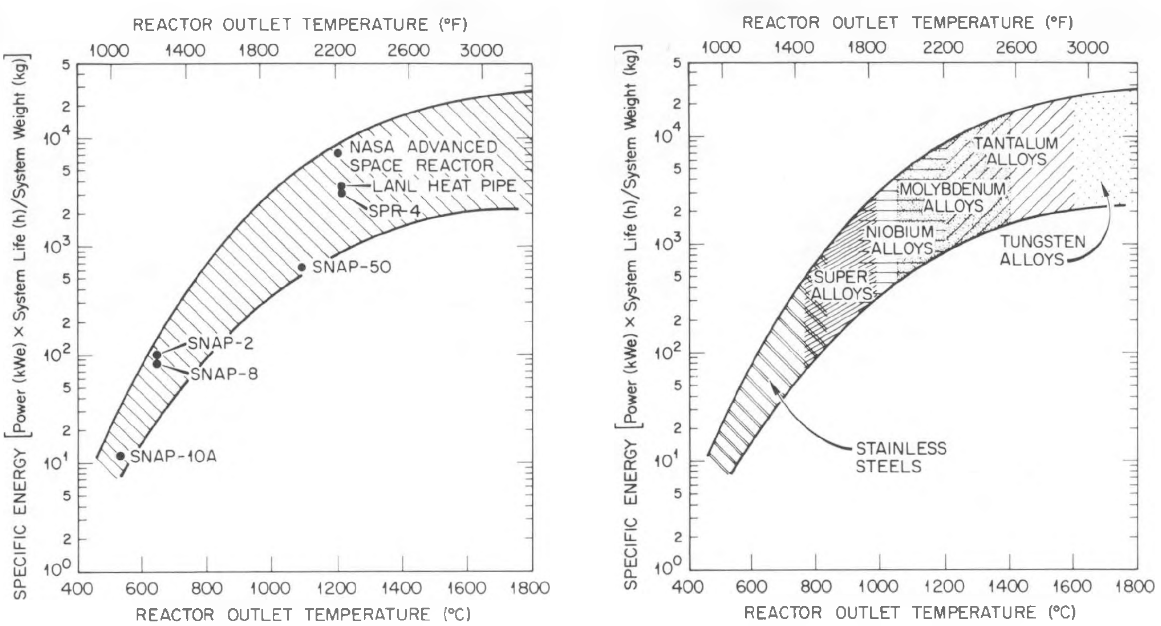

Figure 1.3: (left) Relationships between specific energy and the reactor outlet (desired operating) temperature for theoretical space-based nuclear reactors. (right) Overlay for left, indicating possible temperature limits for stainless steels, superalloys, and refractory alloys. Reproduced from Cooper, R. Potential Refractory Alloy Requirements for Space Nuclear Power Applications. in Refractory Alloy Technology for Space Nuclear Power Applications, Proceedings of a Symposium. (eds. Cooper, R. H. J. & Hoffman, E. E.) 14–17 (United States Department of Energy, 1984). Reproduced with permission [33].

dislocations become more mobile, followed by the onset of an athermal plateau[54]. The plateau persists until the onset of diffusion-based mechanisms at high temperature[54]. The change in dislocation mobility with temperature leads to a ductile-to-brittle transition temperature (DBTT)[55]. Beyond this, the Group 5 elements (Nb and Ta) have distinct behaviors compared to the Group 6 elements (Mo and W). For pure Nb and Ta, the DBTT is reliably below room temperature and they are considered the ductile refractory elements[36, 56, 52]. For Mo and W, the DBTT lies above room temperature and they are considered the brittle refractory metals[52, 57]. Their DBTT properties are also reflective of trends in moduli and diffusivity: Mo and W have higher elastic moduli and lower self-diffusivities than Nb and Ta. This translates to higher creep strength at equivalent homologous temperatures for the Group 6 elements[52].

One key issue for the refractory metals is their high sensitivity to the interstitial elements O, N, and C. This sensitivity to interstitials is two-fold. First, the interstitials can exist within the metal solid solution or form deleterious grain boundary phases, resulting in strengthening and embrittlement[58, 59, 60, 61, 62]. Manufacturing methods must therefore be carefully controlled to prevent the pick up of interstitial elements during processing. Casting must occur in inert atmospheres and pieces worked at high temperatures in air must either be protected through encapsulation in steel and other materials or their surfaces removed prior to subsequent steps. Of more consequence is the lack of protective oxides that form. Unlike Ni-based superalloys, which form an adherent scale of Al_3O_2 that prevents a continued ingress of O, the oxides formed by the refractory metals do not provide any noteworthy protection[58, 63, 64]. In the case of Mo and W, the oxides are particularly volatile and vaporize at intermediate to high temperatures, resulting in rapid disintegration of the sample when exposed to air[65, 66]. This limits the use of unprotected refractory alloys to applications with short lifetimes or inert environments unless their oxidation resistance is improved[35, 46, 49].

If the category of refractory metals is expanded to their frequent alloying agents, it should also be noted that V, another Group 5 element, behaves similarly to Nb and Ta. Cr, the other Group 6 element, behaves similarly to Mo and W though, uniquely among these elements, it is resistant to oxidation, forming a Cr_3O_2 scale that is protective to approximately 900 °C[67]. Nevertheless, it is still highly sensitive to nitridation[67]. The Group 4 metals, Ti, Zr and Hf, posses both hexagonal close packed (HCP, α) and BCC (β) allotrophs. The α form is stable at low temperatures and transforms to β at elevated temperatures. This transformation temperature increases from Ti to Zr to Hf, concurrent with melting point; the transformation temperature is also raised by the presence of interstitials. Due to the higher negative free energy of their interstitial compounds (e.g., nitrides), the Group 4 elements are also referred to as the reactive elements.

Of all the refractory elements, Nb, with a T_m = 2477 °C, a density lower than Ni, and possessing excellent room temperature ductility, rapidly become the principal element of choice for alloy developers except for the highest application temperatures. The strategy for developing Nb-based alloys has focused on maintaining its intrinsic ductility and fabricability while adding solute elements (primarily the other refractory metals) to increase high temperature strength and oxidation resistance. The overall strategy can be represented by[52]:

$$Alloy = Nb + M_{s.s} + M_{r.e} + M_i \tag{1.2}$$

where Nb is the the principal element, $M_{s.s}$ refers to substitutional solutes (Mo, Ta, V, W), $M_{r.e.}$ refers to additions of the reactive elements (Ti, Hf, Zr), and M_i refers to additions of interstitial elements (O, C, N). Substitutional solutes were added to improve the intrinsic strength of the Nb matrix, with V favored only for short term yield strength and low density; for significant improvements to creep strength, Mo and W additions were necessary (Figure 1.4). Additions of $M_{r.e.}$ elements provided two benefits. First, they provide an internal gettering effect by lowering the solubility of interstitials in the Nb matrix and forming a minor population of oxides, nitrides and carbides. These interstitial compounds can provide significant precipitation strengthening, even in small amounts, and therefore additions of M_i elements were added in conjunction with $M_{r.e.}$ additions to form oxide-, nitride-, or carbide-strengthened Nb alloys[38, 68]. The degree of strengthening that could be achieved compared to pure Nb is represented in Figure 1.5.

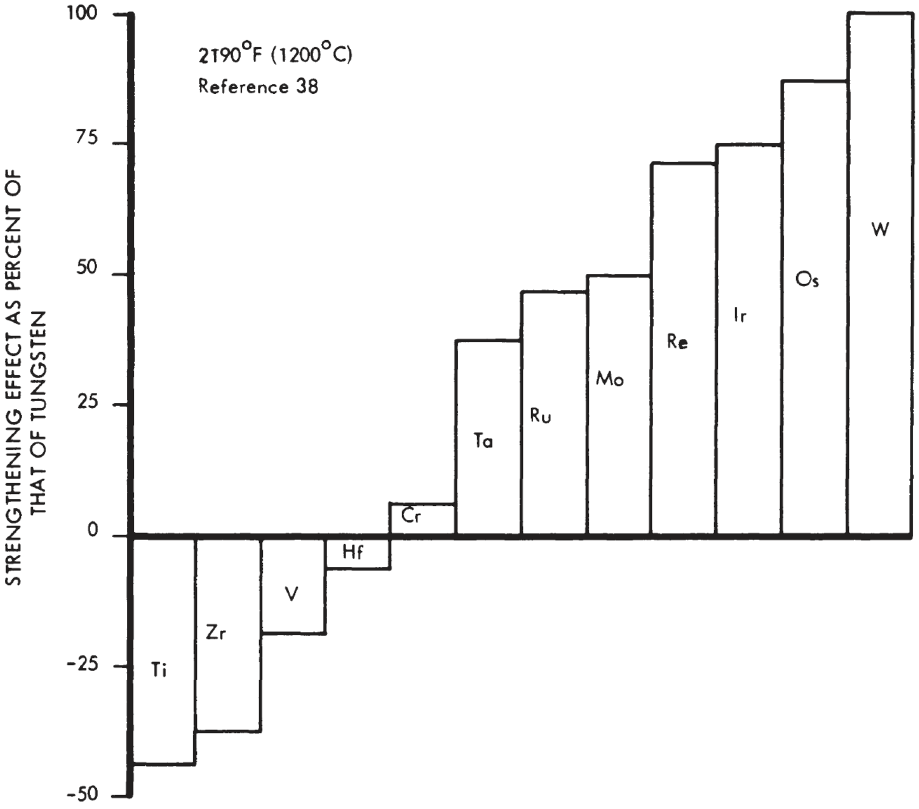

Figure 1.4: Effect of different subsitutional elements on the creep strength of Nb, normalized as a percentage of W. Reproduced from Begley, R. T., Harrod, D. L. & Gold, R. E. High Temperature Creep and Fracture Behavior of the Refractory Metals. in Refractory Metal Alloys Metallurgy and Technology (eds. Machlin, I., Begley, R. T. & Weisert, E. D.) (Springer New York, 1968)[52]. Reproduced with permission from Springer Nature.

However, it proved difficult to develop a Nb-based alloy with a balance of oxidation resistance, high temperature creep strength, and reasonable fabricability[46, 49]. The same alloying agents that promote high temperature strength and creep resistance (e.g., Mo and W) and oxidation resistance (e.g., Al and Cr) are highly detrimental to room temperature ductility and fabricability of Nb-based alloys, either through intrinsic embrittlement of the solid solution or through the formation of deleterious phases on the grain boundaries. Precipitation strengthening, particularly by carbide and nitride compounds, was extremely effective at improving creep strength but were ultimately mi-

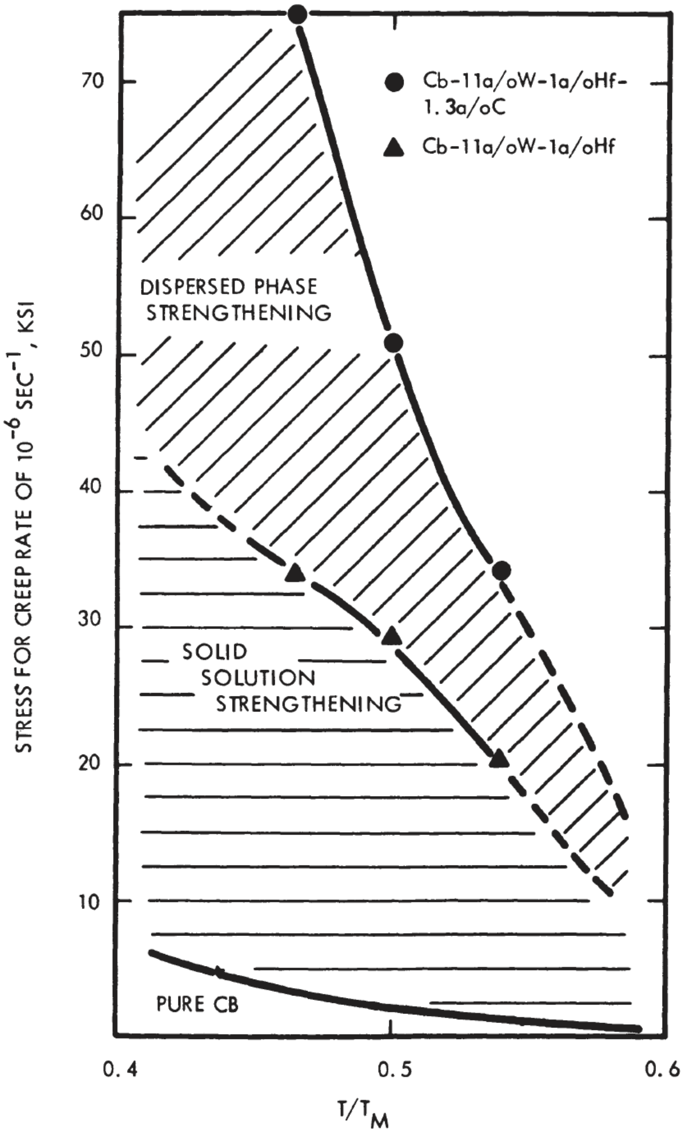

Figure 1.5: Changes in creep stress with homologous temperature of pure Nb (written here as columbium, Cb) and two Nb-based alloys. $T_{m,Nb}$ = 2477 °C. The effect of solid solution and precipitation strengthening decreases with temperature. Note that the labeled compositions are in at%, not wt%, and are ≈ 20 wt% W, 2 wt% Hf and 0.2 wt% C. Reproduced from Begley, R. T., Harrod, D. L. & Gold, R. E. High Temperature Creep and Fracture Behavior of the Refractory Metals. in Refractory Metal Alloys Metallurgy and Technology (eds. Machlin, I., Begley, R. T. & Weisert, E. D.) (Springer New York, 1968)[52]. Reproduced with permission from Springer Nature.

crostructurally unstable, resulting in particle coarsening and weakening at temperatures $\geq$ 1000 °C[38, 68] (discussed in more detail in section 1.4.1). In particular, oxidation resistance proved to be an insurmountable obstacle[49]. Enough Al to form Al_2O_3, the protective oxide of choice for high temperature applications, cannot be added to refractory alloys without resulting in the embrittlement. Similar restrictions exist for Si and Cr. The lack of intrinsic oxidation resistance therefore required the use of protective Si coatings or cladding alloys[49]. Even with protective coatings, the possibility of catastrophic failure in the case of coating damage remained and prevented the use of Nb-based alloys for critical components, where the need for high temperature structural materials is highest.

Example compositions of commercially-available low, moderate, and high strength Nb-based alloys circa 1968, close to the end of the first era of development, are presented in Table 1.1. Overall, the compositions are fairly uniform, with 10-30 wt% W or Ta, 1-3 wt% of a $M_{r.e.}$, and some addition of C. Some alloys included additions of V or larger additions of Hf. Notably, additions of Al or Cr, which improve oxidation resistance but are detrimental to fabricability, are not present, underscoring the difficulties in manufacturing alloys even with small improvements to oxidation resistance.

The first chapter of refractory development ended after making enormous strides in the physical metallurgy and manufacturing of the refractory metals. The discovery of large Nb deposits in Canada and Brazil in the mid-1950's allowed it to become a serious engineering material, joining Mo, Ta, and W[46]. At the time, only a handful of commercial refractory alloys existed, produced primarily though powder metallurgy for electronic applications; high quality, pure material could not be produced in large quantities; and equipment capable of high temperature testing was not available[35]. Within 15 years, dozens of alloys were commercially available after undergoing rigorous characterization from cryogenic to elevated temperatures[32, 35]. However, ultimately, the search for an

Table 1.1: Selected Nb-based alloys from the 1950-1970's period of alloy development. Adapted from the table collected by Frank[46].

			Nominal Composition, wt%									ppmw	
Category	Alloy	Original Investigator	Nb	Hf	Mo	Ta	Ti	V	W	Zr	C	O	N
High Strength and Low Ductility	Cb-1	General Electric	Bal						30	1	0.06	100	300
	B-88	Westinghouse	Bal	2					28		0.067	30	40
	F-48	General Electric	Bal		5				15	1	0.1-0.5	300	100
Moderate Strength and Ductility	FS-85	Fansteel	Bal			28			10	1	0.004	60	50
	Cb-752	Union Carbide	Bal						10	2.5	0.004	60	80
	PWC-11	Pratt & Whitney	Bal							1	0.1	150	100
Low Strength and High Ductility	C-103	Wah Chang/Boeing	Bal	10			1			0.7	0.015	225	150
	B-33	Westinghouse	Bal					5			0.006	120	60
	Cb-1Zr	-	Bal							1	0.005	100	50

alloy possessing high temperature creep resistance, oxidation resistance and good fabricability did not succeed prior to the termination of funding in the 1970's[34]. Only a few commercial refractory alloys are in service today as high temperature structure materials and they are largely solid solution strengthened alloys selected for their ability to be easily manufactured[47, 50]. These include C-103, Nb-1Zr, Mo-based TZM, and Ta-10W (all wt %).

1.3 The emergence of refractory high entropy alloys

A new alloy design concept has prompted a recent resurgence of interest in the refractory metals. Formally proposed in the mid-2000's by Cantor *et al.*[69] and Yeh *et al.*[70, 71], the 'high entropy' design strategy focuses on compositions towards the center of multicomponent phase space, with large additions of multiple constituents. High entropy alloys (HEAs) are a shift from a principal element approach, where a major element like Nb is selected for desirable properties and then alloyed, to a multi-principal element approach, where all elements are considered solutes and no matrix element exists. The name derives from the hypothesis that the higher configurational entropy that arises from the complex chemical solution would result in unusual and improved properties. The four key ideas of the high entropy hypothesis are[71, 72]:

1. The increased configurational entropy of the system will preferentially stabilize disordered solid solutions and suppress the formation of intermetallic phases.
2. The presence of multiple principal elements results in a highly distorted lattice, with significant effects on alloy properties.
3. Diffusion of solutes through the lattice will be sluggish due to variations in site energy as an atom moves through the lattice.

4. Instead of originating from the average, expected interactions between solutes, HEAs experience a 'cocktail effect' occurs where unusual properties can arise from the complex interactions of multiple principal elements.

The original definition of HEA is strictly based on composition. For an alloy to be an HEA it must contain at least five principal metallic elements, each with a composition between 5-35 at%[71]. The HEA hypothesis was originally motivated by observations of disordered solid solution phases in highly complex alloys drawn from the transition metals (e.g., the Al-Co-Cr-Cu-Fe-Ni and Co-Cr-Fe-Mn-Ni systems)[69, 70] but any metallic elements can be used. Minor additions are also allowed[73] and the alloy is not required to be a single disordered solid solution phase at all temperatures[70]. Interest in these materials grew rapidly, with an exponential growth in publications from 2004-2019 (Figure 1.6). Curiously, despite the early publications empathizing the formation of nano-scale secondary phases and multiple solid solution phases[69, 70], a tendency towards single phase equiatomic alloys arose within the community (see comments in [74] and [75]).

The first BCC HEAs primarily composed of the refractory elements were $Mo_{25}Nb_{25}Ta_{25}W_{25}$ and $Mo_{20}Nb_{20}Ta_{20}V_{20}W_{20}$ (all HEA compositions in at%) in 2011[76]. This was quickly followed by $Hf_{20}Nb_{20}Ta_{20}Ti_{20}Zr_{20}$ in 2012, which is frequently referred to as the 'Senkov' alloy[77]. While not the first HEA reported, the high tensile ductility and corresponding cold workability of $Hf_{20}Nb_{20}Ta_{20}Ti_{20}Zr_{20}$ has made it the best studied refractory high entropy alloy (RHEA) in the literature[78]. The motivation for investigating these materials is the same as those from the historical period of development— the drive to develop new high temperature materials that can surpass the capability of Ni-based superalloys and operate at temperatures $\geq$ 1300 °C[79]. The worldwide research efforts on HEAs represent the most significant effort to study refractory metal alloys in decades and hundreds of compositions have been been reported[80, 78].

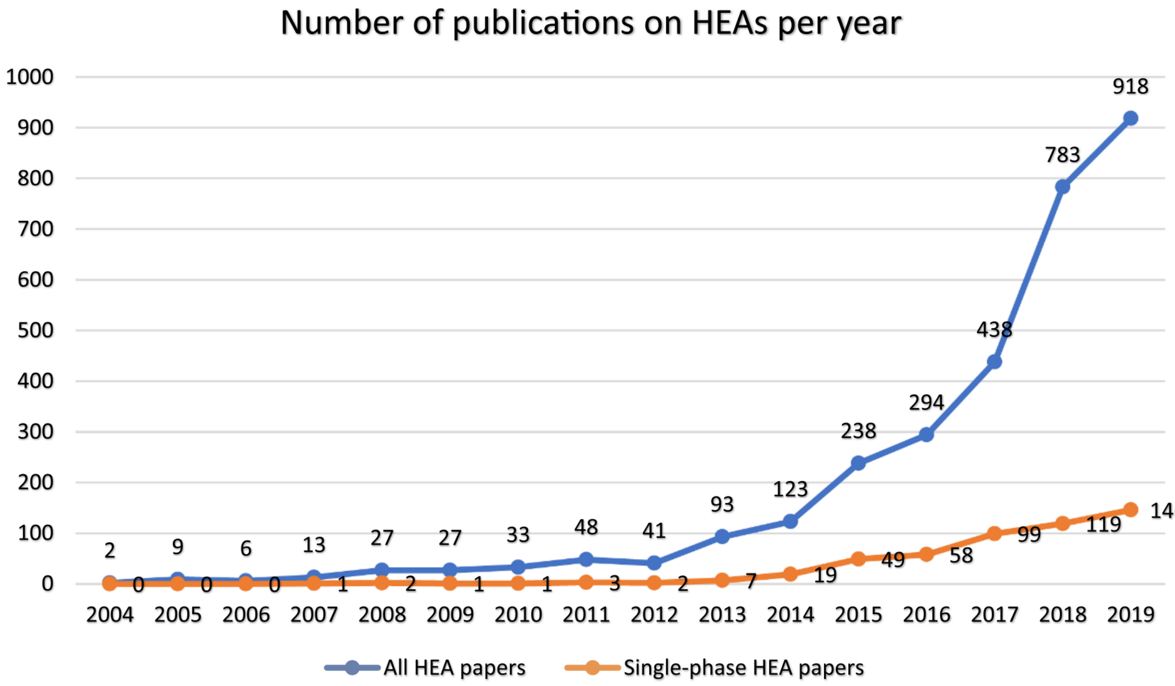

Figure 1.6: Rate of publication for manuscripts investigating high entropy alloys from 2004-2019. Reprinted from Steurer, W. Single-phase high-entropy alloys – A critical update. Mater. Charact. 162, 110179 (2020) [75]. Reproduced with permission from Elsevier.

With time, it is clear that most of the hypotheses that originally motivated the investigation of HEAs do not withstand further scrutiny[72, 74, 75, 81]. Evidence for sluggish diffusion has not been found[82, 83]. In terms of phase stability, many of the early HEA investigations were made on as-cast, sputtered, and rapidly solidified samples, which represent non-equilibrium conditions[69, 70, 84, 73]. This trend continued in RHEAs. Once aging studies began to be reported, it became clear that HEAs demonstrate phase formation that is consistent with their underlying phase diagrams. For example, it would be expected that large additions of Hf, Ti, and Zr would result in the formation of a second BCC or HCP phases at intermediate temperatures, due to the presence of these phase fields in the underlying binary and ternary systems. This is consistent with experimental investigations, where (Hf,Zr)-rich HCP phases and multiple BCC phases can form depending on temperature and composition[85, 86, 87].

Trends in mechanical properties reflect the trends in historical refractory alloys, only at a greater extreme of composition[54]. The high room temperature strengths of RHEAs can be related to their wide spread in lattice parameters or shear moduli[88] and the variation of yield strength with temperature is consistent with dilute BCC metals[54]. Materials with greater additions of Mo or W continue to be stronger at high temperature and remain necessary to improve creep resistance[78, 89, 90]. The large additions of Group 4 elements do introduce new complications. Due to their simple structures, additional HCP and BCC phases phases can form rapidly at intermediate temperatures during deformation. Mills *et al.* reported the formation of a (Nb,Ta)-BCC phase along the grain boundaries of a $Hf_{20}Nb_{20}Ta_{20}Ti_{20}Zr_{20}$ tensile sample tested at 800 °C for six minutes[91]. This resulted in a severe drop in ductility, from 16.0 % at room temperature to 2.0 % at 800 °C[91]. Unfortunately, RHEAs also demonstrate oxidation resistance comparable with their historical counterparts (i.e., poor)[21].

For these reasons, HEAs are now being referred to as compositionally complex or multi-principal element alloys by some sections of the community, removing the reference to an entropy-based effect. There is no longer a strict requirement for five or more elements. For the purposes of this dissertation, these RHEAs will be referred to refractory multi-principal element alloys (RMPEAs), which is used to denote a separation in alloy design strategy from historical alloys, even if the fundamental metallurgical behavior may be similar.

However, it is not necessarily demotivating for MPEs to behave like historical materials. The need for new high temperatures materials persists. One benefit is that the wealth of historical literature can be directly applied moving forward and can be further reassessed in light of modern theories and instrumentation. Advancements in other materials systems, like Ni-based and Co-based superalloys or TiAl, theoretically could provide guidance and tools to accelerate development[16, 92, 93, 94]. Additive manufacturing shows particular promise for reducing material waste and providing alternative processing pathways for refractory alloys[50, 95]. One particular research thrust is highlighted here: the use of computational tools and modeling.

Several new modeling capabilities are being applied to RMPEAs and dilute refractory alloys. Efforts to understand solute clustering[96, 97] and dislocation behavior[98, 99, 100] have been particularly intense. The deformation of BCC materials is classically understood to be controlled by the mobility of screw dislocations, but the compositionally complex lattice present in RMPEA solid solutions results in a fluctuating chemical environment that can change local slip resistances, therefore modifying the expected dislocation behavior[96]. These dislocation behaviors have implications for the origins of strength and ductility[101]. This fluctuating landscape is likely also applicable to historical refractory alloys with high solute additions (Table 1.1) and efforts to understand interstitial-induced embrittlement of refractory metals are in progress[102].

CALculation of PHase Diagram (CALPHAD) methods are a common tool for modern alloy design. These methods assess the underlying thermodynamic parameters of different phases and then construct phase diagrams; should a system be sufficiently characterized, predictions can be made on the phase stability of unexplored compositions[103, 104]. CALPHAD databases specific to RMPEAs have become recently available, though the ternary systems of the refractory metals are not well characterized and interstitials are not included, which limits the accuracy of CALPHAD predictions. However, investigations of the refractory ternary systems are underway, which is promising for future use of CALPHAD tools for refractory alloys[105, 106]. Improved understanding of dislocation motion and other fundamental behaviors can then be extended to predictions of bulk properties[107, 108]. These modeling capabilities can be combined to optimize multiple alloy properties simultaneously, accelerating design. For example, Rao *et al.* combined CALPHAD predictions with a mechanistic model for edge dislocation strengthening to rapidly screen for desirable strength and phase stability behaviors[109].

The biggest limitation for RMPEA alloy design lies in the lack of equipment available for thermo-mechanical processing and high temperature testing. Refractory alloys, particularly high strength alloys, are difficult to process and RMPEAs are usually tested in the as-cast condition under compression[78]. Given the sensitivity of refractory alloys to processing history and purity, this poses a major hurdle to research; compression testing also obscures many noteworthy behaviors, including the deleterious phase formation discussed earlier[91, 110]. Once material is produced, only a few facilities can perform mechanical tests above 1200 °C. However, capabilities are likely to improve should investments in RMPEAs continue.

In many ways, the contemporary era of RMPEA research is an inversion of the first era of refractory metallurgy. The RMPEA community has access to state-of-the-art characterization equipment and computational tools that did not exist in the 1960's, providing an opportunity to understand the fundamental behaviors of refractory metals beyond their macroscopic physical properties. However, unlike the commercial manufacturing facilities of the past, the RMPEA community currently lacks the facilities necessary to produce and test refractory materials for their intended applications. The processing of RMPEAs has been limited to materials that demonstrate significant cold working capability, which has sharply limited investigations of tensile properties or creep strength to RMPEAs composed of Hf, Nb, Ta, Ti, V and Zr[89, 111, 90]. These materials can exhibit significant short-term yield strengths but are unlikely to possess desirable creep strengths due to their low melting points, lack of Mo and W, or strengthening precipitates.

Some of these limitations are changing. The number of tensile tests being reported is increasing. Investigations of multi-phase materials are becoming more common (discussed in section 1.4.3). While the high entropy hypothesis itself was not been borne out by subsequent study, the HEA concept can be credited with reinvigorating the study of refractory metallurgy, bringing new ideas and new tools to bear on materials that have been neglected. As written by Cantor *et al.* in 2004, one of the original motivations for HEAs was ”to investigate the unexplored central region of multicomponent alloy space”[69]. This remains a laudable goal and has been the largest success of the investment in RMPEA research.

1.4 Strengthening of Nb-based alloys by second phases

Despite our improved fundamental understanding of these materials, from the motion of dislocations to the formation of protective oxides to the development of tools for rapid composition screening, the overall alloy design strategy remains unchanged from the conclusions of the 1970's. For a balanced material, it is necessary to alloy the ductile refractory elements with sufficient additions of Mo and W to improve creep strength. It is preferable that this element is Nb due to its lower density compared to Ta and its higher melting point compared to V. The strengthening additions must be limited to prevent high density or limited fabricability, and oxidation resistance remains an distant goal. It is clear that a single phase refractory alloy is unlikely to achieve the necessary combination of properties necessary for critical components at high temperature. Therefore, alternative strategies are necessary.

As noted in section 1.1, strengthening by second phases is a wide spread design strategy used for high temperature materials[10, 112]. Two-phase systems are composite materials that improve strength through the introduction of interfaces and other obstacles to dislocation motion, while also (when properly designed) maintaining the necessary toughness required of critical components. Two-phase materials are typically composed of one ductile phase (for the Nb-based alloys, this phase is a disordered Nb solid solution) and one higher strength, less ductile phase (typically an ordered intermetallic). Nb-based alloys with strengthening phases can generally be broken into three classes: (i) precipitation strengthening with additions of interstitials like O, N, and C; (ii) eutectic Nb silicides; and (iii) precipitation strengthening with coherent intermetallic phases. These materials demonstrate much higher creep and yield strengths than those demonstrated by solid-solution strengthened Nb-based alloys and represent a path forward for achieving balanced mechanical properties.

1.4.1 Precipitation strengthening by interstitial additions

The first attempts to develop two-phase Nb-based alloys focused on interstitial compounds (e.g., oxides, nitrides, carbides) as the strengthening second phase[113, 34]. These efforts occured during the 1960-1980's and continued in the Soviet Union after the termination of refractory research in the United States[38, 68]. Strengthening by interstitial compounds is desirable because of the low cost and density of interstitial additions, and its ability to be combined with solid solution strengthening. While the presence of interstitials within the Nb solid solution is highly detrimental to ductility, the presence of a reactive element (Ti, Hf, Zr) sharply reduces the solubility of interstitials within Nb[38, 114]. Instead, the interstitial content is trapped within interstitial compounds that, when appropriately distributed, improve strength without embrittlement of the solid solution. The interstitial compounds are unshearble obstacles and only low volume fractions ($v_f \leq 5$ %) could be practically achieved; therefore, the precipitates had to be very small (radius <50 nm) to achieve effective strengthening via the Orowan bowing mechanism[38, 68, 115]. When successful, precipitation strengthening was shown to be much more effective than solid solution strengthening at improving creep strength: when equivalent of additions of HfC and W were added to Nb, the HfC was 20 times more effective then W (see Figure 6 in [46]).

Due to the low solubility of interstitials within Nb in the presence of a reactive element, the processing temperatures for Nb-based alloys strengthened by interstitial compounds were very high. Annealing temperature of 1700 °C and above were common[46, 116]. The optimal processing pathways for Cb-1 and B-88, both carbide-containing alloys with excellent creep rupture strengths (Table 1.1), required solution temperatures above 1900 °C[46].

It should be noted that many Nb-based alloys are functionally strengthened by interstitial compounds, even in the absence of intentional interstitial additions. The internal gettering provided by additions of the reactive elements results in populations of intersitital phases, typically oxides, that are present in most commercially pure material. The size and distribution of these phases can be controlled by thermomechanical processing steps[46]. For example, the 1200 °C creep rupture life and creep strength of Cb-1Zr, a low strength alloy without intentional interstitial additions, can be improved by applying a high temperature anneal (1700 °C); the change in mechanical behavior was attributed to the solution and strain-induced reprecipitation of ZrO_2[46, 117].

The major limitation of the interstitial compounds was their lack of microstructural stability above 1000 °C due to their incoherency with the Nb matrix[34, 113]. Rapid overaging occurred at the desired application temperatures and the precipitates could not maintain the small sizes necessary for effective strengthening[38, 115]. Some strategies to reduce the rate of coarsening have been proposed in the literature, but ultimately a microstructurally stable alloy has not yet been reported. For example, in Sheftel *et al.*'s review of Nb-based alloys, it is noted that reactive element atom:interstitial atom ratios >1 (i.e., an excess concentration of the reactive elements) in the solid solution accelerated coarsening; conversely, reactive element atom:interstitial atom ratios <1 reduced coarsening[68]. Of greatest interest is the observation by Cornie *et al.* of a coherent carbonitride phase in a Cb-22W-2Hf-0.05C-0.04N (wt %) alloy[118], but they were unable to reproduce the phase during further investigation[119].

1.4.2 The Nb-silicides

Eutectic alloys are desirable as *in situ* composite materials. Distinct from precipitation strengthening, the microstructures of eutectic composites are formed at the solidifcation step, not through thermo-mechanical processing. The eutectic transformation allows for the formation of the ductile and strengthening phases to happen in one step, resulting in two-phase materials with homogeneous microstructures that are stable to temperatures near their melting points[120]. The fine inter-phase spacings that are achievable and high temperature stability result in materials capable of significant creep resistance at elevated temperatures[120, 121]. The niobium silicide (Nb-Si) system is one example of a refractory eutectic system, with a high eutectic temperature of 1915 °C[122] between a niobium solid solution and an intermetallic silicide (Figure 1.7). Research on the Nb silicides began in the 1990's[44].

Nb silicides are composed of a Nb-based solid solution (Nb_{ss}) and at least one of the Nb-Si phases: Nb_3Si, α-Nb_5Si_3 and β-Nb_5Si_3[124]. Initial Nb-Si alloys were based on the eutectic and eutectoid reactions on the right side of the Nb-Si binary phase diagram[123, 125]. The transformation pathway to the final microstructure is the Nb_{ss} and Nb_3Si eutectic reaction, followed by a eutectoid transformation of Nb_3Si to Nb_{ss} and tetragonal Nb_5Si_3 (α-Nb_5Si_3). The early alloys demonstrated extremely low oxidation resistance at high temperatures and poor fracture resistance[125]. Large amounts of Ti were added to improve the oxidation resistance and ductility at high temperature, followed by small additions of Hf to improve oxidation resistance at lower temperature regimes[45]. Later

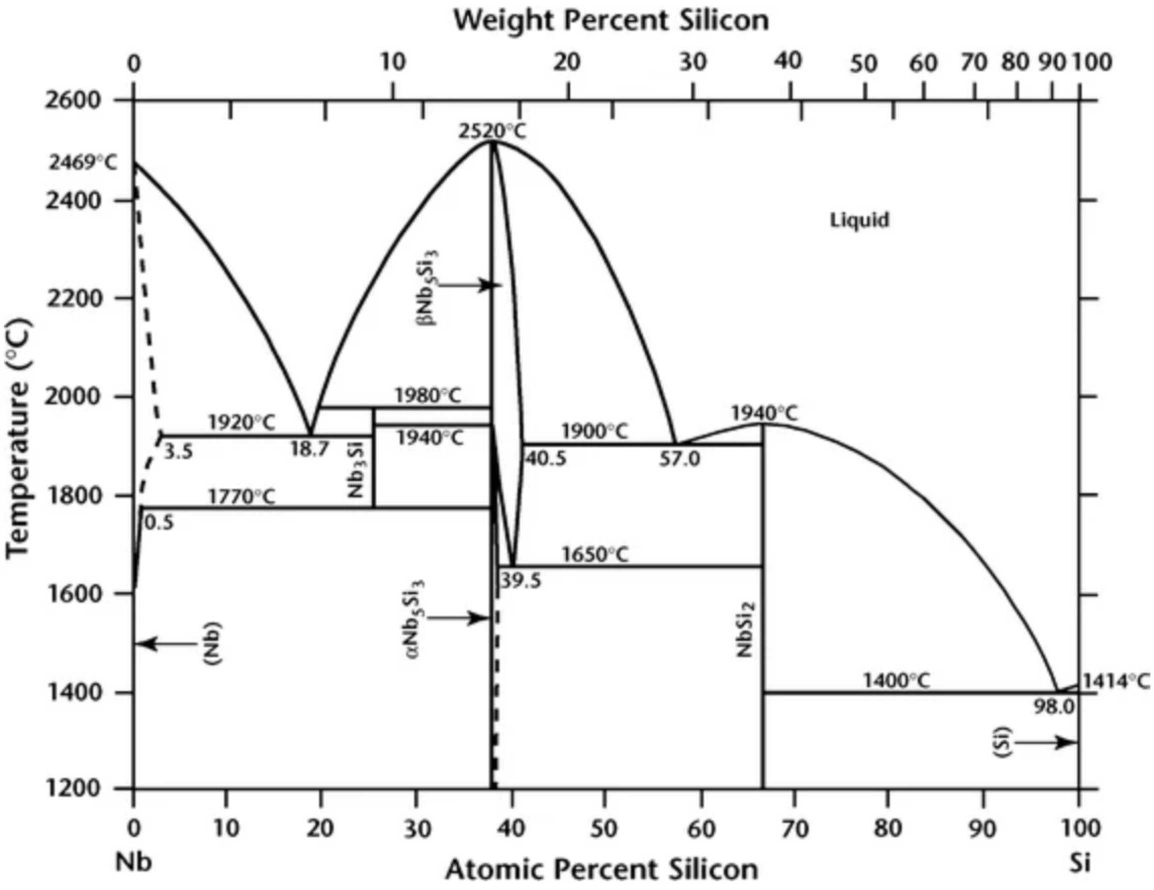

Figure 1.7: Nb-Si binary phase diagram. Nb silicide alloys are based on the compositions between 0-40 at% Si. Reproduced from McKeown *et al.* Silicide characterization at alumina-niobium interfaces. J. Mater. Sci. 46, 3969–3981 (2011). Reproduced with permission [123].

generations of Nb silicides contain significant α stabilizers (e.g., Cr, Al), suppressing Nb_3Si and resulting in direct solidification of Nb_{ss} + α-Nb_5Si_3[126], resulting in improved fracture toughness and strength (Figure 1.8). Recent β-Nb_5Si_3 alloys are Nb silicides with large additions of Mo or W, which stabilizes the high temperature β-Nb_5Si_3 phase to lower temperatures and suppresses α-Nb_5Si_3[127, 128]. β-Nb_5Si_3 alloys exhibit poor oxidation resistance, but they demonstrate desirable lamellar microstructures[129, 130].

Nb silicides are highly studied compared to other classes of Nb-based alloys and the closest to meeting necessary creep and toughness targets for turbine components[132, 124,

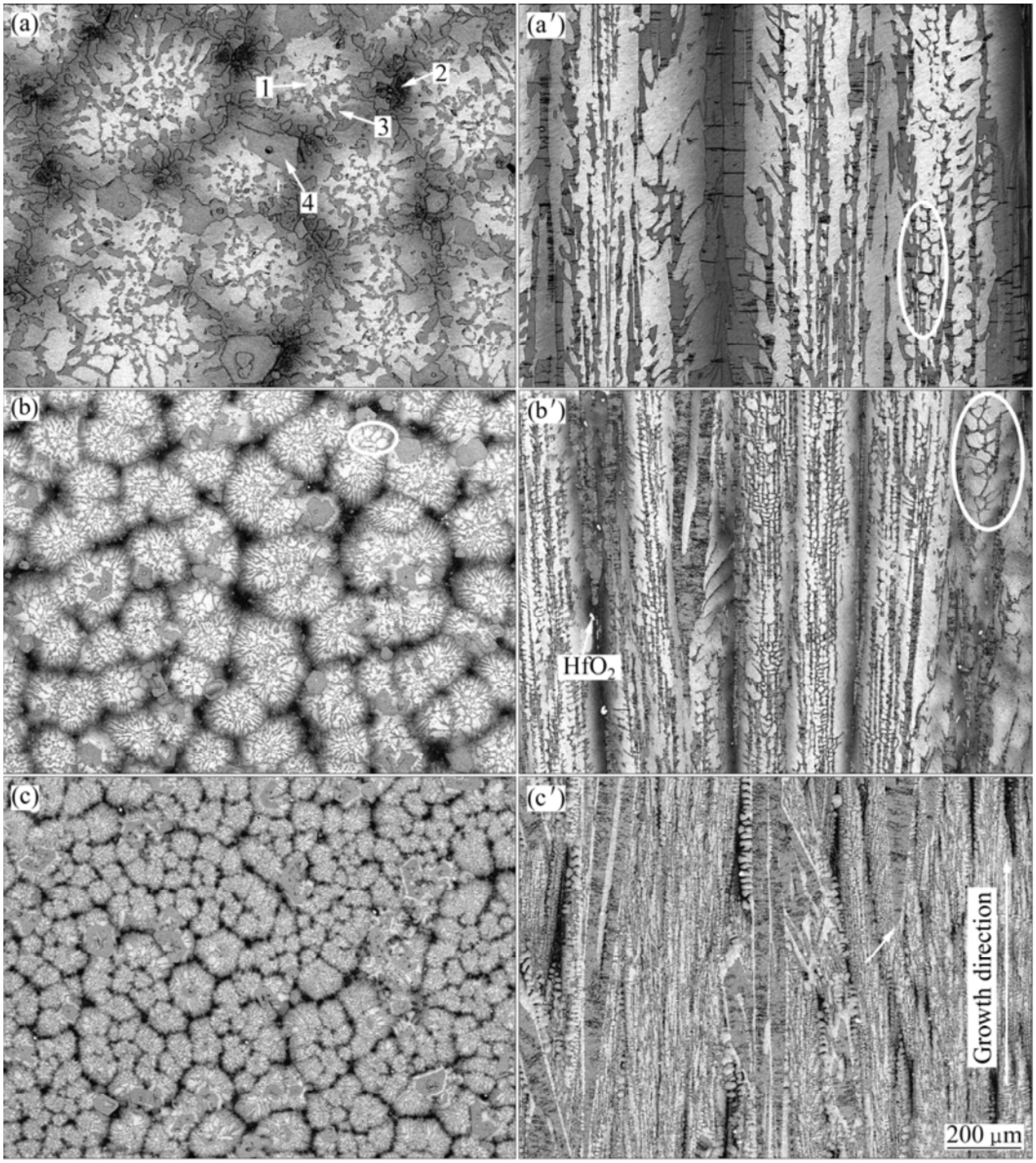

Figure 1.8: Example microstructures of a directionally solidified Nb-Ti-Si based alloy at different withdrawing rates. a-b. are transverse and a'-c'. are longitudinal sections. The bright phase is the Nb_{ss} and the dark phase is α-$(\mathrm{Nb,Ti,Hf})_5\mathrm{Si}_3$. Reprinted from Guo, H. S. & Guo, X. P. Microstructure and microhardness of directionally solidified and heat-treated Nb-Ti-Si based ultrahigh temperature alloy. Trans. Nonferrous Met. Soc. China (English Ed. 21, 1283–1290 (2011)[131]. Reproduced with permission from Elsevier.

133]. Due to the high Si content, they have densities around 7 g/cm^3 and achieve superior oxidation resistance compared to conventional Nb-based alloys, though long-term oxidation resistance is still insufficient. Programs are currently underway to develop manufacturing methods for producing complex components, including through additive manufacturing, investment casting, and directional solidification[133]. In particular, directional solidification, which aligns the silicide and solid solution phases to improve strength and fracture toughness, has been extensively investigated[134, 135, 136, 137]. However, the low room temperature fracture toughness of the Nb silicides, related to challenges in controlling the two-phase microstructure, continues to be a major hurdle to commercialization[133].

1.4.3 Mimicking γ/γ': the refractory superalloys

Strengthening by a large volume fraction of coherent intermetallic precipitates is a highly appealing strategy. The low interfacial energy between the strengthening phase and the matrix reduces the driving force for coarsening and results in improved microstructural stability, which was the point of failure for strengthening by interstitial compounds[4, 112]. Applying this approach to the Nb-based alloys is an attempt to replicate the enormous success of γ/γ' Ni-based superalloys, which are the prototypical materials for extreme environments, only at higher temperatures. Alloys pursuing this strategy are considered $\beta + \beta'$ alloys, where β is a disordered BCC matrix and β' is an ordered derivative of the BCC phase that acts as the strengthening precipitate, though the concept of coherent strengthening phases extends back to the coherent interstitial phase mentioned in section 1.4.1.

Many strengthening intermetallics have been investigated, focused primarily on B2 (CsCl) or Heusler (L2$_1$, AlCu$_2$Mn) phases. However, most $\beta + \beta'$ materials remain in an incipient stage of development. Efforts have focused on achieving the desired microstructure or thermal stability, but rarely progress past initial studies of phase equilibria. Earlier reports discussed phases derived from Al and platinum-group additions in Nb-based alloys, such as investigations into PdAl-B2 and Pd_2HfAl-$L2_1$ by Ghosh *et al.* and Misra *et al.*[138, 139]. More recently, Knowles *et al.* used Fe additions, desirable due to their low cost, to precipitate the TiFe-B2 phase in a (W)-BCC matrix[140]. Within the RMPEA community, Panina and Yurchenko *et al.* have investigated HfCo- and TiCo-B2 phases in equilibrium with (Mo,Nb)-BCC phases[141, 142, 143]. Most of these systems have only a few studies investigating their properties, but some demonstrate promise when an appropriate BCC/B2 pair is selected.

A clear example of the potential and challenges of $\beta + \beta'$ alloys is the Cr (β) + NiAl (β') alloys. Cr (a_{Cr} = 2.878 Å [144]) and NiAl-B2 (a_{NiAl} = 2.860-2.930 Å[145]) have very close lattice parameters, resulting in a misfit below 1 % without alloying. The constituent elements are lightweight and relatively inexpensive. NiAl can also exhibit solvus temperatures up to 1400 °C and and the coarsening rate is very low from 1000-1200 °C, which were the highest temperatures evaluated[146]. However, the greatest limitation for Cr-based $\beta + \beta'$ alloys is the lack of room temperature ductility exhibited by Cr[147]. Cr can exhibit a DBTT below room temperature, but is highly sensitive to impurities, particularly N, and surface condition, leading Cr to be classified as a brittle material. There are potential strategies, such as alloying with Re or reactive elements, that can improve the room temperature ductility of Cr but these have yet to be applied to Cr + NiAl alloys[146].

The $\beta + \beta'$ alloys that have received the most attention are RMPEAs where the B2 phase is derived from Al, Ti and Zr additions[148]. Initially discovered by Naka and Khan in the 1990's[149], these alloys were rediscovered by the RMPEA community in the 2010's[150, 151, 152, 153]. (Al,Ti,Zr)-B2 alloys can have various microstructures, including ordered B2 precipitates embedded in a disordered BCC matrix[154, 155, 156], 'basketweave' microstructures with no distinct matrix phase[157, 158], and 'inverted' microstructures with with an ordered B2 matrix and disordered BCC precipitates[152, 159, 160, 161]. The most common microstructure is the 'inverted' type and these microstructures most closely match the cuboidal γ/γ' microstructures observed in superalloys, with highly coherent BCC phases embedded in thin channels of B2 matrix[162, 163, 161](Figure 1.9). These microstructures are formed either via spindoal decomposition of two BCC phases upon cooling and concurrent ordering of the (Ti, Al, Zr)-rich phase to a B2 structure, or by conventional precipitation reactions, depending on Al composition of the alloy[164, 162, 165]. Zr, with its large binary BCC miscibility gaps with Nb and Ta, drives the formation of the two phase microstructures[164]. Investigations into the mechanical properties of these materials indicate they can possess high yield strengths up to the solvus temperature, after which they weaken rapidly due to the low melting points of the constituent elements[153, 157]. Creep strength has yet to be reported.

The presence and composition of the (Al,Ti,Zr)-B2 phase is surprising because, while a BCC to B2 ordering reaction can be found in many Al-Ti-X ternaries (where X = Group V, VI elements)[166, 167, 168, 169, 170], the stability of this phase in the Al-Ti-Zr ternary remains in dispute[171, 172, 173]. Disorder to order transitions also involve the gradual ordering of a single disordered crystal structure to an ordered one- in this case, the transition of a disordered BCC phase to an ordered B2 intermetallic- rather than a phase field where two distinct BCC and B2 phases are in equilibrium. The major limitations that prevent further development of (Al,Ti,Zr)-B2 alloys can be traced to this lack of stability in the underlying binary and ternary systems[174, 175].

There are currently two major limitations to (Al, Ti, and Zr)-based $\beta + \beta'$ alloys. The first is the degradation and erasure of the desirable $\beta + \beta'$ microstructure after annealing due to the widespread stability of deleterious phases[176, 177, 158]. Brittle

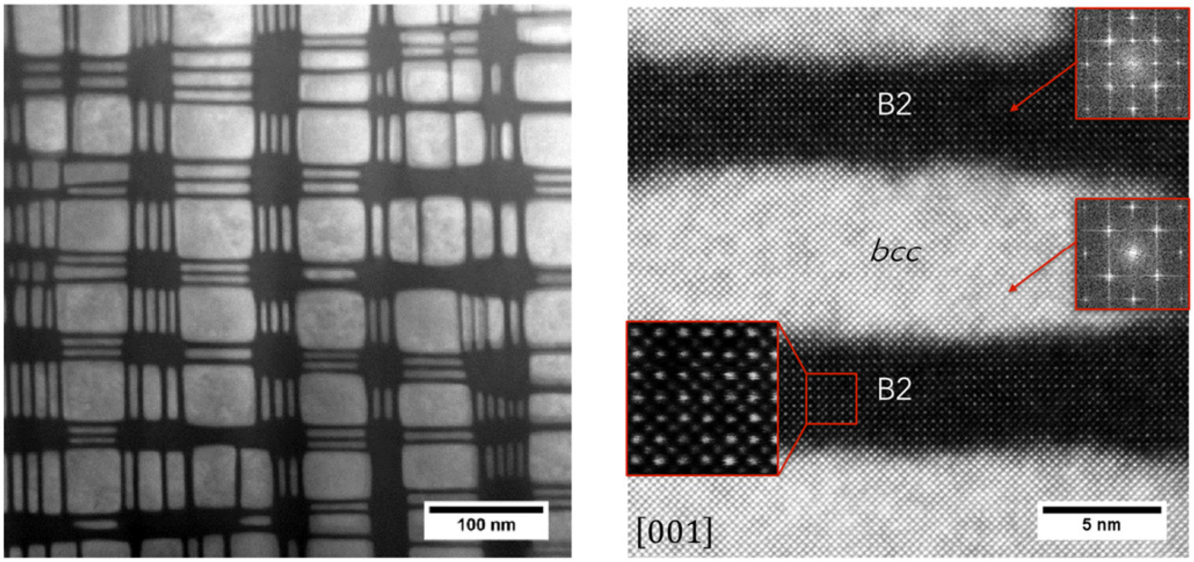

Figure 1.9: STEM-HAADF images of BCC + (Al, Ti, Zr)-B2 structure within $Al_{20}Mo_{10}Nb_{20}Ta_{10}Ti_{20}Zr_{20}$. A. Cuboidal and plate-like precipitates of a disordered BCC phase within a (Al,Ti,Zr)-B2 matrix. B. Fast Fourier transforms for each phase are marked within the red boxes. These reveal a disordered BCC structure for the bright precipitates and an ordered B2 structure for the dark matrix channels. Reprinted from Senkov *et al.* Compositional variation effects on the microstructure and properties of a refractory high-entropy superalloy AlMo0.5NbTa0.5TiZr. Mater. Des. 139, 498–511 (2018) [159]. Reproduced with permission from Elsevier.

(Al,Zr)-rich phases are frequently observed in these materials and can form after short exposures at both the grain boundaries and grain interiors[178, 177]. These phases can coexist with the BCC and B2 phases, resulting in embrittlement, or the B2 phase itself can transform into ordered omega-type phases[179, 158, 110]. Second, and most crucially, the thermodynamic instability of the B2 phase also translates to low B2 solvus temperatures-to date, the (Al, Ti, Zr)-B2 phase has not been stabilized above 1200 °C[180].

1.5 Motivation for Ru-based $\beta + \beta'$ alloys

Two-phase materials continue to demonstrate the best combination of strength and ductility of all Nb-based alloys. However, both historical and modern materials demonstrate limitations that need to be overcome before Nb-based alloys could compete with Ni-based superalloys. Namely, these limitations are the microstructural instability of interstitial compounds (discussed in section 1.4.1), the low fracture toughness of the Nb-silicides (discussed in section 1.4.2) and the thermal instability of (Al,Ti,Zr)-B2 phases (discussed in section 1.4.3). One way to address these issues is to find a precipitate coherent with a ductile Nb-based matrix and which has a thermal stability higher than that of the (Al,Ti,Zr)-B2 phases.

An alternative B2 former is Ru, a platinum group element with a $T_{m,Ru} = 2334$ °C. Ru is a robust B2 former, forming B2 phases with six of the refractory elements, Al, and Si in their binary systems. With Nb, Ta, and V, the B2 phase is the result of a disorder to order transition of the pure BCC phase to an ordered B2 intermetallic with increasing Ru content[181, 182, 183, 184] (Figures 1.10-1.12). This is undesirable and unlikely to produce the desired precipitation reaction. Ru interactions with Hf, Ti, and Zr are more promising: a BCC + B2 phase field exists at elevated temperatures above the α to β transformation temperature[185, 186](Figures 1.13-1.15). While the β-Zr + ZrRu-B2 phase field has a eutectic temperature of 1240 °C, the eutectic temperature for Hf-Ru is 1610 °C, much higher then the current soluvs temperature limitations for the (Al,Ti,Zr)-B2 RMPEAs[186]. The TiRu-B2 phase has a thermal stability similar to HfRu[185]. While the melting temperature of Ti is lower than Hf and Zr, the Ti-Ru system lacks a eutectic on the Ti-rich side of the phase diagram and the solidus temperature of the β-Ti + TiRu-Ru phase field lies at 1575 °C. The thermal stability of the TiRu-B2 and HfRu-B2 phases is promising and the large number of B2 phases suggests that the composition of the B2 phases can be tailored to adjust its properties. While most of the Ru-based B2 phases are significantly smaller than pure Nb ($a_{Nb} = 3.301$ Å[181]), Nb can theoretically be alloyed to be coherent with the largest of the B2 phases, HfRu (a_{HfRu}

= 3.225 Å[187]) and ZrRu (a_{ZrRu} = 3.253 Å[188]). This simple analysis suggests HfRu is the most favorable of the Ru-B2 phases, ignoring considerations of cost or density.

Ru therefore presents an opportunity to form both coherent and thermally stable precipitates. This hypothesis assumes that the phase equilibria present within the binary and ternary systems will persist into multi-component solutions, which is unknown due to the lack of available Ru ternary diagrams. In this dissertation, we explore this question and use it to evaluate the potential of using Ru-based B2 phases as coherent intermetallic precipitates for Nb-based alloys. Ch 2. discusses an investigation of the phase equilibria of $Hf_{20}Nb_{20}Ta_{20}Zr_{20}Ru_{20}$ from 1350-1575 °C, which leads to the first observation of a Ru-based B2 phase in an RMPEA. In Ch. 3, the microstructures of a series of equiatomic Ru-containing RMPEAs are examined by scanning electron and transmission electron microscopy. The high Hf and Ru compositions of these RMPEAs resulted in the concurrent solidification of BCC and B2 phases from the liquid, demonstrating the robustness of Hf as a Ru-B2 former. The insights gained from these materials are leveraged to design solution and ageable HfRu-containing alloys in Ch. 4. One of these alloys was also designed to have a low misfit between the B2 and BCC phases, successfully resulting in cuboidal precipitates. In Ch 5. the B2 solvus lines and potential deleterious phase formation of HfRu- and ZrRu-containing alloys are investigated. In Ch. 6, design guidelines and outstanding questions for further development of Ru-based $\beta + \beta'$ are discussed.

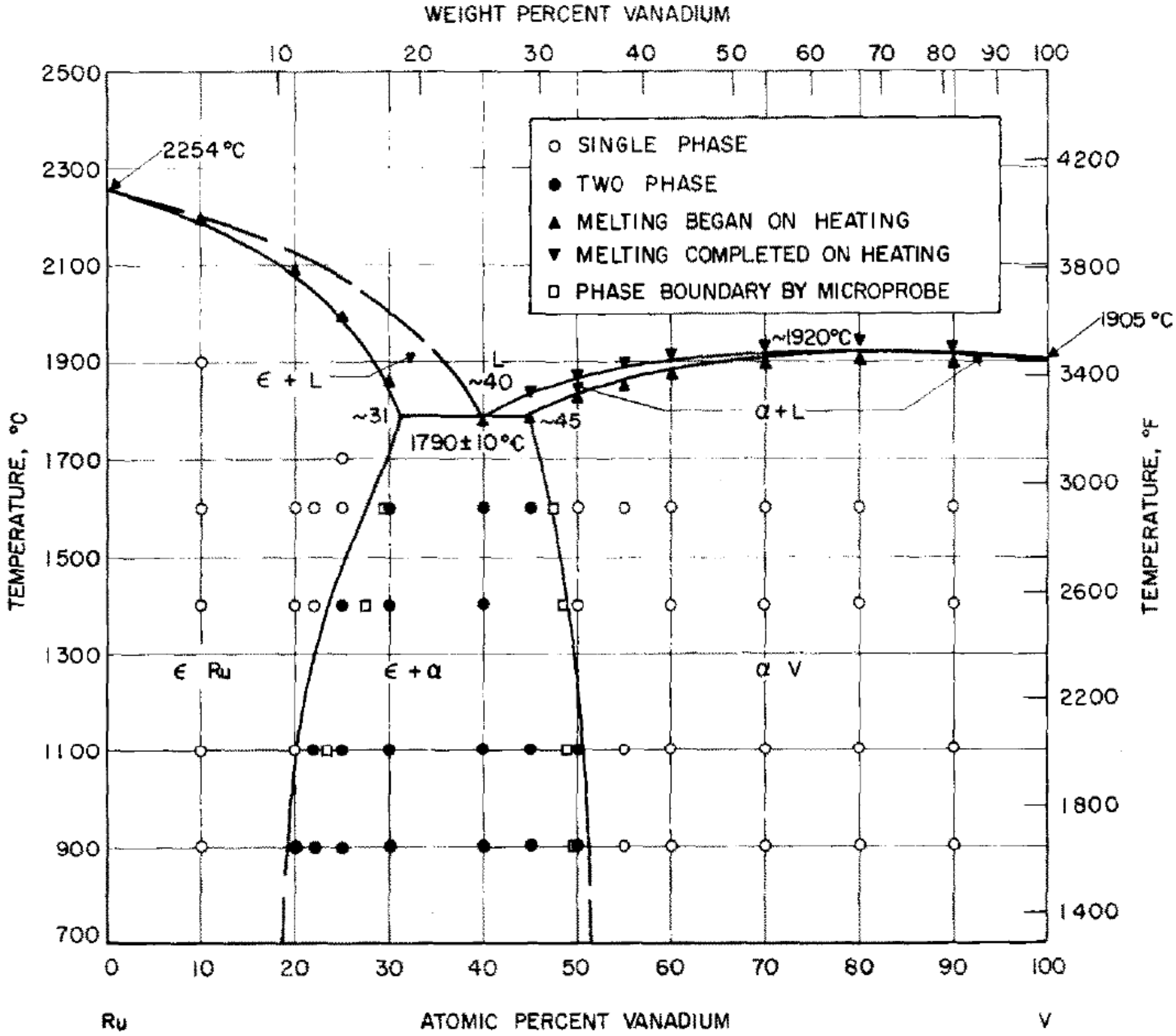

Figure 1.10: The V-Ru phase diagram. α-V is a V-rich solid solution that is BCC at low Ru concentrations and which exhibits B2 ordering at high temperatures and Ru concentrations above 20 at%. Reprinted from Waterstrat, R. M. & Manuszewski, R. C. The vanadium-ruthenium constitution diagram. J. less-common Met. 48, 151–158 (1976) [183]. Reproduced with permission from Elsevier.

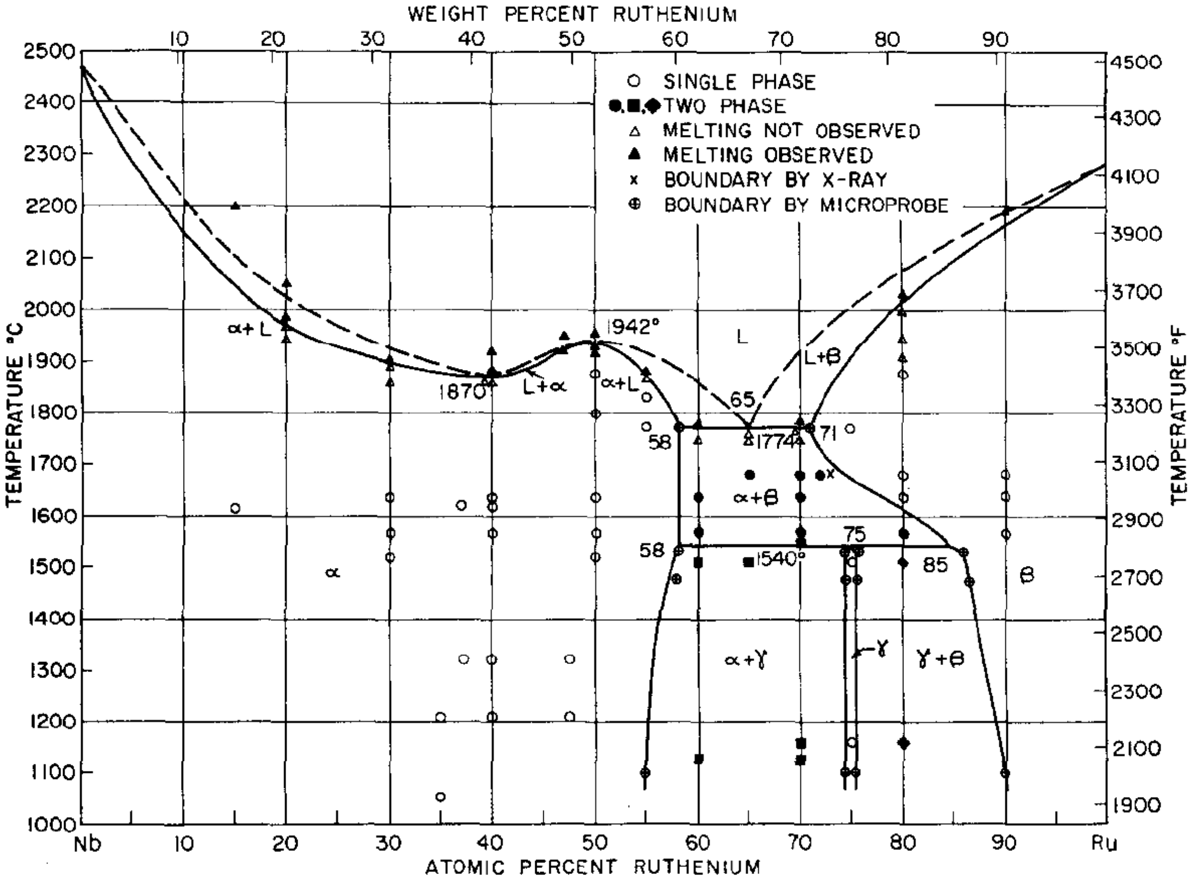

Fig. 3. Niobium–ruthenium diagram.

Figure 1.11: The Nb-Ru phase diagram. α-Nb is a Nb-rich solid solution that is BCC at low Ru concentrations and which exhibits B2 ordering at high temperatures and Ru concentrations above 40 at%[182]. Reprinted from Hurley, G. F. & Brophy, J. H. A constitution diagram for the niobium-ruthenium system above 1100C. J. less-common Met. 7, 267–277 (1964) [181]. Reproduced with permission from Elsevier.

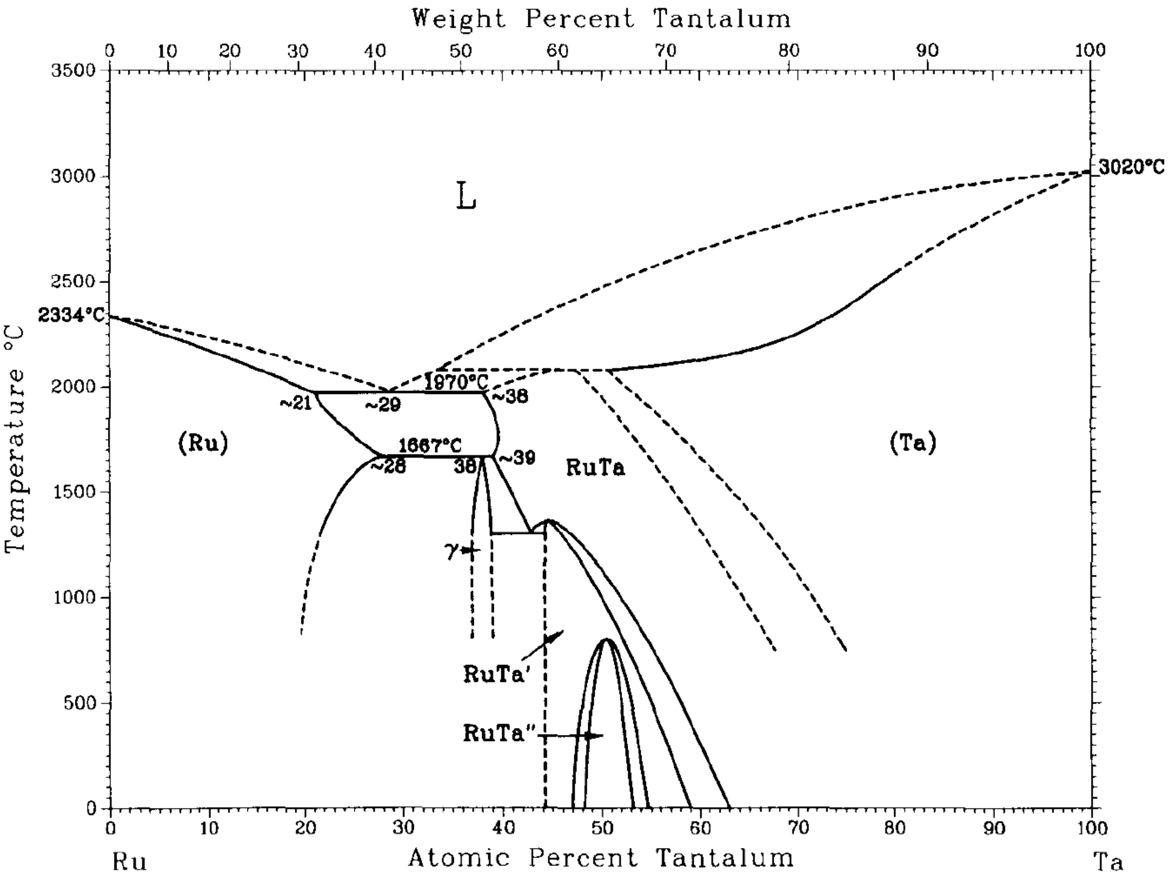

Figure 1.12: The Ta-Ru phase diagram. TaRu is the B2 phase, with different crystal structures forming at lower temperatures. Reproduced from Okamoto, H. Ru-Ta (Ruthenium-Tantalum). J. Phase Equilibria 12, 395–397 (1991) [184]. Reproduced with permission from Springer Nature.

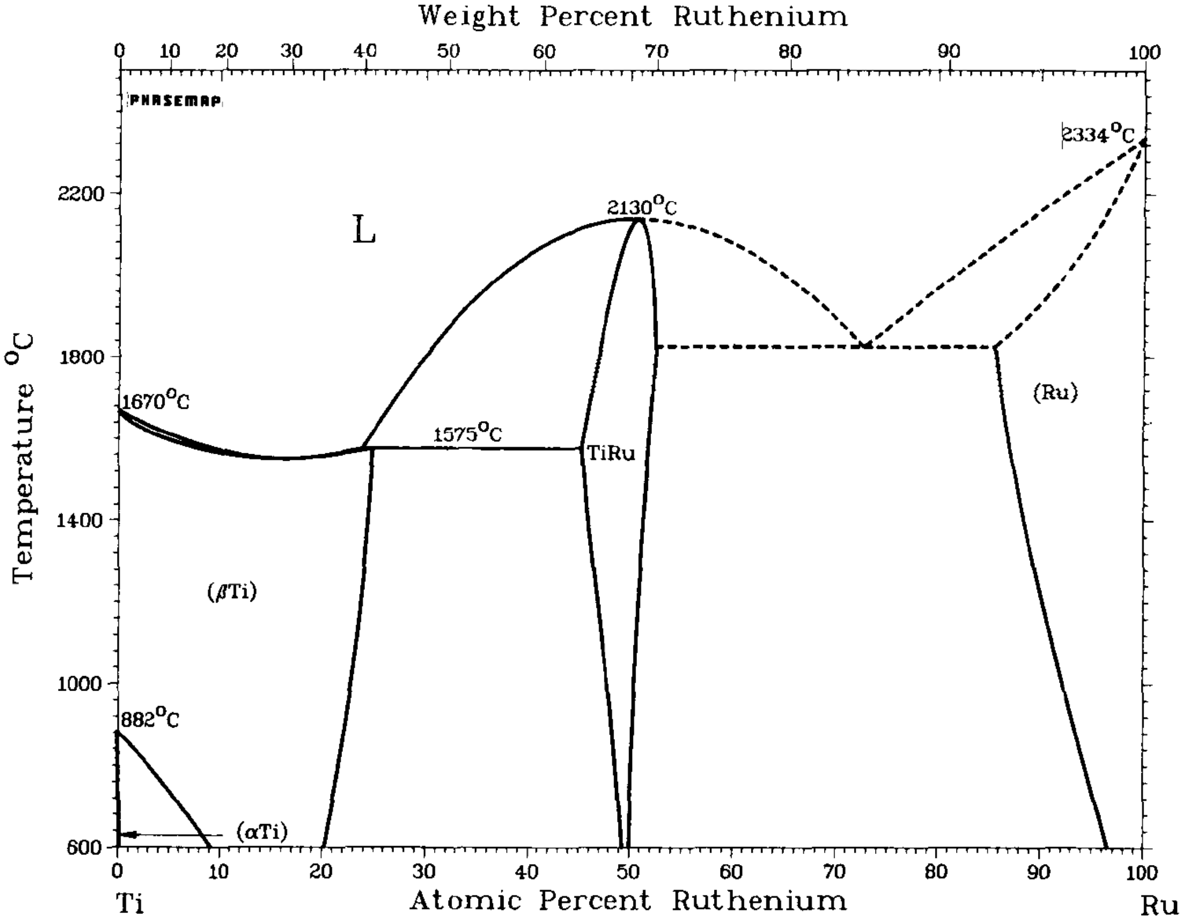

Figure 1.13: The Ti-Ru phase diagram. TiRu is the B2 phase. Reproduced from Murray, J. L. The Ru-Ti (Ruthenium-Titanium) system. Bull. Alloy Phase Diagrams 3, 216–221 (1982) [185]. Reproduced with permission from Springer Nature.

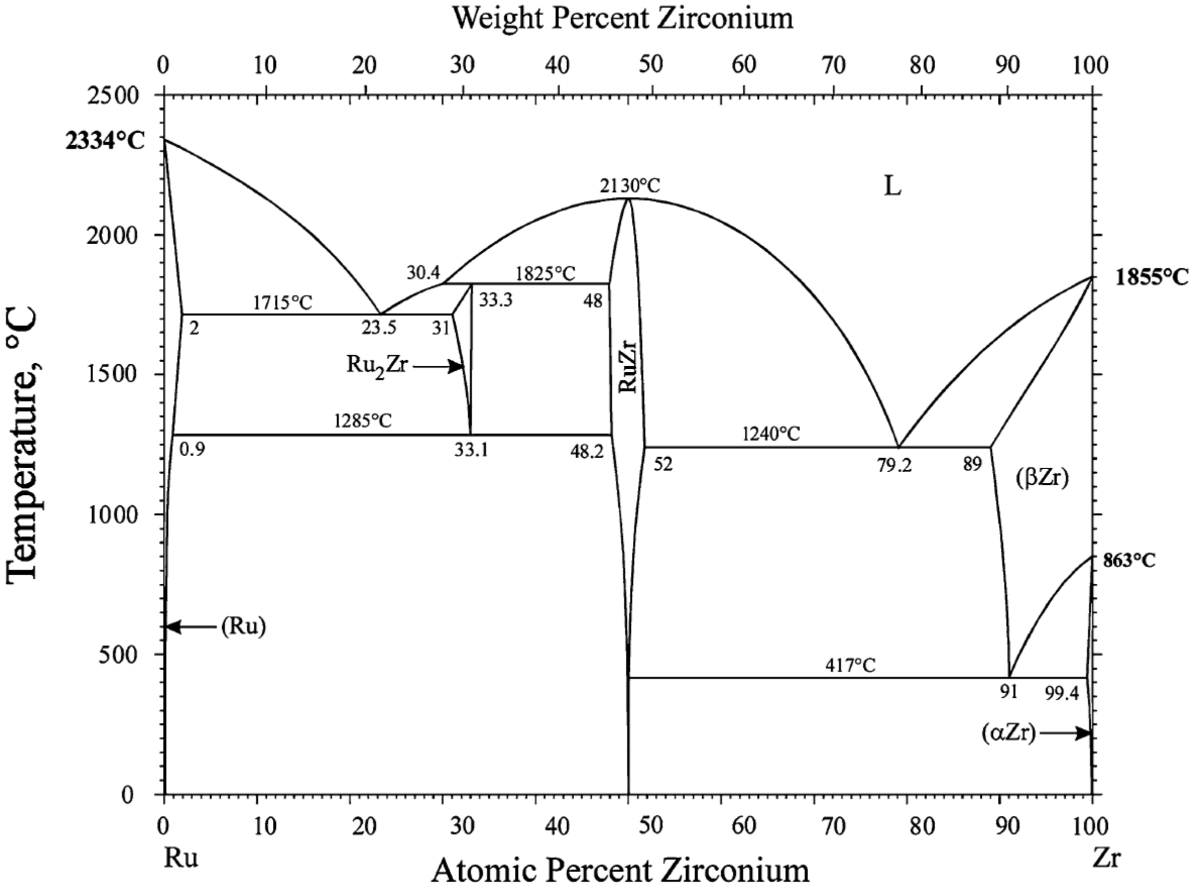

Figure 1.14: The Zr-Ru phase diagram. ZrRu is the B2 phase. Reproduced from Okamoto, H. Ru-Zr (Ruthenium-Zirconium). J. Phase Equilibria Diffus. 33, 82 (2012)[189]. Reproduced with permission from Springer Nature.

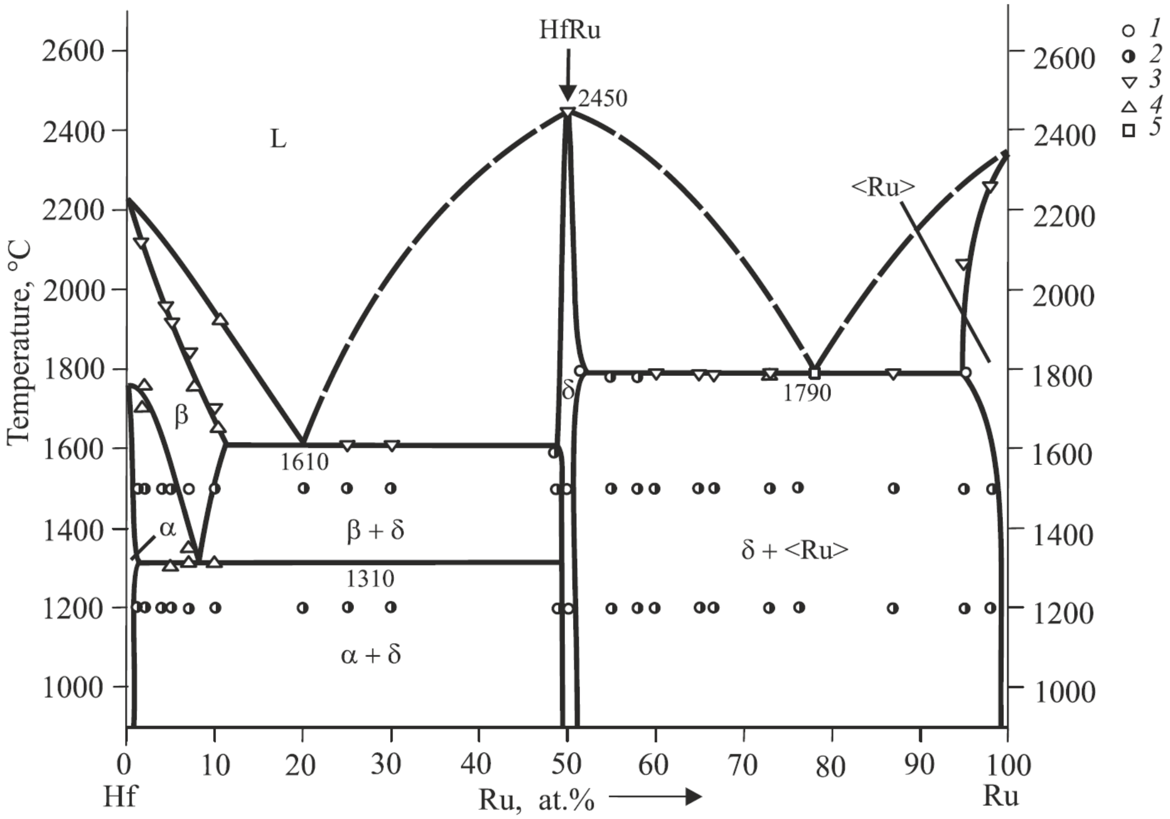

Figure 1.15: The Hf-Ru phase diagram. δ is the HfRu-B2 phase. Reproduced from Kryklya, L. S. *et al.* Physicochemical materials research: Alloy constitution and phase equilibria in the Hf-Ru-Rh system. I. solidus surface of the partial Hf–HfRu–HfRh system. Powder Metall. Met. Ceram. 54, 568–582 (2016)[187]. Reproduced with permission from Springer Nature.

Chapter 2

Discovery of a Ru-B2 Phase with High Thermal Stability[1] Reproduced with permission from Elsevier.

In this chapter, the phase equilibria of an equiatomic Ru-containing refractory multi-principal element alloy (RMPEA), $Hf_{20}Nb_{20}Ta_{20}$-$Zr_{20}Ru_{20}$ (at%), is investigated from 1350 to 1575 °C. The microstructure was investigated in the as-cast and annealed conditions by scanning electron microscopy; additional transmission electron microscopy was performed to investigate regions of discontinuous precipitation. The alloy contained a disordered BCC phase, a HCP phase, and an ordered HfRu-B2 phase at all temperatures. To the author's knowledge, this investigation is the first report of a B2 phase stable above 1200 °C in an RMPEA. Implications for the strengthening of RMPEAs are discussed.

---

[1] Significant portions of this chapter are reproduced from this publication: **Frey, C.**, R. Silverstein, and T. M. Pollock. "A high stability B2-containing refractory multi-principal element alloy". *Acta Materialia* **229**, 117767 (2022). [doi] [190].

2.1 Introduction

Alloys derived from the refractory elements (Cr, Hf, Mo, Nb, Ta, Ti, V, W and Zr) have been of interest for high temperature structural applications since the 1950's due to their high melting temperatures[191, 46, 52, 53, 33]. These applications include hypersonic re-entry vehicles, rocket propulsion systems, earth- and space-based nuclear reactors, and turbine engines[53, 47, 33]. However, attempts to develop refractory alloys for extreme environments have been challenged by the intrinsic trade-offs that exist between critical properties. The same alloying elements that promote high temperature strength (ex. Mo, W) and oxidation resistance (ex. Al, Cr) are severely detrimental to room temperature ductility and fabricability[46, 49]. Decreased interest in space-based power generation and the selection of ceramic materials for the Space Shuttle resulted in a rapid decline in refractory alloy development in the 1970's [33, 37], and only a few commercial refractory alloys are in service today[50]. Interest in refractory alloys has been reinvigorated by the development of refractory high entropy alloys (RHEAs) and multi-principal element alloys (RMPEAs) that combine the refractory elements in equiatomic or near-equiatomic concentrations[74, 192]. While a novel approach, these materials have yet to overcome the same trade-offs that prevented the widespread adoption of historical refractory alloys[21, 89].

Efforts to improve the mechanical properties of refractory alloys at high temperature have generally focused on introducing a second strengthening phase to a ductile matrix[68]. Precipitation and dispersion strengthening, where a second phase is uniformly distributed to provide obstacles for dislocation motion, are widespread design strategies for achieving balanced mechanical properties[10, 112]. For high homologous temperature applications, coherent precipitates with low misfit provide the greatest long-term benefits[38, 68]. The low interfacial energy between the strengthening phase and the matrix reduces the driving force for coarsening and coalescence of the precipitates and results in improved microstructural stability[4, 112]. To develop refractory alloys with coherent precipitates, many investigations have been focused on the B2 (CsCl) phase; the B2 crystal structure is an ordered derivative of the BCC phase, which is the predominant crystal structure of the refractory elements at desired operating temperatures. Refractory alloys of the type BCC (β) + coherent B2 (β') are frequently referred to as refractory 'superalloys' (RSAs)[148, 140, 146] and seek to replicate the cuboidal γ/γ' microstructures of the Ni-based superalloys[4].

A number of β + β' materials have been reported. Additions of Al, Ti, and Zr to RMPEAs can result in high volume fractions of coherent cuboidal (Al, Ti, Zr)-B2 phases within a disordered BCC matrix[149, 150, 160, 148, 162, 193]. These alloys have been the most successful in mimicking the desirable γ/γ' microstructure of Ni-based superalloys, but many have unstable microstructures that form deleterious (Al,Zr)-rich phases[158, 177, 194, 195]. More significantly, given that desired application temperatures are $\geq$ 1300 °C, the (Al,Ti,Zr)-B2 phases lack sufficient thermal stability and have yet to be stabilized above 1200 °C[157, 177]. More promising, Cr alloys with coherent NiAl-B2 precipitates have demonstrated solvus temperatures up to 1400 °C [146]. However, because Cr has the smallest lattice parameter of the refractory metals (a_{Cr} = 2.878 Å [144]), NiAl cannot be used as a coherent precipitate for other refractory matrix materials.

Of interest in this investigation is the large number of reported refractory X-Ru B2 phases (X = Hf, Nb, Ta, Ti, V, Zr). The binary Ru-B2 phases all posses high melting points and are isomorphous, which opens the possibility of adjusting the lattice mismatch between the potential B2 phase and the surrounding BCC matrix[184, 186]. Furthermore, Ru forms B2 phases with Al[196] and Si[197]. Both are desirable alloying additions due to their low density and cost and positive effect on oxidation resistance[21].

To investigate the potential of Ru as a B2 former, an equiatomic $Hf_{20}Nb_{20}Ta_{20}Zr_{20}Ru_{20}$ RMPEA was synthesized and characterized in detail. The alloy contained a disordered BCC phase, a close-packed hexagonal (HCP) phase and an ordered B2 phase. High temperature anneals at 1350 °C, 1475 °C and 1575 °C were performed to test the stability of the phases at potential operating temperatures and evaluate the predictive potential of CALPHAD predictions in this system. The B2 phase was observed to be stable up to 1575 °C. Implications for the strengthening of refractory alloys are discussed.

2.2 Methods

The equiatomic alloy was prepared using pure Hf turnings (99.7 wt%), Nb foil (99.9 wt%), Ru (99.98 wt%) powder, and Ta (99.98 wt%) and Zr (99.2 wt%) sheet. A 20 g button was arc melted on a water-cooled copper hearth and under a gettered argon atmosphere. Elements were added sequentially according to their melting point and remelted once at each step to improve macroscopic homogeneity. Material was heat treated in a vacuum furnace for 48 h at 1350 °C, 24 h at 1475 °C, and 12 h at 1575 °C with a ramp rate of 15 °C/min. All arc-melted samples were sealed in Ta ampoules under vacuum and cooled at the maximum rate of the furnace to room temperature.

As-cast material was cut into samples of approximately 0.2-0.3 g and splat quenched using a modified tri-arc system (Figure 2.1) to produce one inch diameter foils 50-350 μm in thickness. The tri-arc consists of an argon filled chamber containing a water-cooled hearth of high conductivity (i.e. copper) and hammer. Once placed on the hearth, three tungsten stingers are oriented around the sample and ignited to form an arc that melts the material; then the arc is interrupted and the hammer is dropped simultaneously to cast the molten material across the hearth, forming a foil. To accommodate the high melting temperature and prevent adherence of the foils to the hearth, the tri-arc system was modified to use a TZM (molybdenum alloy) hammer and a 70 at% Cu-W alloy hearth. A Ti getter was inserted.

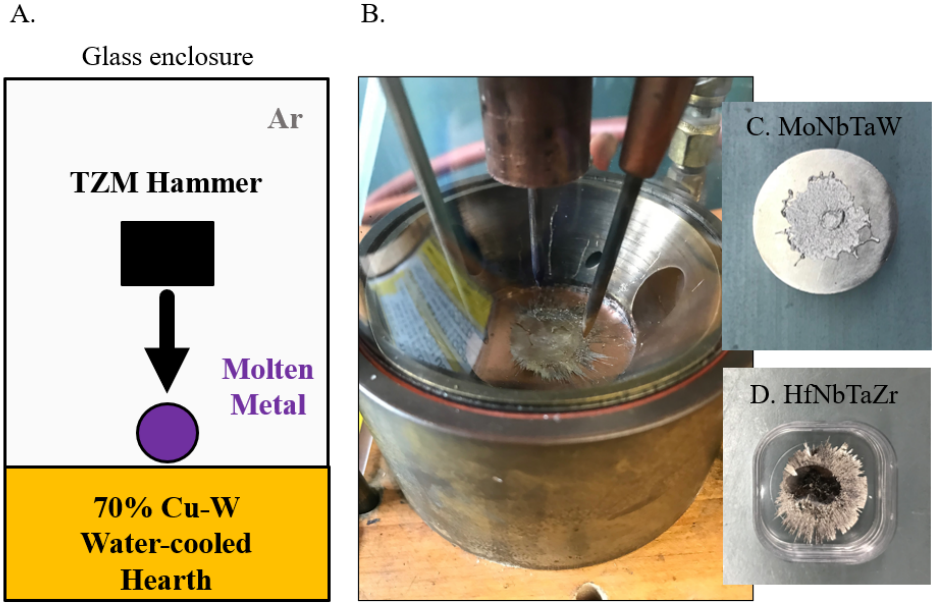

Figure 2.1: A. Schematic representation of the splat quenching process. B. Image of the interior of the splat quenching chamber, with a metal foil resting on a copper–tungsten hearth. C. Example foil made from equiatomic MoNbTaW. D. Example foil made from equiatomic HfNbTaZr.

WDXRF measurements of the composition of the as-cast material were acquired with a Rigaku ZSX Primus IV. Oxygen and nitrogen contents were also measured by inert gas fusion and the carbon content was determined by combustion analysis, with both tests performed by Northern Analytical, Inc. These values are presented in Table 2.1. Back-scattered electron (BSE) and secondary electron (SE) images were acquired on a ThermoFisher Versa3D microscope. BSE images were utilized to determine the area fraction of identified phases via the FIJI software package[198]. The area fraction of the (Hf,Ru)-rich phase in the as-cast material was determined via point counting method according to ASTM standard E562 19e1 with an applied grid of 13x8 points. Compositional values were collected via energy dispersive X-ray spectroscopy (EDS). X-ray diffraction

(XRD) patterns were obtained with a Panalytical X'Pert Pro MPD machine using Cu $K\alpha$ radiation ($\lambda = 0.154nm$). Diffraction patterns were taken from bulk samples with cross-sections polished to a 9 μm finish or better via mechanical polishing. XRD was taken from the bulk of the splat quenched foil without polishing. Curve-fits of diffraction data were performed in GSAS-II[199] to extract lattice parameters. Vickers hardness of the as-cast and splat quenched samples were calculated from at least eight indentations of 2 kg and 0.5 kg, respectively; a 200 μm thick foil section of the foil was used for indentation.

Table 2.1: Chemical composition (at%) and interstitial content (ppmw) of the bulk $Hf_{20}Nb_{20}Ta_{20}Zr_{20}Ru_{20}$.

Hf	**Nb**	**Ta**	**Zr**	**Ru**	**O**	**N**	**C**
20.9	20.0	19.5	19.7	19.9	620	620	75

For a detailed micro- and nano-structural investigation, thin lamella was extracted from the polished sections using a focused ion beam system (FIB, Helios, ThermoFisher). The lamella was examined using transmission electron microscopy (TEM, Talos G2 200X with Chemi-STEM EDS, ThermoFisher) to identify the phases, their morphologies and sizes, and their chemical compositions. STEM analysis included a high angle annular dark field (HAADF) mode. In addition, selected area diffraction patterns (SADPs) were collected from regions of interest. EDS was used to determine the compositions using a SuperX detector and the Velox software.[2]

---

[2] Please note that all FIB and TEM investigations were performed by Dr. Ravit Silverstein.

2.3 Results

2.3.1 Phase Predictions via CALPHAD

An equilibrium diagram was predicted from 500 to 2500 °C using the 2020 TCHEAv4.1 database and 2020 Thermo-Calc® software[200] (Figure 2.2). The equiatomic $Hf_{20}Nb_{20}Ta_{20}Zr_{20}Ru_{20}$ alloy is predicted to have a solidification range from $T_{solidus} = 1492$ °C to $T_{liquidus} = 2197$ °C. A disordered (Nb,Ta)-rich BCC1 phase and an ordered (Hf,Zr)Ru-B2 phase are predicted to be stable from 500 °C to above the solidus temperature, until 2197 °C and 2008 °C, respectively. With decreasing temperature the BCC1 and B2 phases undergo a partial decomposition below 1282 °C into a Zr- and Hf-rich disordered BCC2 phase. Below 650 °C the BCC2 phase undergoes a eutectoid transformation to an disordered HCP phase and BCC1. The HCP and BCC2 phases have the lowest maximum volume fractions, while the volume fraction of the B2 phase increases with increasing temperature to a maximum volume fraction of 0.63 between 1282 and 1492 °C, before decreasing at the onset of melting at $T_{solidus}$.

2.3.2 As-cast $Hf_{20}Nb_{20}Ta_{20}Zr_{20}Ru_{20}$

Three phases are visible in SEM BSE images of the as-cast material (Figure 2.3A,C), with compositions reported in Table 2.2: a (Nb,Ta)-rich matrix, a (Hf,Ru)-rich phase, and a Zr-rich precipitate with the darkest contrast, consistent with its low Z number. The (Nb,Ta)-rich matrix exhibits clear evidence of dendritic segregation, with the segregation of Zr to dark inter-dendritic regions and Nb and Ta concentrated in the intra-dendritic zones (Figure 2.3D). Hf and Ru do not segregate significantly in the matrix, with a slight increase of Hf and slight decrease of Ru in the intra-dendritic regions. The (Hf,Ru)- and Zr-rich phases are concentrated in the inter-dendritic regions of high Zr content, with a

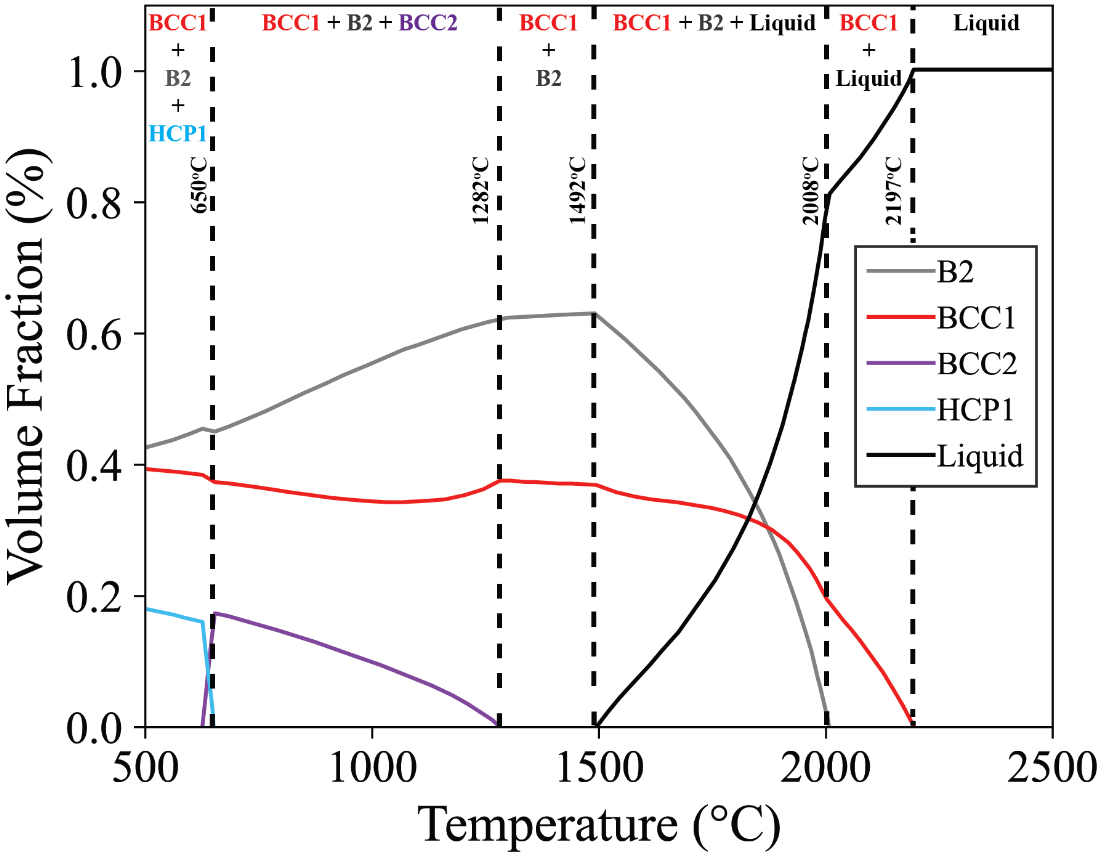

Figure 2.2: Predicted volume fraction of phases with increasing temperature for $Hf_{20}Nb_{20}Ta_{20}Zr_{20}Ru_{20}$. Generated with the Thermo-Calc TCHEA4 v4.1.[200].

small fraction of the (Hf,Ru)-rich phase in the intra-dendritic regions. Periodic segregation was also observed in EDS linescans of the larger (Hf,Ru)-rich phase but is not visible in microscopy images. Small lamellar structures can seen in the inter-dendritic regions and are indicative of a eutectic reaction at the end of solidification (Figure 2.3C). The lamella are too small for compositional measurements via EDS but contain comparable backscattered electron contrast with the three phases already identified. While light elements cannot be accurately quantified via EDS, the measured oxygen and nitrogen content is highest in the Zr-rich phase and lowest in the (Nb,Ta)-rich matrix. Significant

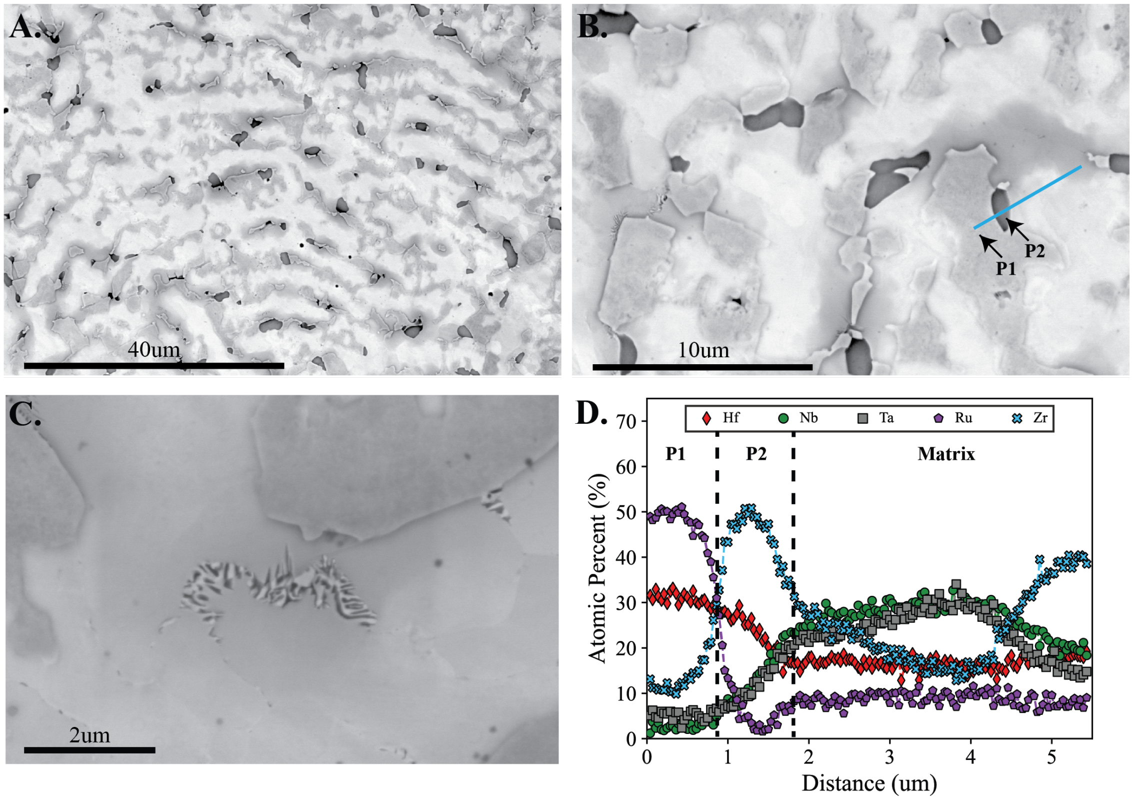

Figure 2.3: A, B, C. Backscatter electron images of as-cast equiatomic $Hf_{20}Nb_{20}Ta_{20}Zr_{20}Ru_{20}$. Three phases are identified. D. EDS linescan of the two precipitate phases and the dendritic segregation in the (Nb, Ta)-rich matrix. P1 is identified as a HfRu-B2 phase and P2 is identified as a Zr-rich HCP phase.

relief of the matrix and Zr-rich phase during mechanical polishing in contrast to the (Hf,Ru)-rich phase is indicative of it being the hardest phase.

Utilizing the measured compositions, theoretical lattice parameters were calculated via Vegard's Law (Table 2.3):

$$a_{calc} = \sum_{i=1}^{n}(a_i * x_i) \tag{2.1}$$

where n is the number of elements in the phase, a_i is the lattice parameter of the isomorphous phase, and x_i is the concentration of the element in atomic fraction. The lattice parameters for BCC Hf, Ru, and Zr were determined by taking the third root of the HCP unit cell volumes.

Two distinct set of peaks are visible in the XRD scan for the as-cast material (Figure 2.4), corresponding to a disordered BCC phase and an ordered B2 phase; the disordered BCC peaks are wide and asymmetric. The fitted lattice parameter of the B2 phase (3.241 Å) is close to the value calculated via Eq. 2.1. (3.221 Å) when the composition of the (Hf,Ru)-rich phase and the lattice parameters of the binary B2 phases are utilized (Table 2.3). The (Hf,Ru)-rich regions are therefore identified as an ordered (Hf,Zr)Ru-B2 phase. Lattice parameters calculated for the intra- and inter-dendritic regions of the (Nb,Ta)-rich phase are consistent with the disordered BCC peaks and the (Nb,Ta)-rich phase is therefore identified as a disordered BCC phase (BCC1).

The hardness of the as-cast material was calculated to be 630 ± 17 HV. A comparison to literature values tabulated in an MPE database of cast materials is shown in Figure 2.5[78]. The literature values are drawn from a review of RMPEAs encapsulating the 2010-2019 publication years and include 123 values of as-cast, annealed, powder and wrought materials.

2.3.3 Samples annealed from 1350 °C to 1575 °C

All annealed samples demonstrated significant coarsening and homogenization of the (Hf,Ru)- and Zr-rich phases and homogenization of the (Nb,Ta)-rich phase (Figure 2.6). Grains of the (Hf,Zr)Ru-B2 and Zr-rich phases lying adjacent to the (Nb,Ta)-rich grain boundaries coarsened more rapidly than phases residing within grain interiors and there was no measured composition difference between intra-granular and grain boundary phases. No new phases or identifiable oxides are observed and the Zr-rich phase continues to contain the highest qualitative content of O and N at both temperatures. There is no

Table 2.2: Compositional measurements (at%), area fractions (%), and identified crystal structures of phases at different annealing conditions. Composition was measured by SEM EDS. Error is the standard deviation of the measurements.

Condition	**Phase**	**Area Fraction** (%)	**Hf**	**Nb**	**Ta**	**Ru**	**Zr**	**Structure**
as-cast	(Nb,Ta)-rich matrix, inter-dendritic region	-	13.6-20.0	15.4-28.1	11.1-24.5	4.3-10.8	24.1-47.5	BCC
	(Nb,Ta)-rich matrix, intra-dendritic region	-	13.3-19.0	24.7-34.4	21.6-32.6	6.5-12.0	12.4-27.0	BCC
	(Hf,Ru)-rich phase	25.6 ± 2.9	32.5 ± 2.4	5.3 ± 2.3	7.6 ± 3.1	45.2 ± 2.5	9.50 ± 0.6	B2
	Zr-rich precipitates	2.3 ± 1.2	28.7 ± 6.0	6.9 ± 0.3	3.8 ± 0.6	6.4 ± 5.7	54.1 ± 10.2	-
1350°C, 48hr	(Nb,Ta)-rich phase	51.0 ± 2.0	12.9 ± 0.8	32.7 ± 1.0	26.4 ± 0.6	6.0 ± 1.3	22.0 ± 0.7	BCC
	(Hf,Ru)-rich phase	44.7 ± 2.5	29.9 ± 1.1	3.2 ± 1.3	3.8 ± 1.4	51.8 ± 1.8	11.3 ± 0.7	B2
	Zr-rich precipitates	4.1 ± 0.6	22.0 ± 1.3	4.3 ± 1.7	1.6 ± 0.3	0.0 ± 0.0	70.7 ± 0.6	HCP
	Lamellar region		13.1 ± 0.3	31.9 ± 0.6	27.1 ± 0.3	5.8 ± 0.6	22.2 ± 0.1	-
1475°C, 24hr	(Nb,Ta)-rich phase	57.1 ± 5.9	12.8 ± 0.2	33.5 ± 0.3	30.0 ± 0.3	7.8 ± 0.5	16.1 ± 0.5	BCC
	(Hf,Ru)-rich phase	34.6 ± 5.0	31.4 ± 1.1	1.3 ± 0.4	2.3 ± 0.4	52.5 ± 0.7	12.6 ± 1.0	B2
	Zr-rich precipitates	8.3 ± 2.4	24.0 ± 0.5	5.4 ± 0.6	1.8 ± 0.2	0.0 ± 0.0	68.8 ± 0.9	HCP
	Lamellar region		14.9 ± 0.1	28.7 ± 0.3	32.9 ± 0.2	5.9 ± 0.3	17.6 ± 0.1	-
1575°C, 12hr	(Nb,Ta)-rich phase	54.9 ± 3.8	12.8 ± 0.2	33.5 ± 0.4	29.1 ± 0.3	8.9 ± 0.2	15.8 ± 0.2	BCC
	(Hf,Ru)-rich phase	35.9 ± 2.9	31.4 ± 0.7	1.4 ± 0.3	1.8 ± 0.2	52.4 ± 1.9	13.0 ± 2.0	B2
	Zr-rich precipitates	9.2 ± 2.4	24.9 ± 0.1	5.4 ± 0.5	1.6 ± 0.2	0.0 ± 0.0	68.1 ± 0.4	HCP
	Lamellar region		15.2 ± 0.7	28.0 ± 0.7	33.2 ± 0.5	7.5 ± 1.3	16.3 ± 0.8	-

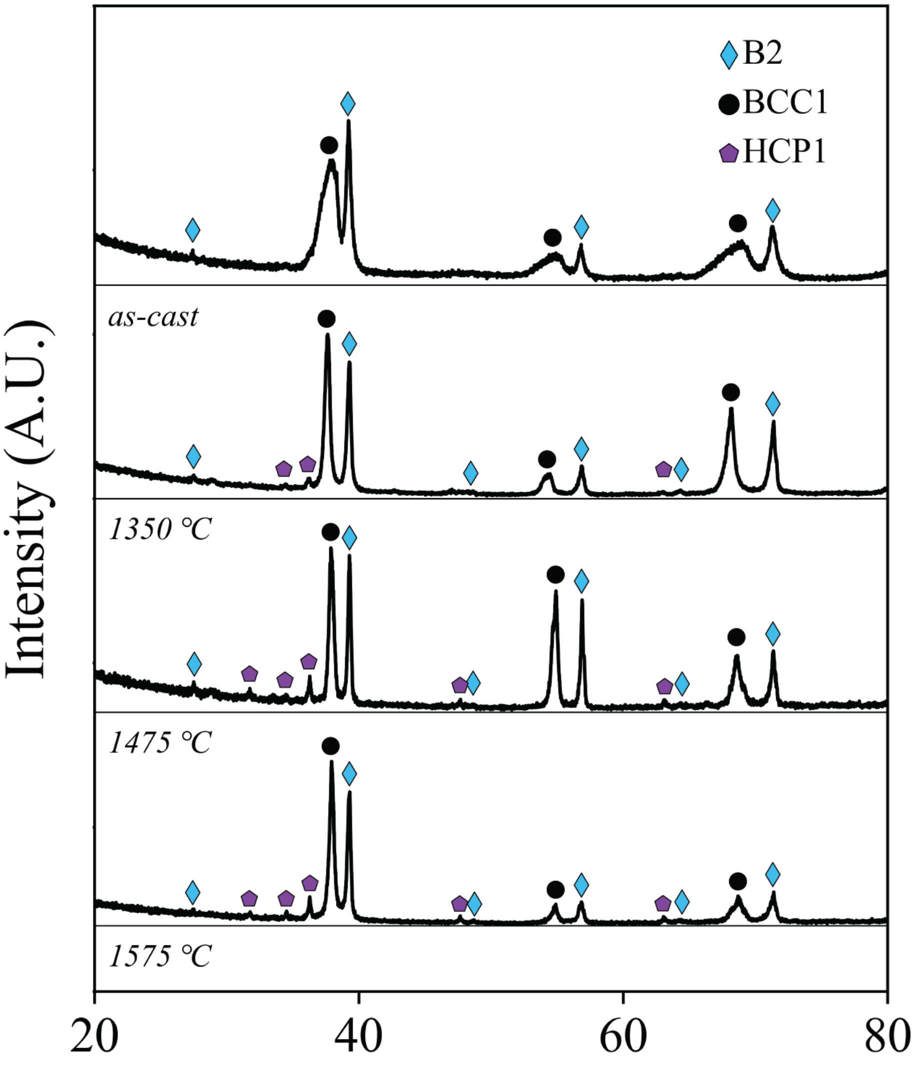

Figure 2.4: Bulk XRD scans for equiatomic $Hf_{20}Nb_{20}Ta_{20}Zr_{20}Ru_{20}$ at different annealing temperatures.

Table 2.3: Experimental (a, c_{exp}) and calculated (a, c_{calc}) lattice parameters (Å) of phases in $Hf_{20}Nb_{20}Ta_{20}Zr_{20}Ru_{20}$ at different annealing temperatures.

Condition	**Phase**	$\mathbf{a}_{calc}$	$\mathbf{a}_{exp}$	$\mathbf{c}_{calc}$	$\mathbf{c}_{exp}$
1350°C, 48 hr	(Nb,Ta)-rich phase	3.374	3.377	-	-
	(Hf,Ru)-rich phase	3.226	3.244	-	-
	Zr-rich phase	3.212	-	5.120	-
1475°C, 24 hr	(Nb,Ta)-rich phase	3.354	3.352	-	-
	(Hf,Ru)-rich phase	3.229	3.242	-	-
	Zr-rich phase	3.212	3.257	5.120	5.192
1575°C, 12 hr	(Nb,Ta)-rich phase	3.354	3.354	-	-
	(Hf,Ru)-rich phase	3.230	3.243	-	-
	Zr-rich phase	3.190	3.255	5.085	5.198

Ru measured in the Zr-rich phase and both the Zr-rich and (Hf,Zr)Ru-B2 phases contain less than 10 at% Nb and Ta after annealing (Table 2.2).

The area fraction of the Zr-rich and the (Hf,Zr)Ru-B2 phase increased at all annealing temperatures (Table 2.2). The 1350 °C sample had the maximum area fraction of the (Hf,Zr)Ru-B2 phase, 44.7%, and the lowest amount of the Zr-rich phase, 4.1%, of the annealed materials. Area fractions of both minor phases were similar in the 1475 °C and the 1575 °C samples, with a decreased amount of the (Hf,Zr)Ru-B2 phase ($\approx$ 35 %) and an increased amount of the Zr-rich phase ($\approx$ 9 %) compared to the 1350 °C sample.

Fine scale lamellar regions appear adjacent to the (Hf,Zr)Ru-B2 and Zr-rich phases (Figure 2.6B). The backscattered electron contrast indicates the presence of alternating laths of the (Nb,Ta)-rich and the Zr-rich phases. Etching observable in secondary electron images also indicate the presence of a small quantity of the B2 phase. The lamellar regions are similar in composition to the composition of (Nb,Ta)-rich phase, Table 2.2, with a small enrichment of Zr and a depletion of Ta and Nb, but the size of the laths continues to hinder the measurement of compositions specific to each phase. These regions are evaluated by TEM in section 2.3.4.

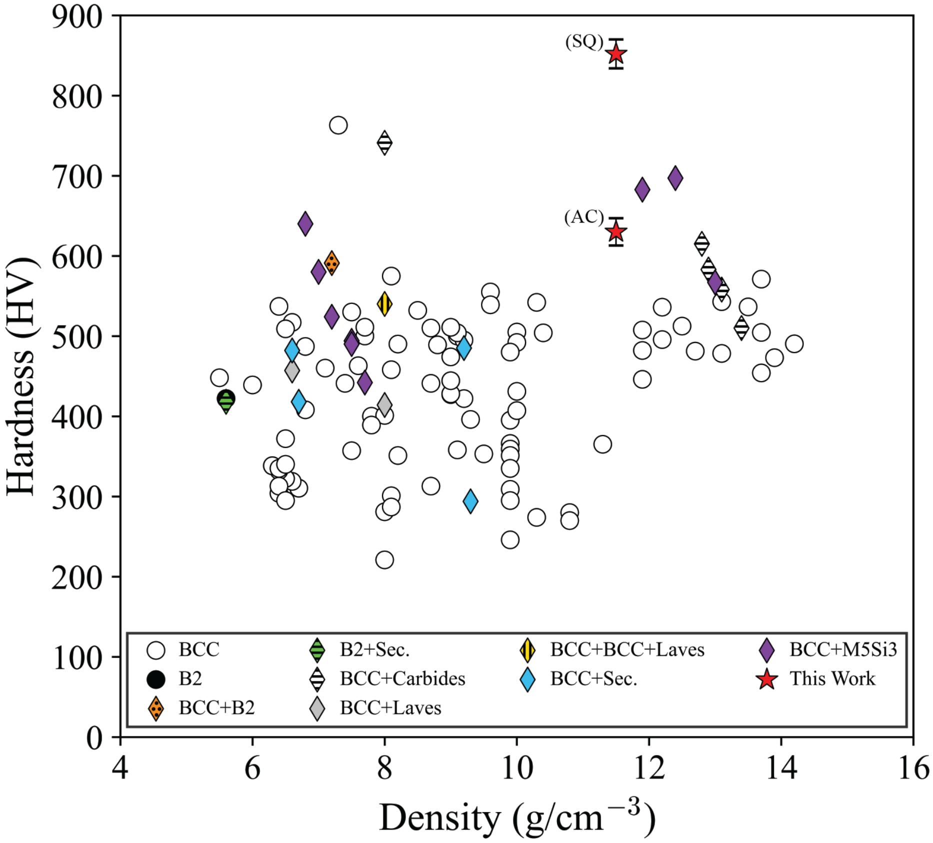

Figure 2.5: Comparison of hardness values reported in this work to values of hardness in the literature. Single phase materials are represented by circles and multi-phase materials are diamonds. Literature values represent as-cast, annealed, powder, and wrought RMPEAs. Values derived from this work come from the as-cast (AC) and splat quenched (SQ) conditions. Data shown here is available in supplementary materials and taken from [78].

Three distinct set of peaks are visible in the XRD scans for the annealed samples (Figure 2.4). Two sets correspond to a disordered BCC phase (BCC1) and an ordered B2 phase, consistent with the XRD scans for the as-cast material. The third set of peaks are consistent with an HCP phase (HCP1) and grow more pronounced with increasing annealing temperature. These peaks are attributed to the Zr-rich phase due to the high concentration of HCP-type elements (Hf, Zr) present in those regions. The intensity of

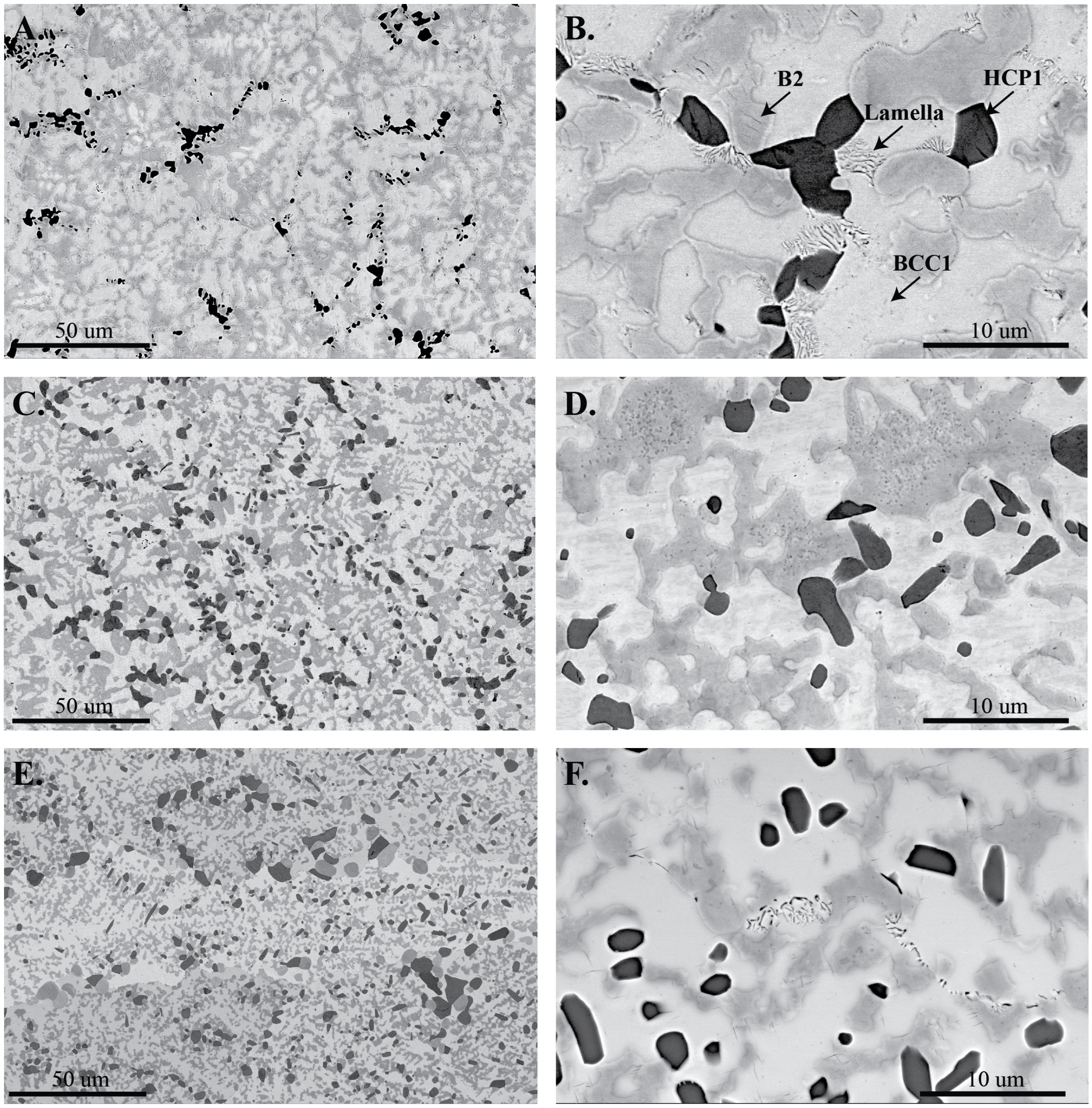

Figure 2.6: Backscatter electron images of $Hf_{20}Nb_{20}Ta_{20}Zr_{20}Ru_{20}$ samples annealed in vacuum at different conditions. A, B. 1350 °C for 48 hr. C, D. 1475 °C for 24 hr. E, F. 1575 °C for 12 hr. All samples contain the three identified phases.

the HCP peaks in the 1350 °C sample prohibit extraction of the lattice parameters, but lattice parameters of the 1475 °C and 1575 °C HCP peaks are presented in Table 2.3.

Indentation of the 1350 °C sample with a 1 kg weight was performed to observe the response of the phases to loading. As shown in Figure 2.7, cracking is visible in the (Hf,Zr)Ru-B2 and Zr-rich phases within and adjacent to the indent. In many cases the cracks are straight through the volume of the brittle phase and stop at the interface with the (Nb, Ta)-rich phase. No cracks were visible in the (Nb, Ta)-rich matrix.

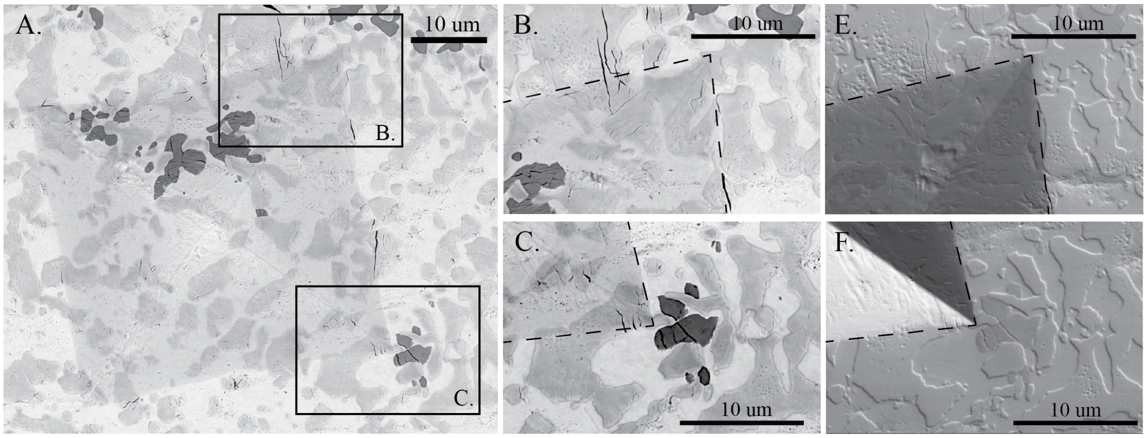

Figure 2.7: A. Backscatter electron image of 1.0 kgf indent in $Hf_{20}Nb_{20}Ta_{20}Zr_{20}Ru_{20}$ annealed at 1350 °C for 48hr. B, C. Magnification of indicated indent corners at regions of interest, showing cracks in the (Hf,Ru)-rich and Zr-rich phases. E, F. Secondary electron images of B and C, respectively.

2.3.4 TEM analysis of sample annealed at 1350 °C

The foil lifted from the sample annealed at the 1350 °C, Figure 2.8, shows multiple coarse grains in the vicinity of the lamellar structure. A HAADF-STEM image reveals contrast from three phases: brighter contrast from the Zr-rich HCP1 phase, a darker contrast from the (Hf,Zr)Ru-B2, and a lighter contrast from the (Nb, Ta)-rich BCC1 matrix phase. The corresponding STEM-EDS maps show Zr-rich and Ru-rich phases along with a relatively homogeneous concentration from the matrix. The compositions of the different regions are shown in Table 2.4 and are in agreement with the EDS-SEM analysis, albeit with some variations in compositions. Note that there is an additional detected BCC phase in the lamellar region with a slightly different composition compared with that of the BCC1 matrix and was labeled BCC2 (lamellar) in Table 2.4.

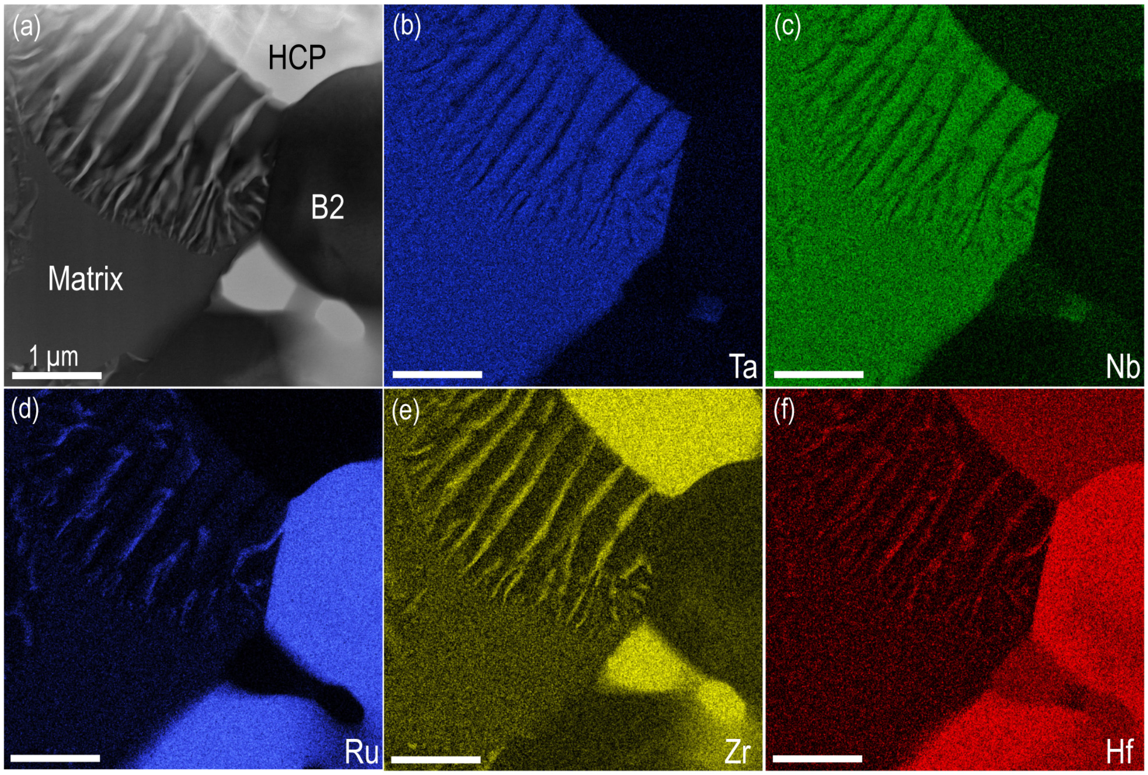

Figure 2.8: TEM analysis of the sample annealed at 1350 °C for 48hr. A. HAADF-STEM image showing three different phases in the vicinity of the lamellar region, where the contrast suggest there are alternating phases in the lamellar region. B-F. STEM-EDS compositional maps showing the enrichment of elements in the different GB phases.

The detected crystal structures in the XRD scans, Figure 2.4, were confirmed by acquiring a series of SADPs from the three different regions. The SADP acquired from the Zr-rich grain shows that it has a HCP structure without any ordering (Figure 2.9g). To differentiate between a BCC and B2 structure, the [001] zone axis (ZA) was acquired from both the Ru-rich grains and the (Nb,Ta)-rich phase (Figure 2.9). The [001] ZA from the matrix in Figure 2.9d shows spots with a fairly uniform intensity, suggesting that the matrix is a single disordered BCC phase. For a comparative analysis, a [001] ZA was acquired from the Ru-rich grains and yielded additional faint spots from the ordering (Figure 2.9f). To rule out $L2_1$ ordering, the sample was tilted to a [101] ZA in Figure 2.9e and the result unambiguously supports ordering from a B2 phase. The lattice parameters of the phases were calculated from the SADPs and are a_{BCC} (matrix) =3.34 Å, a_{BCC} (lamellar) = 3.46 Å, a_{B2} = 3.20 Å, a_{HCP} = 3.20 Åand c_{HCP} = 5.0 Å.

Closer inspection of the interface between the lamellar region and the matrix shows a homogeneous composition that remains consistent up to the lamellar front. A close observation of the lamellar region in Figure 2.9a-c reveals three alternating phases: a (Hf, Ru)-rich phase that appears magenta in Figure 2.9b, a orange (Zr, Hf)-rich phase in Figure 2.9c, and a third phase depleted of Hf, Ru and Zr. Note the Ru-rich lamellae and the Zr-rich lamellae yield the same color in the compositional map as that of the adjacent B2 and HCP grains, respectively, suggesting they have the same crystal structure.

To gain more insight on the crystal structures of the lamellae, a SADP was collected from a dual phase lamellar region, including a (Zr,Hf)-rich lamella and a lamella depleted of Hf, Ru, and Zr (Figure 2.10d). The corresponding HAADF-STEM, taken under two-beam conditions using $\mathbf{g} = [001]_{HCP}$ (Figure 2.10b), shows enhanced contrast from the (Zr, Hf)-rich lamellae, in line with a disordered HCP structure. These lamellae are co-

Table 2.4: Composition of phases present in $Hf_{20}Nb_{20}Ta_{20}Zr_{20}Ru_{20}$ present after annealing at 1350 °C for 48hr. STEM-EDS compositional analysis, in at%, of the different phases.

Elements	**BCC1 (matrix)**	**BCC2 (lamellar)**	**HCP1**	**B2**
Hf	6 ± 1	5 ± 1	15 ± 2	26 ± 5
Nb	38 ± 6	46 ± 8	10 ± 1	0 ± 1
Ta	24 ± 5	32 ± 6	3 ± 0	3 ± 1
Ru	10 ± 4	4 ± 1	3 ± 0	66 ± 12
Zr	22 ± 2	13 ± 2	69 ± 6	5 ± 1

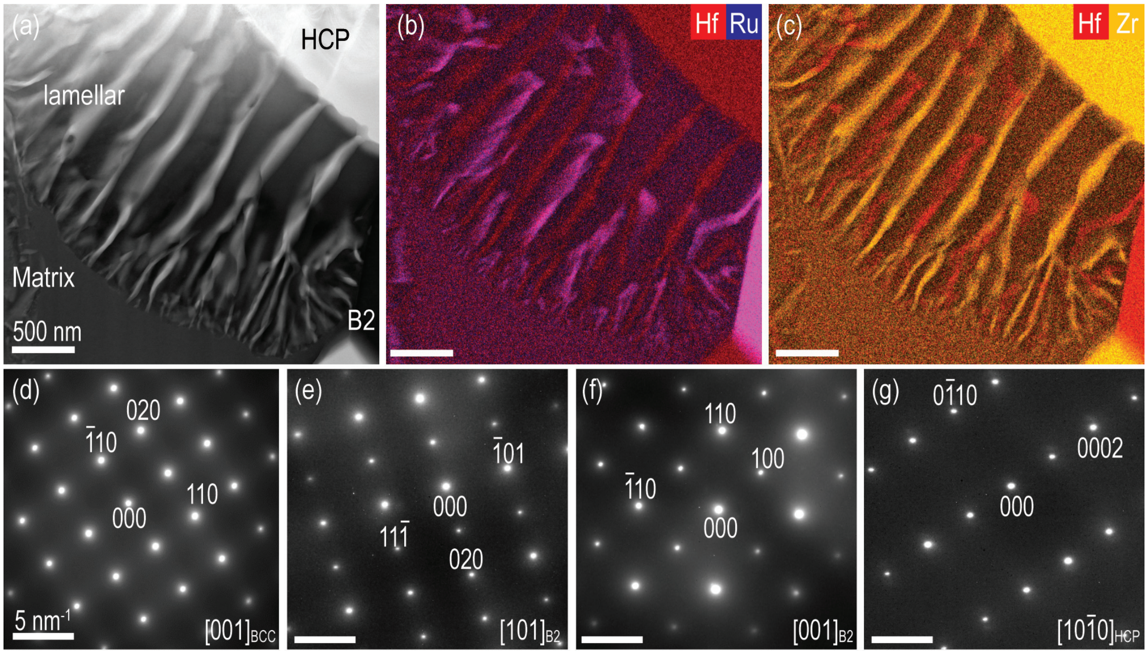

Figure 2.9: TEM analysis of the lamellar microstructure and the GB phases in the vicinity of the lamellar region. A. HAADF-STEM image, B-C. STEM-EDS compositional maps, where in B. Hf and Ru were used to construct the map and in C. Zr and Hf were used. D-G. SADPs acquired from the different phases: D. $[001]_{BCC}$ ZA from the matrix, E-F. $[101]_{B2}$ and $[001]_{B2}$ ZAs, respectively, from the Ru-rich grain and G. $[10\bar{1}0]_{HCP}$ ZA from the Zr-rich precipitate.

herent and correspond to BCC and HCP structures with the orientation relationship (OR) following the Burgers path: $\{110\}<010>_{BCC} \parallel \{0001\}<01\bar{1}0>_{HCP}$. One particularly interesting observation is in the composition fluctuations of the alternating lamellae in Figure 2.10a, b, where oxygen enrichment occurs in the Zr-rich regions, presumably promoting the transformation path to HCP.

2.3.5 Result of reduced precipitate size

To determine the effect of reduced grain and precipitate size on the material microstructure and hardness, 50-200 μm thick foils were produced via splat quenching (Figure 2.11). The higher rate of cooling achieved by splat quenching suppresses secondary phase formation during solidification as compared to arc melting, reduces the

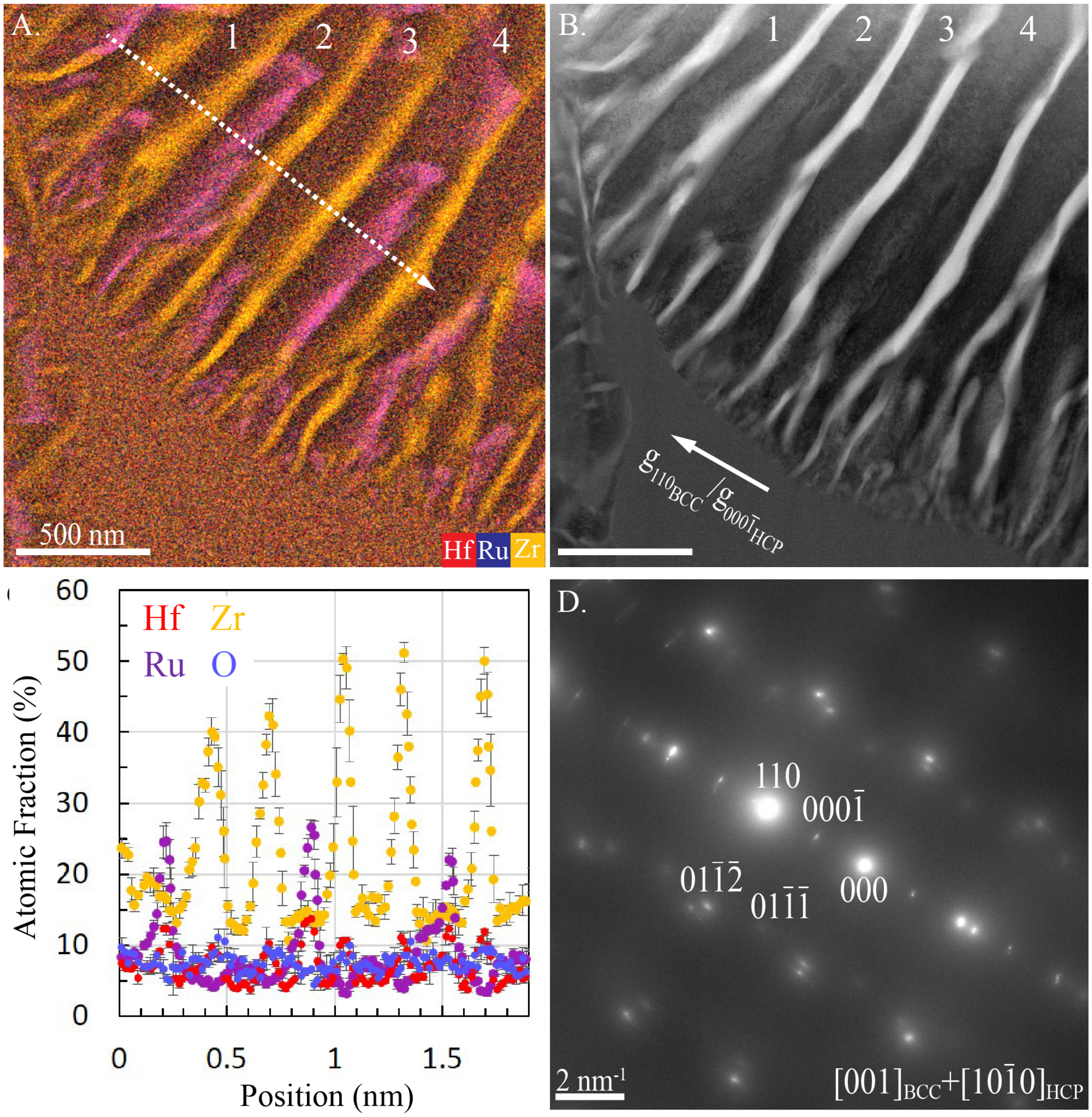

Figure 2.10: TEM analysis of the lamellar structure. A. STEM-EDS compositional maps where Hf, Ru, and Zr were used to construct the map and the compositional scan profile in C. taken along the marked line. B. is the corresponding two-beam HAADF-STEM which clearly reveals preferential contrast from the Zr-Hf rich lamellae, but not from the Ru-Hf lamellae, in line with the superstructure show in the SADP in D. The numbers on the lamellae show the corresponding lamellar in the compositional map in A. D. SADP collected from the Zr, Hf, Ru depleted lamella and a Zr-Hf rich lamella, corresponding to ZAs of $[001]_{BCC}$ + $[10\bar{1}0]_{HCP}$, showing a superstructure from the coherent lamellae.

wavelength of any solidification-induced segregation and reduces the size of the precipitates. Grain interiors at thinner portions of the foil are homogeneous and contain a small number of nanoscale precipitates with back-scatter contrast and etching behavior consistent with the as-cast and annealed arc-melted samples; the density of the intragranular precipitates increases with increasing thickness. Similar phases are highly concentrated at the grain boundaries and are slightly coarser. The XRD scan demonstrates peaks consistent with a disordered BCC structure and smaller peaks representative of an ordered B2 and a disordered HCP phase (Figure 2.11A). The fitted lattice parameter for the BCC phase is 3.328 Å, which is a reduction in magnitude from the (Nb,Ta)-rich BCC1 lattice parameters reported for the annealed materials.

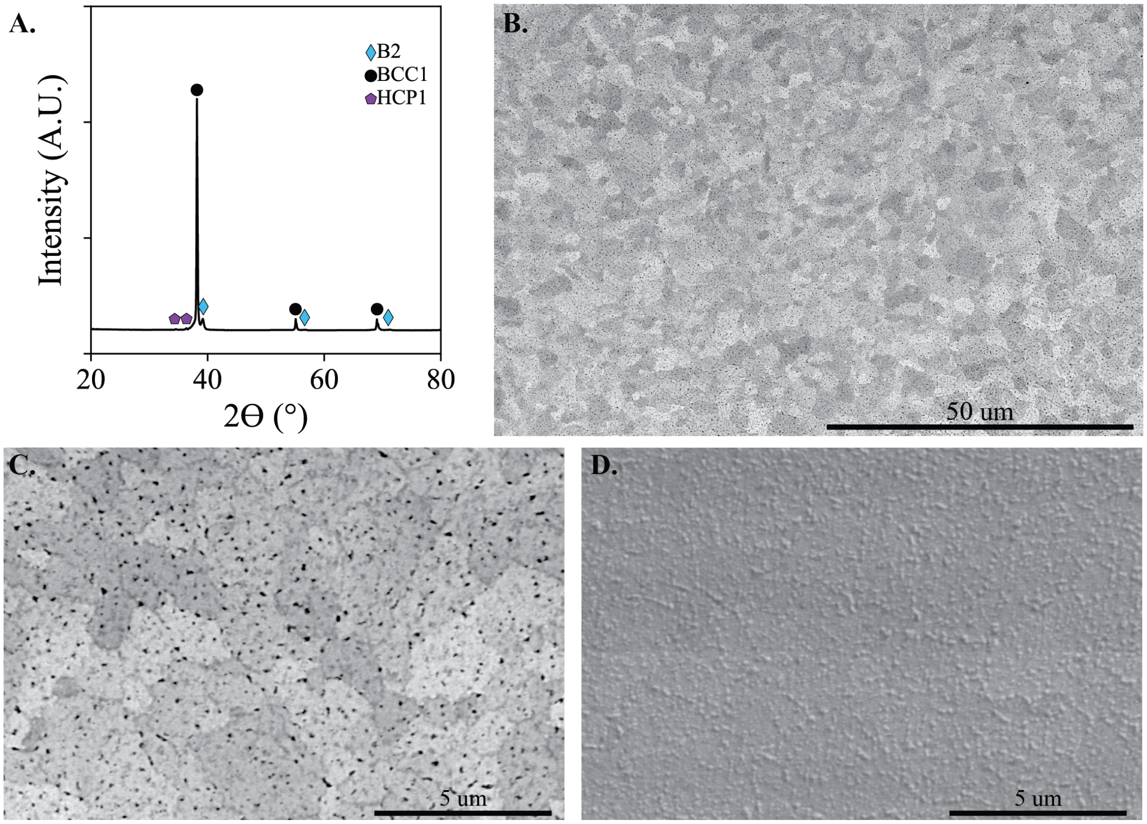

Figure 2.11: A. XRD scan of splat quenched $Hf_{20}Nb_{20}Ta_{20}Zr_{20}Ru_{20}$. B, C. Backscatter electron images of splat quenched $Hf_{20}Nb_{20}Ta_{20}Zr_{20}Ru_{20}$. D. Secondary electron images of C.

A foil was lifted from a section of the splat quenched sample to further characterize the nanoscale precipitates (Figure 2.12). The SADP clearly shows spots from BCC, B2, and HCP phases, consistent with the XRD scans in Figure 2.11. A two-beam HAADF-STEM condition using g = $[020]_{BCC}$ was chosen to show dark B2 contrast in two nearby grains (Figure 2.12A) and discrete 100 nm B2 precipitates can be identified by dark contrast in the magnified HAADF image (Figure 2.12B). The precipitates lie both on the grain boundaries and within the grain core. A STEM-EDS map colored by Hf and Ru confirms the presence of three phases with similar compositions observed in the annealed materials: a dark BCC matrix containing low amounts of Hf and Ru, a HCP grain containing only Hf, and purple regions corresponding to (Hf,Ru)-rich B2 grains. While the lattice parameters of the individual phases were not determined exactly, the presence of aligned Moiré fringes in the larger B2 grains indicate that the B2 grains possess a very close lattice parameter to that of the surrounding BCC matrix. It is also clear that at this stage the small B2 precipitates, in the interior of grains, are coherent with the BCC matrix (Figure 2.12A). This would suggest that the lattice parameters of the BCC and B2 phases in the splat quenched condition are different from the lattice parameters measured in the annealed conditions.

By the intersection method, the average grain size is 1.3 ± 0.6 μm and ranges from 0.5 to 15 μm. Indentations were made at the thickest portion of the splat quenched foil ($\approx$ 200 μm) to guarantee sufficient thickness; diagonals of the indentations were on average 33.5 ± 1.8 μm. The hardness of the splat quenched material was calculated to be 852 ± 18 HV (Figure 2.5).

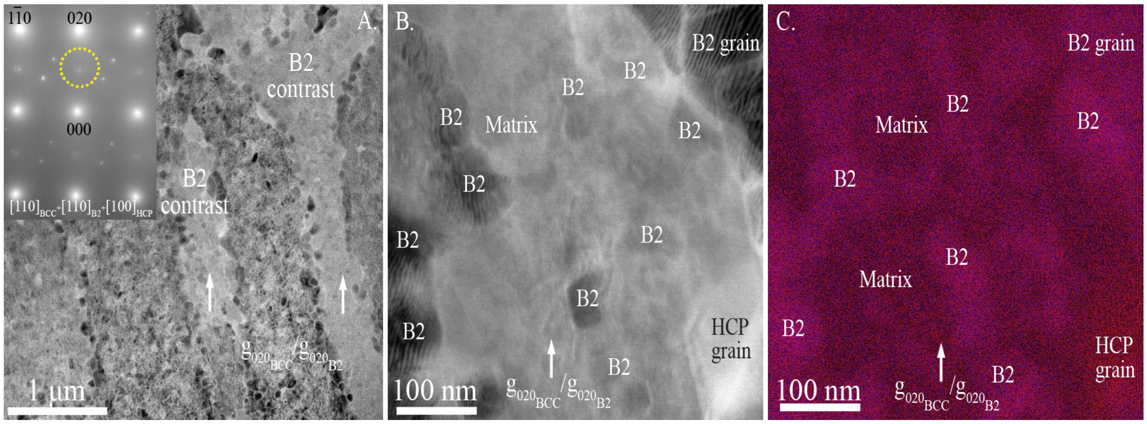

Figure 2.12: TEM analysis of the splat quenched alloy. A. A two-beam HAADF-STEM overview taken using g = $[020]_{BCC}$, shown in the inset, where the marked spot corresponds to the B2 planes. There is a clear indication for the multiple grains with precipitates along the grain boundaries and within the grains' core. The image also reveals diffraction contrast from the two grains, having the same orientation, giving rise to a B2 contrast in the grain's core. B. A closer look from A. reveals a clear contrast from the B2 precipitates within the BCC matrix which can also be indicated from C. the corresponding STEM-EDS map, where Ru (blue) and Hf (red), were used to construct the map. Note that the B2 grains are also characterized by translation Moiré fringes which are forming due to the very close lattice parameter to that of the surrounding BCC matrix. The contrast raised from the HCP is from an individual grain.

2.4 Discussion

The higher order composition space of MPEs enables new designs within the refractory-rich alloy space. In this study we have specifically aimed for precipitation of a high temperature B2 phase within a BCC refractory MPE. Samples have been processed via conventional arc-melting and in a higher temperature splat quenching setup. Alloying, microstructure, phase transformations and the implications for mechanical properties are discussed in the following sections.

2.4.1 Solidification of the as-cast material

Three phases are present in the as-cast material: a (Nb, Ta)-rich BCC phase, an ordered (Hf, Zr)Ru-B2 phase, and a Zr-rich phase. The BCC structure of the (Nb, Ta)-rich matrix is expected as Nb and Ta are BCC elements with no other allotropes, and Zr and Hf transform to a BCC structure at high temperature. Nb and Ta can also dissolve high amounts of Ru prior to precipitation of secondary phases. The ordered (Hf,Zr)Ru-B2 phase is also consistent with the binary phase diagrams of the respective elements. Ru forms a discrete ordered B2 phase in Hf-Ru and Ru-Zr binary phase diagrams and causes a order-disorder transition in the Nb-Ru and Ta-Ru systems, yielding a high likelihood of ordered B2 formation in the quinary[181, 184, 186]. Given the low volume fraction of the Zr-rich phase, no peaks in the XRD scan can be specifically assigned to identify its ordering (Figure 2.4). It is possible for the phase to be a second disordered BCC phase due to the high temperature BCC structures of Hf and Zr, or the extra peaks indicative of potential HCP ordering are obscured by the background measurement of the spectrum. The significant content of Ru (Table 2.2) in the Zr-rich phase is consistent with a BCC structure as HCP-Hf and -Zr have very low Ru solubilities (<1 at%) and additions of Ru stabilize BCC-Hf and BCC-Zr to lower temperatures[186].

Upon solidification, significant segregation of Zr to the intra-dendritic regions occurs, where both the ordered B2 phase and the Zr-rich phase are concentrated. However, a fraction of the B2 phase is present in the intra-dendritic Nb and Ta rich regions and are large enough to demonstrate dendritic segregation. The B2 phases present in the Hf-Ru and Ru-Zr binary phase diagrams persist until melting at equilibrium and can form directly from the melt on cooling, depending on the composition[186]. Combined with the low average content of Ru and Hf present in the (Nb,Ta)-rich matrix, the ordered B2 phase likely begins to form prior to the Zr-rich phase in the solidification process and, potentially, some fraction formed directly from the liquid.

2.4.2 Phase evolution after annealing

After annealing at all temperatures, the dendritic segregation in the (Nb, Ta)-rich matrix was eliminated and the minor phases were homogenized. Increases in the fraction of both the Zr-rich and the B2 phases from the as-cast material indicate that both phases are stable up to 1575 °C.

After annealing, the B2 grains are primarily composed of Hf and Ru, followed by Zr, Ta, and Nb, with nearly equivalent values of Ta and Nb. The isomorphous structure present in the binary diagrams is consistent with the presence of all constituent elements in the B2 phase, with the composition varying as a function of the formation enthalpy. HfRu has the largest enthalpy of formation ($\Delta H_{mix} = -87.6$ kJ/mol) of the three reported intermetallics, versus -56 kJ/mol for ZrRu[186] and -9 kJ/mol for NbRu[201]. The enthalpy of formation of TaRu is currently unreported. The decrease in volume fraction of the (Hf, Zr)Ru-B2 phase (from $\approx 45\%$ to 35%) and increase of the Ru content in the (Nb,Ta)-rich phase with increasing temperature indicates that some of the ordered B2 can be dissolved into the (Nb,Ta)-rich phase and then aged to form smaller precipitates.

Full suppression of B2 phases in certain areas of the splat quenched foil and the discrete B2 precipitates shown in Figure 2.12 also indicate that B2 precipitates can form from the BCC lattice, indicating they can dissolve at elevated temperatures. However, since the solidus temperature was not reached in this investigation it remains to be investigated if some fraction of the B2 in this material can persist to melting and, conversely, form directly from liquid upon solidification. Persistence to melting would present a challenge for traditional thermal processing routes such as solution and aging treatments, which aim to produce a fine dispersion of the strengthening phase by annealing sequentially above and below the solvus temperature. Even with a fraction of the B2 dissolved into solution, any coarse B2 grains remaining could significantly impact mechanical properties. Complete refinement of Ru B2 precipitates via solution and aging in a bulk material would require careful investigation of ternary Ru systems, as currently all known Ru B2s persist to melting in binary alloys.

The stability of the HCP phase to 1575 °C is consistent with the presence of Hf in the alloy and the high concentrations of O and N in the Zr-rich phase. HCP-Hf is stable to 1743 °Cin its elemental state and raises the HCP-to-BCC transition temperature of Zr[202]; additions of O and N can also raise the transition temperature and eventually suppress the BCC structure completely at sufficiently high concentrations[203, 204]. Octahedral interstitial sites in the Hf and Zr HCP structures are more favorable to O and N than the interstitial sites available in BCC structures[205]. The lack of measured Ru in the Zr-rich phase could be attributed to the low solubility of Ru in HCP-Hf and Zr and indicative of the HCP structure being stable at the highest annealing temperature, rather than a BCC to HCP transition on cooling[186]. The OR following the Burgers path is another indication of the oxygen-induced phase transformation, promoting the BCC to HCP transformation. Similar Zr- and O-rich phases have been reported by Senkov *et al.* in a $Nb_{33}Ta_{33}Zr_{33}$ sample hot isostaically pressed at 1400 °C[206], identified by selected area diffraction patterns as an HCP structure. Those phases were more angular and needle-like in morphology than the structures observed in this investigation. It is possible that the reduction of the interstitial content in $Hf_{20}Nb_{20}Ta_{20}Zr_{20}Ru_{20}$ would reduce the volume fraction of the Zr-rich phase or result in a Zr-rich BCC phase, particularly at higher heat treatment temperatures. However, the preferential concentration of O in the Zr-rich phase may require very low interstitial contents to prevent any stabilization of an HCP phase.

Interstitials have detrimental effects on the ductility of solid solution refractory alloys[205, 207, 208] and precipitation of grain boundary oxides are connected to intergranular failure of refractory materials with low interstitial solubilities[209]. Gettering of O and N by a Zr-rich phase has potential benefits if the volume fraction can be controlled to reduce impacts on mechanical properties, as precipitation of BCC and HCP phases on the grain boundaries of $Hf_{20}Nb_{20}Ta_{20}Ti_{20}Zr_{20}$ have also been reported by Mills *et al.* and Yasuda *et al.* to significantly reduce the ductility of the alloy[87, 91].

The experimentally determined XRD lattice parameters of the BCC1 and B2 phases are within 1 % of the lattice parameters calculated via Vegard's Law (Table 2.3) and yield a misfit between the two phases of -4.0 %, -3.3 % and -3.4 % for the samples annealed at 1350 °C, 1475 °C and 1575 °C, respectively (Eq. 1.1). The lattice parameters for the 1350 °C sample determined via TEM yield a slightly greater misfit of 4.3 %. This is significantly higher than the misfits observed between many BCC + B2 (Al, Ti, Zr)-containing RMPEAs (ranging from ≈ 0 to 2.6 % [152, 210]) and Ni superalloys that allow for coherent phase formation ($< \pm 1$ % [4]). However, many isomorphous Ru-containing B2 exist and some are reported to form complete solid solutions[184, 186], suggesting that the lattice parameters in these systems could be tailored for better coherency. Further, at sufficiently small sizes, the B2 precipitates exhibit coherency with the surrounding BCC matrix (Figure 2.12).

The difference between the experimental and calculated lattice parameters for the HCP phases at 1475 °C and 1575 °C are higher, 1.4 % and ≈ 2 % respectively. Nb and Ta do not posses an HCP crystal structure at any temperature and an extrapolation of their HCP lattice parameters from binary solutions for the calculation is less likely to represent their experimental impact on the observed HCP phase.

2.4.3 Mechanism of lamellar growth

The development of the HCP and B2 grains into a lamellar morphology (Figure 2.8), consuming a single disordered phase, suggests that discontinuous precipitation controls the growth front and the partitioning is achieved via a cellular growth mechanism[211]. Comparable lamellar structures have been observed in a $Hf_{25}Nb_{25}Ta_{25}Zr_{25}$ alloy annealed at 1150 °C[212]. The redistribution of solute is achieved via grain boundary diffusion, as evident from the unchanged matrix composition up to the lamellar front. In this case, two transformations are occurring with cooling. The first would be the formation of B2 from a supersaturated BCC1. The second transformation path, from supersaturated BCC1 to HCP1, follows the Burgers path due to the presence of O. As the selected temperatures were insufficient to entirely dissolve the B2 and HCP1, it is unknown which reaction occurs at a higher temperature. Further, the formation of HCP1 will be strongly dependant on the amount of O present.

A second BCC phase, BCC2, was observed in the lamellar region. BCC2 has a slightly different composition (enriched in Nb and Ta and depleted in Zr) and a larger lattice parameter (≈ 3.5 % larger) compared to BCC1. Notably, the composition change from BCC1 to BCC2 results in a decrease in the estimated lattice parameter by Vegard's law. The increase in lattice parameter may be ascribed to maintaining the coherency between the lamellae and the minimization of the interfacial free energy required for the promotion of the lamellar region. Coherency are also shown between B2/HCP1/BCC2 as evident from the maintenance of the B2 lamella shape in the vicinity of the other lamellae. The two transformation paths, BCC1 → BCC2 + B2 and BCC1 → BCC2 + HCP1, therefore result in the three phase (BCC2, B2, and HCP1) lamellar regions.

The splitting of the lamellae appearing in the lamellar front along with a second phase in between (either B2 or BCC2), Figure 2.10, may indicate a branching mechanism. In this type of mechanism, a new lamella is created as a result of significant accumulation of solute of one type at the front of the lamellae, leading to a formation of a second phase[213, 214]. In some sense, this may be considered as the system trying to approach a local equilibrium. The transition from a matrix with coherent precipitates to a homogeneous matrix with coarsened grains may suggest that the discontinuous precipitation mechanism competes with the coarsening of the matrix precipitates.

2.4.4 Evaluation of potential phase ductility

In refractory RMPEAs it will be important to strike a balance of low temperature ductility and high temperature strength. Indentation of the 1350 °C annealed sample resulted in cracks in the ordered B2 and Zr-rich HCP phases and no visible cracks in the (Nb,Ta)-rich phase. Pure Nb and Ta, binary alloys, and RMPEAs drawn from Hf, Nb, Ta, and Zr are known to have extensive compressive plasticity and tensile ductility [46, 88, 215], indicating the matrix phase of this alloy could also possess some degree of tensile ductility, consistent with the absence of cracking. This would yield a potentially desirable matrix material. The effect of Ru on tensile ductility in RMPEAs is currently unexplored but might be significant in this alloy due to the high concentration of Ru remaining in the matrix after annealing ($\approx$ 6-9 at%).

With the exception of anomalously ductile B2 compounds, such as YAg[216], most binary B2 intermetallics demonstrate ductility that is at most a few percent[217, 218]. The (Al, Ti, Zr)-based RMPEAs with two phase B2 and BCC microstructures report limited compressive plasticity when the complex B2 intermetallic is present as the matrix[219]. There is a lack of reported mechanical properties for HfRu-B2 and ZrRu-B2, where Hf and Zr are the primary constituents of the B2 phase reported in this investigation, but the number of cracks present indicate the B2 phase at the composition investigated here also exhibits limited ductility. A similar lack of ductility is evident in the cracking of the Zr-rich HCP phase. HCP structures do not possess five independent slip systems, which decreases their potential ductility in comparison to disordered face-centered cubic and BCC materials; combined with the high concentration of interstitials in the Zr-rich HCP phase and the previously noted embrittlement of HCP and BCC materials by interstitials[205, 207], the Zr-rich phase is likely very brittle. Developing Ru-containing BCC + B2 alloys with appreciable tensile ductility would require controlling the intermetallic volume fraction and preventing complete coverage of the grain boundaries via processing. Understanding the effect of Ru on the ductility of the matrix would also be necessary.

2.4.5 Evaluation of CALPHAD predictions

The CALPHAD predictions (Figure 2.2) were not fully consistent with the experimental results. CALPHAD correctly identified the formation of a (Nb,Ta)-rich disordered BCC1 phase and a (Hf,Zr)-rich ordered B2 phase but no formation of a (Hf,Zr)-rich BCC2 phase was predicted. Annealing temperatures of 1350 °C and 1475 °C lie within the two phase BCC1 + B2 region of the predicted phase diagram but the Zr-rich HCP phase was observed, indicating both the 650 °C eutectoid temperature and the miscibility gap temperature range starting at 1282 °C are incorrect for the current sample. Further, the predicted volume fractions of the BCC1 and B2 phases are inverted, if the area fraction is extrapolated to volume fraction. Within the two phase BCC1 + B2 regime and towards the maximum temperature of the three phase BCC1 + B2 + BCC2 regime, it is predicted that the B2 phase will have a volume fraction of ≈ 0.60 and BCC1 will have a volume fraction of ≈ 0.38. The experimentally measured values of the area fractions for the (Nb,Ta)-rich BCC1 and B2 were 0.51 and 0.45, respectively, at 1350 °C, and 0.57 and 0.35 at 1475 °C. Evaluating the phase fractions over the entire range, the Zr-rich phase is correctly predicted to have the smallest volume fraction at all temperature where it is present.

The annealing temperature of 1575 °C is 83 °C above the predicted $T_{solidus}$ and within a predicted BCC1 + B2 + Liquid regime. No evidence of melting was observed and the phases present and their compositions and area fractions were similar with those observed in the 1475 °C sample.

The interstitial content of the Zr-rich phase could account for the presence of an HCP phase instead of a high temperature Zr-rich BCC phase, as the CALPHAD prediction is made without detailed consideration of interstitials. As discussed in Section 2.4.2, O and N act to stabilize the α-HCP structures of Zr and Hf and there is observed preferential uptake of O and N into the Zr-rich phase. The presence of an unpredicted-by-CALPHAD HCP phase rich in O at high temperature was also reported by Senkov *et al.* in $Nb_{33}Ta_{33}Zr_{33}$[206]. With reduced interstitial content and the potential formation of a Zr-rich BCC2 phase the experimentally observed area fractions could change significantly and improve the validity of the predictions.

2.4.6 Effect of microstructure refinement

Splat quenching of $Hf_{20}Nb_{20}Ta_{20}Zr_{20}Ru_{20}$ results in significant hardening by reducing the crystallite and precipitate size of the material. This method has been supported by comparisons of FCC MPEA foils to material of the same composition processed by cold working and annealing [220]. The indentations were made on sections of the foil that possessed finely dispersed B2 and HCP precipitates, compared to the coarse particles in the as-cast material that formed during slower solidification. While the deformation mechanism requires further investigation, the dispersion of nano-scale precipitates results in a greater number of obstacles in the path of dislocations and reduces the size of the channels between obstacles; depending on the shearability of the B2 precipitates and distribution of particle sizes throughout the foil, this would increase strengthening by Orowan bowing and particle cutting mechanisms and therefore increase hardness. The grain size of the splat material also decreased, which is associated with grain boundary strengthening, although the coverage of the grain boundaries by the precipitates is very high.

2.4.7 Alloy design and the strength of MPEs

Significant solid solution strengthening is present in many RMPEAs, yielding high hardnesses as shown in Figure 2.5. From Figure 4 it is also apparent that multi-phase materials are on average harder in comparison to single-phase BCC and B2 materials. The as-cast $Hf_{20}Nb_{20}Ta_{20}Zr_{20}Ru_{20}$ sample is harder than a significant portion of single and two phase materials, and has comparable hardness to hypo- and hyper-eutectic BCC and silicide, BCC and carbide materials, and the coherent BCC + B2 $Al_{0.2}Mo_{0.1}Nb_{0.2}Ta_{0.2}Ti_{0.2}Zr_{0.2}$[221, 222, 150]. The splat quenched $Hf_{20}Nb_{20}Ta_{20}Zr_{20}Ru_{20}$ is one of the hardest materials in the literature, though still less than the hardnesses reported for powder metallurgical samples with nanocrystalline grain sizes[223] or the annealed BCC + HCP $Al_{0.22}Nb_{0.22}Ta_{0.11}Ti_{0.22}Zr_{0.22}$[224]. Cast eutectic BCC + B2 materials drawn from non-refractory elements have been reported to posses comparable hardness to the the splat quenched material, such as $Al_{0.21}Cr_{0.21}Fe_{0.21}Ni_{0.21}Mo_{0.17}$ (854 HV) [225] and $Al_{0.43}Co_{0.22}Cr_{0.23}Fe_{0.07}Ni_{0.05}$ (883 HV)[226]. Further, Yurchenko *et al.* reported the hardness of eutectic B2 + Laves regions in an $Al_{20}Cr_{10}Nb_{15}Ti_{20}V_{25}Zr_{10}$ alloy as 820 HV, though the hardness of the bulk was not evaluated[227].

While the high temperature properties of this material were not directly evaluated, the high room temperature hardness combined with a precipitate solvus above 1575 °C indicates $Hf_{20}Nb_{20}Ta_{20}Zr_{20}Ru_{20}$ has the potential to posses high strength at desired operating temperatures above 1200 °C. The density of the current alloy is undesirable but lighter elements such as Al, Ti, and Zr form isomorphous B2 intermetallics with Ru and can be potentially substituted for Hf to reduce density. The concentration of the high melting point elements in the BCC1 phase and potential of the Ru-B2 phase to uptake low melting and lower density elements such Zr into the intermetallic phase would potentially be beneficial for the development of creep resistance. Further, a high performing two-phase microstructure would also allow for other heavy elements present in the matrix (i.e. Ta) to be reduced.

2.5 Conclusions

The microstructure of as-cast and annealed equiatomic $Hf_{20}Nb_{20}Ta_{20}Zr_{20}Ru_{20}$ alloy was characterized in detail and compared to thermodynamic predictions. The major findings of this investigated are:

- The as-cast $Hf_{20}Nb_{20}Ta_{20}Zr_{20}Ru_{20}$ microstructure contains three phases: a (Nb, Ta)-rich disordered BCC1 phase, a Zr-rich phase with high O content, and an ordered (Hf, Zr)Ru B2 phase. Both the BCC1 and B2 phases exhibit dendritic segregation.

- Three phases were thermodynamically stable in samples annealed in vacuum at 1350 °C, 1475 °C, and 1575 °C: the (Nb, Ta)-rich BCC1 phase, a Zr-rich HCP1 phase, and the (Hf, Zr)Ru-B2 phase. All three of the phases persist to 1575 °C, with a reduction in volume fraction of the (Hf,Zr)Ru B2 phase with increasing temperature from 44.7 % at 1350 °C to 35.9 % at 1575 °C. The HCP1 phase increases in volume fraction from 4.1 % to 9.2 %.
- Investigation of lamellar regions in the 1350 °C sample via TEM determined them to be composed of the same HCP and B2 phases and a BCC2 phase with a larger lattice parameter. The lamellar growth is controlled via a discontinues precipitation mechanism, where the two BCC transformation paths contribute to the three detected lamellae (BCC2, B2 and HCP). This mechanism competes with the coarsening process of the matrix precipitates.
- The hardness of the three phase as-cast sample is equivalent in hardness to other multi-phase RMPEAs reported in the literature; refinement of the secondary phases to nano-scale precipitates and grain size refinement via splat quenching significantly increased the hardness from 630HV to 852HV. The splat quenched sample had a hardness higher than the 123 materials recorded in an MPE database.

In conclusion, $Hf_{20}Nb_{20}Ta_{20}Zr_{20}Ru_{20}$ possesses three phases stable to 1575 °C. It is encouraging that the binary B2 phases present in the underlying Hf-Ru and Zr-Ru diagrams appear to persist into multi-component solutions. Large lattice misfits on the order of 3-4 % exist between the observed (Nb,Ta)-BCC1 and the (Hf,Zr)Ru-B2 phases, but the misfit can be potentially be tailored by other B2 formers or matrix elements.

Additionally, 1575 °C is significantly above the temperatures reported for coherent B2 phases in (Al, Ti, Zr)-RMPEAs and within the desired operating range for new aerospace alloys, indicating Ru could offer a pathway to high temperature two-phase RMPEAs.

Chapter 3

Solidification Behaviors of Ru-containing RMPEAs[1]

In this chapter, the as-cast and annealed microstructures of 7 Ru-containing equiatomic refractory multi-principal element alloys (RMPEAs) are investigated by scanning electron microscopy. It was found that Hf-containing alloys exhibited complex solidification behavior, including eutectic, peritectic, and dendritic solidification of ordered HfRu-B2 and BCC phases. The Hf-containing alloys also precipitated B2 nanoparticles within the BCC phases upon further cooling in the solid. Room temperature micropillar compression tests were performed on these BCC + HfRu-B2 nanoparticle regions. Post-mortem transmission electron microscopy offers a first look at dislocation behaviors in these systems and revealed the presence of paired dislocations and bowing of dislocations around precipitates. Utilizing the insights from this investigation, compositions for RMPEAs with solutionable B2 precipitates stable above 1200 °C are suggested.

---

[1] Significant portions of this chapter are reproduced from this publication: **Frey, C.** et al. "High temperature B2 precipitation in Ru-containing refractory multi-principal element alloys". *Metall. Mater. Trans. A* **55**, 1739-1764 (2024). [doi] [228]. Reproduced with permission from Springer Nature.

3.1 Introduction

In Ch. 2, the phase equilbria of an equiatomic $Hf_{20}Nb_{20}Ta_{20}Ru_{20}Zr_{20}$ alloy was investigated. It was found that a high volume fraction of a (Hf,Zr)Ru-B2 phase was stable up to 1575 °C, suggesting the thermal stability of the binary B2 phases is maintained in more complex solutions. However, the (Hf,Zr)Ru-B2 phase was likely stable up to the solidus temperature due to the presence of (Hf,Zr)Ru-B2 grains in the intra-dendritic regions of the as-cast microstructure and the low Ru concentration of the disordered BCC matrix. This poses an obstacle to uniformly distributing the B2 precipitates in a matrix via the solution and aging processing pathway typically utilized for Ni-based superalloys. Further investigation of phase equilibria in these higher order compositional spaces is necessary to determine if a high volume fraction of coherent fine-scale Ru-based B2 precipitates can be produced in a ductile matrix.

To further investigate the potential of Ru as a B2 former for refractory alloys, a series of equiatomic Ru-containing RMPEAs were characterized in the as-cast and annealed conditions: $Mo_{25}Nb_{25}Ta_{25}Ru_{25}$, $Mo_{20}Nb_{20}Ta_{20}W_{20}Ru_{20}$, $Hf_{33}Mo_{34}Ru_{33}$, $Hf_{25}Mo_{25}Nb_{25}Ru_{25}$, $Hf_{25}Mo_{25}Ta_{25}Ru_{25}$, $Hf_{20}Mo_{20}Nb_{20}$-$Ta_{20}Ru_{20}$ and $Hf_{25}Nb_{25}W_{25}Ru_{25}$. Candidate materials for this analysis were drawn from a list of alloys produced by GE Research [229] and were selected for their high Ru content. This investigation found HfRu-B2 phases to be stable to at least 1500 °C in all alloys containing Hf. Nano-scale B2 precipitates were also observed in the disordered BCC phases of the Hf-containing alloys and are suggestive of compositions that could be solution and aged. TEM investigations of the as-cast $Hf_{20}Mo_{20}Nb_{20}Ta_{20}Ru_{20}$ alloy found the B2 nanoparticles are coherent with the surrounding BCC matrix. Micropillar compression experiments were conducted to investigate dislocation interactions with the HfRu-B2 phases. Implications for the design of BCC + B2 alloys are discussed.

3.2 Methods

The selected alloys were arc melted in an inert atmosphere from elemental raw materials [229]. For studying the thermal stability of the as-cast microstructures, the five Hf-containing alloys were encapsulated in individual Ta ampoules under vacuum and heat treated in a vacuum furnace. The $Hf_{33}Mo_{34}Ru_{33}$ alloy was annealed at 1500 °C for 40 h. The remaining alloys, with the exception of $Mo_{20}Nb_{20}Ta_{20}W_{20}Ru_{20}$ and $Mo_{25}Nb_{25}Ta_{25}Ru_{25}$, were annealed at 1600 °C for 40 h. NbTi foil was inserted into the ampoules to act as a getter. The samples were heated with a ramp rate of 0.25 °C/s and cooled at the maximum rate of the furnace (initial cooling rate was $\approx$ 6.2 °C/s and decreased with decreasing temperature).

Wavelength dispersive x-ray fluorescence spectroscopy (WDXRF) measurements of the bulk alloy compositions were conducted with a Rigaku ZSX Primus IV and are presented in Table 3.1. Interstitial contents were measured by inert gas fusion, performed by Northern Analytical, Inc. Due to sample quantity limitations, interstitial contents were not measured for $Mo_{25}Nb_{25}Ta_{25}Ru_{25}$, $Hf_{25}Nb_{25}W_{25}Ru_{25}$, and $Hf_{20}Mo_{20}Nb_{20}Ta_{20}Ru_{20}$. Microscopy samples were ground by SiC sandpaper to 800 grit and then polished with sequentially smaller diamond suspensions to 1 μm before finishing with vibratory polishing using colloidal silica. Scanning electron microscopy (SEM) images were acquired on a ThermoFisher Apreo C microscope with backscatter electron (BSE) and secondary electron (SE) contrast; energy dispersive X-ray spectroscopy (EDS) with an EDAX Si-drift EDX detector was used to acquire chemical composition information. Electron probe microanalysis (EPMA, Cameca SX-100) equipped with wavelength-dispersive spectroscopy was used in some cases for higher-accuracy composition measurements. A focused beam, of 20 kV and 10 nA, was used to maximize the spatial resolution. Pure elemental standards were used and the mounts were carbon coated to avoid electron beam charging. All elements had a 30 s on-peak and 30 s off-peak collection time, with analyzing crystals of: LLIF for Hf and Ta, LPET for Ru and Mo, and PET for Nb. X-ray diffraction (XRD) patterns were obtained with a Panalytical Empyrean Powder Diffractometer using Cu Kα radiation ($\lambda = 0.154$nm). Bulk samples were mechanically polished to a surface finish of 12.5 μm or better prior to XRD. Lattice parameters were determined by Bragg's Law from the peak positions. Reported volume fractions were determined via point counting method according to ASTM standard E562 19e1[230]. Each grid had more than 100 pts.

Table 3.1: Chemical composition (at%) and interstitial content (ppmw) of the bulk as-cast alloys.

Alloy	Hf	Mo	Nb	Ru	Ta	W	O	N
$Mo_{25}Nb_{25}Ta_{25}Ru_{25}$	-	24.0	25.9	25.0	25.2	-	-	-
$Mo_{20}Nb_{20}Ta_{20}Ru_{20}W_{20}$	-	18.5	21.7	21.5	20.1	18.2	276	30
$Hf_{33}Mo_{34}Ru_{33}$	32.6	35.3	-	32.1	-	-	1040	30
$Hf_{25}Mo_{25}Nb_{25}Ru_{25}$	25.5	24.7	25.6	24.3	-	-	858	77
$Hf_{25}Mo_{25}Ta_{25}Ru_{25}$	27.8	23.9	-	23.7	24.7	-	744	57
$Hf_{20}Mo_{20}Nb_{20}Ta_{20}Ru_{20}$	20.5	19.7	20.6	18.6	20.6	-	-	-
$Hf_{25}Nb_{25}W_{25}Ru_{25}$	24.8	-	24.0	28.3	-	22.9	-	-

Thin foils of as-cast $Hf_{20}Mo_{20}Nb_{20}Ta_{20}Ru_{20}$ were prepared for transmission electron microscopy (TEM) by using the FIB lift-out method with a Ga^+ ion beam in a FEI Helios Dualbeam Nanolab 600 equipped with an OmniProbe. TEM microstructural investigations were conducted in a FEI Talos F200X S/TEM operated at 200kV. Selected area electron diffraction (SAED) patterns were captured to identify the phases present in the foil. Scanning transmission electron microscopy (STEM) with a high angle annular dark field (HAADF) detector was performed to elucidate nanostructural features in the foil. EDS was employed to determine the local chemical compositions using a SuperX detector and Velox software.[2]

---

[2] FIB and TEM of the as-cast $Hf_{20}Mo_{20}Nb_{20}Ta_{20}Ru_{20}$ foil was performed by Kaitlyn Mullin.

Micropillars were fabricated in $Hf_{20}Mo_{20}Nb_{20}Ta_{20}Ru_{20}$ after heat treatment at 1600 °C using a FEI Nova dualbeam FIB/SEM. Intitially, annular wells with an inner diameter of 7.5 μm and an outer diameter of 35-50 μm were milled to $\approx$ 10 μm depths at an accelerating voltage of 30 kV and current of 21 nA. Circular fiducial markers were then milled into the top of each pillar, and shaped to their final dimensions using the lathe method described by Uchic *et al.* [231] at 30 kV and 93 pA. The final diameters of the micropillars ranged from 5.18 μm to 5.28 μm, with length-to-diameter aspect ratios of $\approx$ 2. The crystal orientation for each micropillar was determined by electron backscatter diffraction (EBSD) in a Thermo Fisher Scientific Apreo C SEM at an accelerating voltage of 20 kV using an Oxford Symmetry S2 detector. Post-deformation characterization of the slip traces was performed in a TFS Apreo C SEM at 5 kV using a beam deceleration of 220 V, as described by Balbus *et al* [232].[3]

Micropillar compression experiments were conducted in a MTS XP Nanoindenter with a 10 μm diamond flat punch. A 10^{-3} s^{-1} intitial strain rate was used for each sample, and experiments were performed to a total displacement of 500 nm ($\approx$ 5 % strain). Thin foils for (S)TEM characterization were prepared from a deformed micropillar, as described by Norfleet *et al.* [233] and Balbus *et al.* [232], where the foil is extracted such that its normal is perpendicular to the slip plane of interest. The samples were thinned to $\sim$ 80 nm in a FEI Nova dualbeam FIB/SEM with a final milling step at 5 kV. Finally, the sample was polished in a Fischione 1040 NanoMill at 600 eV, 100 pA to help reduce FIB damage. Conventional TEM and annular dark field (ADF) STEM experiments were performed in a TFS Talos X (S)TEM at 200 kV. Burgers vectors were determined in a conventional TEM using g.b analysis. Dislocation trace analysis to determine dislocation line direction using ADF STEM images was performed using the pycotem packge [234].

---

[3] Micropillar fabrication, compression, and post-mortem TEM analysis was performed by Dr. Glenn H. Balbus.

3.3 Results

Microstructural observations of the as-cast alloys (utilizing both SEM and TEM) are described first, followed by an investigation of high temperature heat treatments on the Hf-containing alloys. In all alloys, the two major constituent phases are named in order of their solidification sequence (1 or 2) and are identified as either disordered BCC or as an ordered HfRu-B2 intermetallic. Following this, dislocation-precipitate reactions studied via micropillar compression experiments and TEM are reported. Overall, the investigated microtructures provide a promising pathway for the development of solution and ageable BCC + Ru-B2 alloys.

3.3.1 Microstructures of as-cast Hf-free alloys

$Mo_{25}Nb_{25}Ta_{25}Ru_{25}$ and $Mo_{20}Nb_{20}Ta_{20}W_{20}Ru_{20}$ both exhibit dendritic solidification, resulting in segregation throughout the microstructure (Figure 3.1). Compositional variations from the dendritic regions to the inter-dendritic regions measured via SEM-EDS and are reported in Table 3.2. In $Mo_{25}Nb_{25}Ta_{25}Ru_{25}$, Mo and Ta segregated to the dendrite core and Nb and Ru segregated to the inter-dendritic regions. $Mo_{20}Nb_{20}Ta_{20}W_{20}Ru_{20}$ exhibited segregation of Nb and Ru to the inter-dendritic regions and Mo and W to the dendrite core. Segregation of Ta was less pronounced, with a slightly elevated concentration in the inter-dendritic regions. The center of the dendrite core regions in $Mo_{20}Nb_{20}Ta_{20}W_{20}Ru_{20}$ were also enriched in Nb and depleted in Ta. The inter-dendritic regions of both alloys contain (Nb,Ta,O)-rich phases, indicating the formation of oxides, and a small amount of porosity. The pores and oxides are both black in backscatter electron contrast.

The XRD scan of $Mo_{20}Nb_{20}Ta_{20}W_{20}Ru_{20}$ exhibits a set of disordered BCC peaks (Figure 3.2), while the XRD scan for $Mo_{25}Nb_{25}Ta_{25}Ru_{25}$ exhibits additional B2 ordering

Table 3.2: Identified phases, assigned crystal structures, and their compositions (at%) as measured by EDS of the as-cast alloys. Error is on the order of a few at% percent.

Alloy	Region	Crystal Structure	Hf	Mo	Nb	Ru	Ta	W
$Mo_{25}Nb_{25}Ta_{25}Ru_{25}$	Interdendritic Region	B2	-	12.7-23.7	18.1-36.2	21.9-33.3	10.3-27.7	-
	Intradendritic Region	B2	-	15.8-30.5	15.3-25.2	12.7-29.0	17.5-30.5	-
$Mo_{20}Nb_{20}Ta_{20}Ru_{20}W_{20}$	Interdendritic Region	BCC	-	15.5-23.1	15.6-21.7	16.1-30.2	20.4-26.6	10.7-23.7
	Intradendritic Region	BCC	-	19.1-26.0	11.6-18.6	9.8-22.4	17.8-25.5	16.9-31.7
$Hf_{33}Mo_{34}Ru_{33}$	Phase 1	B2	51.0	3.3	-	45.7	-	-
	Phase 2	BCC	^{a}	^{a}	-	^{a}	-	-
	Phase 3	σ	4.8	47.9	-	47.4	-	-
	Lamellar B2 +BCC	B2 + BCC	21.6	57.3	-	21.1	-	-
	Nanoparticle B2 + BCC	B2 + BCC	7.5	83.4	-	9.1	-	-
$Hf_{25}Mo_{25}Nb_{25}Ru_{25}$	Phase 1	B2	43.0	7.0	9.7	40.3	-	-
	Phase 2	BCC	15.1	22.3	58.1	4.5	-	-
	Phase 3	-	74.3	5.5	19.5	0.7	-	-
	Phase 4	-	38.0	11.0	49.6	1.4	-	-
	Nanoparticle B2 + BCC	B2 +BCC	17.4	24.5	49.7	8.4	-	-
$Hf_{25}Mo_{25}Ta_{25}Ru_{25}$	Phase 1, Interdendritic Region	-	22.7-26.8	19.9-23.4	-	24.0-29.5	24.4-30.0	-
	Phase 1, Intradendritic Region	-	20.1-25.2	20.9-25.3	-	23.0-27.8	26.8-31.2	-
	Phase 2	-	47.7	24.0	-	10.1	17.9	-
	Phase 3	-	84.0	5.0	-	3.4	7.6	-
	Phase 4	-	94.7	0.9	-	0.5	3.9	-
$Hf_{20}Mo_{20}Nb_{20}Ta_{20}Ru_{20}$	Phase 1	BCC	10.4	29.1	20.2	10.6	29.5	-
	Phase 2	B2	43.8	4.6	7.4	38.7	5.5	-
	Phase 3	-	24.2-40.0	9.1-16.8	28.0-35.5	5.7-9.8	9.6-20.5	-
	Phase 4	-	82.1	2.2	9.4	1.0	5.4	-
	Nanoparticle B2 + BCC (last liquid)	B2 + BCC	14.6	25.3	21.1	12.8	26.3	-
	Nanoparticle B2 + BCC (dendrite core)	B2 + BCC	18.8	19.9	29.4	10.3	21.7	-
$Hf_{25}Nb_{25}W_{25}Ru_{25}$	Phase 1, inderdendritic region	BCC	4.2-15.2	-	28.2-58.6	2.4-9.8	-	16.8-64.6
	Phase 1, intradendritic region	BCC	0.0-9.7	-	18.6-42.1	0.0-7.4	-	43.1-77.2
	Phase 1	B2	45.5	-	6.4	45.6	-	2.4
	Nanoparticle B2 + BCC	BCC	17.2	-	57.8	8.3	-	16.8

^{a}: Regions too small to evaluate by EDS.

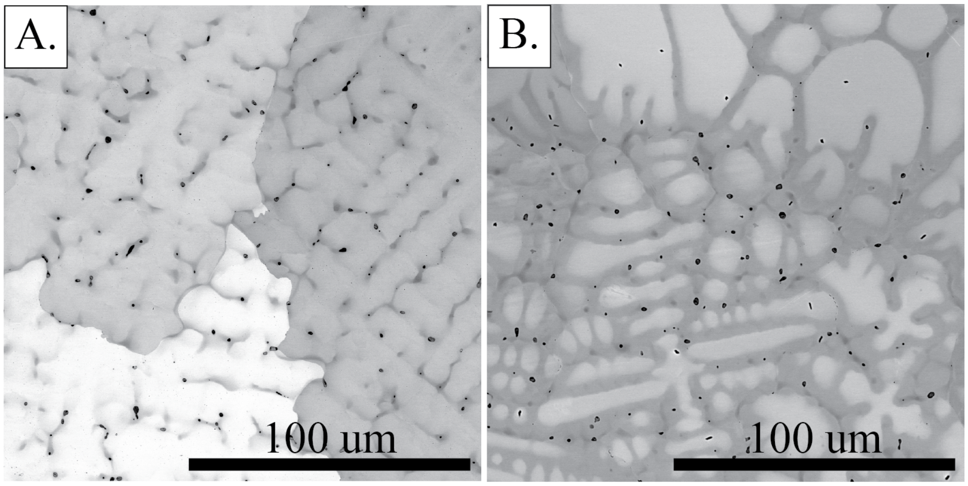

Figure 3.1: BSE images of the microstructures of as-cast A. $Mo_{25}Nb_{25}Ta_{25}Ru_{25}$ and B. $Mo_{20}Nb_{20}Ta_{20}Ru_{20}W_{20}$. In both alloys, the spherical regions with black contrast are primarily (Nb,Ta,O)-rich phases. A minor number of the black regions are pores.

peaks. Only one set of peaks is visible for each alloy, consistent with the lack of significant secondary phase formation observed via SEM. TEM diffraction also provides evidence for the B2 phase in $Mo_{25}Nb_{25}Ta_{25}Ru_{25}$ in both the dendrite core and inter-dendritic regions (Figure 3.3). $Mo_{25}Nb_{25}Ta_{25}Ru_{25}$ can therefore be identified as a single-phase B2 alloy. While $Mo_{20}Nb_{20}Ta_{20}W_{20}Ru_{20}$ does not demonstrate the extra B2 peaks in XRD, the dendritic segregation in the microstructure resulted in regions where the Ru concentration is equivalent to that of $Mo_{25}Nb_{25}Ta_{25}Ru_{25}$, suggesting regions of $Mo_{20}Nb_{20}Ta_{20}W_{20}Ru_{20}$ could also be ordered. The lattice parameters of the identified phases are presented in Table 3.3.

3.3.2 Microstructures of as-cast Hf-containing alloys

$Hf_{33}Mo_{34}Ru_{33}$

Four phases are visible in the BSE microstructure images of $Hf_{33}Mo_{34}Ru_{33}$ (Figure 3.4): a light grey (Hf,Ru)-rich Phase 1, a dark grey (Mo)-rich Phase 2, a medium grey (Mo,Ru)-rich Phase 3, and a bright grey (Hf, O)-rich Phase 4 with internal striations.

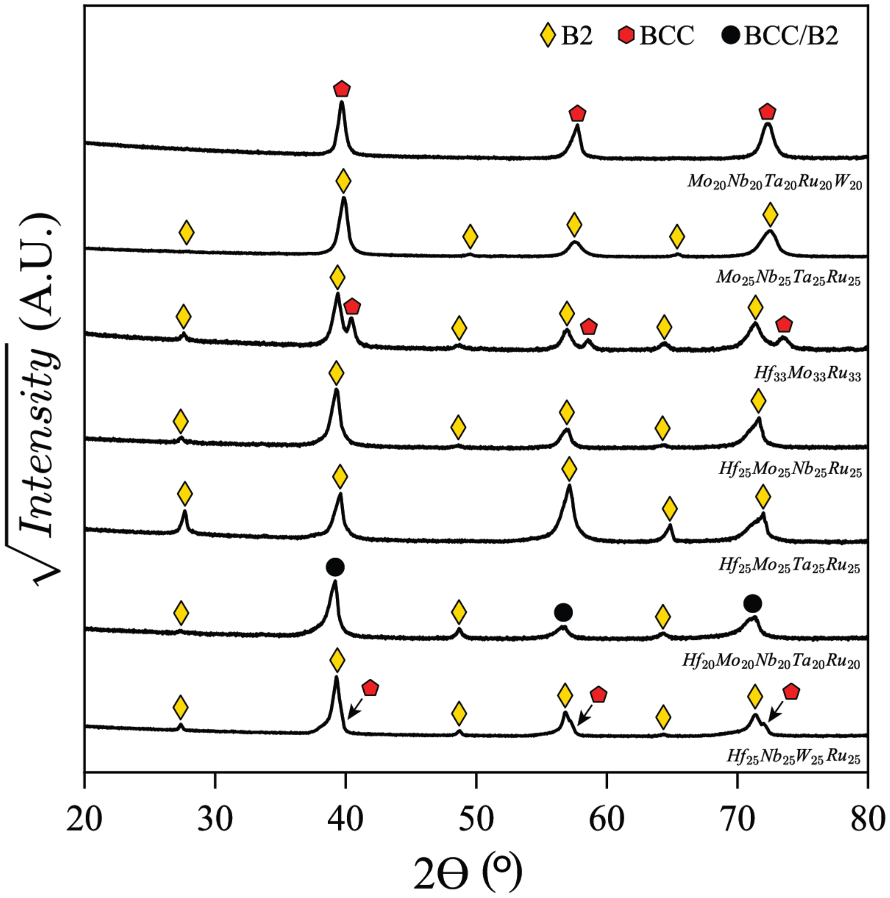

Figure 3.2: XRD scans of the as-cast alloys. Only BCC and B2 peaks were observed. Asymmetry in the observed peaks may be the result of a low misfit between the BCC and B2 phases, causing overlapping peaks, or chemistry and lattice parameter variations within the disordered BCC phases.

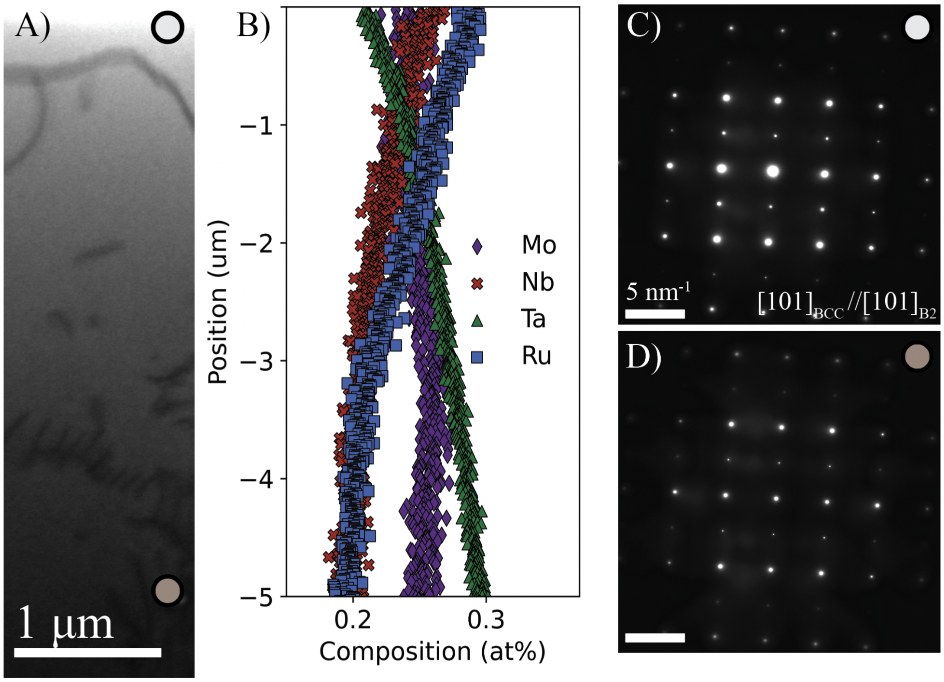

Figure 3.3: TEM analysis of as-cast $Mo_{25}Nb_{25}Ta_{25}Ru_{25}$. A. DF-STEM image of the intra-dendritic region transitioning into the inter-dendritic region. B. STEM-EDS chemical measurement into the interdendritic region in A. Enrichment of Ru and Nb is observed in the intra-dendritic region, along with enrichment of Mo and Ta in the inter-dendritic region. C., D. Selected area diffraction patterns at the corresponding locations marked in A. Diffraction patterns confirm B2 ordering throughout both regions.

Table 3.3: Identified phases and calculated lattice parameters of the as-cast alloys.

Alloy	Phase	Prototype	Lattice Parameter (Å)
$Mo_{25}Nb_{25}Ta_{25}Ru_{25}$	B2	CsCl	3.194
$Mo_{20}Nb_{20}Ta_{20}Ru_{20}W_{20}$	BCC	W	3.199
$Hf_{33}Mo_{34}Ru_{33}$	B2	CsCl	3.232
	BCC	W	3.152
$Hf_{25}Mo_{25}Nb_{25}Ru_{25}$	B2	CsCl	3.238
	BCC/B2	-	3.233
$Hf_{25}Mo_{25}Ta_{25}Ru_{25}$	B2	CsCl	3.216
$Hf_{20}Mo_{20}Nb_{20}Ta_{20}Ru_{20}$	B2	CsCl	3.246
	BCC/B2	-	3.242
$Hf_{25}Nb_{25}W_{25}Ru_{25}$	B2	CsCl	3.240
	BCC	W	3.216

Phase 1 is present in three length scales in the microstructure, with similar Z-contrast in BSE and preferential polishing behavior SE images at all length scales. Phase 1 is present as dendrites, in alternating lamellar regions with the dark grey Phase 2, and as nano-scale precipitates embedded in Phase 2. The two-phase lamellar region would be consistent with a eutectic reaction. Some nanoparticles appear coarsened and form chainlike structures but remain submicron in size. The combined area fraction (a_f) of the dendritic and lamellar Phase 1 is 0.62. Phase 2 is continuous throughout the microstructure and surrounds all three forms of Phase 1.

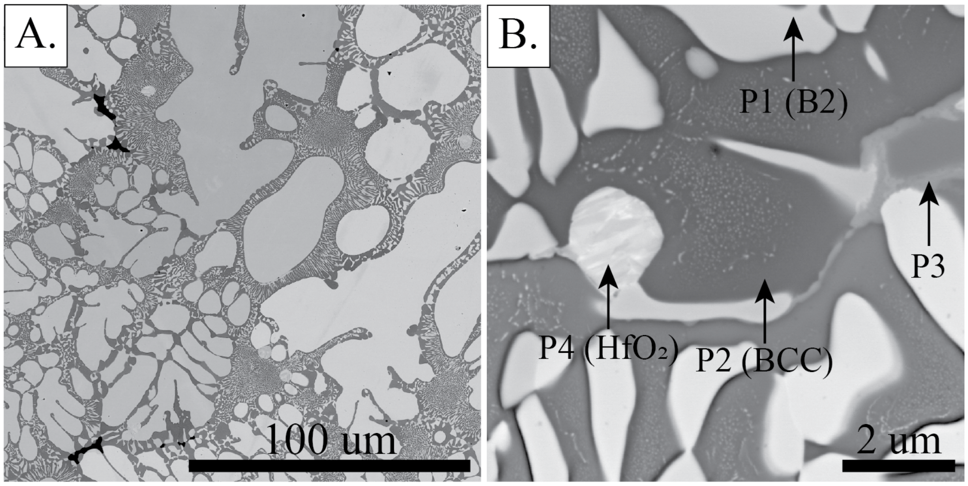

Figure 3.4: A., B. BSE images of the microstructure of as-cast $Hf_{33}Mo_{34}Ru_{33}$. Four phases are identified and present throughout the sample. Phase 1 nanoparticles are visible in the Phase 2 regions in B. P1 is an ordered HfRu-B2 phase and P2 is a disordered (Mo)-BCC phase.

Phase 3 and Phase 4 are present in minor amounts (less than 0.10 area fraction). In some instances Phase 4 is embedded in the Phase 1 dendrites, varying from submicron to 20 microns in diameter.

A XRD scan of the as-cast $Hf_{33}Mo_{34}Ru_{33}$ alloy is presented in Figure 3.2. Two sets of peaks are clearly visible: one set of peaks corresponds to a disordered BCC phase with no additional ordering peaks and the other set corresponds to an ordered B2 phase. There are no ordered B2 phases found in the Mo-Ru [235] or Hf-Mo [236] binary phase diagrams and the composition of Phase 1 as measured by SEM-EDS corresponds to the composition of the ordered B2 intermetallic in the Hf-Ru phase diagram [186]. Therefore, Phase 1 is identified as a HfRu-B2 phase. While the composition of Phase 2 cannot be directly measured because of the nanoparticles, the uptake of Hf and Ru into the HfRu-B2 nanoparticles would result in a highly enriched Mo phase, and the calculated lattice parameter of Phase 2 (Table 3.3) is close to the lattice parameter of pure Mo (3.152 Å vs 3.147 Å). Phase 2 is therefore identified as a disordered (Mo)-BCC phase. Due to their small volume fraction, no additional peaks are present to identify Phases 3 and 4. However, given the high O content of Phase 4 and the lack of significant amounts any elements other than Hf, it is identified as a hafnium oxide (HfO_2) phase.

Corresponding compositions of the phases are presented in Table 3.2, with the exception of the dark contrast (Mo)-rich BCC phase that was present in regions too small to probe with EDS. Compositions for the lamellar BCC and B2 inter-dendritic regions and the nanoparticle B2 + BCC regions are also presented. The composition of the B2 phase was also measured with EPMA and is presented in Table 3.4.

Table 3.4: Identified phases in the as-cast alloys and their compositions (at%) as measured by EPMA. All reported compositions represent the average of multiple (at least 10) measurements.

Alloy	Region	Hf	Mo	Nb	Ru	Ta	W
$Hf_{33}Mo_{34}Ru_{33}$	B2	50.0 ± 0.2	3.5 ± 0.2	-	46.5 ± 0.2	-	-
$Hf_{25}Mo_{25}Nb_{25}Ru_{25}$	B2	42.6 ± 0.8	6.6 ± 0.8	8.6 ± 0.7	42.3 ± 0.8	-	-
	B2 + BCC	18.4 ± 1.3	18.8 ± 1.1	52.9 ± 2.3	9.7 ± 1.4	-	-
$Hf_{20}Mo_{20}Nb_{20}Ta_{20}Ru_{20}$	B2	35.0 ± 2.3	8.5 ± 1.4	8.1 ± 1.6	39.2 ± 2.1	9.2 ± 1.5	-
	B2 + BCC	13.7 ± 1.5	24.6 ± 1.8	27.1 ± 1.9	12.3 ± 0.9	22.4 ± 1.4	-
$Hf_{25}Nb_{25}W_{25}Ru_{25}$	B2	45.5 ± 0.5	-	5.7 ± 0.5	47.0 ± 0.4	-	1.9 ± 0.5

$Hf_{25}Mo_{25}Nb_{25}Ru_{25}$

Similar to $Hf_{33}Mo_{34}Ru_{33}$, $Hf_{25}Mo_{25}Nb_{25}Ru_{25}$ consists primarily of two phases (Figure 3.5): a (Hf,Ru)-rich Phase 1 that appears light grey in backscatter electron contrast and a second (Mo,Nb)-rich Phase 2 that is darker. Phase 1 solidified both as large blocky regions tens of microns across that are surrounded by a nano-scale layer of Phase 2 and as nano-scale fibrous rods alternating with Phase 2. This microstructure would be consistent with the formation of pro-eutectic Phase 1 surrounded by a fine-scale eutectic structure of Phases 1 and 2. When adjacent to the larger Phase 1 structures, the nano-scale Phase 1 is oriented with its longest direction perpendicular to the Phase 2 boundary. Layers of Phase 2 are also found independent of the large Phase 1 structures, resulting in the appearance of rings.

In some regions of the ingot there is elongated phase morphology and coarsening of Phase 1 towards grain boundaries (Figure 3.5B, D). Larger regions of Phase 2 are also found at some grain boundaries. Within these regions are patches of nano-scale precipitates embedded in Phase 2. Compositional segregation is evident, with the nano-scale particles appearing in regions enriched in Hf and Nb and depleted in Mo (Figure 3.6A and B). Some of the nanoparticles appear coarsened along a chain. Consistent with $Hf_{33}Mo_{34}Ru_{33}$, the nanoparticles demonstrate backscatter electron contrast and preferential polishing behavior in SE consistent with Phase 1, indicating the nanoparticles and Phase 1 are the same phase. HfO_2 particles of similiar composition and high O content to those observed in $Hf_{33}Mo_{34}Ru_{33}$ are also present with varying sizes and locations. The intergranular regions also contain a Hf-enriched phase (Phase 3) and a Nb-rich phase (Phase 4) with lower oxygen content than the HfO_2 particles. Phase 3 appears bright in backscatter contrast and is primarily composed of Hf, with an appreciable content of Nb (19.5 at%) and minor amounts of Mo and Ru. Phase 4 appears darker in backscatter electron contrast and is enriched in Nb, containing on average 49.6 at% Nb and 38.0 at% Hf and equivalent amounts of Mo and Ru as Phase 3.

A XRD scan of $Hf_{25}Mo_{25}Nb_{25}Ru_{25}$ is presented in Figure 3.2. The peaks indicate the presence of an ordered B2 phase. Only Phase 1 and Phase 2 are present in high enough

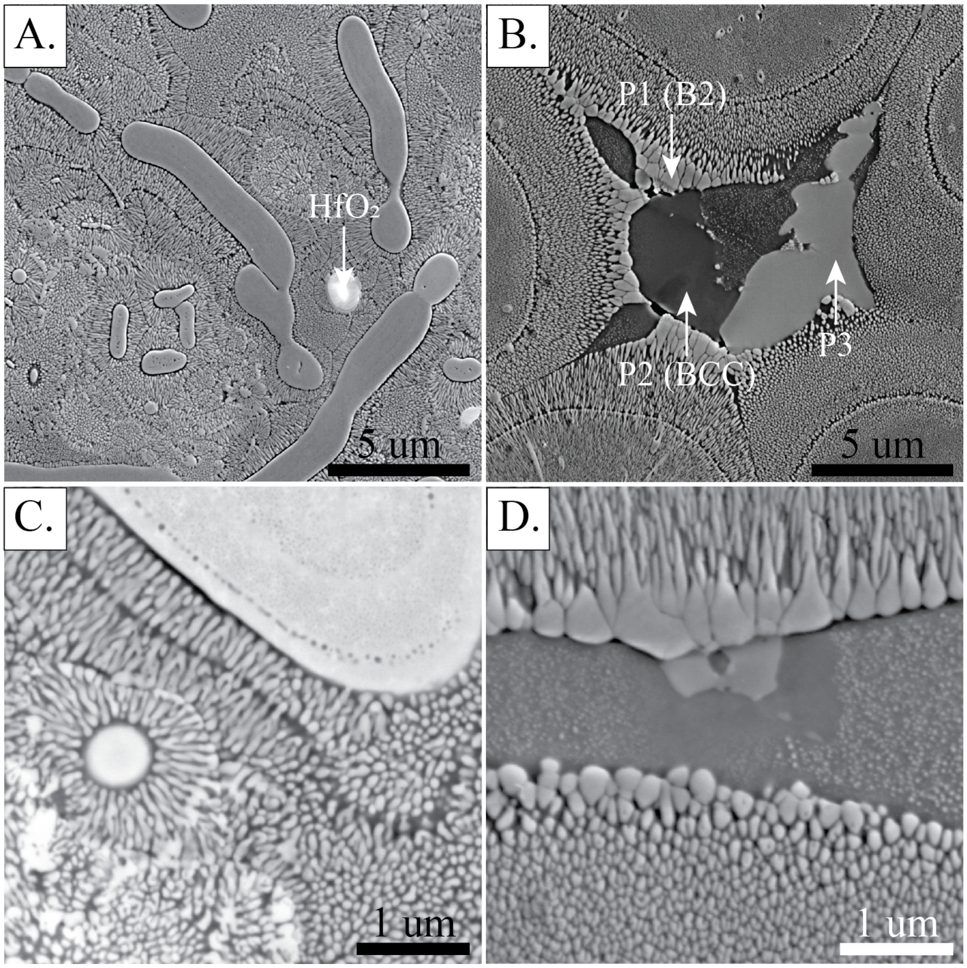

Figure 3.5: A., B. SE images of as-cast $Hf_{25}Mo_{25}Nb_{25}Ru_{25}$. Higher magnification C. BSE and D. SE images of the regions shown in A. and B., respectively. Four phases are identified. Precipitation of Phase 1 nanoparticles is visible in the Phase 2 regions in B. and D. P1 is an ordered HfRu-B2 phase and P2 is a disordered (Mo, Nb)-BCC phase.

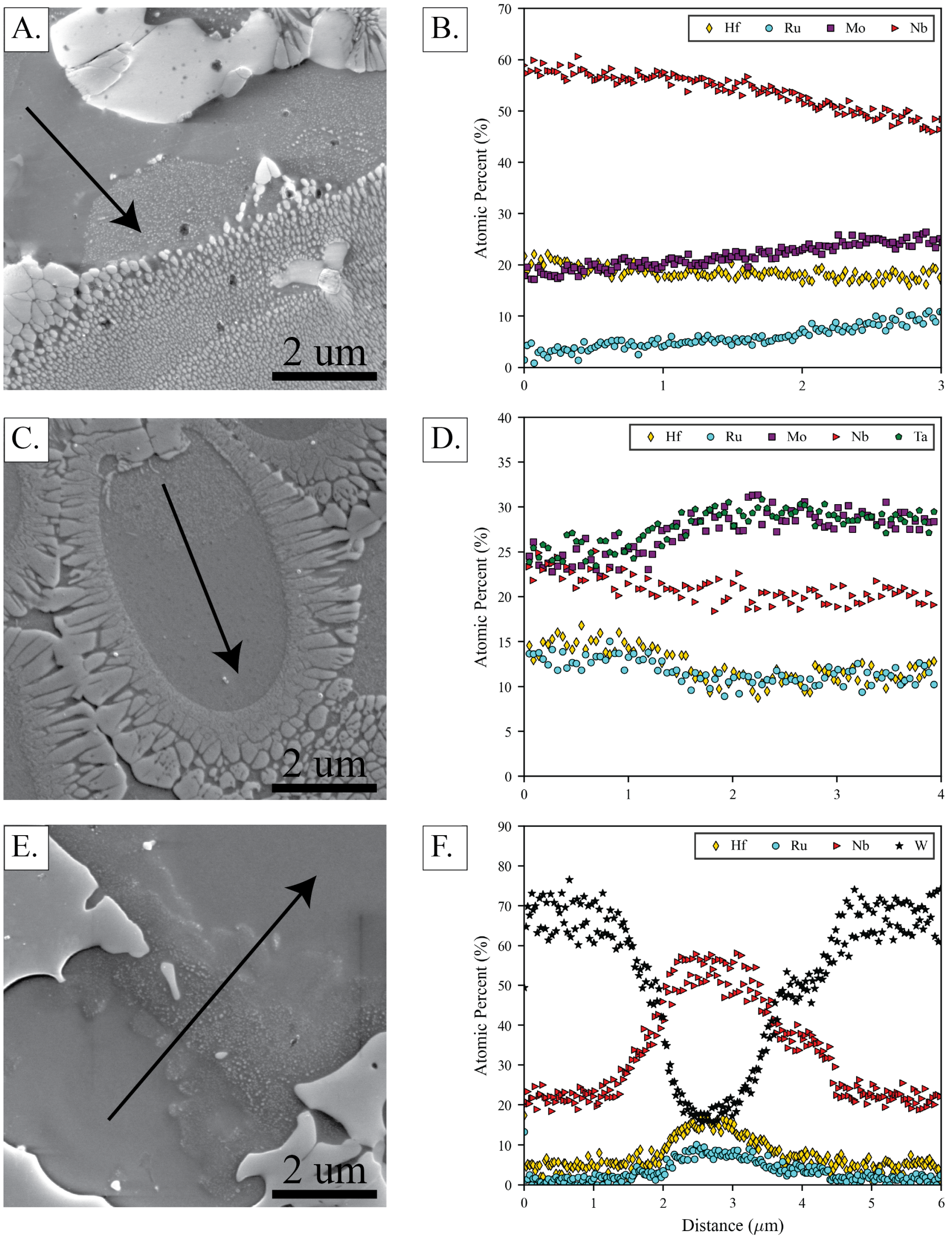

Figure 3.6: A. BSE micrograph of $Hf_{25}Mo_{25}Nb_{25}Ru_{25}$ with marker indicating direction of compositional linescan in B. Nanoparticles occur in region enriched in Mo and Ru. C. SE micrograph of $Hf_{20}Mo_{20}Nb_{20}Ta_{20}Ru_{20}$ with marker indicating direction of EDS linescan in D. Nanoparticles occur in region enriched in Hf, Nb and Ru. E. SE micrograph of $Hf_{25}Nb_{25}W_{25}Ru_{25}$ with marker indicating direction of EDS linescan in F. Nanoparticles appear in regions enriched in Hf, Nb, and Ru.

volume fractions to produce XRD peaks of the observed intensities. The composition of the (Hf,Ru)-rich Phase 1 is consistent with a HfRu-B2 phase; while Nb and Ru can potentially form an ordered B2 phase, the the (Mo,Nb)-rich phase contains only 4.5 at% Ru. This is significantly below the composition necessary for ordering in the Nb-Ru binary phase diagram (∼40 at%) [181]. Therefore, Phase 1 is identified as an ordered HfRu-B2 phase. Phase 2 is composed primarily of Nb with significant additions of Mo (22.3 at%) and Hf (15.1 at%); both elements have large solubilities in disordered BCC Nb [235, 237]. Phase 2 is therefore tentatively identified as a disordered BCC phase. Given the shared peaks are insufficiently separated to allow calculation of both experimental lattice parameters, the lattice parameter of the B2 phase is derived only from the 1st, 3rd, and 5th peaks and the calculated lattice parameter of the remaining peaks is reported separately in Table 3.3 as BCC/B2. Phase 3 and Phase 4 were not identified.

Corresponding compositions for the four identified phases are recorded in Table 3.2, along with the composition of the BCC + B2 nanoparticle regions. The compositions of the B2 grains and the BCC + B2 nanoparticle regions were also measured by EPMA and reported in Table 3.4.

$\mathbf{Hf_{25}Mo_{25}Ta_{25}Ru_{25}}$

$Hf_{25}Mo_{25}Ta_{25}Ru_{25}$ is composed primarily of a single near-equimolar (22.9 at% Hf, 23.0 at% Mo, 28.7 at% Ta, and 25.4 at% Ru) Phase 1 (Figure 3.7). The segregation present in Phase 1 is dendritic in appearance, with the inter-dendritic regions enriched slightly in Hf and Ru, and the dendrite cores enriched slightly in Mo and Ta (Table 3.2). The grain boundaries are Hf-enriched with three distinct Hf-rich phases: a phase exhibiting solidification segregation (referred to as Phase 2), a phase darker in backscatter electron contrast and composed of primarily Hf (84 at%, referred to as Phase 3) and a bright phase enriched in Hf, O, and less than 3 at% Mo + Ru (referred to as Phase 4). Phase 2 exhibits areas enriched in Hf and others enriched in Mo and Ta; Ru is distributed evenly throughout the phase. Pores are also preferentially located in the intergranular regions. At the border of the intergranular region, Phase 1 exhibits a significant enrichment of Hf (45.7 at%) and Ru (27.3 at%), and a depletion of Mo and Ta. HfO_2 particles of similar composition and high O content to those observed in $Hf_{33}Mo_{34}Ru_{33}$ are also present with varying sizes and locations. Phases 3 and 4 contain significantly less O than the HfO_2 particles. Corresponding compositions for the four identified phases are recorded in Table 3.2.

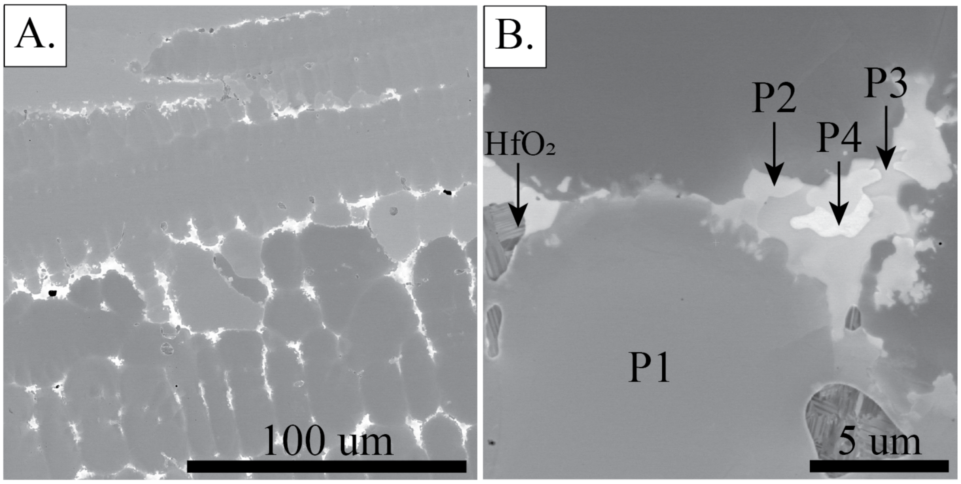

Figure 3.7: A., B. BSE images of as-cast $Hf_{25}Mo_{25}Ta_{25}Ru_{25}$. Five phases are identified, with three of them occupying the intergranular region.

An XRD scan of the alloy is presented in Figure 3.2. A single set of peaks are present that are indicative of an ordered B2 phase (with a peak missing for the (111) reflections). Phase 1 contains large amounts of Ru, which is the necessary component to form the B2 phase, indicating it is the source of the B2 reflections [186, 237]. However, approximately one micron from the edge of the intergranular regions nano-scale height variations can be observed in the SE images of Phase 1, indicating potential phase decomposition within the near-equimolar region that effects polishing behavior. Further evidence for the decomposition of Phase 1 into BCC and B2 regions requires further TEM analysis.

$Hf_{20}Mo_{20}Nb_{20}Ta_{20}Ru_{20}$

$Hf_{20}Mo_{20}Nb_{20}Ta_{20}Ru_{20}$ exhibits an apparent cored peritectic microstructure, with dark (Mo,Ta)-rich Phase 1 dendrites surrounded by a (Hf,Ru)-rich Phase 2 (Figure 3.8A, C). The Phase 2 rings are irregular and broken up by another phase consistent in backscatter electron contrast with Phase 1, yielding an irregular 'cobblestone' appearance. Outside the Phase 2 rings are regions of a third phase (Phase 3) significantly enriched in Nb and Hf and depleted in Mo and Ta. Segregation is present within Phase 3, with variations in composition resulting in brighter Hf-enriched regions (reaching 40 at% Hf) and darker (Mo,Ta)-rich regions ($\approx$ 15-20 at% Mo/Ta); Nb and Ru content vary slightly. Present within Phase 1 and Phase 3 regions are nano-scale precipitates consistent in backscatter electron contrast and preferential polishing behavior in SE images with Phase 2. Within the Phase 1 dendrites, the location of the nanoparticles is consistent with regions enriched in Hf and Ru; a compositional linescan is presented in Figure 3.6C and D demonstrating the disappearance of the nanoparticles with increasing Mo and Ta content. Outside of the nanoparticle regions, there is little segregation within the dendrite cores. In contrast, while nanoparticles are nearly always present in Phase 3, the nanoparticles appear with decreasing Hf content and increasing Mo and Ta content. Some of the nanoparticles appear coarsened in chain-like arrangements.

Within Phase 3, there is another minor phase concentrated in the Hf-rich regions. This is noted as Phase 4; it has a bright white contrast in BSE images and is composed of 82 at% Hf. This phase contains comparable O content to Phase 1. A fifth minor phase rich in Hf and O and containing internal striations in BSE images is identified as HfO_2, consist with the previous alloys.

The peritectic Phase 1 and Phase 2 microstructure is not uniform throughout the ingot, with some regions demonstrating incomplete rings of Phase 2 (3.8B, D). In these

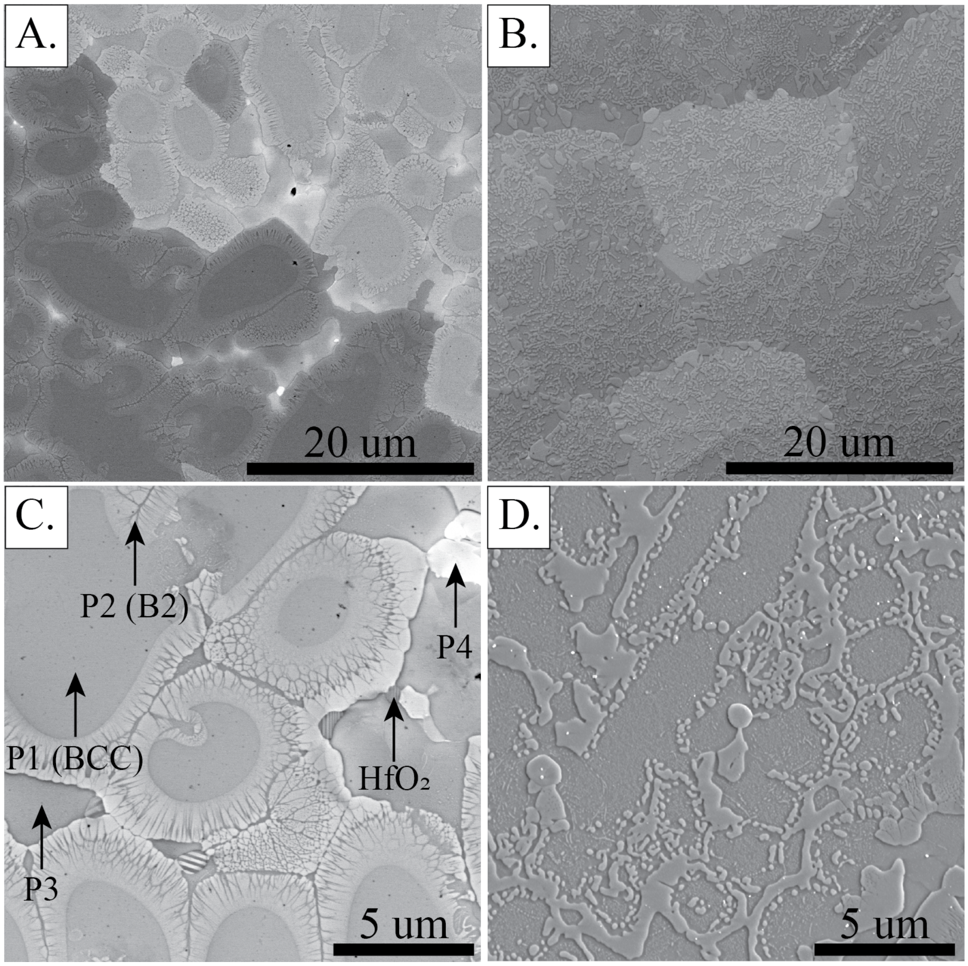

Figure 3.8: A., C. BSE images of a peritectic solidification zone in as-cast $Hf_{20}Mo_{20}Nb_{20}Ta_{20}Ru_{20}$. B.,D. SE images of a different region from A.,C. where the ring structure is incomplete. Five phases are identified and present throughout the sample. Precipitation of Phase 1 nanoparticles is visible throughout the Phase 2 regions in D. and in some locations in C. P1 is a disordered (Mo)-BCC phase and P2 is an ordered HfRu-B2 phase.

regions, all Phase 1 regions contain nano-scale precipitates of Phase 2, excepting the areas directly adjacent to the larger Phase 2 grains. The bulk composition does not change between these regions.

A XRD scan of the alloy is presented in Figure 3.2. One set of peaks is visible, demonstrating reflections consistent with an ordered B2 phase; however, slight shouldering is visible in the (110), (200), and (211) reflections. Similar to previous alloys, the (Hf,Ru)-content of the Phase 2 grains is consistent with an ordered HfRu-B2 phase and Phase 2 is therefore identified as an ordered B2 phase. Phase 1 is composed of large amounts of Mo and Ta, which form a disordered BCC phase, and insufficient Ru is present to result in ordering, indicating Phase 1 is likely a disordered BCC phase. Similar to $Hf_{25}Mo_{25}Nb_{25}Ru_{25}$, the lattice parameter of the B2 phase is derived only from the 1st, 3rd, and 5th peaks and the calculated lattice parameter of the remaining peaks is reported separately in Table 3.3 as BCC/B2. The crystal structures of Phases 3 and 4 are not identified.

Corresponding compositions for the four identified phases are recorded in Table 3.2, along with the composition of the BCC + B2 nanoparticle regions. The compositions of the B2 grains and the BCC + B2 nanoparticle regions were also measured by EPMA (Table 3.4).

$\mathbf{Hf_{25}Nb_{25}W_{25}Ru_{25}}$

$Hf_{25}Nb_{25}W_{25}Ru_{25}$ exhibits significant dendritic segregation (Figure 3.9), with the formation of highly W-rich dendrite cores (composed of 65-78 at% W) and inter-dendritic regions enriched in Nb (28-59 at%), Hf (4-15 at%) and Ru (2-10 at%). Within the inter-dendritic regions are larger grains of a (Hf,Ru)-rich phase. The dendritic matrix phase is defined as Phase 1 and the (Hf,Ru)-rich phase is referred to as Phase 2. Phase 2 is present in multiple morphologies: (i) large continuous regions tens of microns across, (ii) nano-scale 'feathery' regions that alternate with Phase 2 and which coarsen from a core towards the edges, and (iii) nano-scale precipitates embedded in the interdendritic regions. While the nanoparticles cannot be compositionally measured by EDS due to their size, the similarity in backscatter electron contrast and preferential polishing behavior indicate the nanoparticles are the same phase as the larger (Hf,Ru)-rich grains and particles. In some regions, the appearance of nanoparticles follows a compositional trend (Figure 3.6E and F.); their presence is associated with decreasing W-content and increasing Nb, Hf, and Ru content. Channeling contrast and particle coarsening consistent with sub-grain or grain boundaries are also visible in Nb-rich inter-dendritic regions. Near the edges of the ingot the dendritic morphology is less apparent and the Phase 2 regions are more globular in appearance and aligned towards the center of the ingot. Here the highly W-enriched Phase 1 regions do exhibit the formation of small nanoparticles, with slightly coarser particles in the (Nb,Ru)-enriched regions. A small area fraction of a third phase bright in backscatter electron contrast was observed but was found in sizes too small to evaluate with EDS. HfO_2 particles similar in oxygen content and composition as those observed in the other alloys are also present with varying sizes and locations.

The XRD scan associated with this alloy demonstrates two sets of peaks: one set of peaks consistent with an ordered B2 phase, and a second set consistent with a disordered BCC phase (Figure 3.2). The calculated lattice parameters are reported in Table 3.3. The disordered BCC peaks are smaller than the B2 peaks and shifted slightly to higher 2θ, indicating the BCC phase has a smaller lattice parameter than the B2 phase. W does not form a B2 phase in the W-Ru binary[238] and the Ru concentrations in the inter- and intra-dendritic regions of Phase 1 are ≤ 10 at %, which is insufficient for ordering in the Nb-Ru phase diagram[181]. Therefore, the (Hf,Ru)-rich Phase 2 is identified as the ordered B2 phase, consistent with previous alloys, and the dendritic (Nb, W)-rich Phase

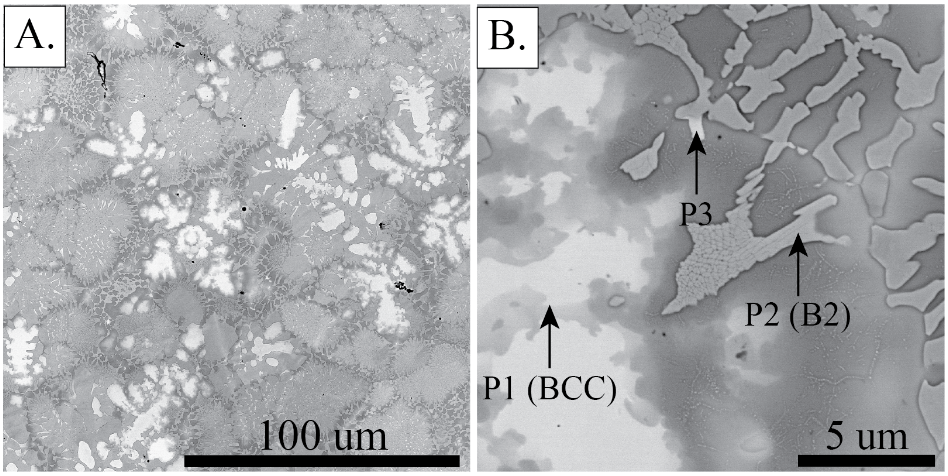

Figure 3.9: A., B. BSE images of as-cast $Hf_{25}Nb_{25}W_{25}Ru_{25}$. Three phases are identified and present throughout the sample. Nanoparticles are visible in the regions of Phase 2 demonstrating darker chemical contrast. P1 is a disordered (Nb, W)-BCC phase and P2 is an ordered HfRu-B2 phase.

1 is tentatively identified as a disordered BCC phase. Using the experimental lattice parameters, the two phases would have a misfit of 0.75%.

Corresponding compositions for the three identified phases are recorded in Table 3.2, along with the composition of the BCC + B2 nanoparticle regions. The composition of the B2 grains was also measured by EPMA (presented in Table 3.4).

3.3.3 TEM analysis of $Hf_{20}Mo_{20}Nb_{20}Ta_{20}Ru_{20}$

Nano-scale precipitates are visible in four of the seven alloys, all Hf-containing: $Hf_{33}Mo_{34}Ru_{33}$, $Hf_{25}Mo_{25}Nb_{25}Ru_{25}$, $Hf_{20}Mo_{20}Nb_{20}Ta_{20}Ru_{20}$, and $Hf_{25}Nb_{25}W_{25}Ru_{25}$. These nanoparticles are present both in the as-cast condition and form in some alloys in the heat treated conditions (section 3.3.4). The nanoparticles are consistent in appearance in both BSE and SE images with the B2 phases identified in each alloy and are relatively similar in size across alloys. The nanoparticles consistently appear in Hf- and/or Ru-enriched regions. To further characterize the nanoparticles, a TEM foil was lifted out from a region of the as-cast $Hf_{20}Mo_{20}Nb_{20}Ta_{20}Ru_{20}$ containing a high density of nanoparticles (the regions presented in Figure 3.8B and D).

The low angle dark field image in Figure 3.10A shows a collection of coarse (Hf, Ru)-rich B2 grains at the bottom and upper left of the image, and an aligned group of coarsened (Hf,Ru)-rich B2 nanoparticles through the center of the image. The remaining area is occupied by nanoparticles ranging from 50 to 100 nm in diameter embedded in a (Mo,Nb,Ta)-rich BCC phase. The coarsened nanoparticles in the diagonal of the image are rectangular in appearance and can reach up to 150 nm in their longest dimension. Larger nanoparticle-free BCC regions are visible adjacent to the nanoparticle chain and the coarse B2 grains. Overlapping the coarse B2 grains in Figure 3.10B are networks of dislocations with a spacing of 44 ± 5 nm; these dislocation networks are typical of misfit dislocations at a two-phase interface. The Burgers vector of the misfit dislocations was confirmed to be 1/2[111] by **g•b** analysis in conventional TEM (Table 3.5).

Lattice parameters of the BCC and B2 phases were calculated from the SAED pattern taken from the BCC + B2 nanoparticle region. The lattice parameters are $a_{BCC} = 3.27$ Å and $a_{B2} = 3.29$ Å, resulting in a lattice misfit of +0.61 % (Eq. 1.1). Further, utilizing the spacing between the dislocations in Figure 3.10B and the following equation:

$$\delta = b/s \tag{3.1}$$

where δ is the calculated misfit between the BCC matrix and the coarse B2 grains, b is the magnitude of the BCC a/2$\langle 111\rangle$ Burgers vector, a is the lattice parameter of the BCC phase derived from TEM, and s is the spacing between the misfit dislocations at the BCC/B2 interface, a misfit of +0.53 % ± 0.07 % can be calculated. This value is consistent with the misfit derived directly from the SAED pattern lattice parameters.

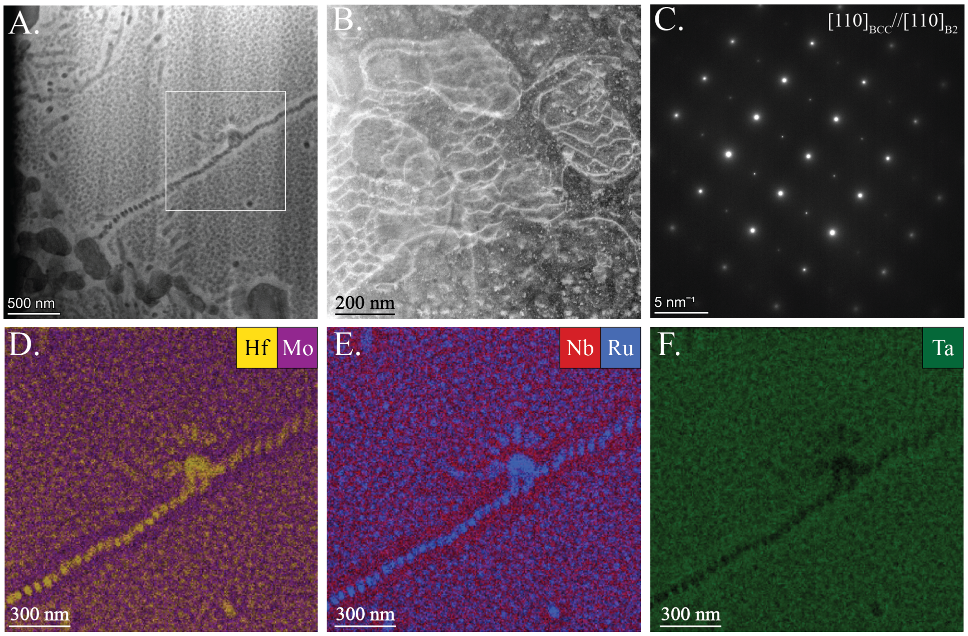

Figure 3.10: TEM analysis of a nanoparticle dense region in as-cast $Hf_{20}Mo_{20}Nb_{20}Ta_{20}Ru_{20}$. A. STEM image taken in two-beam condition from a low angle dark field detector. Condition was chosen to maximize phase contrast between BCC and B2. B. A higher magnification HAADF-STEM image of dislocation cells present at a BCC-B2 interface within the foil, visible at the lower left corner in A. C. SAED pattern acquired from the nanoparticle + matrix array on the $[110]_{BCC}$ zone axis, indicating BCC ordering with a B2 superlattice. No additional Heusler ($L2_1$) reflections are visible. D-F. STEM-EDS maps of area marked in A, showing enrichment of Hf and Ru in the nanoparticles and depletion of Mo, Nb, and Ta.

Table 3.5: G-dot-b analysis of misfit dislocations observed in Fig. 3.8B in $Hf_{20}Mo_{20}Nb_{20}Ta_{20}Ru_{20}$. The Burgers vector direction was determined to be $\frac{1}{2}[111]$.

g	$(12\bar{3})$		$(10\bar{1})$		$(1\bar{1}0)$		(011)	
Burgers Vector	**g.b**	**Visible? (Y/N)**	**g.b**	**Visible? (Y/N)**	**g.b**	**Visible? (Y/N)**	**g.b**	**Visible? (Y/N)**
$[111]$	2	Y	0	N	0	N	0	Y
$[\bar{1}11]$	0		-2		-2		2	
$[1\bar{1}1]$	6		0		2		0	
$[11\bar{1}]$	-4		2		0		0	

3.3.4 Microstructural evolution after high temperature heat treatment

The alloys were heat treated at 1500 °C ($Hf_{33}Mo_{34}Ru_{33}$) and 1600 °C ($Hf_{25}Mo_{25}Nb_{25}Ru_{25}$, $Hf_{25}Mo_{25}Ta_{25}Ru_{25}$, $Hf_{20}Mo_{20}Nb_{20}Ta_{20}Ru_{20}$, $Hf_{25}Nb_{25}W_{25}Ru_{25}$) to investigate the thermal stability of the BCC and B2 phases (Figures 3.11 and 3.12). After heat treatment, any structures formerly described in the as-cast samples remain in the heat-treated (HT) microstrucutres and demonstrate coarsening and homogenization; the only exception is the decomposition of near-equimolar region of $Hf_{25}Mo_{25}Ta_{25}Ru_{25}$ into two phases. Compositions of the observed phases are reported in Table 3.6. Except for HT-$Hf_{33}Mo_{34}Ru_{33}$, all the coarse B2 phases showed a decrease in Mo, Nb, Ta and W content and an increase in Hf and Ru. The composition of the $Hf_{33}Mo_{34}Ru_{33}$ HfRu-B2 phases remained constant.

The XRD scans presented in Figure 3.13 are consistent with the XRD scans from the as-cast samples (Figure 3.2). Monoclinic HfO_2 peaks are additionally visible in the HT-$Hf_{25}Mo_{25}Nb_{25}Ru_{25}$ diffraction scan. The lattice parameters are reported in Table 3.7.

Interestingly, in the HT-$Hf_{33}Mo_{34}Ru_{33}$ (Figure 3.11A,C), significant cracking occurred in the microstructure after heat treatment. Regions of dark BSE contrast in Figure 3.11A show where cracking occurred, with a concentration of cracks at interfaces between the Mo-BCC phase and the HfRu-B2 phase (Figure 3.11B). Coarsening of the B2 nanoparticles embedded in the BCC phase also occurred. The nanoparticles are irregular in shape and size and range from 34 μm to 404 μm in length along their longest dimension.

In the HT-$Hf_{25}Mo_{25}Nb_{25}Ru_{25}$ (Figure 3.11C,D), the segregation in the intergranular BCC phases has been eliminated and the pre-exisitng nanoparticles have coarsened to 60-400 nm in diameter. They are still spherical in appearance. The larger B2 grains at the border of the inter-granular and intra-granular regions further coarsened to form a

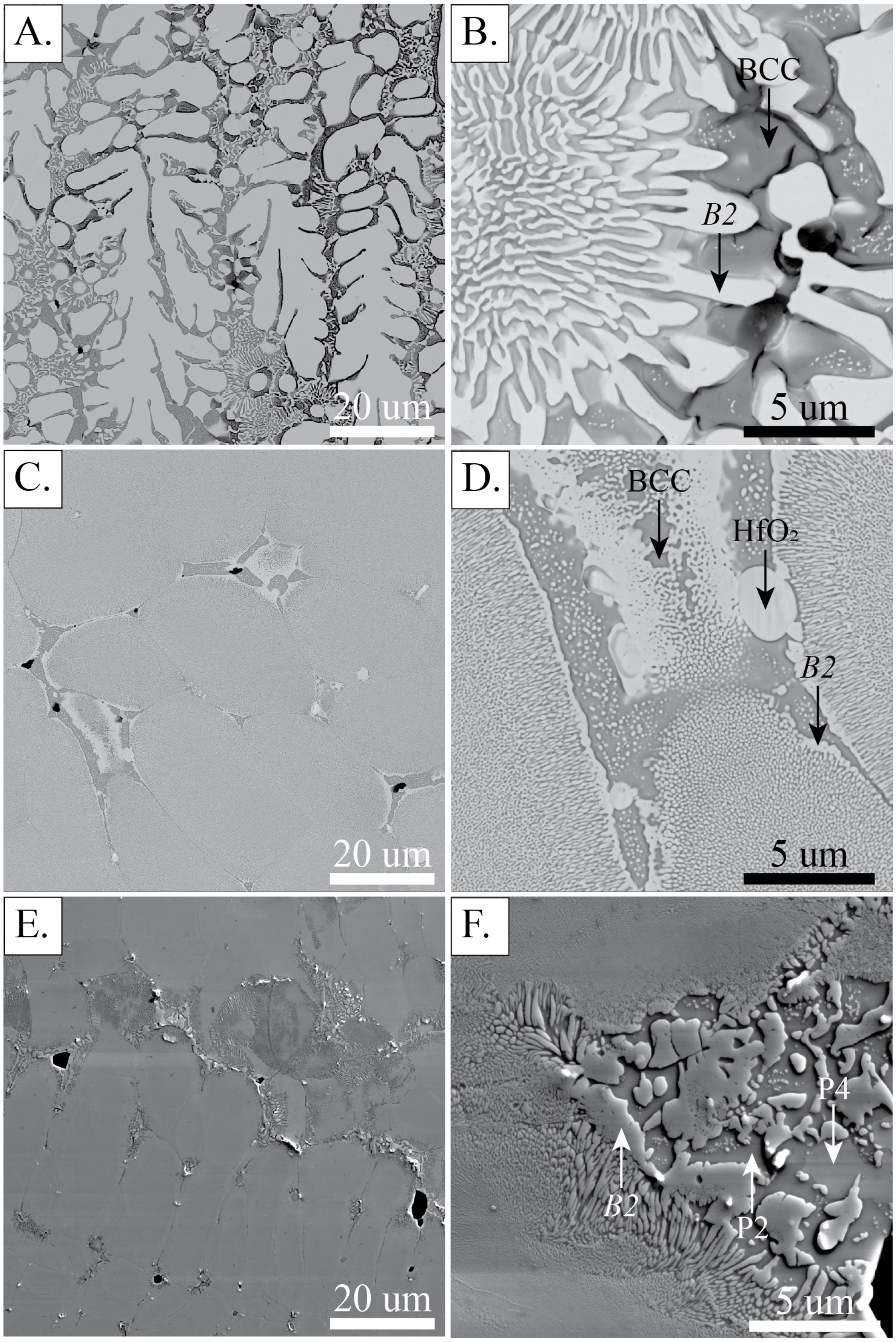

Figure 3.11: Microstructure images of alloys after heat treatment at 1500 °C ($Hf_{33}Mo_{34}Ru_{33}$) and 1600 °C ($Hf_{25}Mo_{25}Nb_{25}Ru_{25}$ and $Hf_{25}Mo_{25}Ta_{25}Ru_{25}$) for 40 h. A-B. BSE images of $Hf_{33}Mo_{34}Ru_{33}$. Areas with cracking visible exhibit dark contrast in A. C-D. BSE images of $Hf_{25}Mo_{25}Nb_{25}Ru_{25}$. Larger BCC regions are visible at grain boundaries. E-F. SE images of $Hf_{25}Mo_{25}Ta_{25}Ru_{25}$.

Table 3.6: Identified phases, assigned crystal structures, and their compositions (at%) as measured by EDS of the heat-treated alloys. Error is on the order of a few at% percent.

Alloy	Region	Crystal Structure	Hf	Mo	Nb	Ru	Ta	W
$Hf_{33}Mo_{34}Ru_{33}$	Phase 1	B2	51.0	3.2	-	45.8	-	-
40 h at 1500	Phase 2	BCC	3.0	90.0	-	7.0	-	-
	Lamellar B2 + BCC	B2 + BCC	22.6	53.6	-	23.8	-	-
	Nanoparticle B2 + BCC	B2 + BCC	5.1	85.3	-	9.7	-	-
$Hf_{25}Mo_{25}Nb_{25}Ru_{25}$	Phase 1	B2	44.9	5.5	6.8	42.7	-	-
40 h at 1600	Phase 2	BCC	11.2	38.3	47.0	3.6	-	-
	Nanoparticle B2 + BCC	B2 + BCC	13.8	34.8	41.8	9.6	-	-
$Hf_{25}Mo_{25}Ta_{25}Ru_{25}$	Phase 1	B2	47.0	8.3	-	39.2	5.6	-
40 h at 1600	Phase 2	-	27.3	34.9	-	8.4	28.7	-
	Phase 3	-	94.8	0.9	-	0.5	3.7	-
	Phase 4	-	62.7	15.3	-	6.6	15.4	-
$Hf_{20}Mo_{20}Nb_{20}Ta_{20}Ru_{20}$	Phase 1	BCC	7.7	28.1	29.8	3.7	30.7	-
40 h at 1600	Phase 2	B2	47.2	2.8	2.5	44.1	3.5	-
	Phase 3	-	82.7	6.4	6.7	0.0	5.2	-
	Nanoparticle B2 + BCC (fine)	B2 + BCC	11.1	27.6	22.3	9.3	29.8	-
	Nanoparticle B2 + BCC (coarse)	B2 + BCC	16.2	20.9	27.3	12.5	23.1	-
$Hf_{25}Nb_{25}W_{25}Ru_{25}$	Phase 1, Intradendritic Region	BCC	2.6-18.1	-	32.0-69.1	0.-7.9	-	14.5-65.3
40 h at 1600	Phase 2	B2	46.5	-	5.8	45.6	-	2.1
	'fuzzy' W-rich Region	-	4.8	-	20.2	1.6	-	73.4
	Lamellar B2 + BCC	B2 + BCC	5.2	-	19.8	2.5	-	72.6
	Nanoparticle B2 + BCC (new)	B2 + BCC	10.2	-	34.2	5.8	-	49.8
	Nanoparticle B2 + BCC (coarse)	B2 + BCC	15.8	-	42.3	11.2	-	30.8

Table 3.7: Identified phases and calculated lattice parameters of the heat treated alloys.

Alloy	Condition	Phase	Prototype	Lattice Parameter (Å)
$Hf_{33}Mo_{34}Ru_{33}$	40 h at 1500 °C	B2	CsCl	3.230
	40 h at 1500 °C	BCC	W	3.145
$Hf_{25}Mo_{25}Nb_{25}Ru_{25}$	40 h at 1600 °C	B2	CsCl	3.225
	40 h at 1600 °C	B2/BCC	-	3.224
$Hf_{25}Mo_{25}Ta_{25}Ru_{25}$	40 h at 1600 °C	B2	CsCl	3.227
$Hf_{20}Mo_{20}Nb_{20}Ta_{20}Ru_{20}$	40 h at 1600 °C	B2	CsCl	3.229
	40 h at 1600 °C	B2/BCC	-	3.240
$Hf_{25}Nb_{25}W_{25}Ru_{25}$	40 h at 1600 °C	B2	CsCl	3.224
	40 h at 1600 °C	BCC	W	3.200

continuous layer of the B2 phase. Similarly, coarsening of the 'feathered' B2 within the grains resulted in a continuous network of the B2 phase with embedded BCC regions. Phases 3 and 4 were present in very small volume fractions ($a_f < 0.01$) and could not be evaluated for their compositions.

In the HT-$Hf_{25}Mo_{25}Ta_{25}Ru_{25}$ (Figure 3.11E,F), the near-equimolar (Hf, Mo, Ta, Ru)-rich regions have decomposed into two phases: Phase 1 and Phase 5. Phase 1 is more resistant to polishing and demonstrates slightly lighter backscatter electron contrast compared to Phase 5. The phases are too small in the core of the grains to measure their compositions with EDS, but Phase 1 coarsens sufficiently towards the grain boundaries to measure an average composition of 47.0 at% Hf and 39.2 at% Ru. Consistent with the other alloys, Phase 1 is therefore identified as a HfRu-B2 phase. Phase 5 is tentatively identified as a disordered BCC phase rich in Mo and Ta, though further investigation is required. The low Mo and Ta content of the measured B2 grains would necessarily require the rejection of Mo and Ta to the surrounding phase and in the other Hf-containing alloys the Mo-, Nb-, Ta- and W-rich phases have all been disordered BCC. All three Hf-rich phases identified in the as-cast sample (section 3.3.2) remain after heat treatment. Phase 2 experienced a significant reduction in Hf content from 47.7 at% to 27.3 at% and an enrichment of Mo (+10.9 at%) and Ta (+10.8 at%); it is no longer composed primarily

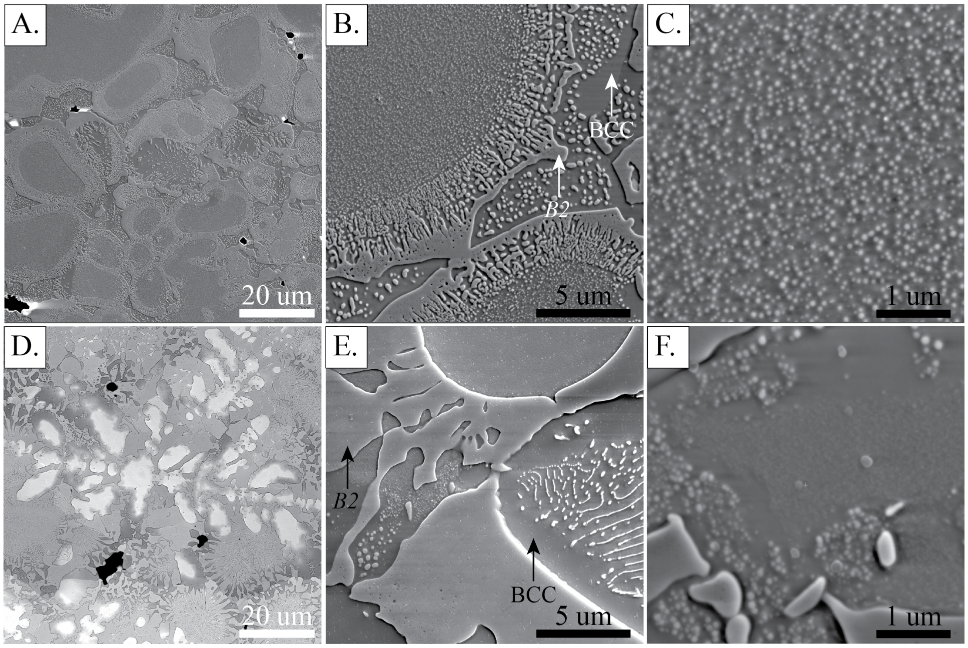

Figure 3.12: Microstructure images of $Hf_{20}Mo_{20}Nb_{20}Ta_{20}Ru_{20}$ and $Hf_{25}Nb_{25}W_{25}Ru_{25}$ after 40 h at 1600 °C. A-C. SE images of $Hf_{20}Mo_{20}Nb_{20}Ta_{20}Ru_{20}$. Nanoparticle precipitation can be observed throughout the dendrite cores and is magnified in C. D. BSE and E-F. SE images of $Hf_{25}Nb_{25}W_{25}Ru_{25}$. Precipitation of nano-scale features can be observed between the B2 grains in E. and in the W-rich dendrite cores in E-F.

of Hf. The Ru content decreased only by 1.5 at%. Nanoparticles with similar backscatter and polishing behavior as the coarse B2 grains precipitated within Phase 2 regions in small quantities. These two-phase regions are too small to measure with EDS.

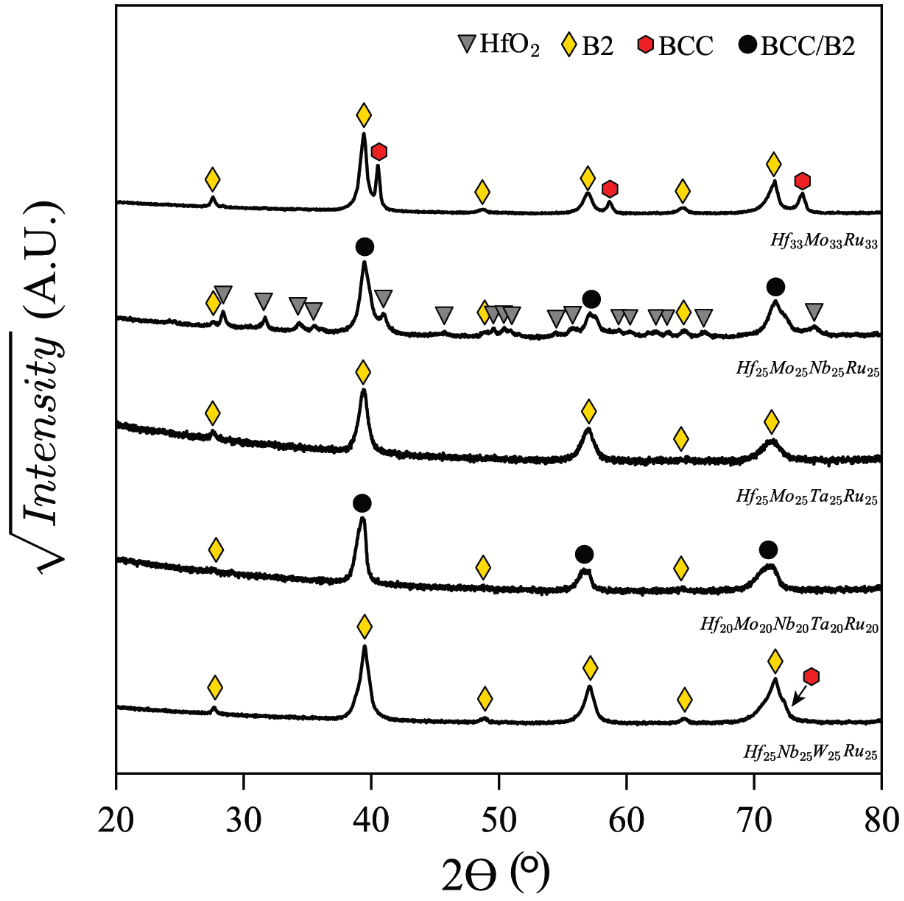

Figure 3.13: XRD scans of the heat treated alloys. $Hf_{33}Mo_{34}Ru_{33}$ was heat-treated at 1500 °C for 40 h. All other alloys were heat-treated at 1600 °C for 40 h. Peaks associated with a B2 phase were observed in all alloys. Asymmetry in the observed peaks may be the result of a low misfit between the BCC and B2 phases, causing overlapping peaks, or chemistry and lattice parameter variations within the disordered BCC phases.

In the HT-$Hf_{20}Mo_{20}Nb_{20}Ta_{20}Ru_{20}$ (Figure 3.12A-C), new HfRu-B2 nanoparticles precipitated throughout the formerly single phase BCC dendrite cores. The nanoparticles are uniformly dispersed throughout the cores and appear spherical in shape, with an area fraction of 0.29 ± 0.09. The particles range in size from 30-100 nm in diameter. The nanoparticles that formed prior to heat treatment exhibit coarsening from 50-100 nm to 70-500 nm in size along their longest dimension, with the particles in the Hf-enriched zones coarsening faster than the particles in the peritectic cores. EDS measurements of sufficiently large BCC regions indicate the BCC phase is depleted of Hf and Ru compared to the BCC phase formerly present within the peritectic cores and inter-peritecitc regions in the as-cast regions, with the combined quantity of Hf + Ru reducing to $\approx$ 10 at%.

In the HT-$Hf_{25}Nb_{25}W_{25}Ru_{25}$ (Figure 3.12D-F), the dendritic segregation in the disordered (Nb, W)-rich BCC phase remains. Coarsening of the pre-existing nanoparticles is also observed. Similar to HT-$Hf_{20}Mo_{20}Nb_{20}Ta_{20}Ru_{20}$, new nanoparticles have precipitated in the Nb-rich intra-dendrtic regions and in between the HfRu-B2 grains (Figure 3.12E,F). The heat treatment also resulted in the formation of two new two-phase regions in the highly W-enriched dendrite cores ($\approx$ 65-73 at% W): irregular B2 lamellae (with an average Ru content of 2.5%) and regions with a 'fuzzy' appearance (with an average Ru content of 1.6 at%). Regions directly adjacent to those morphologies but which contain no evidence of particles are completely depleted of Ru (0 at% Ru) and contain only small amounts of Hf ($\leq$ 3 at% Hf).

3.3.5 Micro-pillar compression of HT-$Hf_{20}Mo_{20}Nb_{20}Ta_{20}Ru_{20}$ nanoparticle regions

To investigate the mechanical behavior of new BCC + B2 nanoparticle microstructures, targeted regions in the HT-$Hf_{20}Mo_{20}Nb_{20}Ta_{20}Ru_{20}$ material were identified for micropillar compression experiments. Micropillars were fabricated towards the center of the dendrite cores in order to avoid the influence of grain boundaries and variations in precipitate morphology. The compression axis (Z) crystal direction for each micropillar is shown in the inset in Figure 3.14A.

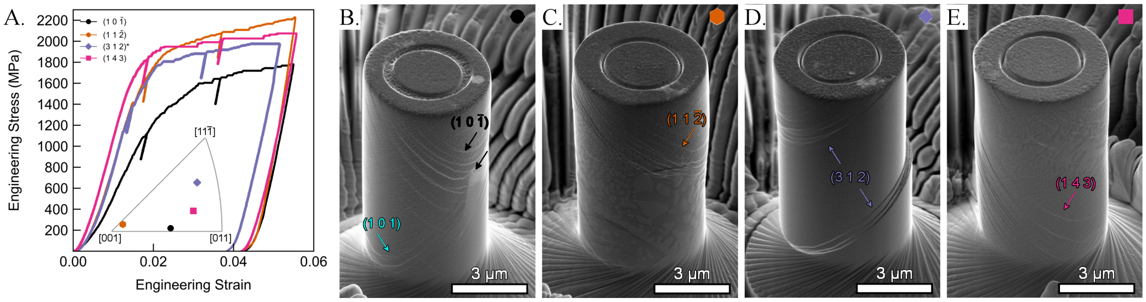

Figure 3.14: A. Micropillar compression stress-strain curves for all four micropillars investigated. Curves are colored and labeled according to the maximum resolved shear stress (MRSS) plane. The (312) pillar was selected for subsequent (S)TEM analysis (marked by an asterix). The inset shows the compression axis direction for each pillar, colored and marked accordingly. B-E. Surface morphology of deformed micropillars. The MRSS planes are annotated according to the coloring in A. Additional slip traces in B. (MRSS plane (10$\bar{1}$)) along the (101) plane are noted in cyan. Variations in the B2 precipitate morphology are evident in C. and E., where large grains of the B2 phase significantly impact the slip morphology.

The engineering stress-strain curves (Figure 3.14A) exhibit high 0.2 % offset yield strengths of 1250, 1630, 1770, and 1835 MPa, respectively. These values correspond to critical resolved shear stresses of 616, 810, 830, and 917 MPa, assuming the that the deformation is accommodated on the maximum resolved shear stress (MRSS) plane. The MRSS planes are noted for each pillar in Figure 3.14 and the yield strength, resolved shear strengths and modulus of each pillar are reported in Table 3.8. Slip traces on the surface of each deformed micropillar (Figure 3.14B-E) are consistent with deformation on the MRSS plane. Pillars oriented for glide along the (10$\bar{1}$), (01$\bar{2}$), and (143) planes exhibited additional slip traces corresponding to secondary highly stressed slip systems. All pillars exhibited signs of cross-slip, though due to the presence of the nanoparticles, identification of cross slip traces on the surface of the pillars could not be accurately performed. The influence of size effects on the yield strengths measured in these experiments was estimated using the single-arm source model of Parthasarathy *et al.* [239]. Using a shear modulus determined as a rule of mixtures for the pure elements [240, 241, 242], the pillar size contributed approximately 23 MPa to the yield strength, which is less than 2% of the smallest value measured.

An electron transparent sample was prepared from the deformed pillar oriented for glide on the (312) plane (Figures 3.14D and 3.15) such that the foil normal was close to the glide plane. This pillar was the only sample tested oriented in a ”single slip” orientation, thus likely to contain dislocations of predominately a single burgers vector. The sample was single crystalline and contained a relatively uniform distribution of B2 nanoparticles on the surface (Figure 3.14D). ADF-STEM images of the sample (Figure 3.15D-F) show two regions with dense B2 nanoparticle precipitates and a high density of dislocations. Many dislocations appear in paired configurations, likely a result of cooperative shearing of the B2 precipitates by APB-coupled dislocations. Many dislocations have formed Orowan loops, suggesting a combined shearing and looping behavior. A conventional dark field (DF) TEM image of the top region of the micropillar shows the high density of B2 nanoparticles alongside numerous dislocations (Figure 3.15C). The precipitates in this sample range from ≈ 43 to 75 nm in diameter. A $\mathbf{g}\bullet\mathbf{b}$ analysis (Table 3.9) was performed in conventional TEM, and the Burgers vector direction was determined to be $1/2[\bar{1}11]$ for the dislocations examined. This Burgers vector and surface trace agrees with the corresponding slip system with the highest Schmid factor for this pillar, $(312)[\bar{1}11]$, m = 0.47.

Trace analysis was performed on ADF STEM images collected at several two-beam tilt conditions to determine the line direction of the dislocation segments (Figure 3.15E). Three segments of a single dislocation were used for this analysis: one nearly-screw orientation segment and two mixed/edge-like segments. The nearly-screw character segment (segment 1) has an average line direction of [-1.7, 2.3, 1.6], which is less than 10 degrees from perfect screw orientation. The shorter segments have line directions of [1.83,

Table 3.8: Compression axis and resulting mechanical properties of each $Hf_{20}Mo_{20}Nb_{20}Ta_{20}Ru_{20}$ micropillar.

Compression Axis	Slip System with Highest Schmid Factor $(u,v,w)[h,\ k,\ l]$	Schmid Factor (m)	Yield Strength at 0.2% offset (MPa)	Resolved Shear Stress on MRSS Plane (MPa)	Young's Modulus, *h, k, l¿h, k, l* E (GPa)
[0,4,9]	$(1,0,\bar{1})[1,1,1]$	0.492	1250	616	173
[1,1,12]	$(1,1,\bar{2})[1,1,1]$	0.497	1630	810	207
[3,5,7]	$(3,1,2)[\bar{1},1,1]$	0.469	1769	830	188
[4,1,6]	$(1,4,3)[\bar{1},\ 1,\ 1]$	0.500	1835	917	166

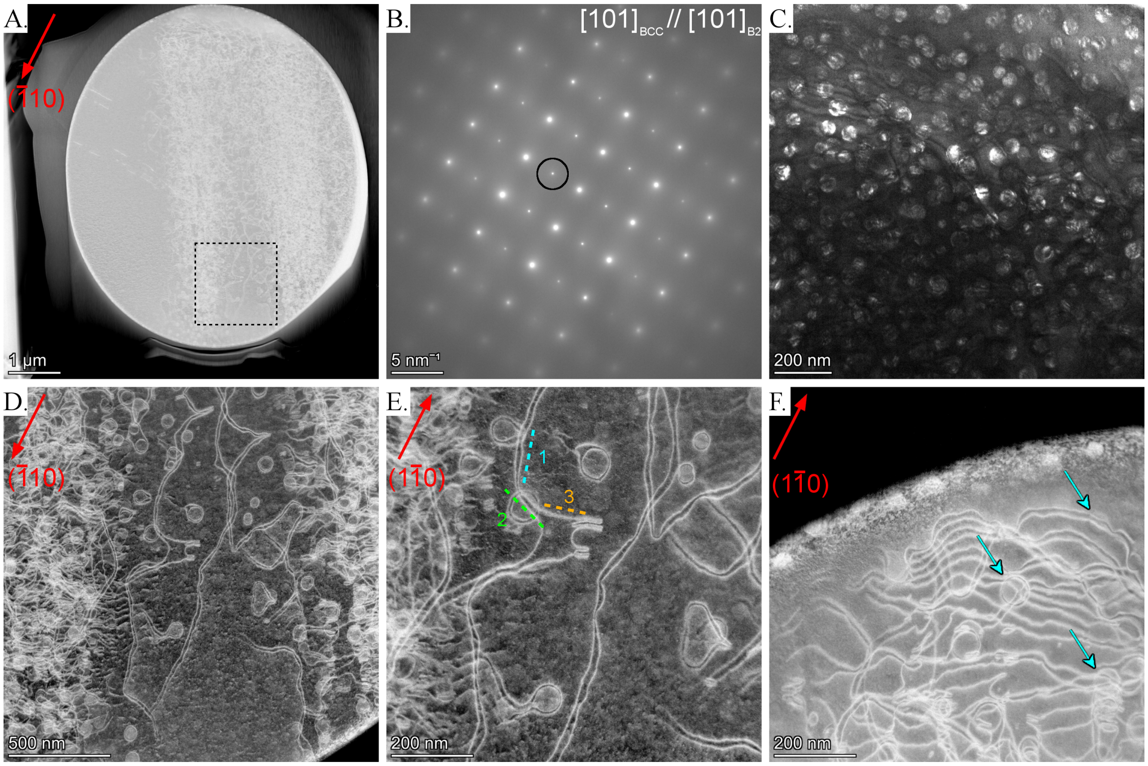

Figure 3.15: A. STEM overview of sample prepared from the (312) pillar in Figure 3.14A, D. Sample was prepared so the foil normal is near the (312) plane. Dashed lines in A correspond to the region where dislocation trace analysis was performed in D,E. B. SAED pattern acquired from the [101] zone axis. The black circle indicates the placement of the objective aperture for subsequent dark field (DF) imaging of the B2 precipitates. C. DF TEM image of the B2 nanoparticle precipitates near the top of the sample. Black wavy lines present in this image are dislocations interacting with precipitates. D-F. ADF STEM images of dislocation structure in the deformed micropillar. Two-beam conditions are noted in red. Dislocations between the two nanoparticle and dislocation dense regions were selected for detailed analysis. These dislocations are paired, indicating cooperative shearing of the B2 precipitates. Dislocations are also looped around dislocations, indicating both Orowan bowing and precipitate shearing mechanisms are active. Trace analysis was performed on segments 1-3 in E. of the same dislocation. The line directions for these segments are [-1.7, 2.3, 1.6], [1.83, 0.23, -2.65], and [1, 1.85, -2.45] for segments 1, 2, and 3, respectively. F. Dislocation morphology near the top of the pillar. Regions with B2 particles undergoing shearing are noted with arrows.

Table 3.9: G-dot-b analysis of dislocations observed in $Hf_{20}Mo_{20}Nb_{20}Ta_{20}Ru_{20}$ after micropillar compression.

Burgers vectors	**g** $(10\bar{1})$		$(0\bar{1}1)$		$(1\bar{1}0)$		$(1\bar{2}3)$	
	g.b	Visible? (Y/N)	g.b	Visible? (Y/N)	g.b	Visible? (Y/N)	g.b	Visible? (Y/N)
[111]	0	Y	0	N	0	Y	2	N
$[11\bar{1}]$	2	Y	-2	N	0	Y	-4	N
$[1\bar{1}1]$	0	Y	2	N	2	Y	6	N
$[\bar{1}11]$	-2	Y	0	N	-2	Y	0	N

0.23, -2.65] (segment 2) and [1, 1.85, -2.45] (segment 3), which are $\approx$ 40 and 74 degrees from perfect screw orientation. The error associated with each of these line direction determinations is less than 10 degrees. The glide plane was determined by taking the cross product of the two short segments and the Burgers vector ($[\bar{1}11]$). The glide planes determined using this method were (2.9, 0.8, 2) and (2.97, 1, 1.97), both of which agree well with the surface trace and MRSS of (312).

3.4 Discussion

Ru additions present an opportunity for design of high temperature $\beta + \beta'$ precipitation strengthened systems in the high dimensional refractory composition space. The HfRu-B2 phases in the investigated alloys are stable to at least 1600 °C and nano-scale precipitate regions suggest targeted compositions that could be solution and aged. The individual alloy solidification behaviors, trends in the phase compositions, and dislocation interactions with the HfRu-B2 particles are discussed in the following sections. Finally, the possibilities of alloy design utilizing HfRu-B2 particles are discussed.

3.4.1 Solidification behavior of the as-cast alloys

Understanding the solidification behavior of each alloy can provide insight for future alloying strategies. Controlling the solidification pathway is important for reducing segregation that can lead to casting defects and developing microstructures with improved mechanical properties. Further, segregation of alloying agents can result in varying phase formation behavior along the solidification path that can suggest new, more optimal compositions.

In the absence of Hf, $Mo_{25}Nb_{25}Ta_{25}Ru_{25}$ and $Mo_{25}Nb_{25}$-$Ta_{25}Ru_{20}W_{20}$ solidify as single-phase dendritic alloys. In both cases, there is segregation of the highest melting point element (W or Ta) to the intra-dendritic regions, along with Mo, and segregation of Nb and Ru to the inter-dendritic region. From this investigation, it is unknown if the B2 ordering of the $Mo_{25}Nb_{25}Ta_{25}Ru_{25}$ alloy persists until melting. The closest equivalent phases, the NbRu and TaRu B2 phases, are indicated to persist to very high temperatures in their binary phase diagrams at Ru contents above 40 at%, but that is much greater than the amount of Ru present in $Mo_{25}Nb_{25}Ta_{25}Ru_{25}$ [181, 182, 237]. It is possible that there is an ordering transition at elevated temperatures where the alloy becomes disordered; further investigations are required.

The Hf-containing alloys have microstructures indicative of either disordered BCC or ordered B2 that solidifies directly from the liquid. In $Hf_{33}Mo_{34}Ru_{33}$ and $Hf_{25}Mo_{25}$-$Nb_{25}Ru_{25}$, the B2 phase solidifies first, forming B2 dendrites; a disordered BCC phase then solidifies concurrently with more B2, forming two-phase inter-dendritic regions that are consistent with eutectic reactions. In $Hf_{25}Nb_{25}W_{25}Ru_{25}$ and $Hf_{20}Mo_{20}Nb_{20}Ta_{20}Ru_{20}$, the disordered BCC phases solidifies first, followed by solidification of the B2 phase in Hf/Ru enriched regions. Additional phases form from the remaining segregated liquid later in the solidification process. These microstructural observations are generally consistent with Scheil curves predicted via CALPHAD (CALculation of PHAse Diagrams) methods, shown in Figure 3.16A,B. The exception is $Hf_{25}Mo_{25}Ta_{25}Ru_{25}$, which did not form a distinct combination of BCC and B2 phases in the as-cast condition. The Scheil curve for $Hf_{25}Mo_{25}Ta_{25}Ru_{25}$ first predicts the formation of a disordered BCC phase, followed by a B2 phase.

The following solidification pathways were determined from the microstructural observations:

Similar to the other W-containing alloys, $Hf_{25}Nb_{25}W_{25}Ru_{25}$ first forms W-enriched BCC dendrites with the segregation of Hf, Nb, and Ru to the inter-dendritic regions. Within these inter-dendritic regions, large continuous islands of B2 have formed, along with B2 grains that outline the dendritic arms and others that are elongated in the direction of the grain boundaries. The size and shape of these B2 grains, coupled with the low content of Ru ($<$ 10 at%) in both the inter- and intra-dendritic regions, indicate they formed directly from the liquid. Further cooling after solidification may have resulted in the B2 nanoparticles observed in the dendritic regions. Solid-state precipitation of the nanoscale B2 is discussed in more depth in section 3.4.2.

In $Hf_{33}Mo_{34}Ru_{33}$, the B2 phase first forms large dendrites; the remaining liquid potentially reaches a eutectic composition and forms an alternating lamellar microstructure of micron-scale B2 and BCC grains. The proposed solidification path is:

$$L \rightarrow L + HfRu \rightarrow HfRu + BCC(Mo)$$

While any binary reactions and compositions are necessarily modified by the presence of the third element, the Hf-Ru binary contains a steep eutectic and a Ru concentration of 33 at% would fall on the pro-eutectic B2 side of the diagram, consistent with the observed morphologies. The two phase region of the $Hf_{33}Mo_{34}Ru_{33}$ Scheil curve has the shallowest slope of all the alloys (Figure 3.16), which is consistent with the narrow freezing ranges of eutectic materials; it is predicted that 58 % of the solid forms between 2211.0 and 2209.5 °C.

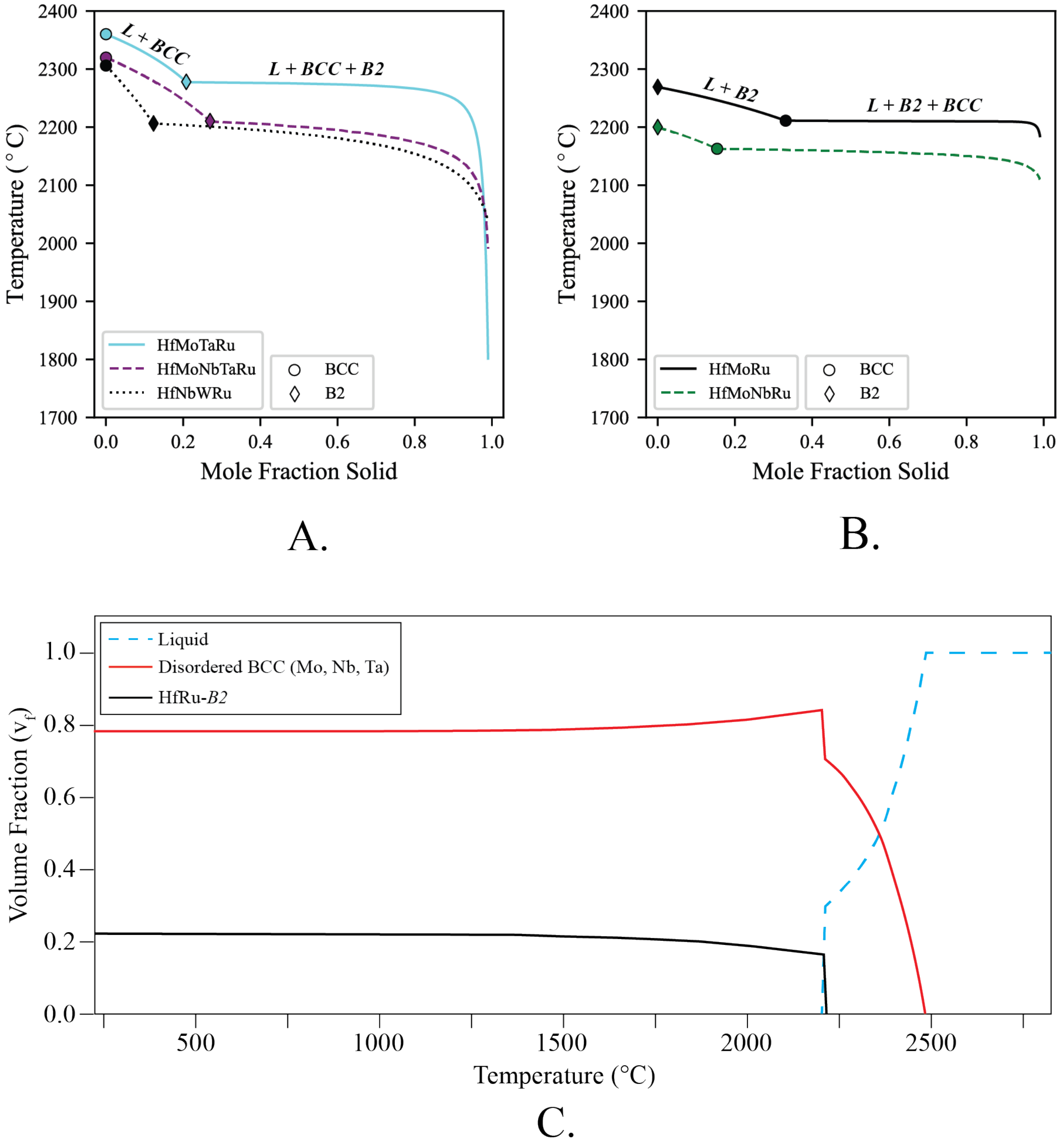

Figure 3.16: A. Predicted Scheil curves for alloys where the first phase to solidify is disordered BCC. B. Predicted Scheil curves for alloys where the first phase to solidify is HfRu-B2. Predictions were made in Thermo-Calc using the TCHEA4 database [200]. Alloy legend is arranged in order of liquidus temperature and the phase (B2 or BCC) markers indicate where the respective phase begins to solidify from the liquid. C. Phase volume fraction versus temperature for $Hf_{11.1}Mo_{27.6}Nb_{22.3}Ta_{29.7}Ru_{9.3}$. Two phases, a B2 phase and a disordered BCC phase, are predicted to be stable until melting.

In $Hf_{25}Mo_{25}Nb_{25}Ru_{25}$ (Figure 3.5A,C), the size of the large HfRu-B2 microstructural regions and the elongation of the smaller B2 particles perpendicular to the large structures indicates the large B2 regions solidified first. The small B2 particles then began to precipitate from the liquid and grew in the direction of the solidification front. Some regions (Figure 3.5B, D) lack the large B2 structures, but elongation of the B2 'feathers' towards observable grain boundaries indicates similar precipitation and growth along a solidification front. Continuous rejection of Mo and Nb from the B2 phase into the liquid would result in the formation of the nano-scale BCC regions visible in between the B2 particles, followed by the solidification of the last (Mo,Nb)-enriched liquid at the grain boundaries. Similar to $Hf_{33}Mo_{34}Ru_{33}$, the predicted Scheil curve for $Hf_{25}Mo_{25}Nb_{25}Ru_{25}$ is quite shallow in the two-phase regime, suggesting a eutectic reaction.

The disordered BCC dendrites in $Hf_{20}Mo_{20}Nb_{20}Ta_{20}Ru_{20}$ are enriched in Mo and Ta, indicating they solidified first and were depleted in the remaining liquid. The (Hf,Ru)-B2 would have nucleated on the surface of the BCC dendrites, resulting in the observed rings; the formation of the B2 phase would also reject Mo, Nb, and Ta back into the liquid, resulting in the higher concentration of these elements in Phase 3 which solidified from the last liquid.

Of the Hf-containing alloys, only $Hf_{25}Mo_{25}Ta_{25}Ru_{25}$ does not form a combination of BCC and B2 phases in the as-cast condition. In the first phase to form, Phase 1, some segregation of Mo and Ta to the intra-dendritic regions and Hf and Ru to the inter-dendritic regions is measurable but the magnitude of the segregation is the smallest of among all the alloys and there are no distinct phase boundaries except for the transition to the inter-granular phases. Therefore $Hf_{25}Mo_{25}Ta_{25}Ru_{25}$ likely formed as a single phase alloy and the rejection of Hf results in the formation of the intergranular phases from the remaining liquid. As noted previously, this result is inconsistent with the predicted Scheil curve (Figure 3.16A), which predicts the formation of both BCC and B2 phases during solidification. Under the current non-equilibrium solidification conditions, it is possible that the formation of a distinct B2 phase was suppressed by the speed of solidification. After heat treatment at 1600 °C, Phase 1 does decompose into two phases. One has a composition much closer to the other observed B2 phases (47.0 at% Hf, 39.2 at% Ru) and the other has a high concentration of BCC elements (34.9 at% Mo, 28.7 at% Ta).

After heat treatment, the coarsening of pre-existing phases and nucleation of new HfRu-B2 particles indicates the B2 phase is stable to at least 1600 °C (or 1500 °C in the case of $Hf_{33}Mo_{34}Ru_{33}$).

3.4.2 Nanoparticle regions in the Hf-containing alloys

Designing two phase BCC + B2 alloys with precipitates thermally and morphologically stable at potential use temperatures of 1300-1400 °C is desirable for advanced high temperature applications. The nanoparticle regions observed in $Hf_{33}Mo_{34}Ru_{33}$, $Hf_{25}Mo_{25}$-$Nb_{25}Ru_{25}$, $Hf_{20}Mo_{20}Nb_{20}$-$Ta_{20}Ru_{20}$ and $Hf_{25}Nb_{25}W_{25}Ru_{25}$ present a starting point for alloy design utilizing HfRu-B2 precipitates to strengthen a BCC matrix. The size of the nanoparticles, particularly in contrast with the coarse B2 grains that clearly derived from the liquid, suggest they formed after solidification was complete and during cooling of the solid disordered BCC phases. This indicates they might be subject to a solution and aging behavior pathway as commonly utilized for processing Ni-based superalloys. In Hf-Ru binary phase diagram, there exists a steep solvus line dividing the BCC-Hf field from the BCC-Hf + B2-HfRu phase field from 8 at% to 11 at% Ru in Hf. A binary BCC Hf-Ru alloy along this line would have solutionizable B2 precipitates of varying volume fractions. The compositions of the as-cast nanoparticle regions range from 3-12 at% Ru, which lie near that solvus line. Similarly, after heat treatment at 1600 °C, the formerly single phase BCC regions ($\approx$ 10 at% Ru) in HT-$Hf_{20}Mo_{20}Nb_{20}Ta_{20}Ru_{20}$ formed a significant volume fraction of new B2 nanoparticles.

CALPHAD predictions were made on all of the compositions of the nano-particle regions observed in the as-cast and heat treated alloys. An example set of phase and temperature predictions is presented in Figure 3.16C for the precipitated dendrite cores in HT-$Hf_{20}Mo_{20}Nb_{20}Ta_{20}Ru_{20}$ ($Hf_{11.1}Mo_{27.6}Nb_{22.3}Ta_{29.8}Ru_{9.3}$). Experimentally this region did not form nanoparticles upon cooling, but formed them upon aging at 1600 °C for 40 h and would be a likely candidate for a composition with solutionable particles. Only two phases are predicted by Thermo-Calc to be in equilibrium from 500 to 3000K: a disordered BCC phase and an ordered B2 phase with a volume fraction of approximately 0.22 (close to the experimentally measured B2 volume fraction of 0.29). The volume fractions are nearly constant with temperature. This is representative of the predictions for the rest of the nanoparticle regions, with only changes to the volume fraction of the B2 phase and the appearance of a minor amount of disordered HCP phase at low temperature varying from alloy to alloy. Interestingly, the B2 phase always persists to melting unless the Ru content is reduced to 1-2 at% (with Nb substitution). Further investigation of these compositions will be necessary to determine if the formation of nanoparticles is a result of the non-equilibrium solidification conditions or if Thermo-Calc is overpredicting the stability of the HfRu-B2 precipitates. The investigation detailed in Ch. 4 tackles this question and demonstrates that these compositions are solution and ageable.

A similar approach could be taken with other Ru-containing RMPEAs that form B2 nanoparticles. $Ti_{20}Al_{20}V_{20}Ru_{20}$ contained a large number of small TiRu-B2 precipitates after annealing at 1200 °C for 24 h [243]. Similarly, the formation of HfCo-B2 nano-scale precipitates in disordered (Nb,Mo)-BCC regions was reported by Panina *et al.* in as-cast and annealed Hf-Co-Mo-Nb alloys[142, 143]. It is likely BCC + B2 alloys derived from those two-phase regions would also be capable of a solution and aging processing pathway.

3.4.3 Composition of the HfRu-B2 phase

Of the investigated alloying elements, the formation of HfRu appears significantly more thermodynamically stable than any other B2 phase. While the single phase B2 $Mo_{25}Nb_{25}Ta_{25}Ru_{25}$ alloy demonstrates that Mo, Nb, and Ta can all participate and form a B2 intermetallic at sufficiently high concentrations of Ru, the HfRu-B2 phase is always formed when Hf is present. These observations are consistent with the known enthalpies of formation reported for HfRu (-91.8 kJ/mol [244]), NbRu (-9 kJ/mol [201]), and the lack of B2 phases in the Mo- and W-Ru binaries. While the formation enthalpy of TaRu has not been reported to the authors' knowledge, it is likely similar in magnitude to the formation enthalpy of NbRu due to the chemical similarity of Nb and Ta and the similarity of formation enthalpies for the Group IV elements (HfRu (-91.8 kJ/mol), TiRu (-77.0 kJ/mol[244]), and ZrRu (-68.7 kJ/mol [244]).

As measured by SEM-EDS and EPMA, the HfRu-B2 phase can accommodate up to 17 at% total of the other elements (Mo, Nb, Ta, W) after heat treatment at 1500/1600 °C, though there is a range of 3 to 17 at% (Tables 3.2, 3.4 and 3.6). After heat treatment, when Nb and/or Ta were present in an alloy, the HfRu-B2 phase contained on average 6.7 at% Nb + Ta and 4.7 at% of Mo + W. In contrast, when Ti and Zr (with formation enthalpies greater then Nb or Ta but less than Hf) are present in combination with Hf, their solubility in the HfRu-B2 phase is significant at 11-15 at% [190, 243]. Considering a binary Hf-Ru alloy within the BCC-Hf + HfRu-B2 phase field, the alloy would have an equilibrium B2 composition of 48 at% Hf and 52 at% Ru. The average composition of the investigated B2 phases was reduced to 47 at% Hf and 43.5 at% Ru, indicating Ru is preferentially substituted for Mo, Nb, Ta and W at 1500/1600 °C in these compositions. In contrast, Hf was preferentially substituted for Zr in $Hf_{20}Nb_{20}Ta_{20}Ru_{20}Zr_{20}$ [190] and for Ti/Zr in $Hf_{20}Ru_{20}Ti_{20}Zr_{20}$ [243]. Overall, the composition of the HfRu-B2 phases in these multi-component systems appears to scale with formation enthalpy of the binary B2 phases.

3.4.4 Interaction of dislocations with HfRu-B2 precipitates

The interaction of dislocations with precipitates directly influences the extent of precipitate strengthening and resulting bulk mechanical properties. While the alloys in this investigation do not have carefully controlled microstructures in the bulk and small-scale testing may not be completely reflective of bulk properties, the more uniform and fine-scale BCC + B2 nanoparticle regions offer an opportunity study to dislocation-precipitate interactions via micromechanical testing. Micropillar compression experiments were performed in the two phase BCC + B2 regions of the HT-$Hf_{20}Mo_{20}Nb_{20}Ta_{20}Ru_{20}$ alloy and post-mortem (S)TEM analysis reveals complex dislocation behavior (Figures 3.14 and 3.15). Similar to other RMPEAs, the room temperature deformation in the BCC phase of $Hf_{20}Mo_{20}Nb_{20}Ta_{20}Ru_{20}$ is accommodated largely by the motion of tortuous, wavy screw dislocations (Figure 3.15D,E.) [172, 245, 246, 232]. The long, paired segments in Figure 3.15A, D-F are approximately screw in character. The surface slip traces and dislocation trace analysis (line direction determination) indicate that these predominantly screw-character dislocations can glide along higher order planes, such as the (312) plane in Figure 3.14. Near the top and bottom surfaces of the sample, we observe some edge dislocations, indicating that their motion is sluggish compared to simple or pure BCC metals [172, 247, 248], but that edge segments are still more mobile than screws in this system at room temperature.

The dislocations present in Figure 3.15 D-F are paired with a spacing ranging from 6 to 20 nm. Paired (or coupled) dislocations are frequently observed during shearing of ordered precipitates, as the successive motion of two dislocations through the ordered precipitate effectively preserves its original ordering [249]. This coupled dislocation motion has been observed in many ordered B2 systems, including β brass [250, 251], FeCo [252], NiAl [253], duplex steels [254], and other high entropy alloys [255]. The strong coupling between the dislocations in this system suggest that the energetic penalty for disordering the B2 phase, i.e. the anti-phase boundary (APB) energy, is high. An estimate of the APB energy can be made by assuming that the shear stress necessary to shear the precipitates, τ_c, is equivalent to the Orowan bowing stress, τ_b. Dislocations would shear precipitates when the stress necessary to do so falls below the Orowan bowing stress, as is the case for small shearable particles[4]; therefore, this assumption would yield an estimate for the maximum APB energy. The Orowan bowing stress is equivalent to:

$$\tau_b = \frac{Gb}{L} \tag{3.2}$$

where G is the shear modulus of the matrix, b is the Burgers vector of the matrix, and L is the distance between the particles. The cutting stress is expected to be on the order of:

$$\tau_c \approx \frac{\gamma_{APB}}{b} \tag{3.3}$$

where γ_{APB} is the APB energy [4].

A value of 69.8 GPa was calculated for G from a weighted average of the elemental shear moduli and the composition of the BCC phase reported in Table 3.6. The elemental shear moduli used are presented in Table 3.10. The magnitude of the Burgers vector, b

Table 3.10: Shear moduli, G, of the pure refractory metals. The shear modulus of BCC Hf was derived single crystal elastic constants using $G = (C_{11}\text{-}C_{12}\text{+}C_{44})/2$[256].

Element	G (GPa)	Ref
Hf	24	[257]
Mo	126.4	[258]
Nb	31.5	[259]
Ta	72.2	[259]
Ru	-	Not found; shear modulus of Hf substituted

$= a/2\langle 111\rangle$, was calculated from the lattice parameter of the BCC phase determined by TEM in Section 3.3.3 and is equal to 0.283 nm. The average precipitate spacing, L, can be estimated by measuring the distance between the points in Figure 3.15D where the paired dislocations 'pinch' together and equals 104 nm. Using Eq. 3.2, τ_b is calculated to be 190 MPa; assuming τ_b is equivalent to τ_c, an APB energy of 54 mJ/m^2 is estimated, similar to other intermetallics[251]. Alloying strategies that increase the APB energy would be desirable for further increasing strength.

Interestingly, Figure 3.15E displays the formation of several jogs near the segment selected for trace analysis. These jogged segments appear in pairs (i.e. there are two jogs nearby), even though they are formed by a single dislocation (i.e. the trailing dislocation in Figure 3.15E). They do not appear to be formed as a result of precipitate shearing by two paired dislocations that each form a single jog. There are also many paired dipole loops in the sample (Figure 3.15E) which form as a single jogged screw dislocation with two nearby jogs advances and pinches off. The presence of many of these paired dipole loops suggests that this process is common during room temperature deformation.

While this paired or coupled dislocation motion is a strong indication that precipitate shearing is a predominant deformation mechanism, there are also numerous instances of Orowan looping, where the dislocations bow out and pinch off around the precipitates rather than shear them. Many of these loops are visble in Figure 3.15D, E where the circular precipitates are outlined by the contrast from the looped dislocations. The presence of both shearing and looping may arise due to the polydispersity of nanoparticle sizes, where smaller precipitates are sheared and larger precipitates exhibit bowing. However, the precipitate size distribution appears fairly narrow in this sample (Figure 3.14C), and there are several precipitates undergoing shearing (Figure 3.15F) that are larger than small precipitates that have been looped around by dislocations (Figure 3.15E, F). Thus it is unlikely that the particle size is solely responsible for this behavior. The high stresses present during micropillar compression experiments may facilitate bowing in the case of a single dislocation arriving at the precipitate, though many of the looped precipitates appear to be looped by two dislocations. Stresses can also be elevated by multiple dislocations of the same Burgers vector piling up behind precipitates; many parallel dislocations are apparent in Figure 3.15F. There may be additional complexity causing this dual behavior, such as interfacial structure and interactions between the lattice and misfit dislocations at the BCC-B2 interface [161], the slip transfer behavior from a higher order (312) slip plane in the BCC phase to a (101) or (211) plane in the B2 phase, or other chemical effects at the BCC-B2 interface that hinder precipitate shearing. The details of the deformation mechanisms and the value of APB energies, interfacial structure, and the transition from shearing to looping, are actively being investigated. Nevertheless, the present results emphasize that the development of appropriate processing and ageing workflows for controlling nanoparticle sizes and distributions, akin to that in Ni-based superalloys, will be effective in promoting high temperature strength in BCC-B2 alloys.

3.4.5 Implications for Design of Ru-containing BCC+B2 alloys

A coherent B2 precipitate in a BCC matrix would hypothetically provide high temperature strength and creep resistance if the precipitate is morphologically and thermodynamically stable at target temperatures. Ru appears to be a promising alloying addition for achieving stable coherent precipitates above 1200 °C in RMPEAs.

Overall, Ru consistently forms a B2 phase in the presence of Hf, forms only small volume fractions of other, less desirable phases at the investigated temperatures, and the nanoparticle regions previously described in Section 3.4.2 are suggestive of compositions that would have precipitates that can be solutioned and aged. The hardness values reported by Detor *et al.* for the investigated alloys range from 623-859 HV [229], on par with the hardest materials reported in the literature, demonstrating a potential for high strengths in these alloys [78, 190]. The compositions of the two-phase nanoparticle regions contain much less Ru and Hf than the equiatomic compositions, with a range of Ru content of 1.6 to 12.8 at% and 4.8 to 18.8 at% of Hf. These values are consistent with the BCC/BCC+B2 solvus lines in the Hf-Ru phase diagram [260] and are beneficial for reducing weight and cost of future alloys. Ti and Zr both participate significantly in the HfRu-B2 phase when present with Hf, providing an alternative route for increased light weighting if Ti or Zr could be substituted for Hf [190, 243, 261]. Further property adjustments of the B2 phases may be possible by modifying the composition of the other minor elements that partition to that phase. The B2 phases are also stable above 1500 °C, above new target temperatures of 1300-1500 °C for turbine applications. However, significant challenges and questions remain for developing these alloys.

One challenge to developing coherent Ru-based B2 phases is the small lattice parameters of the known B2 phases in comparison to the lattice parameters of desirable matrix elements like Nb or Ta, which possess significant room temperature ductility and high melting temperatures. The lattice parameter of Nb is 3.301 Å and the lattice parameters of HfRu and ZrRu are 3.225 Å (-2.3% misfit) and = 3.253 Å (-1.5%), respectively. Additions of small atoms like Al [262, 263], Cr (a_{Cr} = 2.878 Å [144]), Mo (a_{Mo} = 3.147 Å [264]), V (a_V = 3.026 Å [265]), and W (a_W = 3.1648 Å [144]) can reduce the matrix lattice parameter of Nb, as shown by the less than 1% misfit between the as-cast HfRu nanoparticles and the surrounding (Mo, Nb, Ta)-rich matrix in $Hf_{20}Mo_{20}Nb_{20}Ta_{20}Ru_{20}$ (Figure 3.10). These additions would need to be carefully balanced with their potential impacts on room temperature tensile ductility, deleterious phase formation, and effect on the the lattice parameter of the B2 phase.

Another challenge for these alloys is the development of a processing pathway to produce an evenly dispersed high volume fraction of B2 particles in a BCC matrix. The two phase nanoparticle regions measured present a starting point for alloys that might possess a solution and aging window comprable to Ni- and Co-based superalloys. However the two phase γ-γ' phase field in the Ni-Al binary is much narrower than the BCC+B2 phase field in the Hf-Ru binary, indicating high enough volume fractions of solutionable B2 precipitates may be more difficult to achieve due to the steepness of the solvus line. However, given the complex compositions proposed, more understanding is needed of the ternary and quaternary spaces involved. Alternative, less explored, processing methods are possible if the solvus temperature of the B2 phases cannot be suppressed to accommodate a true solution and aging protocol. Powder-based methods that suppress the formation of the B2 phase through rapid cooling could be used to produce a bulk piece, followed by an aging protocol to evolve the B2 precipitates.

3.5 Conclusions

The microstructures of a series of as-cast and annealed Ru-containing RMPEAs have been characterized in detail. The investigated RMPEAs form high volume fractions of intermetallic phases and undergo complex dendritic, eutectic, and peritectic solidification reactions. The major findings of this investigation are:

- In the presence of Hf, the RMPEAs preferentially form a HfRu-B2 phase, with the remaining elements forming a disordered BCC phase. The HfRu-B2 phase formed both during solidification, in the form of B2 dendrites and other large B2 grains, and during further cooling in the solid, in the form of HfRu-B2 nanoparticles that precipitated in the disordered BCC phases.

- In as-cast $Hf_{20}Mo_{20}Nb_{20}Ta_{20}Ru_{20}$, the lattice mismatch between the nanoparticles and the (Mo, Nb, Ta)-disordered BCC lattice was determined by TEM to be $< 1\%$.

- After 40 h anneals at 1500-1600 °C, all previously observed phases coarsened and new HfRu-B2 nanoparticles precipitated in $Hf_{20}Mo_{20}Nb_{20}Ta_{20}Ru_{20}$ and $Hf_{25}Nb_{25}$-$W_{25}Ru_{25}$.

- Micropillar compression cylinders were milled into the BCC + nanoparticle B2 regions of $Hf_{20}Mo_{20}Nb_{20}Ta_{20}Ru_{20}$ and compressed to a strain of approximately 5 %. Post-mortem TEM analysis found both shearing of precipitates by dislocations and bowing of dislocations around nanoparticles.

In the next chapter, the compositions of the BCC + HfRu-B2 nanoparticle regions are used to design solution and ageable alloys.

Chapter 4

RMPEAs with solution and ageable HfRu-B2 precipitates

In this chapter, the insights gleaned from the as-cast microstructures investigated in Ch. 3. are applied to design solution and ageable BCC + HfRu-B2 refractory mutli-principal element alloys (RMPEAs). Three RMPEAs with 9 at% Ru and varying BCC matrix compositions were arc melted and their phase equilibra investigated from 1300-1900 °C. The as-cast and annealed microstructures were characterized with scanning electron microscopy. In all alloys, the HfRu-B2 phase was present as precipitates embedded in a disordered BCC phase. From sequential annealing experiments, the solvus temperature of the HfRu-B2 phase was found to be consistently above 1750 °C. The $Hf_{11}Nb_{52}V_{28}Ru_9$ alloy was additionally designed to result in a < 1 % misfit between the HfRu-B2 and (Nb,V)-BCC phases. After slow cooling, the HfRu-B2 precipitates evolved in morphology from spheres to cubes to cuboidal arrays with increasing aging time, characteristic of a low misfit between the matrix and precipitate.

4.1 Introduction

In Ch. 3, the as-cast and annealed microstructures of a series of equiatomic Ru-containing RMPEAs were investigated by scanning electron and transmission electron microscopy. It was found that Ru reliably forms HfRu-B2 phases in the presence of Hf. At equiatomic concentrations of Hf and Ru, the HfRu-B2 phases are likely stable to the melting point and the alloys exhibited complex solidification behavior, including eutectic, peritectic, and dendritic solidification. Of greatest interest were the presence of HfRu-B2 nanoparticles embedded within disordered BCC phases- these nanoparticles likely formed within the BCC phases during cooling, as the Ru solubility of the BCC phase decreased with temperature. The Ru concentrations within these two-phase regions were similar to the concentrations that lie on the binary β-Hf $\rightarrow$ β-Hf + HfRu-B2 solvus line[260], suggesting that these compositions could be developed directly into solution and ageable alloys. A solution and aging pathway allows for the homogeneous distribution of precipitates throughout the matrix, providing control over the microstructure and resulting mechanical properties, making it a highly desirable property. To investigate this hypothesis, in this chapter three HfRu-containing alloys were synthesized by arc melting and their phase equilibria investigated from 1300-1900 °C.

Of the measured compositions in Ch 3., $Hf_{11}Ru_9$-$Mo_{28}Nb_{22}Ta_{30}$[1] (at%) was chosen as the starting alloy composition. This composition is derived from the BCC + HfRu-B2 nanoparticle regions that formed in $Hf_{20}Ru_{20}$-$Mo_{20}Nb_{20}Ta_{20}$ after annealing at 1600 °C for 40 h (Figure 3.12A-C). Two further alloys were synthesized: $Hf_{11}Ru_9$-$Mo_{28}Nb_{52}$, with Ta replaced by Nb to reduce density, and $Hf_{11}Ru_9$-$Nb_{52}V_{28}$, with the substitution of Mo by V to reduce misfit between the Nb matrix and HfRu-B2 phase. V was chosen to

---

[1] Given that the HfRu-B2 phases that form only contain minor amounts of other constituent elements (e.g. Mo, Nb, Ta, and W), the compositions in the remainder of this dissertation will be grouped by B2 and BCC formers (e.g. $Hf_{20}Mo_{20}Nb_{20}Ta_{20}Ru_{20}$ becomes $Hf_{20}Ru_{20}$-$Mo_{20}Nb_{20}Ta_{20}$) to improve readability.

tailor the lattice parameter of the BCC phase due to its neutral impact on the tensile ductility of Nb[56]. Using the room temperature lattice parameters of pure Nb (3.301 Å [181]), V (3.026 Å [265]) and HfRu-B2 (3.225 Å [187]), and Vegard's Law (Eq. 2.1), approximately 27.6 at% V is required to make a Nb-based matrix coherent with binary HfRu-B2. Therefore V was directly substituted for Mo.

Scanning electron microscopy was used to characterize the as-cast and annealed microstructures. Contrary to the CALPHAD predictions (Section 3.4.2), all three alloys can be solution and aged. After aging, the HfRu-B2 phase was present as precipitates embedded in a disordered BCC phase. The HfRu-B2 phase was stable up to 1750 °C and additional Hf- and V-rich phases were stable at 1300 °C. After slow cooling, the HfRu-B2 precipitates in $Hf_{11}Ru_{9}$-$Nb_{52}V_{28}$ evolved in morphology from spheres to cubes to cuboidal arrays with increasing aging time, characteristic of a low misfit between the HfRu-B2 and BCC phases. Compared to other Ru-B2 phases that have been recently reported, namely TiRu and AlRu by Kube *et al.*, HfRu appears to be the most thermally stable of the Ru-B2 phases[261].

4.2 Methods

An ingot of each alloy composition was arc melted from elemental raw materials with purities $\geq$ 99.0 %. Excess Ru powder was included to compensate for Ru loss from the final composition. The stock materials were arranged in order of melting temperature, except for the Ru powder, which was placed on the bottom. Arc melting occurred in an inert Ar atmosphere and on a water-cooled copper hearth. A Ti getter was included and melted prior to each melting cycle. Each button was melted at least four times and flipped between melts to ensure homogeneity. After arc melting, bulk compositions were determined by wavelength-dispersive x-ray fluorescence spectroscopy with a Rigaku ZSX

Primus IV instrument and the O and N contents were determined via inert gas fusion (Table 4.1). The inert gas fusion tests were performed by ATI.

Table 4.1: Chemical composition (at%) and interstitial content (ppmw) of the bulk as-cast alloys.

Alloy	Hf	Mo	Nb	Ru	Ta	V	O	N
$Hf_{11}Ru_9$-$Mo_{28}Nb_{22}Ta_{30}$	11.7	27.8	23.1	8.0	29.5	-	180	20
$Hf_{11}Ru_9$-$Mo_{28}Nb_{52}$	11.8	26.8	52.6	8.8	-	-	170	23
$Hf_{11}Ru_9$-$Nb_{52}V_{28}$	11.5	-	53.0	8.9	-	26.6	300	36

To evaluate the solvus temperatures of the HfRu-B2 phase, annealing treatments at 1750 and 1900 °C for 2 and 10 h were performed in an Vacuum Industries Hot Press. Due to a CALPHAD predicted solidus temperature of 1830 °C, $Hf_{11}Ru_9$-$Nb_{52}V_{28}$ was omitted from the 1900 °C anneal out of concerns that it would melt. To protect the samples from oxidation, they were wrapped in Ta foil and encapsulated inside Ta ampoules with Hf foil. Additional unsealed Ta ampoules containing Hf and NbTi foil were also included during the anneal to getter oxygen. The Hot Press had an estimated peak cooling rate of 45 °C/min.

To study equilibrium phase formation, two aging treatments were performed using the solutioned samples: 1600 °C for 40 h and 1300 °C for 200 h. For $Hf_{11}Ru_9$-$Nb_{52}V_{28}$, the 1750 °C for 10 h sample was used as the homogenization treatment. The aging treatments were performed in a Vacuum Industries resistive furnace. Samples were heated at a rate of 15 °C/min and cooled at the maximum speed of the furnace (with an estimated maximum cooling rate of 270 °C/min). The samples were encapsulated inside Ta ampoules with NbTi foil.

After annealing, the samples were prepared for scanning electron microscopy (SEM) by mechanical and vibratory polishing. SEM was performed with a ThermoFisher Apreo C microscope. Backscatter electron (BSE) and secondary electron (SE) micrographs were collected. Chemical composition information was acquired with energy dispersive X-ray spectroscopy (EDS) using an EDAX Si-drift EDX detector. SE images from each condition were used to determine the volume fraction of the B2 phase via point counting method using ASTM standard E562 19e1. The minimum grid size was 15x15 pts. Phases that formed on slow cooling were omitted from the count.

Hardness values were determined for all annealing conditions and calculated from at least 10 indents placed with weights between 1-2 kg. To assist in the identification of major constituents and their lattice parameters, XRD patterns were collected on bulk polycrytalline samples after mechanical polishing on 320 grit SiC paper. The patterns were collected on a Panalytical Empyrean Powder Diffractometer using Cu Kα radiation (λ = 0.154nm).

4.3 Results

4.3.1 As-cast Microstructures

All three alloys solidified dendritically (Figure 4.1). Overall, Mo, Nb, and Ta were enriched in the dendrite cores and Hf, Ru, and V were rejected to the inter-dendritic regions. In $Hf_{11}Ru_9$-$Mo_{28}Nb_{22}Ta_{30}$, Nb did not segregate to either region. The increased concentration of Hf and Ru in the inter-dendritic regions resulted in the formation of coarse (Hf,Ru)-rich phases that lengthen and coarsen towards the grain boundaries. The (Hf,Ru)-rich phase in as-cast $Hf_{11}Ru_9$-$Mo_{28}Nb_{22}Ta_{30}$ is large enough to be measured by SEM-EDS and contained 38 at% Hf and 36 at% Ru. Consistent with the parent alloy, nanoparticles can be observed within the matrix phase in the areas enriched with Hf and Ru. These nanoparticles are largest adjacent to the coarse (Hf,Ru)-rich grains and decrease in size towards the dendrite cores. With the introduction of V, the $Hf_{11}Ru_9$-

$Nb_{52}V_{28}$ alloy also formed a V-rich phase (V1) in the center of the inter-dendritic regions, in-between layers of the (Hf,Ru)-rich phase (Figure 4.1F). V1 contains 40.8 at% V, 26.0 at% Hf, 20.7 at% Nb, and 12.4 at% Ru (Table 4.2).

The XRD scans of the as-cast samples all demonstrate a single set of (110), (200), and (211) peaks, which is associated with disordered BCC phases in the absence of other peaks (Figure 4.2). The as-cast alloys also exhibit additional, smaller, (100), (111), and (211) peaks that are associated with B2 ordering. If both a disordered BCC phase and an ordered B2 phase are present, and their lattice parameters are sufficiently close, their (110), (200), and (211) peaks could overlap, obscuring the presence of two phases in the XRD scan. Consistent with the results of Chs. 2 and 3, the matrix phases are therefore identified as disordered BCC phases and the (Hf,Ru)-rich phases are identified as HfRu-B2. The shared peaks are labeled BCC/B2.

The XRD scan for $Hf_{11}Ru_9$-$Nb_{52}V_{28}$ exhibits additional peaks that cannot be attributed to the BCC or HfRu-B2 phases (Figure 4.2C). These peaks likely stem from the V1 phase. However, the composition of the V1 phase is not directly equivalent to a known binary or ternary phase. The closest candidate phase is the C14 Laves phase found in the the Hf-Nb-V ternary phase diagram from 1000-1300 °C recently evaluated by Zhang *et al.*[105]. The C14 phase is present in alloys with higher Nb contents and can contain 5-21 at% Nb and 26-36 at% Hf, consistent with the composition of the V1 phase. The additional peaks also match those reported for the C14 Laves, though some are missing[105]. Further investigation is required to determine if V1 is a C14 Laves phase containing significant amounts of Ru. The composition is distinct (richer in V and Ru and depleted in Hf) from the tentatively identified orthorhombic phase discussed in Ch 5.

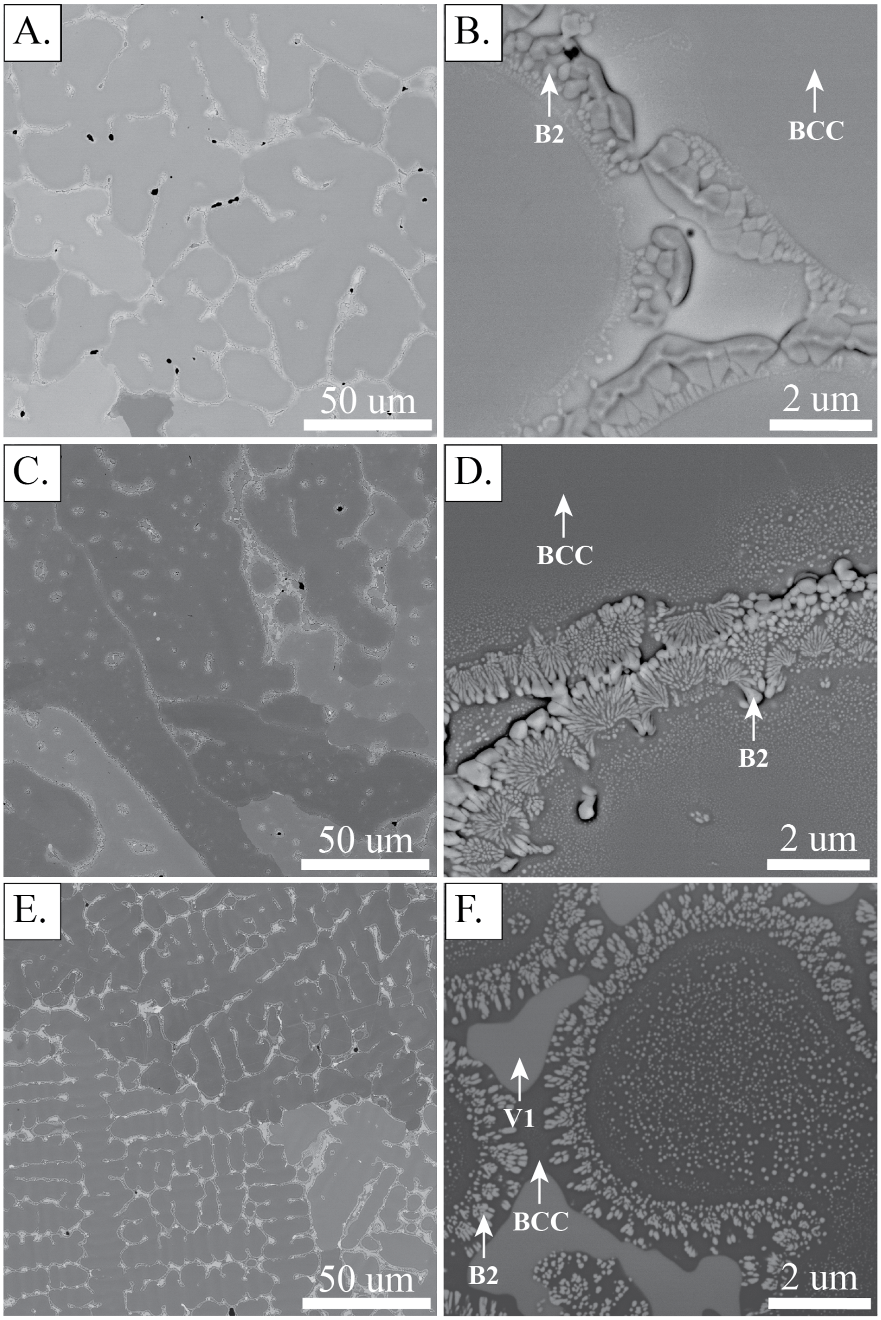

Figure 4.1: Backscatter electron (BSE) micrographs of as-cast alloys. A, B. $Hf_{11}Ru_9$-$Mo_{28}Nb_{22}Ta_{30}$. C, D. $Hf_{11}Ru_9$-$Mo_{28}Nb_{52}$. E, F. $Hf_{11}Ru_9$-$Nb_{52}V_{28}$. The alloys solidified with disordered BCC dendrites that rejected Hf, Ru, and V to the liquid, resulting in the formation of coarse HfRu-B2 phases in the inter-dendritic regions. Adjacent to the coarse HfRu-B2 phases are smaller HfRu-B2 nanoparticles that formed within the BCC phase on cooling. An additional unidentified V-rich phase, V1, is visible in the inter-dendritic regions of $Hf_{11}Ru_9$-$Nb_{52}V_{28}$.

Table 4.2: Chemical compositions (at%) and volume fractions (a_f) of the identified phases in the as-cast and heat treated alloys. The compositions were determined via SEM-EDS. Error is on the order of a few at% percent.

Alloy	**Condition**	**Phase**	**Hf**	**Mo**	**Nb**	**Ru**	**Ta**	**V**
$Hf_{11}Ru_9$-$Mo_{28}Nb_{22}Ta_{30}$	1750 °C 10 h	B2	43.9	4.3	2.9	42.4	6.4	-
	1750 °C 10 h	BCC^a	8.1	30.7	20.8	4.2	36.2	-
$Hf_{11}Ru_9$-$Mo_{28}Nb_{52}$	1900 °C 10 h + 1600 °C 40 h	BCC	8.7	32.4	56.0	2.9	-	-
	1750 °C 10 h	B2	47.3	3.2	4.9	44.7	-	-
	1750 °C 10 h	BCC^a	9.1	31.5	54.2	5.2	-	-
$Hf_{11}Ru_9$-$Nb_{52}V_{28}$	as-cast	V1	26.0	-	20.7	12.4	-	40.8
	1750 °C 10 h	B2	49.8	-	2.2	43.6	-	4.3
	1750 °C 10 h	BCC^a	11.1	-	56.1	6.9	-	26.0
	1750 °C 10 h	HF2	96.3	-	2.2	0.0	-	1.4
	1750 °C 10 h	V1	25.7	-	17.3	13.3	-	43.7
	1750 °C 10 h + 1600 °C 40 h	B2	50.3	-	1.5	45.8	-	2.4
	1750 °C 10 h + 1600 °C 40 h	BCC^a	11.6	-	53.2	6.9	-	28.2
	1750 °C 10 h + 1300 °C 200 h	B2	49.6	-	2.1	44.8	-	3.5
	1750 °C 10 h + 1300 °C 200 h	BCC	7.6	-	56.8	2.9	-	32.8
	1750 °C 10 h + 1300 °C 200 h	HF2	97.0	-	1.7	0.0	-	1.3
	1750 °C 10 h + 1300 °C 200 h	V1	24.3	-	18.9	12.7	-	44.0

[a]: The BCC phase contains new HfRu-B2 precipitates that formed on cooling.

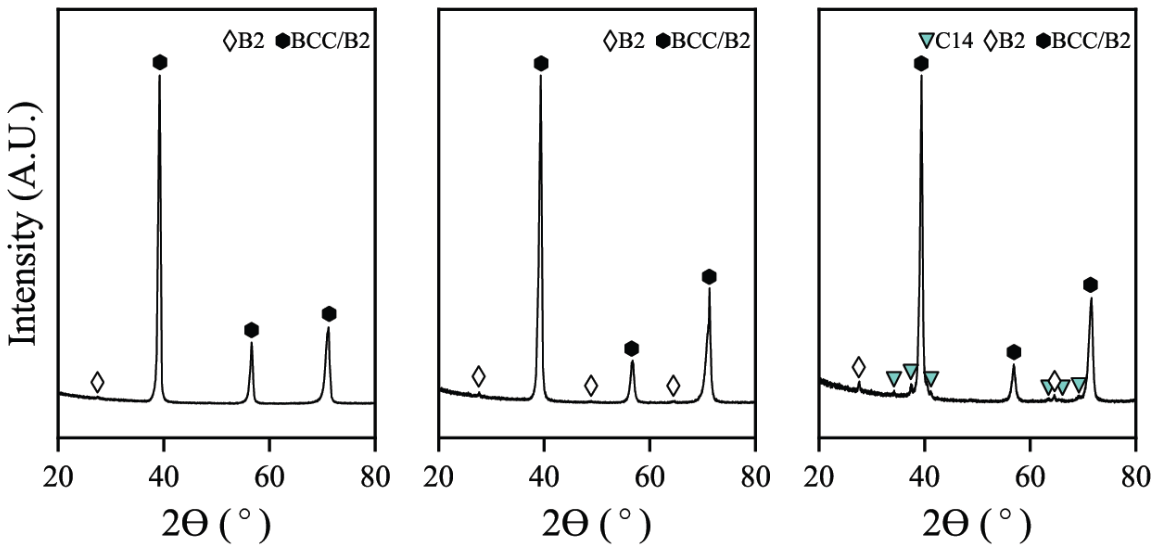

(a) (b) (c)

Figure 4.2: XRD scans of the as-cast alloys. a. $Hf_{11}Ru_9$-$Mo_{28}Nb_{22}Ta_{30}$, b. $Hf_{11}Ru_9$-$Mo_{28}Nb_{52}$, and c. $Hf_{11}Ru_9$-$Nb_{52}V_{28}$. All scans demonstrate peaks associated with BCC and B2 ordering. Additional peaks in the $Hf_{11}Ru_9$-$Nb_{52}V_{28}$ scan are consistent with a C14 laves phase, though some are missing[105]. Is it assumed that these peaks correspond to the V1 phase in the as-cast micrograph in Figure 4.1F.

Table 4.3: Identified phases and their lattice parameters (Å) as determined from XRD.

Alloy	Condition	a_{B2} (Å)	$a_{B2/BCC}$ (Å)
$Hf_{11}Ru_9$-$Mo_{28}Nb_{22}Ta_{30}$	as-cast	3.220	3.247
	1900 °C 10 h	3.231	3.250
	1900 °C 10 h + 1600 °C 40 h	3.209	3.246
	1900 °C 10 h + 1300 °C 200 h	3.220	3.251
	1750 °C 10 h	-	3.257
$Hf_{11}Ru_9$-$Mo_{28}Nb_{22}Ta_{30}$	as-cast	3.225	3.244
	1900 °C 10 h	3.212	3.241
	1900 °C 10 h + 1600 °C 40 h	3.230	3.250
	1900 °C 10 h + 1300 °C 200 h	3.223	3.243[a]
	1750 °C 10 h	3.229	3.243
$Hf_{11}Ru_9$-$Nb_{52}V_{28}$	as-cast	3.230	3.231
	1750 °C 10 h	3.223	3.228
	1750 °C 10 h + 1600 °C 40 h	3.228	3.232
	1750 °C 10 h + 1300 °C 200 h	3.234	3.239

[a]: The misfit between the BCC and B2 phases was sufficiently large to split the (200) peaks apart. Value represents the lattice parameter of the BCC phase.

4.3.2 Anneals at 1750 and 1900 °C

After annealing at 1750 °C for 10 h, the HfRu-B2 phase remains at the grain boundaries and in the former inter-dendritic regions of the three alloys (Figure 4.3). After increasing the temperature to 1900 °C, the inter-dendritic B2 was eliminated in $Hf_{11}Ru_9$-$Mo_{28}Nb_{22}Ta_{30}$ and $Hf_{11}Ru_9$-$Mo_{28}Nb_{52}$ (Figure 4.3C,G) and only a disordered BCC phase remained. Therefore, the solvus temperature of the B2 phase must lie between 1750-1900 °C and the alloys can be solution and aged. The composition of all homogenized phases at 1750 °C are reported in Table 4.2.

The slow cooling of the vacuum furnace (with an estimated peak cooling rate of ≈ 45 °C/min) resulted in the formation of new HfRu-B2 precipitates within the BCC matrices after cooling from 1750 °C and 1900 °C (Figure 4.3). The precipitates increase in size with the reduction of Mo and Ta content, which lowers the overall melting temperature of the alloy and increases the rate of diffusion. In the $Hf_{11}Ru_9$-$Mo_{28}Nb_{22}Ta_{30}$ and $Hf_{11}Ru_9$-$Mo_{28}Nb_{52}$ alloys, the precipitates are spherical in appearance; in $Hf_{11}Ru_9$-$Mo_{28}Nb_{22}Ta_{30}$, the precipitates are also are larger at grain and sub-grain boundaries (Figure 4.3D). In contrast, the HfRu-B2 precipitates in $Hf_{11}Ru_9$-$Nb_{52}V_{28}$ vary in morphology from spheres (with diameters ≤ 110 nm) to cubes (with side lengths (a) = 120-450 nm) to arrays of cubes (a = 1160-1420 nm), (Figure 4.3J).

Some additional phases are also present. After annealing at 1750 and 1900 °C, $Hf_{11}Ru_9$-$Mo_{28}Nb_{52}$ forms a minor amount of a Hf-rich tertiary phase (HF1) at the grain boundaries and homogeneously throughout the intragranular regions (Figure 4.4A). HF1 forms with a needle-like morphology inside of the grains. In $Hf_{11}Ru_9$-$Nb_{52}V_{28}$, two other coarse phases are present at 1750 °C: a V-rich phase, V1, that was present in the as-cast microstructure, and a Hf-rich phase, HF2 (Figure 4.3K). HF2 is 97 at% Hf but does not demonstrate an elevated O content that would be consistent with HfO_2. Long, thin

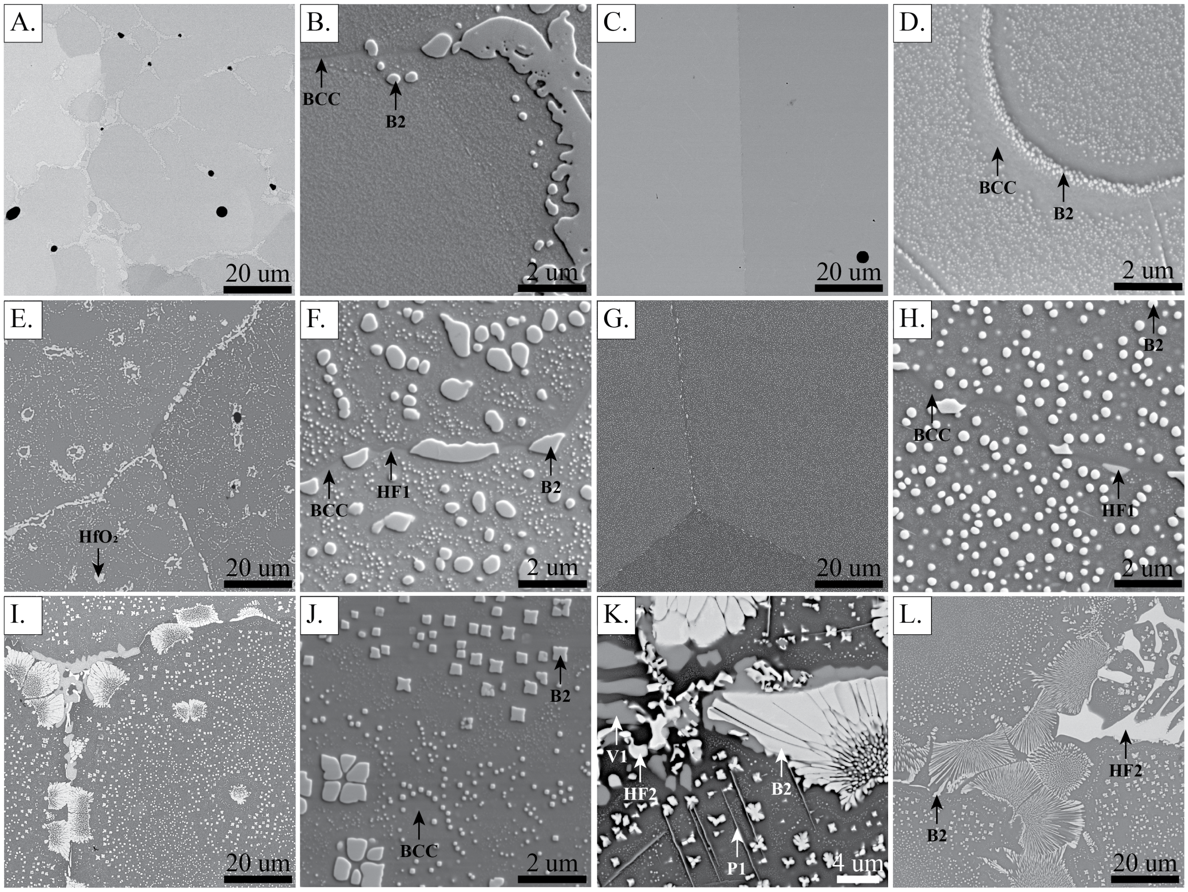

Figure 4.3: A. BSE and B. SE micrographs of $Hf_{11}Ru_9$-$Mo_{28}Nb_{22}Ta_{30}$ after 10 h 1750 °C. C. BSE and D. SE micrographs of $Hf_{11}Ru_9$-$Mo_{28}Nb_{22}Ta_{30}$ after 10 h at 1900 °C. Two phases are visible: a (Mo, Nb, Ta)-BCC matrix and HfRu-B2. E. BSE and F. SE micrographs of $Hf_{11}Ru_9$-$Mo_{28}Nb_{52}$ after 10 h at 1750 °C. G. BSE and H. micrographs of $Hf_{11}Ru_9$-$Mo_{28}Nb_{52}$ after 10 h at 1900 °C. Three phases are visible: a (Nb, Mo)-rich BCC matrix, HfRu-B2, and a light grey HF1 that is rich in Hf. I., K. BSE and J. SE micrographs of $Hf_{11}Ru_9$-$Nb_{52}V_{28}$ after 10 h at 1750 °C. Five phases are visible: a (Nb,V)-BCC matrix, HfRu-B2, the dark grey V1, the white HF2 (rich in Hf), and the bright white P1, a needle-like phase rich in Hf. HF2 and P1 may be the same phase at different lengthscales. L. BSE micrograph of $Hf_{11}Ru_9$-$Nb_{52}V_{28}$ after annealing at 1750 °C for 2 h. Compared to the 10 h anneal, the grain boundary HfRu-B2 is less coarse and compact, confirming the HfRu-B2 phase is stable at 1750 °C. In contrast, the intragranular HfRu-B2 phases did not change in size and morphology, confirming they formed on cooling.

lamelle (P1) that are 40-80 nm wide also formed. The lamellae appear rich in Hf and depleted of all other elements after mapping with SEM-EDS, consistent with the composition of HF2 (Figure 4.4B). Therefore, it is possible that the lamellae and HF2 are the same phase. Given the sizes of the HF1 and P1 regions, it is likely they also formed on cooling and were not present at $\geq$ 1750 °C.

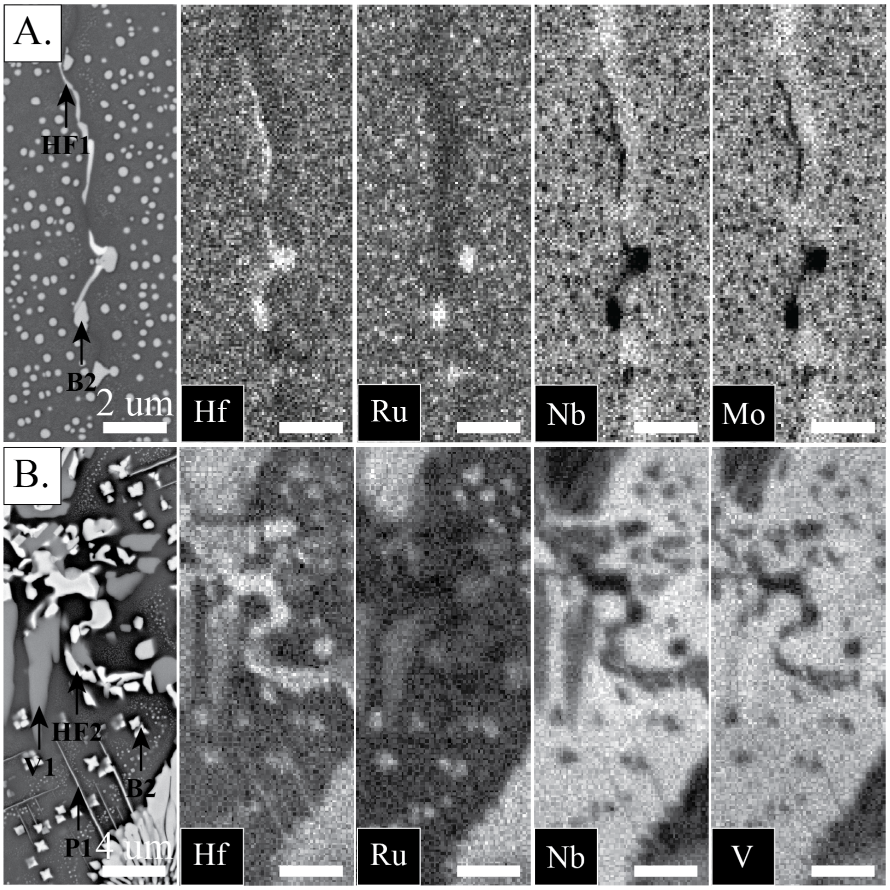

Figure 4.4: A. BSE micrograph (left) and SEM-EDS (Hf, Ru, Nb, and Mo) maps of a grain boundary in $Hf_{11}Ru_9$-$Mo_{28}Nb_{52}$ after annealing for 10 h at 1900 °C. Three phases are visible: a (Mo, Nb)-BCC matrix, HfRu-B2 (rich in both Hf and Ru), and a white grain boundary phase, HF1, that is rich only in Hf. B. BSE micrograph (left) and SEM-EDS (Hf, Ru, Nb, and V) maps of a multi-phase region in $Hf_{11}Ru_9$-$Nb_{52}V_{28}$ after annealing at 1750 °C for 10 h. Five phases are visible: a (Nb,V)-BCC matrix, HfRu-B2 (rich in both Hf and Ru), the dark grey V1 (depleted in Nb and enriched with V), the white HF2 (rich in Hf), and the bright white P1, a needle-like phase rich in Hf. No phases demonstrated an enrichment in O or N.

After annealing at 1750 °C and 1900 °C, the peaks present in the XRD scans are similar to those exhibited by the as-cast samples (Figure 4.5). All scans contained peaks associated with a disordered BCC phase and most scans contained additional B2 ordering peaks. Some peaks that could not be directly attributed to a known phase were also observed in the $Hf_{11}Ru_9$-$Mo_{28}Nb_{52}$ and $Hf_{11}Ru_9$-$Nb_{52}V_{28}$ scans but were not sufficient to identify the crystal structures of HF1, HF2, and V1. The lattice parameters derived from the experimental (100), (111), and (211) B2 ordering peaks (Table 4.3) are very close to the lattice parameter of the binary HfRu-B2 phase (3.220-3.230 Å vs 3.225 Å[266, 187]).

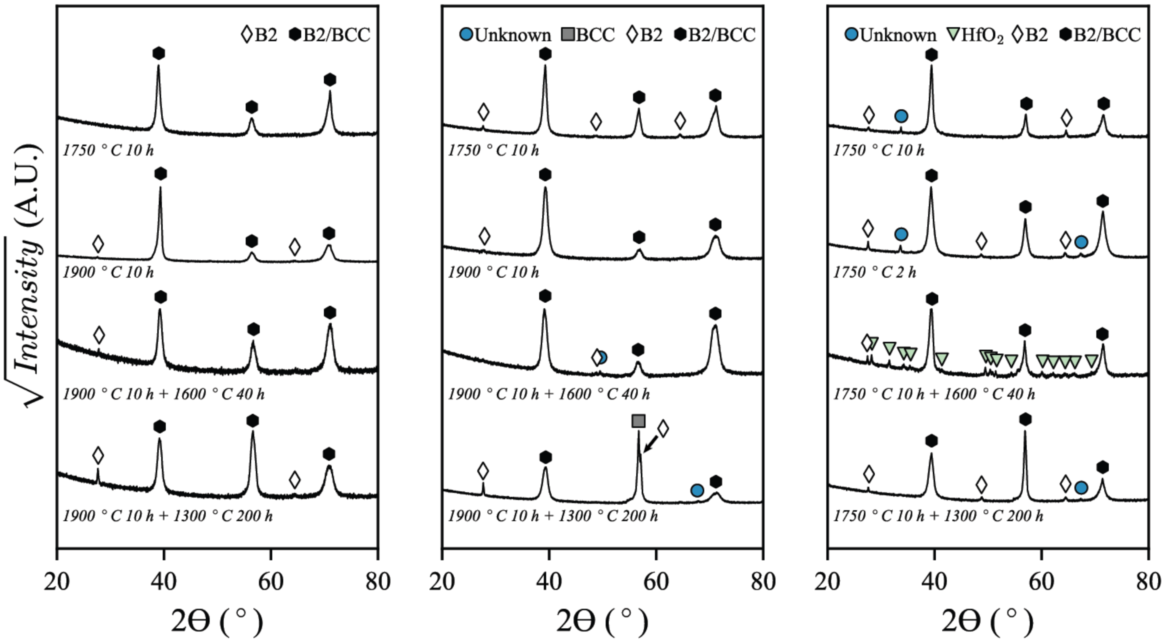

(a) (b) (c)

Figure 4.5: XRD scans of a. $Hf_{11}Ru_9$-$Mo_{28}Nb_{22}Ta_{30}$, b. $Hf_{11}Ru_9$-$Mo_{28}Nb_{52}$ and c. $Hf_{11}Ru_9$-$Nb_{52}V_{28}$ in the annealed conditions. Peaks associated with a disordered BCC are visible in all alloys and conditions, with additional B2 ordering peaks present in some samples.

4.3.3 Anneals at 1300 and 1600 °C

Due to the slow cooling of furnace used for the heat treatments $\geq$ 1750 °C, the investigated microstructures in Figure 4.3 contain non-equlibrium phase formation. To investigate equilibrium phase formation, two further aging treatments were performed at 1600 °C for 40 h and 1300 °C for 200 h.

The microstructures of $Hf_{11}Ru_{9}$-$Mo_{28}Nb_{22}Ta_{30}$ and $Hf_{11}Ru_{9}$-$Mo_{28}Nb_{52}$ change very little after aging at 1600 and 1300 °C (Figure 4.6A-H). At 1300 °C, $Hf_{11}Ru_{9}$-$Mo_{28}Nb_{22}Ta_{30}$ develops a minor phase (P2) at the grain boundaries that is too small to map with SEM-EDS (Figure 4.6B). At 1600 °C, discontinuous precipitation of the B2 phase occurred at the grain boundaries of $Hf_{11}Ru_{9}$-$Mo_{28}Nb_{22}Ta_{30}$ (Figure 4.6C,D) and $Hf_{11}Ru_{9}$-$Mo_{28}Nb_{52}$ (Figure 4.6H).

After aging for 200 h at 1300 °C, all of the pre-existing phases in $Hf_{11}Ru_{9}$-$Nb_{52}V_{28}$ experienced homogenization without significant changes in composition (Figure 4.6I,J). HF2 and V1 are minor phases present only at the grain boundaries. The largest of the pre-existing HfRu-B2 precipitates evolved into spherical precipitates 500-2000 nm in diameter; the smaller spherical and cuboidal precipitates were eliminated by coarsening. Including the intragranular and grain boundary HfRu-B2 phases, the combined volume fraction is $\approx$ 0.13. After increasing the aging temperature to 1600 °C, the V1 and HF2 phases were eliminated from the grain boundaries and none of the thinner P1 laths remain. In the grain interiors, rounded cuboidal precipitates 100-200 nm in diameter are observed (Figure 4.6L). Considering that the sizes of the intragranular B2 precipitates at 1600 °C are smaller then the largest cuboidal arrays that were pre-existing in the microstructure, the intragranular B2 precipitates likely formed on cooling and were not present at 1600 °C.

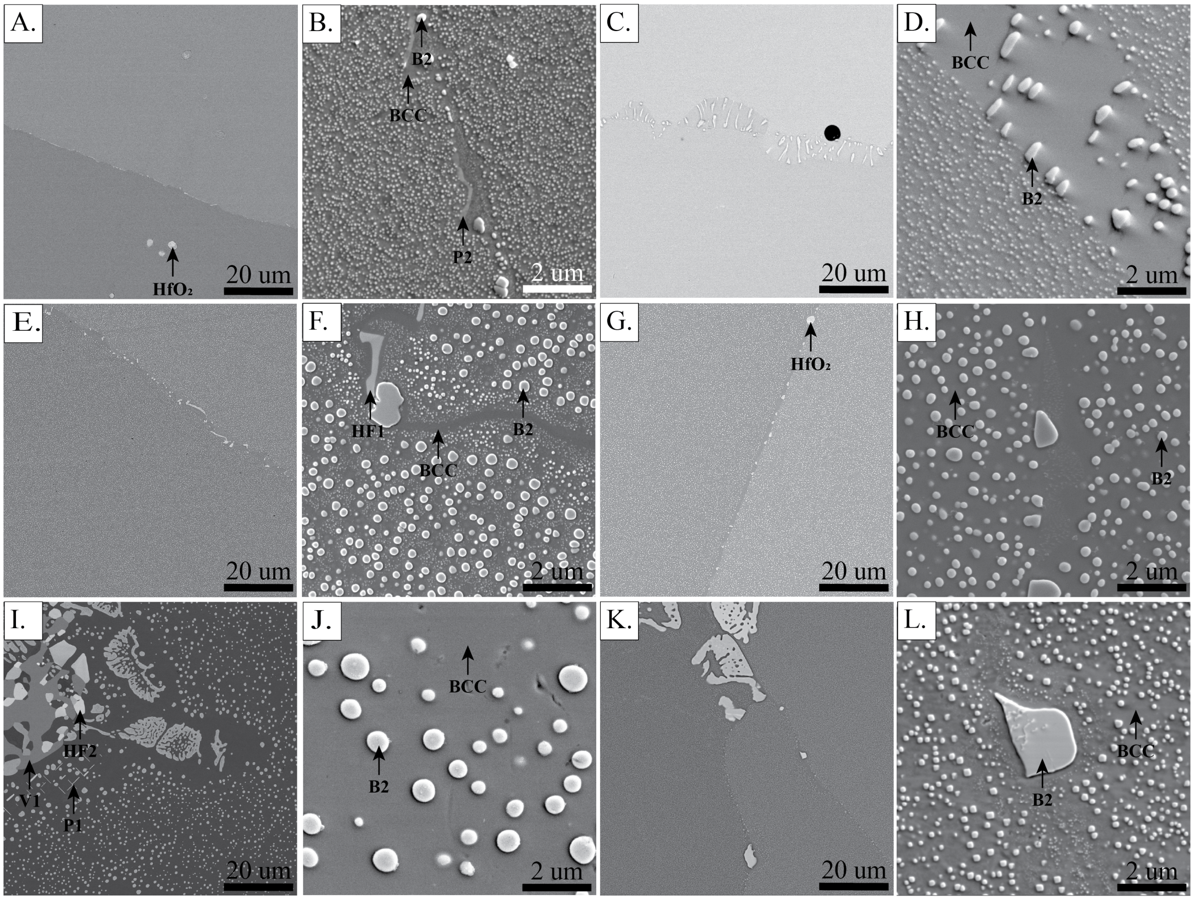

Figure 4.6: Microstructures of the investigated alloys after aging at 1300 °C for 200 h and 1600 °C for 40 h. Both $Hf_{11}Ru_9$-$Mo_{28}Nb_{22}Ta_{30}$ and $Hf_{11}Ru_9$-$Mo_{28}Nb_{52}$ were solutioned at 1900 °C for 10 h; $Hf_{11}Ru_9$-$Nb_{52}V_{28}$ was homogenized at 1750 °C for 10 h. In all conditions, a HfRu-B2 phase is stable within a disordered BCC matrix. A. BSE and B. SE micrographs of $Hf_{11}Ru_9$-$Mo_{28}Nb_{22}Ta_{30}$ at 1300 °C. A minor unidentified phase, P2, is visible at the grain boundary in B. C. BSE and D. SE micrographs of $Hf_{11}Ru_9$-$Mo_{28}Nb_{22}Ta_{30}$ at 1600 °C. E. BSE and F. SE micrographs of $Hf_{11}Ru_9$-$Mo_{28}Nb_{52}$ at 1300 °C. G. BSE and H. SE micrographs of $Hf_{11}Ru_9$-$Mo_{28}Nb_{52}$ at 1600 °C. Discontinuous precipitation of HfRu-B2 is visible at the grain boundaries in C, D, and H. I. BSE and J. SE micrographs of $Hf_{11}Ru_9$-$Nb_{52}V_{28}$ at 1300 °C. Two Hf-rich phases, HF1 and P1, and a V-rich phase, V1, are visible in I. K. BSE and L. SE micrographs of $Hf_{11}Ru_9$-$Nb_{52}V_{28}$ at 1600 °C. HF1, P1, and V1 were not observed. The small cuboidal precipitates of HfRu-B2 that are present in the intra-granular regions formed on cooling and only the coarse HfRu-B2 observed at the grain boundaries was present at 1600 °C.

The presence of V1 and HF2 at 1300 °C but not 1600 °C suggests that the V1 and HF2 grains observed after annealing at 1750 °C formed during slow cooling and that they coarsened more rapidly than the intragranular B2 phases due to their incoherence with the BCC matrix and location on the grain boundaries. To determine whether the grain boundary B2 phase was stable at 1750 °C or also formed on cooling, a second 1750 °C anneal for 2 h was performed. In both anneals the overall 'feathered' morphology of the B2 phase, originating from the as-cast microstructure, is maintained but the laths thicken from 2 to 10 h (Figure 4.3I, L). In contrast, the HfRu-B2 present in the intergranular regions did not change in size or morphology between the two annealing times. This confirms that the grain boundary HfRu-B2 phase is stable at 1750 °C and that the intra-granular B2 formed on cooling.

The volume fractions of the B2 phase were determined for all annealing conditions and are presented in Table 4.4 and Figure 4.7. The B2 volume fraction increased with decreasing temperature. $Hf_{11}Ru_{9}$-$Mo_{28}Nb_{52}$ consistently had the highest volume fraction of the B2 phase at all temperatures. $Hf_{11}Ru_{9}$-$Nb_{52}V_{28}$ had the lowest.

4.3.4 Hardness

Hardness values were determined from the as-cast and annealed conditions (Figure 4.7). $Hf_{11}Ru_{9}$-$Mo_{28}Nb_{22}Ta_{30}$ was slightly harder in all annealed conditions despite having a lower volume fraction of the B2 phase compared to $Hf_{11}Ru_{9}$-$Mo_{28}Nb_{52}$. The precipitates in the Ta-containing alloy were much smaller compared to the precipitates in the Mo-containing alloy, likely improving its hardness. With further aging, hardness decreased in both $Hf_{11}Ru_{9}$-$Mo_{28}Nb_{22}Ta_{30}$ and $Hf_{11}Ru_{9}$-$Mo_{28}Nb_{52}$ due to precipitate coarsening. $Hf_{11}Ru_{9}$-$Nb_{52}V_{28}$ was the softest of the three alloys, despite V being considered a more potent room temperature strengthener than Mo[56]. The precipitate

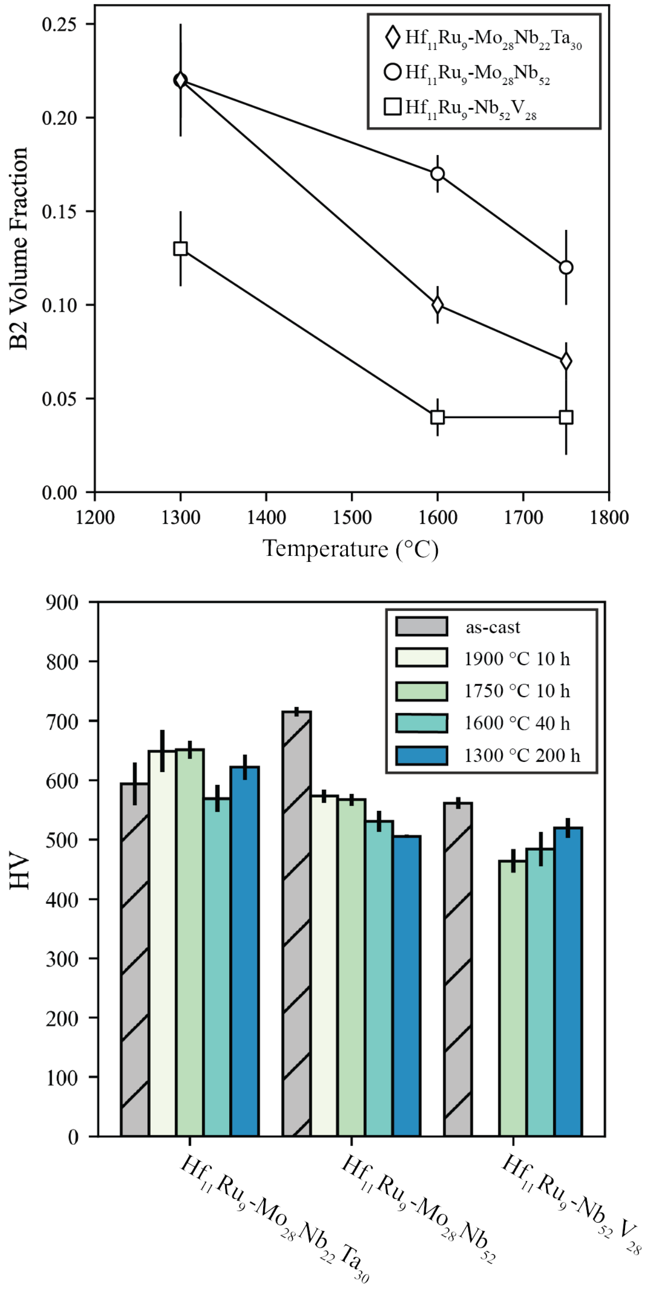

Figure 4.7: (top) Volume fraction of the B2 phase present at each annealing temperature. Error represents the 95% confidence interval for the value. Volume fractions may be slightly over estimated due to the etching of the BCC matrix during vibratory polishing. Additions of Nb and Mo appear to increase the volume fraction of the B2 phase relative to Ta and V, respectively. (left) Vickers Hardness of as-cast and annealed samples. The volume fractions and hardness values are also recorded in Table 4.4.

Table 4.4: Hardness (HV) and volume fraction (%) of the HfRu-B2 phase in the as-cast and annealed alloys.

Alloy	Condition	Hardness	Volume Fraction
$Hf_{11}Ru_9$-$Mo_{28}Nb_{22}Ta_{30}$	As-cast	594 ± 36	-
	1900 °C 10 h	649 ± 36	-
	1750 °C 10 h	651 ± 15	7 ± 1
	1900 °C 10 h + 1600 °C 40 h	569 ± 23	10 ± 1
	1900 °C 10 h + 1300 °C 200 h	622 ± 21	22 ± 3
$Hf_{11}Ru_9$-$Mo_{28}Nb_{52}$	As-cast	715 ± 9	-
	1900 °C 10 h	573 ± 11	-
	1750 °C 10 h	567 ± 10	12 ± 2
	1900 °C 10 h + 1600 °C 40 h	531 ± 18	17 ± 1
	1900 °C 10 h + 1300 °C 200 h	505 ± 3	22 ± 2
$Hf_{11}Ru_9$-$Nb_{52}V_{28}$	As-cast	561 ± 10	-
	1750 °C 10 h	464 ± 20	4 ± 2
	1750 °C 10 h + 1600 °C 40 h	484 ± 29	4 ± 1
	1750 °C 10 h + 1300 °C 200 h	519 ± 17	13 ± 2

sizes in the V-containing alloy are much larger and the volume fraction lower then in $Hf_{11}Ru_9$-$Mo_{28}Nb_{52}$. The hardness of $Hf_{11}Ru_9$-$Nb_{52}V_{28}$ increases with decreasing annealing temperature, potentially due to the decreased precipitate size at 1600 °C and the increased volume fraction of the B2 phase at 1300 °C.

4.4 Discussion

The phase equilibria of three HfRu-containing alloys were investigated. The reduction in Ru content from 20-33 at% to 9 at% results in alloys that can be successfully solution and aged, with the solvus temperature of the HfRu-B2 phase lying between 1750 °C and 1900 °C. In the following sections, compositional trends in the constituent phases and the morphology of the HfRu-B2 precipitates are discussed.

4.4.1 Trends in BCC and B2 composition

The HfRu-B2 composition is fairly constant across all alloys and conditions. After homogenization, the HfRu-B2 phases had a minimum Hf content of ≈ 44 at% and a minimum Ru content of ≈ 42 at% (Table 4.2). Minor amounts (≤ 5 at%) of Mo, Nb, and V partition to the HfRu-B2, with the largest participant being Ta at 6.4 at%.

Within the BCC phase, the replacement of Mo with V increases the solubility of Ru in the BCC matrix. In $Hf_{11}Ru_9$-$Mo_{28}Nb_{22}Ta_{30}$ and $Hf_{11}Ru_9$-$Mo_{28}Nb_{52}$, the BCC phases that were single phase at 1750 °C contain ≤ 5 at% Ru. The Ru content rises to 7 at% Ru in $Hf_{11}Ru_9$-$Nb_{52}V_{28}$. This change in solubility results in $Hf_{11}Ru_9$-$Nb_{52}V_{28}$ having the lowest volume fraction of B2 at all investigated temperatures (Figure 4.7). This is consistent with the trends reported by Kube *et al.*- the B2 volume fraction tends to be higher in Mo-containing matrices for various B2 formers[261].

As the temperature decreases, the solubility of Ru within the BCC matrix decreases significantly, resulting in an increase of the B2 volume fraction (Figure 4.7). In $Hf_{11}Ru_9$-$Nb_{52}V_{28}$, the Ru concentration of the BCC matrix in $Hf_{11}Ru_9$-$Nb_{52}V_{28}$ decreases from 6.9 at% at 1750 °C to 2.9 at% at 1300 °C. Similarly, the BCC matrix of $Hf_{11}Ru_9$-$Mo_{28}Nb_{52}$ contains 5.2 at% Ru at 1750 °C and 2.9 at% at 1600 °C. This change in solubility with temperature is consistent with the precipitation of HfRu-B2 precipitates in the BCC matrix phases with slow cooling from 1750 and 1900 °C. This also suggests that Ru concentrations ≤ 7 at% would produce alloys with solvus temperatures below 1750 °C, with the specific Ru content dependent on the matrix composition.

4.4.2 Morphology of HfRu-B2 precipitates

The lattice parameter of the HfRu-B2 phase does not change significantly from its binary lattice parameter, even with significant changes in matrix composition (Table 4.3).

This is due to the low concentrations of other solute elements that dissolve in the B2 phase (Table 4.2). This allows a weighted average of the constituent lattice parameters to be used to design coherent BCC + B2 alloys with a δ less than 1 %. This is shown by the formation of cuboidal precipitates in $Hf_{11}Ru_9$-$Nb_{52}V_{28}$ after slow cooling from 1750 °C.

Multiple HfRu-B2 precipitate morphologies are present in the intragranular regions of $Hf_{11}Ru_9$-$Nb_{52}V_{28}$ (Figure 4.3J). Consistent with the slope of the solvus line in the binary Hf-Ru phase diagram, a lower Ru content would result in a lower B2 solvus temperature[260]. The regions containing only spherical precipitates had lower Ru contents (3.3 at%) than the regions containing both spherical and cuboidal precipitates (6.9 at% Ru), indicating the spherical particles formed at a lower temperature. Therefore, due to their higher precipitation temperature, the cuboidal precipitates were aged longer during cooling. The evolution from spherical to cuboidal precipitates with aging is similar to the morphological changes experienced by coherent γ' precipitates in Ni superalloys and is highly indicative of a low misfit between the HfRu-B2 phase and the BCC matrix[267]. The cuboidal morphology also suggests that the BCC and HfRu-B2 phases have a cube-cube orientation relationship, given by $\{100\}_{BCC}//\{100\}_{B2}$ and $<010>_{BCC}//<010>_{B2}$. This is confirmed in Ch. 5 and consistent with the orientation relationships observed for cuboidal (Al,Ti,Zr)-B2's in other RMPEAs[152] and Cr alloys with NiAl-B2 precipitates[146].

4.4.3 Comparison between Hf and other Ru-B2 formers

The HfRu-B2 phase is highly thermally stable. With 9 at% additions of Ru, the HfRu-B2 solvus temperature lies above 1750 °C in all alloys investigated. While the dissolution of the B2 phase was not directly observed in $Hf_{11}Ru_9$-$Nb_{52}V_{28}$ due to its exclusion from the 1900 °C anneal, the higher Ru solubility and lower B2 volume fraction at 1750 °C compared to the other alloys indicates the B2 solvus temperature also lies between 1750 and 1900 °C. This is significantly higher then the solvus temperatures achievable by (Al,Ti,Zr)-B2's, which are currently limited below 1200 °C.

The solvus temperatures of other Ru-B2 phases in various refractory matrices have recently been reported, including TiRu and AlRu[261]. HfRu appears to be the most thermally stable of the Ru-B2 phases, with additions of Hf resulting in higher solvus temperatures compared to Ti and Al at equivalent Ru concentrations. For example, with 15 at% Ru, the HfRu phase was reported to be stable at 1900 °C in all investigated matrices while the TiRu solvus temperature ranged between 1300-1900 °C[261]. In this investigation, reducing the Ru concentration to 9 at% was necessary to reduce the solvus temperature below 1900 °C. AlRu is the least thermodynamically stable, only forming B2 in Mo-containing matrices and forming deleterious sigma phases in the presence of Nb or Ta[261], which are the desired matrix elements. Hf additions therefore reduce the amount of Ru necessary to achieve B2 phases that are thermally stable above 1300 °C in Nb-based alloys, which is desirable due to the high cost of Ru[268].

However, the stability of the HfRu-B2 phase is not sufficient to completely suppress the formation of potential deleterious phases. At 1300 °C, two additional phases, one Hf-rich and one V-rich, were present in $Hf_{11}Ru_9$-$Nb_{52}V_{28}$ and minor Hf-rich phases were present in $Hf_{11}Ru_9$-$Mo_{28}Nb_{22}Ta_{30}$ and $Hf_{11}Ru_9$-$Mo_{28}Nb_{52}$. While the observed tertiary phase populations were minor, their preferential nucleation on the grain boundaries could result in degradation of mechanical properties if not properly controlled[91, 87].

4.5 Conclusions

In conclusion, in all investigated matrices, the HfRu-B2 phase is stable to temperatures above 1750 °C with additions of ≥ 9 at% Ru. At 1300 °C, minor tertiary phases develop in all three alloys. Only the BCC and HfRu-B2 phases appear stable above 1600 °C. In comparison to other Ru-B2 formers like Al and Ti, Hf produces the most thermally stable B2 phase and can achieve higher soluvs temperatures with lower Ru contents[261]. The lattice parameter of the B2 phase remains close to that of the binary HfRu-B2 phase, allowing a weighted average of the constituent lattice parameters to be used to develop alloys with low misfit between the B2 and BCC phases. The coherent HfRu-B2 precipitates in $Hf_{11}Ru_9$-$Nb_{52}V_{28}$ evolve from spherical to cuboidal morphologies with increasing aging time, which is consistent with the coarsening behavior of γ' precipitates in Ni superalloys[267]. Overall, HfRu-based B2 phases appear promising for the development of Nb-based BCC + B2 alloys with coherent precipitates that are thermally stable above 1300 °C.

Chapter 5

Solvus Temperatures of HfRu and ZrRu precipitates in Nb-based Alloys

In this chapter, design guidelines for Nb-based alloys strengthened by Ru-B2 precipitates are developed. For that purpose, a series of Nb-based alloys with coherent (misfit $\leq 0.5\%$) HfRu- and ZrRu-B2 precipitates were investigated to determine the dependence of phase stability, misfit, and solvus temperatures on composition. Sequential anneals from 1000-1500 °C were used to determine the B2 solvus temperature ($T_{s,B2}$) of each alloy and solvus lines were constructed for each system. For alloys with $T_{s,B2}$ above 1200 °C, additional anneals at 1000 and 1200 °C provide insight into B2 volume fractions and tertiary phase formation with varying temperature. HfRu is found to be more thermally stable than ZrRu, with Hf-based alloys demonstrating higher $T_{s,B2}$s at equivalent Ru concentrations and smaller populations of tertiary phases at the grain boundaries. Implications for the design of Nb-based alloys with Ru-B2 precipitates are discussed throughout, including strategies to mitigate deleterious phase formation and increase B2 solvus temperatures.

5.1 Introduction

Through the investigations in Chs. 2-4, the HfRu-B2 phase has been shown to be a highly stable phase that forms in many multi-component solutions. A number of desirable properties have been demonstrated, including: (i) B2 phase stability at temperatures above 1300 °C, (ii) the presence of solution-and-aging pathways when the Ru concentration is reduced from equiatomic concentrations, and (iii) a tailorable misfit between the BCC and B2 phases. However, the relationships between significant attributes such as Ru concentration, B2 volume fraction, and B2 solvus temperature have yet to be defined. Therefore, the investigation described in this chapter sought to develop design guidelines for Nb-based alloys strengthened by Ru-B2 precipitates.

In this investigation, a series of Nb-based alloys with coherent HfRu- and ZrRu-B2 precipitates were synthesized to investigate the dependence of phase stability, misfit, and solvus temperatures on composition. The selected alloys were characterized in both the arc melted and annealed conditions by scanning electron and transmission electron microscopy. After homogenization at 1600 °C, sequential anneals were performed to determine the solvus temperature of each alloy and solvus lines from 1000 °C to 1400 °C were constructed for each system. For alloys with solvus temperatures above 1200 °C, additional anneals at 1000 °C and 1200 °C provide insight into variations in B2 volume fraction and tertiary phase formation with temperature. HfRu-B2 was found to be more stable than ZrRu-B2, demonstrating higher solvus temperatures at equivalent Ru additions. In addition to the ZrRu-B2 phase, the Zr-containing alloys also formed significant populations of Zr- and V-rich phases at the grain boundaries and grain interiors. Small additions of Hf to Zr-containing alloys result in an increased solvus temperature, an increased volume fraction of the B2 phase, and significant suppression of the tertiary phases. Design principles for Nb-based alloys with Ru-B2 precipitates are discussed throughout.

5.2 Alloy Selection

For reference, all the relevant lattice parameters have been collected in Table 5.1. For a Nb-based alloy with target operating temperatures between 1300-1500 °C, Hf and Zr are the most desirable Ru-B2 formers. The binary HfRu- and ZrRu-B2 phases have the largest lattice parameters of the known Ru-B2 phases (where $a_{HfRu} = 3.225$ Å[187] and $a_{ZrRu} = 3.253$ Å[188]) and therefore have the lowest lattice misfit with Nb. Furthermore, Hf and Zr have the lowest Ru solubilities of the B2-forming refractory metals, suggesting higher volume fractions and higher solvus temperatures can be achieved with smaller additions of Ru. This assumption has already been shown to be accurate for HfRu in comparison to TiRu and AlRu, but the thermal stability of ZrRu has yet to be evaluated.

HfRu- and ZrRu-B2 have a misfit of -2.3 % and -1.5 %, respectively, with pure Nb (Eq. 1.1). Of the remaining refractory elements that have lattice parameters smaller than both Nb and the selected B2 phases (Figure 5.1), only V is not detrimental to the tensile ductility of the matrix[191, 275, 47, 276]. Al could also reduce the lattice parameter of the Nb matrix [262, 263] while improving oxidation resistance, but Al has a tendency to form deleterious phases with Nb and Zr[110, 261] and would likely reduce the lattice parameter of the resulting B2 phase due to the small lattice parameter of AlRu ($a_{AlRu} \approx 3.0$ Å). For these reasons, the following quaternary systems were selected for this investigation: (X)Ru-B2 (X = Hf,Zr) + (Nb,V)-BCC.

Specific compositions within the quaternary systems were selected to probe the relationship between Ru concentration and the resulting B2 solvus temperatures ($T_{s,B2}$) in a Nb-based matrix. Once a Ru concentration was selected, an excess 1 at% of Hf and

Table 5.1: Structure, enthalpy of formation (ΔH_f), and lattice parameters (a, c) of selected binary *B2* (CsCl, Pm$\bar{3}$m) intermetallics and pure metals.

Phase	Structure	a (Å)	c (Å)	Source	ΔH_f (kJ/mol)	Source
Hf	α-HCP	3.1946	5.051	[269]	-	-
	β-BCC	3.610	-	[269]	-	-
Ru	α-HCP	2.7058	4.2816	[185]	-	-
	β-BCC	2.9775^a	-	[181]	-	-
Ti	α-HCP	2.9506	4.6835	[196]	-	-
	β-BCC	3.30165	-	[196]	-	-
Zr	α-HCP	3.23217	5.1476	[188]	-	-
	β-BCC	3.609	-	[188]	-	-
Cr	BCC	2.878	-	[144]	-	-
Mo	BCC	3.147	-	[264]	-	-
Nb	BCC	3.301	-	[181]	-	-
Ta	BCC	3.303	-	[184]	-	-
V	BCC	3.026	-	[265]	-	-
W	BCC	3.1648	-	[144]	-	-
AlRu	B2	2.9915-3.036	-	[196]	-54.5	[270]
HfRu	B2	3.225	-	[187]	-91.8	[244]
NbRu	B2	3.184	-	[182]	-9.0,-0.7	[201, 271]
TaRu	B2	3.1870	-	[184]	-	-
TiRu	B2	3.060-3.070	-	[185]	-77.0	[244]
SiRu	B2	2.913	-	[197]	-58.1	[272]
VRu	B2	2.986-3.000	-	[273, 274]	-	-
ZrRu	B2	3.253	-	[188]	-68.7	[244]

[a]: lattice parameter of the BCC structure extrapolated from the experimental Nb-Ru lattice parameters

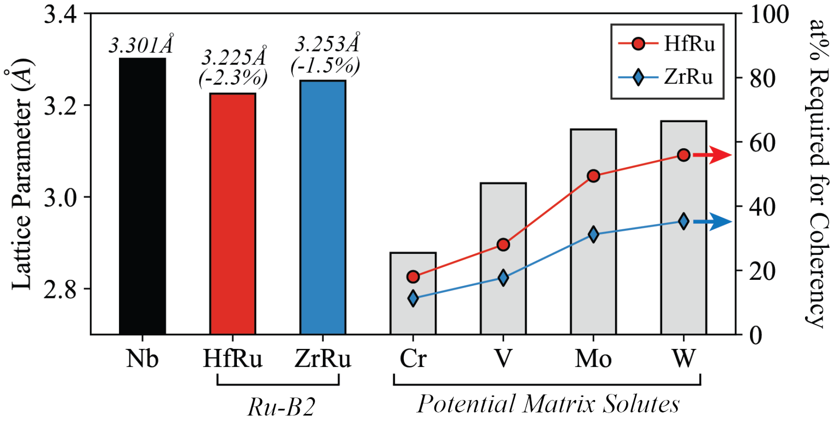

Figure 5.1: Lattice parameter analysis of potential Ru-B2 phases and matrix solutes for Nb-based alloys. The misfit between HfRu- and ZrRu-B2 and Nb are given below the respective lattice parameters. Ta and β-Ti have equivalent lattice parameters to Nb and are therefore excluded. The matrix composition necessary to make Nb coherent with the HfRu-B2 phase (red line) and the ZrRu-B2 phase (blue line) are superimposed on the potential refractory alloying elements. This analysis uses the lattice parameters present in Table 5.1 and a weighted average of the constituent lattice parameters. Readers should note that the desired composition of the matrix (represented here) and the overall composition of the alloy are not necessarily equivalent.

Zr was added (i.e. the concentration of Hf/Zr is equal to 1 + the concentration of Ru). It was hypothesized that this would reduce the amount of Ru remaining in the matrix and maximize B2 volume fraction. To determine the V concentration desired for the matrix, a weighted average of the constituent binary lattice parameters was used. The prior investigations in Chs. 2-4 have found that the lattice parameter of HfRu-B2 does not change significantly when in equilibrium with various BCC matrices. This approach also successfully produced cuboidal precipitates in $Hf_{11}Ru_9$-$Nb_{62}V_{28}$ in Ch. 4. Following the same approach, the matrices of Hf-containing alloys require ≈ 28 at% V and of Zr-containing alloys require ≈ 18 at% V to achieve coherency. The ideal V concentrations for the matrices were used to set the target V concentrations for the overall alloy compositions- enrichment of V in the matrix due to partitioning at higher B2 volume fractions was not considered. It was also assumed that equilibrium concentrations of Hf, Zr, and Ru remaining in the matrix would not significantly effect the matrix lattice parameter- the large BCC lattice parameters of Hf and Zr ($a_{\beta-Hf/Zr} \approx 3.6$ Å) would be balanced by the small BCC lattice parameter of Ru ($a_{\beta-Ru} = 2.978$ Å).

As the solvus temperature of a Hf-containing alloy with 9 at% Ru has already been determined in Ch. 4, two alloys were investigated for the Hf system and three alloys were investigated for the Zr system. Because the V contents were fixed for each system, alloys are referred to by their concentration of β' formers (i.e. $Hf_{11}Ru_9$-$Nb_{52}V_{28}$ is denoted as $Hf_{11}Ru_9$). To investigate the HfRu-B2 solvus line, two alloys were investigated:

1. Hf_3Ru_2-$Nb_{67}V_{28}$ (Hf_3Ru_2)
2. Hf_5Ru_4-$Nb_{63}V_{28}$ (Hf_5Ru_4)

For the ZrRu-B2 solvus line, three Zr-containing alloys were synthesized:

1. Zr_5Ru_4-$Nb_{73}V_{18}$ (Zr_5Ru_4)
2. Zr_8Ru_7-$Nb_{67}V_{18}$ (Zr_8Ru_7)
3. $Zr_{10}Ru_9$-$Nb_{63}V_{18}$ ($Zr_{10}Ru_9$)

Hf_5Ru_4, Zr_5Ru_4, and $Zr_{10}Ru_9$ were the first alloys to be characterized and their results utilized to choose subsequent alloys. Finally, $Hf_2Zr_8Ru_9$-$Nb_{63}V_{18}$ ($Hf_2Zr_8Ru_9$) was synthesized to probe the effect of Hf additions to the less thermally stable ZrRu-B2.

5.3 Methods

An ingot of each alloy composition was arc melted from elemental raw materials with purities $\geq$ 99.0 %. Excess Ru powder was included to compensate for Ru loss from the final composition. The raw material was arranged from top to bottom in order of melting point, except for the Ru powder which was placed on the bottom.

Melting was performed on a water-cooled copper hearth in an inert Ar atmosphere. A Ti getter was included and melted prior to each melting cycle. After arc melting, bulk compositions of each ingot were determined via wavelength dispersive x-ray fluorescence spectroscopy (WDXRF) with a Rigaku ZSX Primus IV instrument (Table 5.2). O and N concentrations were determined via inert gas fusion and the testing was perfromed by either ATI (Hf_5Ru_4, Zr_5Ru_4, $Zr_{10}Ru_9$) or Northern Analytical, Inc (Hf_3Ru_2, Zr_8Ru_7). Additional measurements of the bulk Ru content of Hf_3Ru_2 and Zr_8Ru_7 were made via standardized electron probe microanalysis (EPMA) equipped with wavelength-dispersive spectroscopy (Cameca SX-100) and with inductively coupled plasma optical emission spectroscopy (ICP-OES). The ICP-OES was performed by Northern Analytical, Inc. Bulk composition was estimated with EPMA using a focused beam (20 kV at 10 nA) to average at least 100 analysis points per sample. A rectangular array of grid points was used and covered multiple mm of the sample. All elements were quantified against pure element standards, with counting times of 40 s on peak and 40 s off peak for each element. These additional measurements are reported in Table 5.3.

Table 5.2: Chemical composition (at%), interstitial contents (ppmw), and calculated density, ρ_{calc} (g/cm^3), of the bulk as-cast alloys.

Alloy	Hf	Zr	Ru	Nb	V	O	N	ρ_{calc}
Hf_3Ru_2-$Nb_{67}V_{28}$	3.0	-	1.7	69.0	26.3	442	22	8.10
Hf_5Ru_4-$Nb_{63}V_{28}$	5.2	-	4.2	64.6	26.1	360	45	8.27
Zr_5Ru_4-$Nb_{73}V_{18}$	-	4.6	3.9	74.1	17.4	330	47	8.18
Zr_8Ru_7-$Nb_{67}V_{18}$	-	5.8	6.4	70.9	16.9	487	21	8.23
$Zr_{10}Ru_9$-$Nb_{63}V_{18}$	-	9.7	8.4	64.6	17.3	380	30	8.27
$Hf_2Zr_8Ru_9$-$Nb_{63}V_{18}$	2.2	7.9	8.5	64.6	16.8	420	34	8.40

All annealing treatments were performed in a Vacuum Industries resistive furnace. Samples were wrapped in Ta foil. For annealing temperatures below 1200 °C, samples were also placed on a NbTi sheet and an additional Ti getter was included. Samples were heated at a rate of 15 °C/min and cooled at the maximum rate of the furnace.

Table 5.3: Ru concentrations (wt%) of selected alloys as determined by various methods.

Alloy	Nominal	ICP-OES	WDXRF	EPMA	SEM-EDS
Hf_3Ru_2-$Nb_{67}V_{28}$	2.4	1.84	2.0	1.84	1.2
Zr_8Ru_7-$Nb_{67}V_{18}$	8.2	7.28	7.5	7.10	7.3

The estimated peak cooling rate was 270 °C/min. Unless otherwise specified, all samples were solutioned at 1600 °C for 20 h prior to subsequent annealing treatments. Annealing treatments with a target temperature $\leq$ 1100 °C had a duration of 200 h; anneals with a target temperature from 1200-1400 °C had a duration of 40 h; and annealing treatments with a target temperature $\geq$ 1500 °C had a duration of 20 h.

Sample microstructures were investigated using scanning electron microscopy (SEM). Samples surfaces were prepared by mechanical and vibratory polishing. Backscatter electron (BSE) and secondary electron (SE) micrographs were acquired with a ThermoFisher Apreo C microscope and a ThermoFisher Apreo S microscope. Energy dispersive X-ray spectroscopy (EDS) with an EDAX Si-drift EDX detector in the Apreo C was used to acquire site specific chemical composition information. Further characterization of grain boundary phases in Hf_5Ru_4 and $Zr_{10}Ru_9$ after aging at 1000 °C was performed using transmission electron microscopy (TEM). Thin foils were lifted from each sample using the FIB lift-out method with a Ga^+ ion beam in a FEI Helios Dualbeam Nanolab 600 equipped with an OmniProbe. TEM was conducted in a FEI Talos F200X S/TEM operated at 200kV. For each phase present in the foil, selected area diffraction patterns (SADP) were captured, and EDS was performed using a SuperX detector and Velox software[1].

For each annealing temperature where a B2 phase was present, at least 20 SE micrographs were used to determine the B2 volume fraction and particle size distributions. For annealing temperatures $\geq$ 1100 °C, the B2 particles were segmented in FIJI using a

---

[1] The foils were prepared and characterized by Kaitlyn Mullin.

binary intensity threshold[198]. The B2 volume fraction and particle size distributions were determined using the analyze particle functions in FIJI. For the 1000 °C micrographs, the B2 particles were segmented using the U-Net machine learning architecture, a state-of-the-art convolutional neural network designed for semantic segmentation [277]. With a relatively small training data requirement and high classification accuracy, U-Net has demonstrated significant success identifying features of interest within the biomedical imaging and electron microscopy fields [278, 279, 280]. For each sample, a U-Net model was trained on two manually annotated 3072x2042 pixel SE images (manual annotation performed in FIJI). The models were trained using a maximum of 40 epochs, a batch size of 16, the Adam optimizer, a sigmoid activation function, and a Binary Focal Crossentropy loss function, all of which were implemented using Tensorflow / Keras 2.10.1 and Python 3.9.18. Once trained, the model outputs a mask of the B2 particle locations based on the provided image. Finally, all 1000 ºC micrographs were passed to the model and subsequently post-processed in FIJI using the analyze particles functions to determine the volume fractions and particle radii. Example inputs and outputs of the U-Net models are provided in Supplemental Figure 1. To estimate the volume fractions of the Zr- and V-rich phases present in $Zr_{10}Ru_9$-$Nb_{63}V_{18}$ after aging at 1300 °C for 40 h, the point counting method according to ASTM standard E562 19e1 was used [230].

To assist with phase identification, X-ray diffraction (XRD) patterns of all samples were obtained with a Panalytical Empyrean Powder Diffractometer using Cu Kα radiation (λ = 0.154nm). Samples were mechanically polished to 320 grit or better prior to XRD. Lattice parameters were determined by Bragg's Law from the peak positions. Vickers hardness values for the annealed samples were determined from at least 9 indents placed with weights ranging from 1-2 kg.

5.4 Results

Sequential annealing experiments to determine the B2 solvus temperatures were performed on each alloy and ranged in temperature from 1000 to 1500 °C. DTA was not performed due to concerns about the reactivity of the alloys with the crucibles. For alloys with B2 solvus temperatures above 1200 °C, additional aging treatments were performed at 1000 and 1200 °C. Microstructures were characterized by SEM and B2 volume fractions and particle size distributions are reported for each condition. In most conditions, the alloys form homogeneous distributions of spherical B2 precipitates, with some alloys also demonstrating concurrent formation of Hf-, Zr-, and V-rich tertiary intermetallic phases at the grain boundaries and in some cases grain interiors. To determine the misfit between the B2 and BCC phases and allow further identification of the grain boundary phases, TEM liftouts were taken from grain boundaries in the samples annealed at 1000 °C.

5.4.1 XRD

The XRD patterns did not change appreciably with different heat treatments and only representative scans are provided in Figure 5.2. All scans contained peaks associated with a disordered BCC phase. Some samples exhibited additional peaks associated with B2 ordering and the presence of HfO_2 and ZrO_2. The calculated BCC lattice parameters were in the range of 3.225-3.257 Å for Hf-containing alloys and 3.251-3.263 Å for Zr-containing alloys.

5.4.2 As-cast microstructures of HfRu-B2 Alloys

The Hf-containing alloys solidify as disordered BCC alloys with the segregation of Hf, Ru, and V to the inter-dendritic regions (Figure 5.3). In Hf_5Ru_4, chains of HfRu-

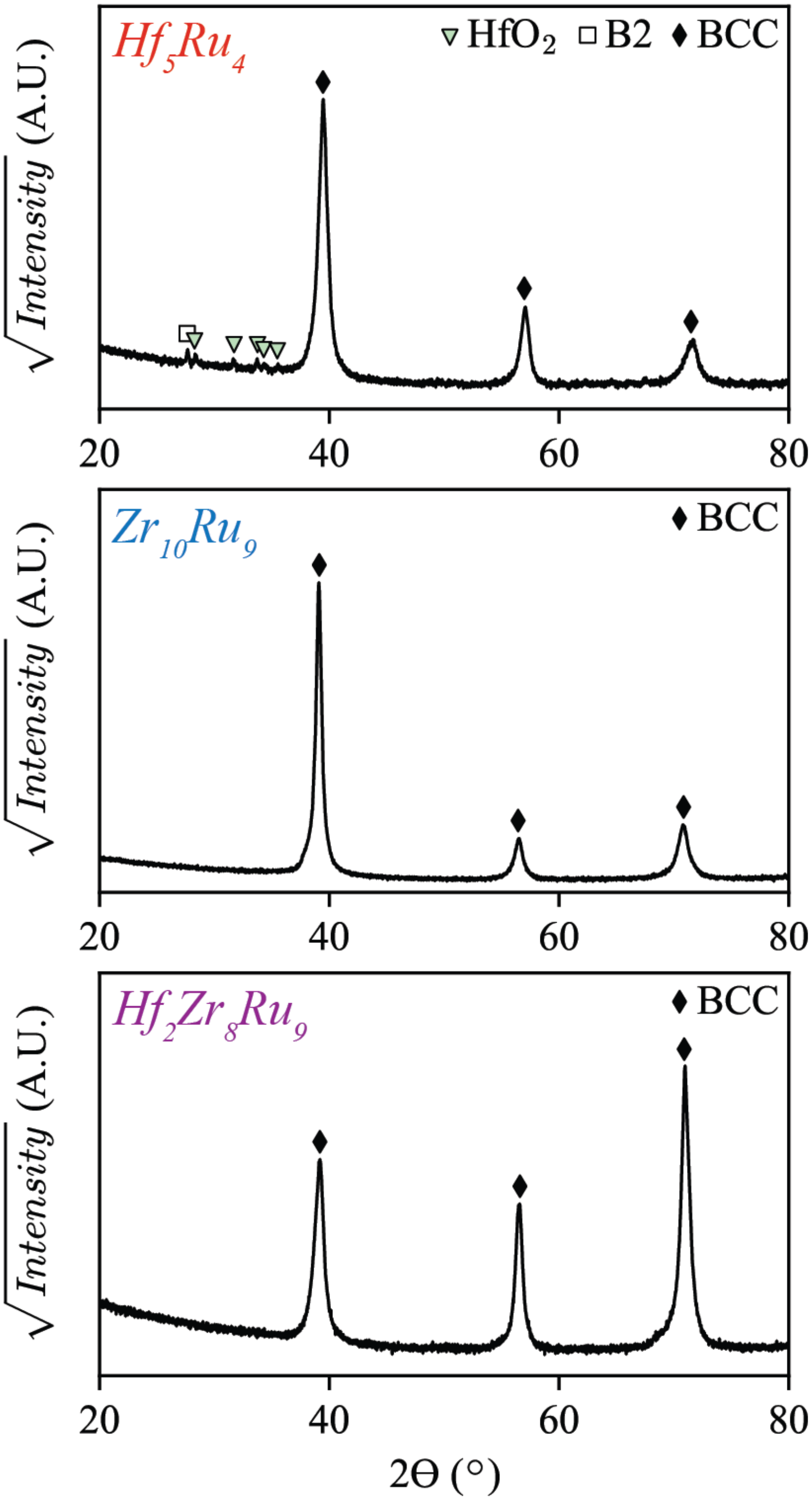

Figure 5.2: XRD patterns of (top) Hf_5Ru_4, (center) $Zr_{10}Ru_9$, (bottom) $Hf_2Zr_8Ru_9$ after homogenization at 1600 °C for 20 h and aging at 1000 °C for 200 h.

B2 are present at the center of some inter-dendritic regions; smaller HfRu-B2 particles formed adjacent to the coarser chains and decrease in size towards the center of the intra-dendritic regions (Figure 5.3D, F.). A small quantity of a V-rich phase, V1, is present within the HfRu-B2 chains. With decreasing Hf and Ru content, the inter-dendritic regions no longer form HfRu-B2 and V1. The overall microstrutures are very similar to the as-cast microstructure of $Hf_{11}Ru_9$-$Nb_{62}V_{28}$ (Ch. 4, Figure 4.1).

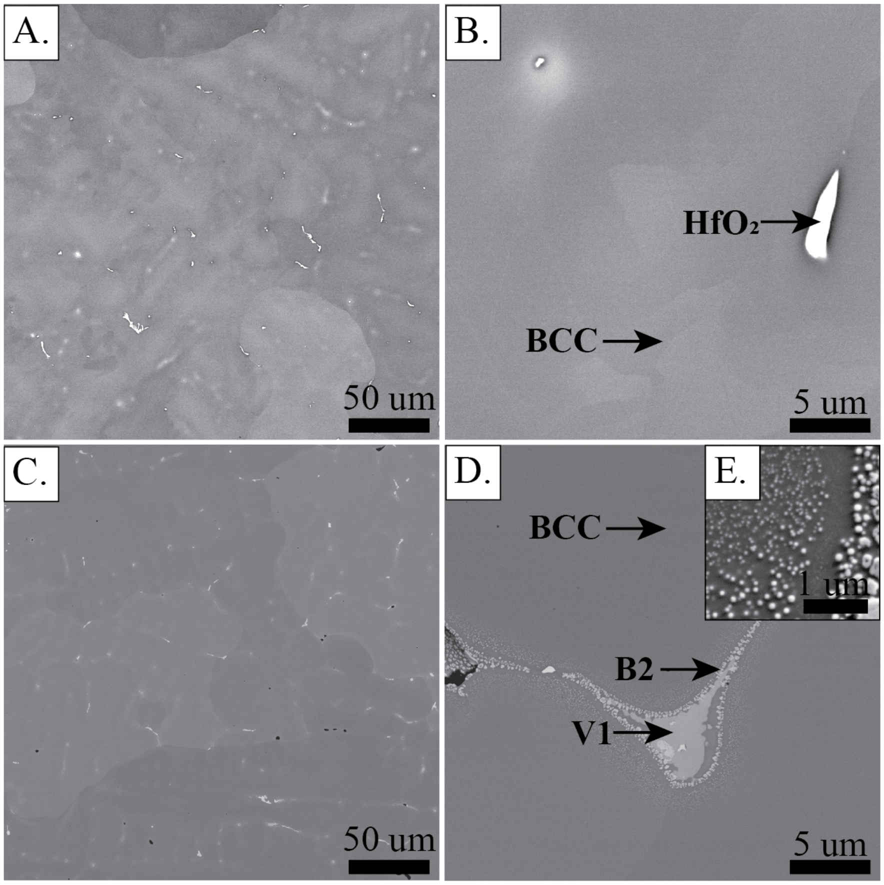

Figure 5.3: As-cast microstructures of the Hf-containing alloys. A, B. BSE micrographs of Hf_3Ru_2. C., D. BSE and E. SE micographs of Hf_5Ru_4. E. is a higher magnification view of the inter-dendritic regions in D. Both alloys solidify dendritically with segregation of Hf, Ru, and V to the inter-dendritic regions. Within Hf_5Ru_4, the segregation results in the formation of HfRu-B2 particles and a light grey V-rich phase (V1). Only bright grains of HfO_2 are found in the inter-dendritic regions of Hf_3Ru_2.

5.4.3 As-cast microstructures of ZrRu-B2 Alloys

The Zr-containing alloys also solidify as dendritic BCC alloys, with the segregation of Ru, V, and Zr to the inter-dendritic regions (Figure 5.4). In all Zr-containing alloys, two phases formed within the the inter-dendritic regions: P1, a near equiatomic phase rich in all elements, and P2, a small phase that is black in BSE contrast and rich in Zr and O. Due to the high O content, P2 appears to be small grains of ZrO_2. No particles of ZrRu-B2 are visible. With decreasing Zr and Ru content, the P1 and ZrO_2 phases reduce in quantity but are still present.

5.4.4 Determination of solvus temperatures from 1000-1400 °C

To determine the B2 solvus temperature ($T_{s,B2}$) range of the selected alloys, sequential annealing experiments were performed. The range is defined by the lowest temperature where B2 was not observed (a solutioning temperature) and the highest annealing temperature where B2 was observed (an aging temperature). All alloys were homogenized at 1600 °C for 20 h prior to lower temperature anneals. The microstructures after homogenization and sequential anneals are shown in Figure 5.5; the microstructures of the alloys that did not form B2 are not shown. It is apparent that the rate of cooling in the vacuum furnace was not fast enough to fully suppress B2 formation on cooling from 1400-1600 °C, resulting in fine-scale phase separation in the matrices. Smaller grain boundaries phases, including coarser B2 grains and a thin dark phase in Zr_8Ru_7 and $Zr_{10}Ru_9$, were also likely not present at 1400-1600 °C and formed on cooling. The compositions of the observed phases as measured by SEM-EDS are recorded in Table 5.4.

Hf_5Ru_4, the Hf-containing alloy with the highest Ru content, has a $T_{s,B2}$ range from 1300-1400 °C (Figure 5.5A-D). At 1300 °C, the HfRu-B2 precipitates are uniformly distributed and spherical with an average radius of 137 ± 27 nm. Some subgrain boundaries

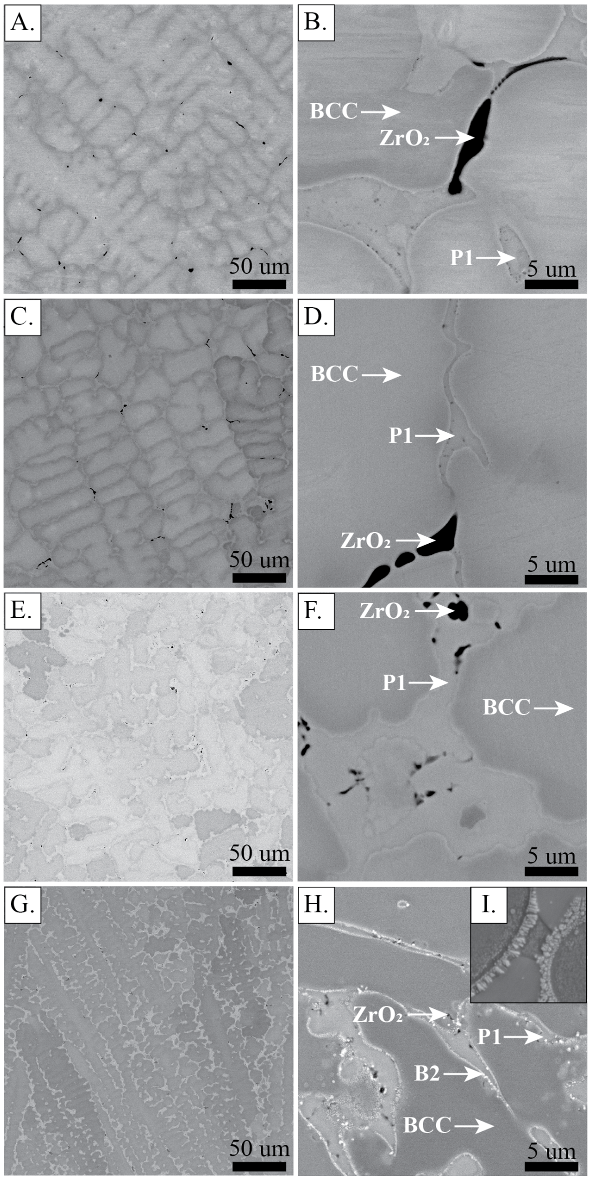

Figure 5.4: As-cast microstructures of the Zr-containing alloys. BSE micrographs of A., B. Zr_5Ru_4, C., D. Zr_8Ru_7, E., F. $Zr_{10}Ru_9$ and G., H. $Hf_2Zr_8Ru_9$. I. Higher magnification SE micrograph of the inter-dendritic regions of $Hf_2Zr_8Ru_9$. All alloys solidified dendritically with the segregation of Hf, Ru, V, and Zr to the inter-dendritic regions. The segregation results in the formation of a light grey near-equiatomic phase (P1) within the inter-dendritic regions; additionally, $Hf_2Zr_8Ru_9$ forms layers of a (Hf,Zr)Ru-B2 phase that outlines the P1 phase. Black grains of ZrO_2 are also present, with larger particles within the inter-dendritic regions and smaller particles studded within P1.

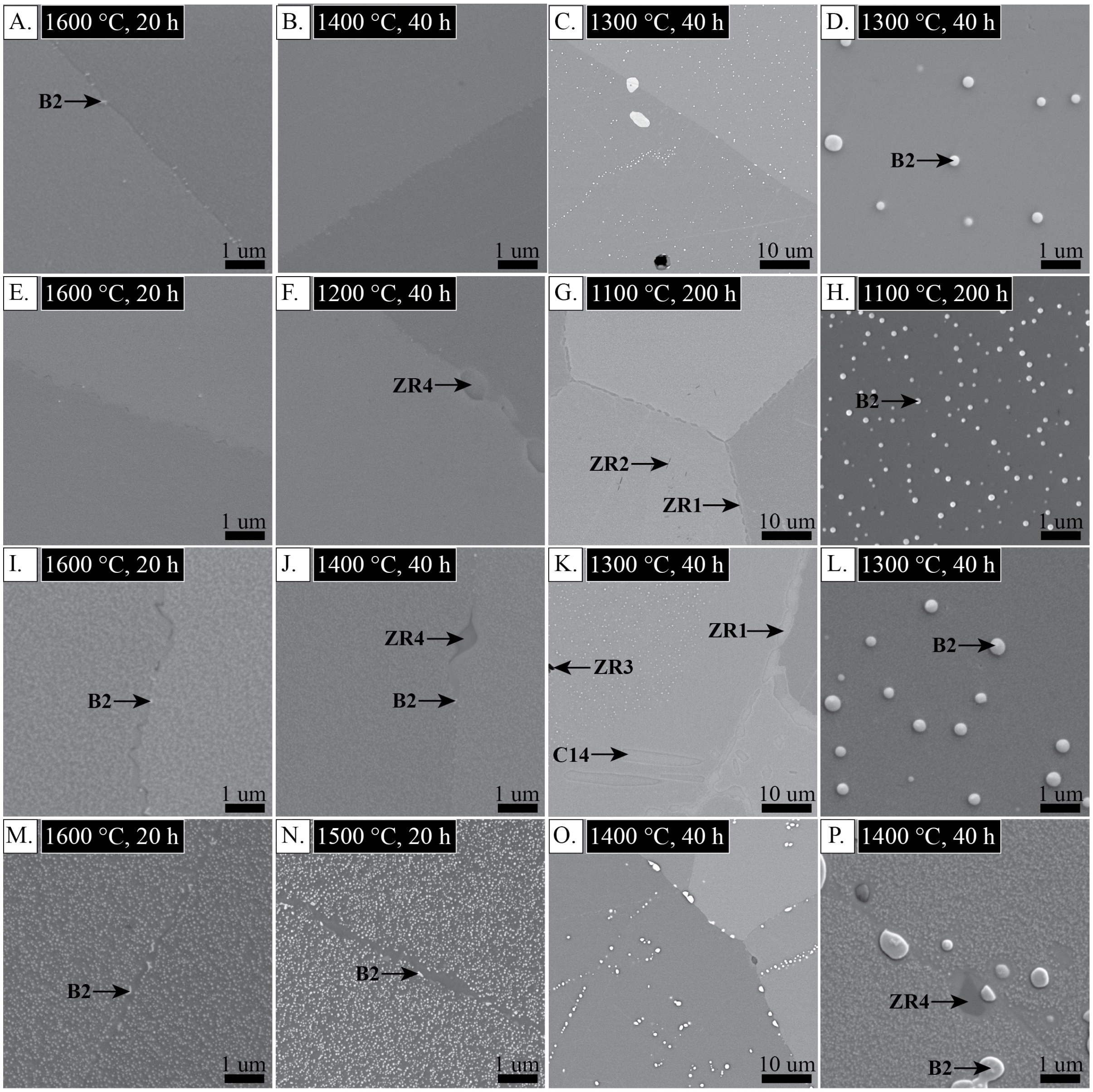

Figure 5.5: Microstructures of B2 forming alloys after sequential annealing treatments. All alloys were homogenized at 1600 °C for 20 h prior to subsequent aging. A-D. Hf_5Ru_4. E-H. Zr_8Ru_7. I-L. $Zr_{10}Ru_9$. M-P. $Hf_2Zr_8Ru_9$. All images are SE micrographs, except for the BSE micrographs in C., G., K., and O. In all conditions, the matrix is a disordered (Nb,V)-BCC phase. When present, the B2 precipitates formed as spherical particles that are brighter in backscatter contrast compared to the matrix. The Zr-containing alloys form the following additional phases: a C14 Laves phase (within grains and on the grain boundaries), ZR1 (within grains and on the grain boundaries), ZR2 (a needle-like phase within the grains), Z3 (a globular dark phase within the grains), and ZR4 (a dark phase on the grain boundaries).

Table 5.4: Chemical compositions (at%) and identified crystal structures of different phases in the annealed samples. Compositions measured by SEM-EDS.

Alloy	Condition	Phase	Prototype	Hf	Zr	Ru	Nb	V
Hf_5Ru_4-$Nb_{63}V_{28}$	as-cast	V1	-	27.0	-	8.3	20.7	44.0
Hf_5Ru_4-$Nb_{63}V_{28}$	1600 °C 20 h 1300 °C 40 h	(Nb,V)-BCC	W	5.3	-	3.2	62.4	29.0
Hf_5Ru_4-$Nb_{63}V_{28}$	1600 °C 20 h 1200 °C 40 h	(Nb,V)-BCC	W	5.0	-	2.4	63.2	29.4
Zr_5Ru_4-$Nb_{73}V_{18}$	as-cast	P1	-	-	37.3	15.1	22.6	25.0
Zr_8Ru_7-$Nb_{67}V_{18}$	as-cast	P1	-	-	30.9	18.7	24.0	26.4
Zr_8Ru_7-$Nb_{67}V_{18}$	1600 °C 20 h 1100 °C 200 h	(Nb,V)-BCC	W	-	6.4	5.2	70.0	18.5
$Zr_{10}Ru_9$-$Nb_{63}V_{18}$	as-cast	P1	-	-	29.0	20.2	24.0	26.8
$Zr_{10}Ru_9$-$Nb_{63}V_{18}$	1600 °C 20 h 1400 °C 40 h	(Nb,V)-BCC	W	-	11.7	8.2	61.5	18.6
$Zr_{10}Ru_9$-$Nb_{63}V_{18}$	1600 °C 20 h 1400 °C 40 h	ZR1	CuAu	-	48.2	20.6	15.3	15.8
$Zr_{10}Ru_9$-$Nb_{63}V_{18}$	1600 °C 20 h 1400 °C 40 h	ZR4	-	-	77.8	0.2	18.2	3.8
$Zr_{10}Ru_9$-$Nb_{63}V_{18}$	1600 °C 20 h 1300 °C 40 h	(Nb,V)-BCC	W	-	10.5	7.7	63.2	18.6
$Zr_{10}Ru_9$-$Nb_{63}V_{18}$	1600 °C 20 h 1300 °C 40 h	ZR1	CuAu	-	47.8	19.9	15.2	17.0
$Zr_{10}Ru_9$-$Nb_{63}V_{18}$	1600 °C 20 h 1300 °C 40 h	C14	$MgZn_2$	-	27.7	20.3	21.5	30.4
$Zr_{10}Ru_9$-$Nb_{63}V_{18}$	1600 °C 20 h 1200 °C 40 h	(Nb,V)-BCC	W	-	8.3	6.3	66.1	19.3
$Zr_{10}Ru_9$-$Nb_{63}V_{18}$	1600 °C 20 h 1200 °C 40 h	ZR1	CuAu	-	45.7	18.1	17.2	18.9
$Zr_{10}Ru_9$-$Nb_{63}V_{18}$	1600 °C 20 h 1200 °C 40 h	C14	$MgZn_2$	-	26.1	18.3	23.5	32.0
$Hf_2Zr_8Ru_9$-$Nb_{63}V_{18}$	as-cast	P1	-	4.7	24.0	18.5	26.2	26.6
$Hf_2Zr_8Ru_9$-$Nb_{63}V_{18}$	1600 °C 20 h 1400 °C 40 h	(Nb,V)-BCC	W	2.3	9.4	8.0	61.4	18.9
$Hf_2Zr_8Ru_9$-$Nb_{63}V_{18}$	1600 °C 20 h 1400 °C 40 h	ZR4	-	13.2	74.1	0.0	10.9	1.8
$Hf_2Zr_8Ru_9$-$Nb_{63}V_{18}$	1600 °C 5 h 1400 °C 40 h	(Nb,V)-BCC	W	2.4	9.6	8.2	61.4	18.4
$Hf_2Zr_8Ru_9$-$Nb_{63}V_{18}$	1600 °C 5 h 1400 °C 40 h	B2	CsCl	19.6	27.5	47.0	4.2	1.8

are decorated with HfRu-B2 particles. When the Ru content is reduced to 2 at% in Hf_3Ru_2, HfRu-B2 is not present down to 1000 °C.

In general, ZrRu-B2 is less thermally stable than HfRu. $Zr_{10}Ru_9$ has a B2 $T_{s,B2}$ range between 1300-1400 °C, equivalent to Hf_5Ru_4 despite the higher Ru content (Figure 5.5I-L). With a decrease in Ru content to 7 at%, the $T_{s,B2}$ falls to between 1100-1200 °C (Figure 5.5E-H); with a further decrease to 4 at% Ru, Zr_5Ru_4 does not form ZrRu-B2 at 1000 °C. When present, the ZrRu-B2 precipitates are spherical and do not decorate grain or subgrain boundaries. The average radius of the ZrRu-B2 precipitates is 53 ± 14 nm at 1100 °C (in Zr_8Ru_7) and 152 ± 33 nm at 1300 °C (in $Zr_{10}Ru_9$).

Unlike the Hf-containing alloys, where only minor amounts of HfO_2 are present on the grain boundaries at 1300 °C, the Zr-containing alloys can form multiple tertiary phases at both the grain boundaries and grain interiors. The number and type of phases vary with alloy and temperature. Four tertiary phases are present in $Zr_{10}Ru_9$ at 1300 °C (Figure 5.5K). At the grain boundaries and intragranular regions are a C14 Laves phase rich in both V and Zr, and ZR1, a Zr-rich phase. Both contain significant concentrations of all alloying elements and are analyzed by TEM in section 5.4.6. Two other Zr-rich phases are only within the grain interiors: ZR2, a thin phase with a needle-like morphology, and ZR3, a small globular phase. The compositions of ZR2 and ZR3 could not be directly measured with SEM-EDS and are distinguished by their morphology. With an increase in temperature to 1400 °C, the C14 Laves phase is no longer present; ZR1 remains at the grain boundaries and intragranular regions; ZR2 and ZR3 remain in the intragranular regions; and an additional Zr-rich phase, ZR4, is found at the grain boundaries (Figure 5.5J). In Zr_8Ru_7 at 1100 °C, the C14 Laves phase and ZR2 needles are present in the intragranular regions and ZR1 is present at the grain boundaries (Figure 5.5G). At 1200 °C, ZR4 is present at the grain boundaries and ZR2 within the grains (Figure 5.5F).

Precipitate free zones (PFZs) that are depleted of B2 particles form adjacent to the tertiary phases and were 10-40 μm wide (measured from the grain boundary).

5.4.5 Aging at 1000 and 1200 °C

At aging temperatures near the $T_{s,B2}$, the B2 volume fractions are low ($v_{f,B2} \approx 1$ %) and most of the Ru remains within the BCC matrix. To investigate the effect of temperature on phase stability and distribution, two further aging treatments were performed on Hf_5Ru_4 and $Zr_{10}Ru_9$: 1000 °C for 200 h and 1200 °C for 40 h (Figure 5.6). The compositions of the observed phases as measured by SEM-EDS are recorded in Table 5.4, and the volume fractions and average radii of the B2 precipitates are recorded in Table 5.5.

At both annealing temperatures, the alloys form a homogeneous distribution of spherical B2 precipitates (Figure 5.6) and the B2 volume fraction increases with decreasing annealing temperature (Figure 5.7). In Hf_5Ru_4, the HfRu-B2 volume fraction increases from 1.1 % at 1300 °C to 8.9 % at 1000 °C. The ZrRu-B2 volume fraction in $Zr_{10}Ru_9$ rises more rapidly, with a volume fraction of 0.9 % at 1300 °C and 18.3 % at 1000 °C. As the B2 volume fraction increases, the Ru concentration of the BCC matrix decreases (Table 5.4).

With decreasing temperature, the average radii of the B2 precipitates also decrease (Figure 5.8A). For both alloys, the average radii roughly double from 1000 °C to 1200 °C, and double again from 1200 °C to 1300 °C. Overall, Hf_5Ru_4 formed smaller B2 precipitates with narrower distributions than $Zr_{10}Ru_9$ at all temperatures.

The Hf-containing alloys and the Zr-containing alloys demonstrate opposite trends with regards to the temperature stability of their respective tertiary phases. Only BCC and B2 phases were present in Hf_5Ru_4 at 1300 °C. At lower temperatures, three additional

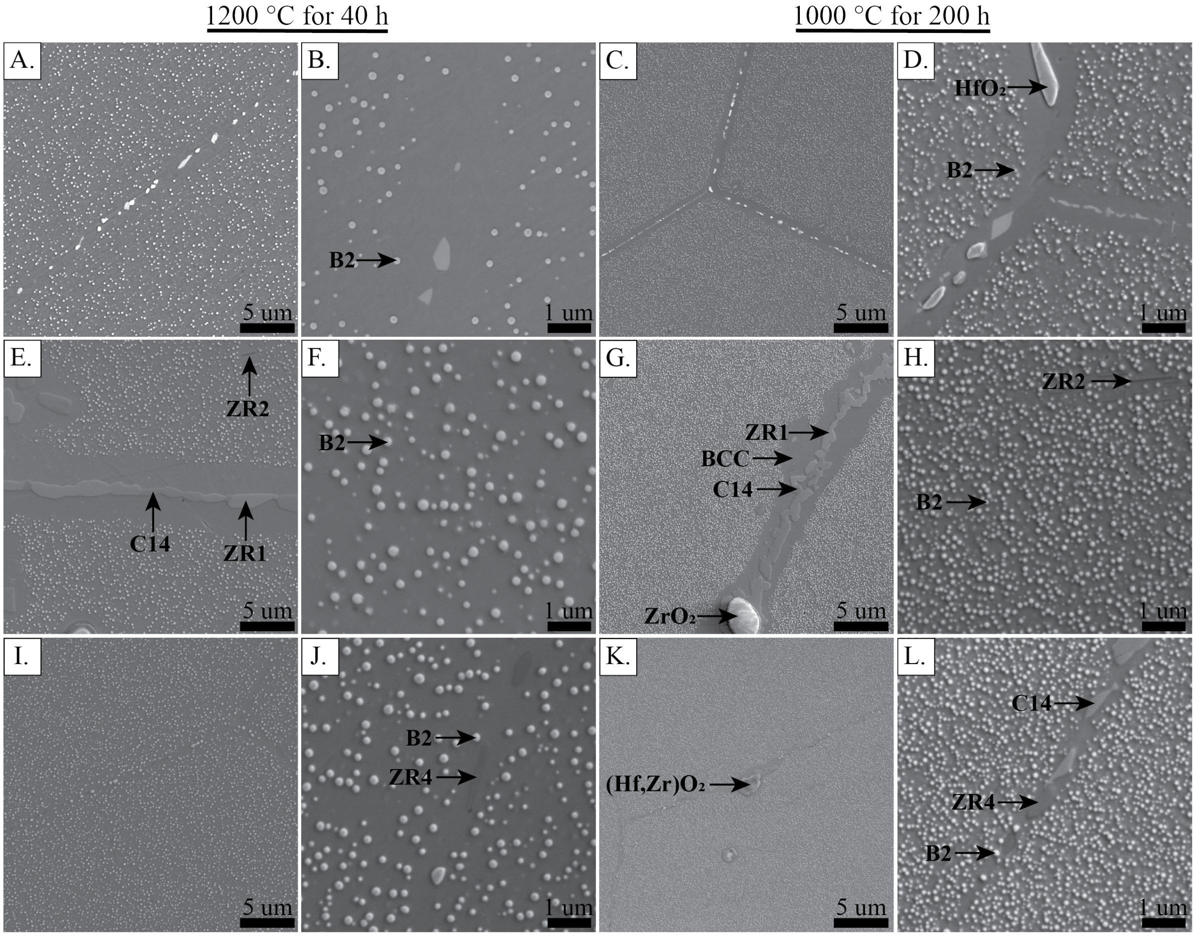

Figure 5.6: SE micrographs of A-D. Hf_5Ru_4, E-H. $Zr_{10}Ru_9$, and I-L. $Hf_2Zr_8Ru_9$ after aging at 1200 °C for 40 h (A-B, E-F, I-J) and 1000 °C for 200 h (C-D, G-H, K-L). All samples were homogenized at 1600 for 20 h prior to aging. In all conditions, the matrix is a disordered (Nb,V)-BCC phase. The B2 precipitates formed as spherical particles and are distributed homogeneously throughout the grain interiors, with no preference for subgrain boundaries. Additional phases are visible at the grain boundaries. In Hf_5Ru_4, two distinct grain boundary phases are present at both temperatures, HF1 (light grey contrast), and P3, a Hf- and V-rich phase (also with light grey contrast). The two phases cannot be distinguished by contrast in SE or BSE micrographs and are left unlabeled. In $Zr_{10}Ru_9$, three additional phases are present. ZR1 and the C14 Laves phase are present both in the grain boundaries and grain interiors. The microstructure regions adjacent to the grain boundary phases are depleted of B2 particles. ZR2 is present as needles within the grains. ZR4 and the C14 Laves are also present in $Hf_2Zr_8Ru_9$ at both temperatures, but their population is significantly decreased compared to $Zr_{10}Ru_9$.

Table 5.5: Volume Fractions ($a_{f,B2}$) and average radii (r_{ave}) of the B2 precipitates in the annealed alloys.

Alloy	Condition	$a_{f,B2}$ (%)	r_{ave} (nm)
Hf_5Ru_4-$Nb_{63}V_{28}$	1300 °C 40 h	1.1 ± 0.2	137 ± 27
Hf_5Ru_4-$Nb_{63}V_{28}$	1200 °C 40 h	2.6 ± 0.1	69 ± 11
Hf_5Ru_4-$Nb_{63}V_{28}$	1000 °C 200 h	8.9 ± 0.5	33 ± 8
Zr_8Ru_7-$Nb_{67}V_{18}$	1100 °C 200 h	2.7 ± 0.2	53 ± 14
$Zr_{10}Ru_9$-$Nb_{63}V_{18}$	1300 °C 40 h[a]	0.9 ± 0.7	152 ± 33
$Zr_{10}Ru_9$-$Nb_{63}V_{18}$	1200 °C 40 h	7.0 ± 0.5	75 ± 17
$Zr_{10}Ru_9$-$Nb_{63}V_{18}$	1000 °C 200 h	18.3 ± 2.0	42 ± 11
$Hf_2Zr_8Ru_9$-$Nb_{63}V_{18}$	1400 °C 40 h	1.9 ± 0.2	$\geq$ 200
$Hf_2Zr_8Ru_9$-$Nb_{63}V_{18}$	1200 °C 40 h	10.2 ± 0.7	76 ± 14
$Hf_2Zr_8Ru_9$-$Nb_{63}V_{18}$	1000 °C 200 h	18.0 ± 1.4	37 ± 8

[a]: The estimated volume fraction of ZR1 was 0.04 ± 0.01 % and of the C14 Laves phase was 0.03 ± 0.01 %

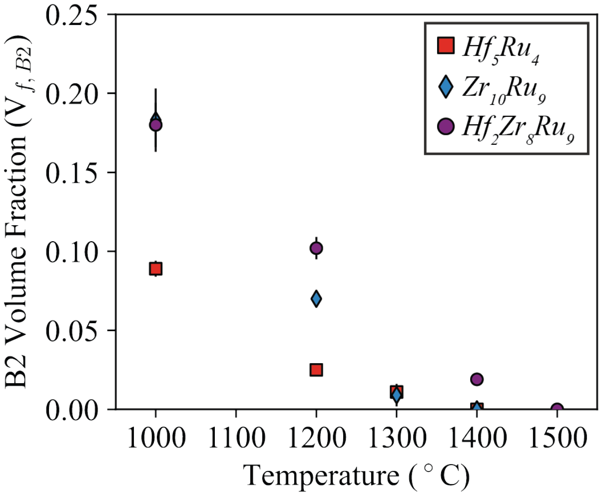

Figure 5.7: B2 volume fractions at different aging temperatures for Hf_5Ru_4, $Zr_{10}Ru_9$, and $Hf_2Zr_8Ru_9$. B2 volume fractions increase with decreasing aging temperature.

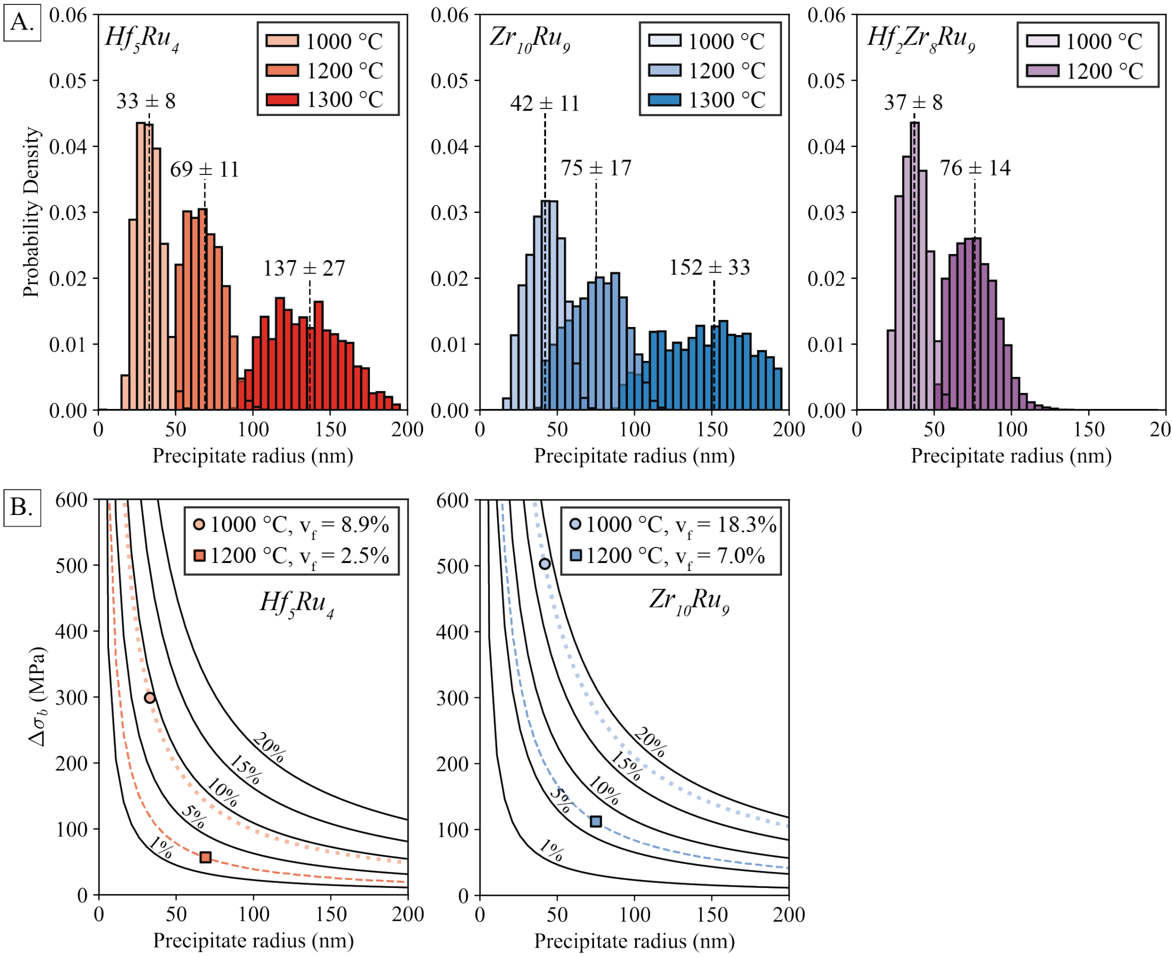

Figure 5.8: A. Distributions of particle radii for (left) Hf_5Ru_4, (center) $Zr_{10}Ru_9$, and (right) $Hf_2Zr_8Ru_9$ at different aging temperatures. Distributions are plotted as probability densities and represent varying numbers of particles. Average particle radius for each distribution is represented by a dashed line and annotated with the value. With increasing temperature, the average radius increases and the distributions widen. B. Predicted change in yield strength with varying particle radius and B2 volume fraction for (left) Hf_5Ru_4 and (right) $Zr_{10}Ru_9$ using the Orowan Bowing mechanism (Eq. 5.4). Theoretical B2 volume fractions (1-20 %) are represented by solid black lines. Predictions using the experimentally measured volume fractions at different aging temperatures are represented by dashed (1200 °C) and dotted (1000 °C) lines; a discrete strength prediction that uses the experimentally measured average radius is marked on each curve.

phases form: HF1, a grain boundary phase rich only in Hf; HF2, a second Hf-rich phase that forms within the grains with a needle-like morphology similar to ZR2; and P3, another Hf-rich phase that is not depleted in V (Figure 5.9A). The density of the grain boundary phases increases from 1200 °C to 1000 °C, and a narrow PFZ forms adjacent to the grain boundary at 1000 °C (Figure 5.6D).

In $Zr_{10}Ru_9$, significant quantities of the C14 Laves phase and ZR1 are still present at the grain boundaries at lower aging temperatures but their prevalence decreased within the grain interiors compared to 1300 °C (Figure 5.9B). The PFZs are also narrower: 1-2 μm wide at 1000 °C and 3-10 μm wide at 1200 °C. ZR2 needles were still present within the grains.

5.4.6 TEM investigations of Hf_5Ru_4 and $Zr_{10}Ru_9$

The tertiary phases could not be identified by XRD due to their low volume fractions. To provide further identification, foils were milled from the grain boundaries of Hf_5Ru_4 and $Zr_{10}Ru_9$ after annealing at 1000 °C and characterized using TEM. Diffraction patterns were also taken of the BCC and B2 phases in order to determine the lattice misfit between the two phases. Compositions and lattice parameters of the phases as measured by TEM-EDS are presented in Table 5.6.

The foil taken from Hf_5Ru_4 captured five phases: the (Nb,V)-BCC matrix, HfRu-B2, HfO_2, HF1, and P3 (Figure 5.10). Other than the oxide, none of the phases demonstrated O or N enrichment. The Hf-rich needles, HF2, that are present in the intragranular regions were not captured. With the improved spatial resolution, HF1 is measured by STEM-EDS to be a nearly pure Hf-rich phase composed of 96 at% Hf; the Ru content is near zero. It is identified as BCC-Hf (β-Hf) (Figure 5.10D). P3 is a ternary phase composed of $\approx$ 37 at% Hf, 36 at% Nb, and 26 at% V; the Ru content is $<$ 1.0 at% Ru.

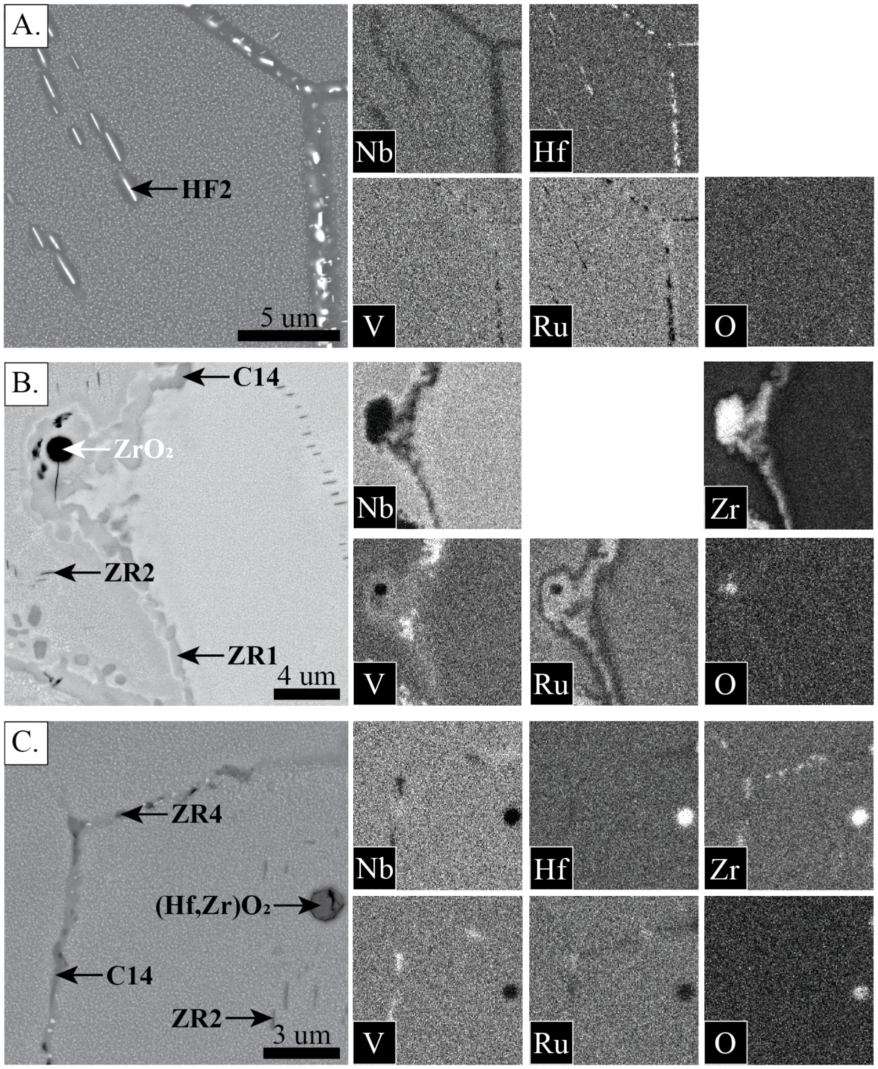

Figure 5.9: EDS mapping of grains boundaries in selected alloys after annealing at 1000 °C for 200 h. A. BSE micrograph (left) and EDS maps (Nb, Hf, V, Ru, and O) of Hf_5Ru_4. Four phases are visible: a (Nb,V)-rich BCC matrix, HF1 (a Hf-rich phase on the grain boundary), HF2 (a Hf-rich phase within the grain that has a needle-like morphology), and P3 (rich in both Hf and V on the grain boundary). It is difficult to distinguish between HF1 and P3 and they are left unlabeled. B. BSE micrograph (left) and EDS maps (Nb, Zr, V, Ru, and O) of $Zr_{10}Ru_9$. Five phases are visible: a (Nb,V)-rich BCC matrix, ZrO_2 (rich in O and Zr), ZR1 (rich in Ru and Zr on the grain boundary), ZR2 (needles present within the grain in the BSE micrograph but not in EDS maps), and a C14 Laves phase (rich in Ru, V, and Zr on the grain boundary). C. BSE micrograph (left) and EDS maps (Nb, Hf, Zr, V, Ru and O) of $Hf_2Zr_8Ru_9$. Five phases are visible: a (Nb,V)-rich BCC phase, $(Hf,Zr)O_2$ (rich in Hf, O, and Zr), ZR4 (rich in Zr on the grain boundaries), ZR2 (needles present within the grain in the BSE micrograph but not in EDS maps), and a C14 Laves phase (rich in Ru, V, and Zr on the grain boundaries).

Table 5.6: Identified crystal structures, their lattice parameters (Å), and measured compositions (at%) of different phases in samples aged at 1000 °C for 200 h. Compositions measured by STEM-EDS.

Alloy	Designation	Phase	Prototype	a	b	c	Hf	Zr	Ru	Nb	V
Hf_5Ru_4-$Nb_{63}V_{28}$	(Nb,V) Matrix	BCC	W	3.259	-	-	1.8 ± 0.3	-	0.8 ± 0.1	68.3 ± 3.0	29.1 ± 2.8
	HfRu	B2	CsCl	3.275	-	-	[a]	-			
	HF1	BCC	W	3.299	-	-	96.3 ± 0.5	-	0.0 ± 0.0	2.8 ±0.4	0.9 ± 0.1
	P3	P	$Cr_9Mo_{21}Ni_{20}$	5.234	7.855	13.081	37.2 ± 3.0	-	0.9 ± 0.1	35.5 ± 3.2	26.4 ± 2.0
$Zr_{10}Ru_9$-$Nb_{63}V_{18}$	(Nb,V) Matrix	BCC	W	3.295	-	-	-	3.5 ± 0.6	3.3 ± 0.5	77.3 ± 2.3	15.9 ± 1.7
	ZrRu	B2	CsCl	3.280	-	-	[a]				
	V-rich Phase	C14	$MgZn_2$	5.340	-	8.489	-	24.1 ± 2.5	15.6 ± 1.7	23.6 ± 2.4	36.7 ± 2.2
	ZR1	$L1_0$	CuAu	3.702	-	4.654	-	44.5 ± 3.5	15.4 ± 1.8	18.7 ± 2.2	21.4 ± 1.7

[a]: Through thickness STEM-EDS measurements of the B2 precipitates were not obtained.

It is tentatively identified as a topologically close packed (TCP) orthorhombic phase, typically referred to as a ”P” phase (*Pnma*) in the Ni-based superalloy literature[281] (Figure 5.10B).

The matrix had a lattice parameter of 3.259 Å and the HfRu-B2 precipitates had a lattice parameter of 3.275 Å. Using Eq. 1, the lattice misfit is +0.49 %. No dislocations were visible at the interface between the matrix and B2 precipitates (Figure 5.10C).

The foil taken from $Zr_{10}Ru_9$ captured four phases: the (Nb,V)-BCC matrix, ZrRu-B2, the V-rich C14 Laves phase, and ZR1 (Figure 5.11). The Zr-rich needles, ZR2, that are present in the intragranular regions were not captured. The compositions of ZR1 and the C14 Laves phase as measured by STEM-EDS at 1000 °C are close to the values measured by SEM-EDS at 1200 °C. The C14 Laves phase demonstrates reflections corresponding to the $[5\bar{4}\bar{1}0]$ and [0001] zone axes of a C14 Laves phase (Figure 5.11D,E.). However, defect contrast within the C14 Laves grains and streaking in the diffraction pattern taken on the $[5\bar{4}\bar{1}0]$ zone axis suggests the presence of stacking faults, which is common in Laves phases[282]. The ZR1 phase is tentatively identified as $L1_0$, a tetragonal phase with a P4/mmm space group (Figure 5.11F,G.); this is equivalent to the tetragonal NbRu′ phase found in the Nb-Ru binary phase diagram at intermediate temperatures[181]. Contrast associated with planar defects within the ZR1 grains is similar to that of twin planes[283].

The matrix had a lattice parameter of 3.295 Å and the ZrRu-B2 precipitates had a lattice parameter of 3.280 Å. The lattice misfit is therefore -0.46 %. No dislocations were visible at the interface between the matrix and B2 precipitates (Figure 5.11C).

5.4.7 Effect of small Hf additions on $Zr_{10}Ru_9$

The tertiary phases present within the Zr-containing alloys are likely highly detrimental to ductility due to their complete coverage of the grain boundaries. Given that fewer

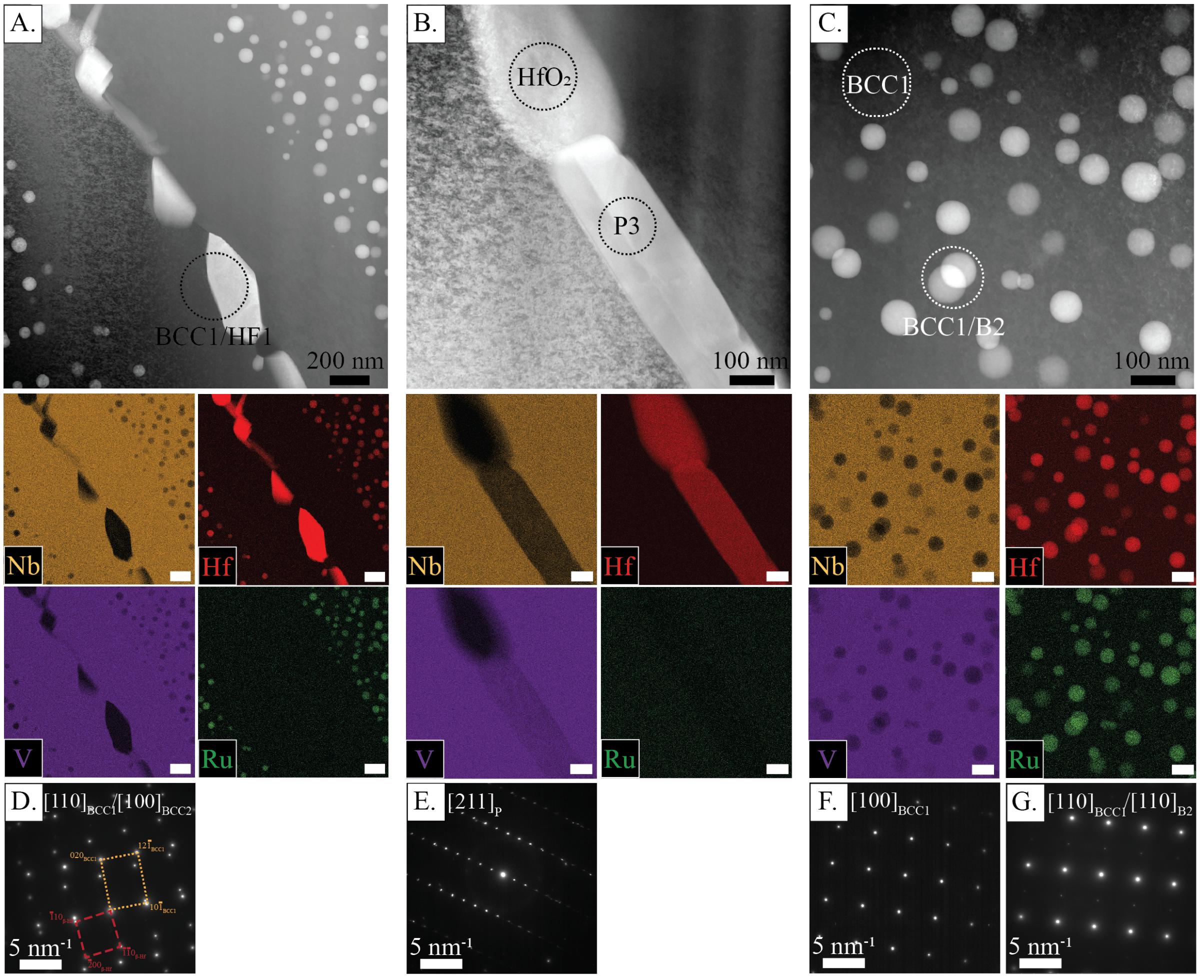

Figure 5.10: TEM analysis of Hf_5Ru_4 after aging at 1000 °C for 200 h. A. HAADF-STEM image of a section of grain boundary (top) and corresponding STEM-EDS maps (Nb, Hf, V, and Ru). The phases at the grain boundary are depleted in Nb and V compared to the matrix (BCC1) and are enriched in Hf, corresponding to the HF1 phase. No enrichment in O was observed. B. HAADF-STEM image of a section of grain boundary (top) and corresponding STEM-EDS maps (Nb, Hf, V, and Ru). Two grain boundary phases are visible: HfO_2 and the P3 phase, enriched in Hf and depleted in V and Nb. C. HAADF-STEM image (top) of a region in the grain interior with spherical HfRu-B2 particles and corresponding STEM-EDS maps (Nb, Hf, V, and Ru). No dislocations are visible at the BCC1/B2 interface. D. SADP acquired from the phases marked "BCC1" and "β-Hf" in A. Two sets of reflections are visible, corresponding to two BCC phases of different orientations. The two visible zone axes are $[110]_{BCC1}$ and $[100]_{\beta-Hf}$. E. SADP acquired from the phase marked "P3" in B. The reflections correspond with the [211] zone axis of an orthorhombic topologically packed phase typically denoted as the "P" phase. F. SADP acquired only from the matrix, labeled "BCC1" in C. Pattern was acquired from $[100]_{BCC}$ zone axis. G. SADP from the circular region labeled "BCC1/B2" in C. Pattern was acquired on the $[110]_{BCC}$ zone axis, indicating BCC ordering with B2 superlattice.

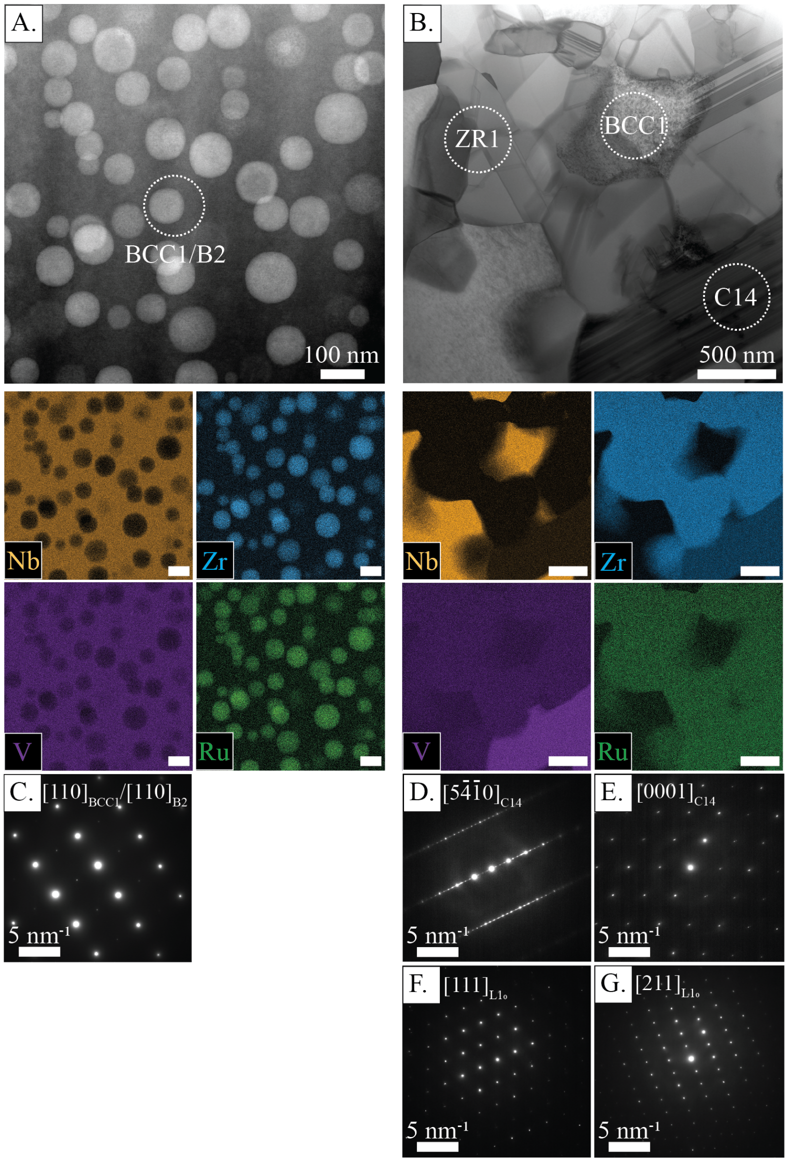

Figure 5.11: TEM analysis of $Zr_{10}Ru_9$ after aging at 1000 °C for 200 h. A. HAADF-STEM image (top) of a region in the grain interior with spherical ZrRu-B2 particles and corresponding STEM-EDS maps (Nb, Zr, V, and Ru). No dislocations are visible at the BCC1/B2 interface. B. HAADF-STEM image (top) of the grain boundary and corresponding STEM-EDS maps (Nb, Zr, V, and Ru). Two grain boundary phases are visible: a C14 Laves phase richer in Ru and V, and ZR1, rich in Ru, V, and Zr and depleted in Nb. C. SADP acquired from phases marked "BCC1" and "B2" in A. Pattern was acquired on the $[110]_{BCC}$ zone axis, indicating BCC ordering with B2 superlattice. D,E. SADPs acquired from the phase marked "C14" in B. D. Pattern corresponds to the $[5\bar{4}\bar{1}0]_{C14}$ zone axis. E. Pattern corresponds to the $[0001]_{C14}$ zone axis. F, G. SADPs acquired from the phase marked "ZR1" in B. F. Pattern corresponds to the [111] zone axis of a tetragonal $L1_0$ P4/mmm phase. G. Pattern corresponds to the [211] zone axis of a tetragonal $L1_0$ P4/mmm phase.

tertiary phases formed within the Hf-containing alloys, that the HfRu-B2 phase is more thermally stable, and that the B2 phase can incorporate both B2 formers[190, 243], it is of interest to determine whether Hf additions can be used to improve the properties of Zr-containing alloys. To investigate this question, 2 at% Zr in $Zr_{10}Ru_9$ was substituted for Hf, yielding the $Hf_2Zr_8Ru_9$-$Nb_{63}V_{18}$ alloy ($Hf_2Zr_8Ru_9$). Consistent with the previous alloys, the $T_{s,B2}$ range was determined by sequential annealing and the alloy was aged at 1000 and 1200 °C.

The 2 at% addition of Hf to $Zr_{10}Ru_9$ has a significant effect on phase stability. The as-cast microstructure is similar to the microstructure $Zr_{10}Ru_9$, but the inter-dendritic regions also contains chains of a (Hf,Zr)Ru-B2 phase, comparable to the as-cast microstructure of the Hf-containing alloys (Figure 5.4G-I). The Hf additions increase the thermal stability of the B2 phase, raising the $T_{s,B2}$ range to 1400-1500 °C (Figure 5.5M-P) and increasing the volume fractions of the B2 phase between 1200-1400 °C (Figure 5.7). The spherical B2 particles that formed had comparable average radii to the ZrRu-B2 particles in $Zr_{10}Ru_9$ (Figure 5.8). Most importantly, the tertiary phases were nearly eliminated at 1000 and 1200 °C (Figure 5.6I-L). ZR1 is no longer present at any temperature investigated. A small quantity of the C14 Laves phase and ZR4 are present at the grain boundaries and ZR2 needles remain within the grains (Figure 5.9C), but the grain boundaries are no longer completely obscured. The suppression of the tertiary phases also result in B2 precipitation directly adjacent to the grain boundary, reducing the size of PFZs. The addition of Hf did not seem to have an effect on the ZR4 phase at 1400 °C, which is still present in small quantities at the grain boundaries (Figure 5.5L).

5.4.8 Effect of incomplete homogenization on precipitate coarsening behavior

Properly homogenizing the samples prior to subsequent aging treatments is important for achieving a homogeneous distribution of precipitates. The consequences of incomplete homogenization are shown in Figure 5.12. When Hf_5Ru_4 is homogenized at 1400 °C for 20 h and then aged at 1200 °C for 20 h, the HfRu-B2 precipitates coarsen differently in different sections of the sample. In some areas, the precipitates are spherical (Figure 5.12B) and demonstrate a similar size and morphology to the HfRu-B2 precipitates that formed after homogenizing at 1600 °C for 20 h (Figure 5.6H). In other areas, the precipitates coarsened much more rapidly, resulting in cuboidal (Figure 5.12C) and cuboidal array morphologies (Figure 5.12D). A similar behavior was observed in the B2 precipitates in $Hf_2Zr_8Ru_9$ after homogenizing at 1600 °C for 5 h and aging at 1400 °C for 20 h (Figure 5.12E). In comparison to the approximately spherical precipitates observed previously (Figure 5.5N), the precipitates in the sample with a shorter homogenization time have large cuboidal array morphologies. The coarsening behavior is similar to that observed in a model Ni-based superalloy with low lattice misfit and was attributed to compositional fluctuations that result in solvus temperature variations in the local microstructure[267].

The larger sizes achieved by the B2 precipitates in $Hf_2Zr_8Ru_9$ allowed the composition of the B2 phase to be measured by SEM-EDS (Table 5.4). The mixed (Hf,Zr)Ru-B2 phase had an average composition of 19.6 at% Hf, 27.5 at% Zr, and 47.0 at% Ru at 1400 °C. The ZR4 phase was not observed.

5.4.9 Hardness

Hardness values were measured for selected alloys after homogenization at 1600 °C and then aging at 1000 °C and 1200 °C (Table 5.7). Hardness was highest for Hf_5Ru_4,

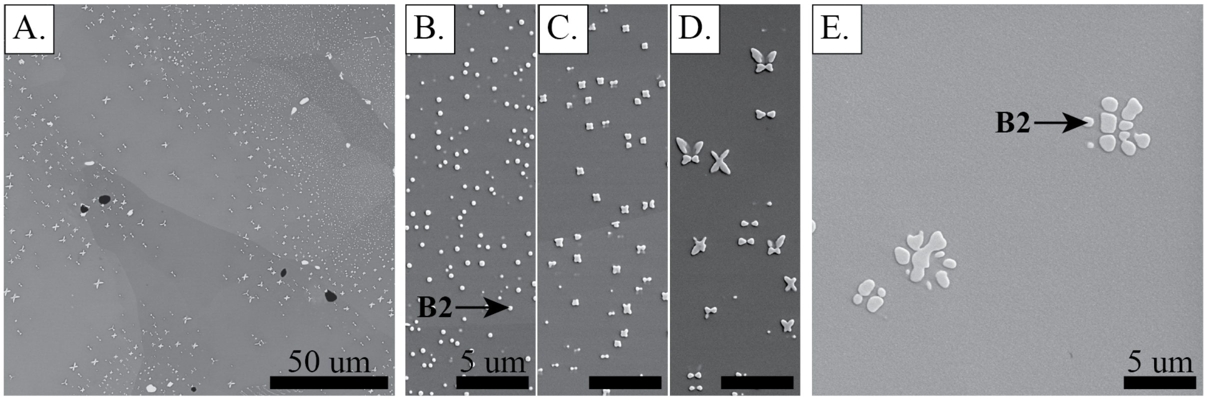

Figure 5.12: Insufficient homogenization of the matrix results in rapid coarsening of the B2 grains. A. BSE and B-D. SE micrographs of Hf_5Ru_4 after solutioning at 1400 °C for 20 h and aging at 1200 °C for 20 h. Light grey HfRu-B2 particles are embedded in a (Nb,V)-BCC matrix. Inhomogenous coarsening of the HfRu-B2 particles resulted in various morphologies and sizes. Compare to Figure 5.6D. E. SE micrograph of $Hf_2Zr_8Ru_9$ after solutioning at 1600 °C for 5 h and aging at 1400 °C for 20 h. The (Hf,Zr)Ru-B2 grains were more uniform in size and shape than the HfRu-B2 particles in A-D., but still coarsened more rapidly than the B2 particles in the samples solutioned at 1600 °C for 20 h. Compare to Figure 5.5P.

$Zr_{10}Ru_9$, and $Hf_2Zr_8Ru_9$ after homogenization, and then decreased with decreasing annealing temperature (Figure 5.13). Hf_5Ru_2 and Zr_5Ru_4, which do not form B2 at any investigated temperature, were the softest materials out of all conditions.

5.5 Discussion

Ru remains a promising alloying addition for developing Nb-based $\beta + \beta'$ alloys. With sufficient additions of Ru and a tailored V content for adjusting misfit, both HfRu- and ZrRu-B2 alloys can form homogeneous distributions of spherical precipitates above 1200 °C. Depending on the Ru concentration and temperature, B2 volume fractions range from 0.01-0.20, with higher Ru concentrations resulting in larger volume fractions at equivalent temperatures. The formation of tertiary phases (including β-Hf and various Zr-rich phases) on the grain boundaries is of significant concern and requires mitiga-

Table 5.7: Hardness of the annealed alloys.

Alloy	Condition	Hardness (HV)
Hf_3Ru_2-$Nb_{67}V_{28}$	1600 °C 20 h	342 ± 5
Hf_5Ru_4-$Nb_{63}V_{28}$	1600 °C 20 h	485 ± 9
Hf_5Ru_4-$Nb_{63}V_{28}$	1200 °C 40 h	389 ± 8
Hf_5Ru_4-$Nb_{63}V_{28}$	1000 °C 200 h	359 ± 9
Zr_5Ru_4-$Nb_{73}V_{18}$	1600 °C 20 h	374 ± 12
Zr_8Ru_7-$Nb_{67}V_{18}$	1600 °C 20 h	466 ± 12
Zr_8Ru_7-$Nb_{67}V_{18}$	1100 °C 200 h	376 ± 12
$Zr_{10}Ru_9$-$Nb_{63}V_{18}$	1600 °C 20 h	500 ± 31
$Zr_{10}Ru_9$-$Nb_{63}V_{18}$	1200 °C 40 h	486 ± 24
$Zr_{10}Ru_9$-$Nb_{63}V_{18}$	1000 °C 200 h	429 ± 8
$Hf_2Zr_8Ru_9$-$Nb_{63}V_{18}$	1600 °C 20 h	487 ± 17
$Hf_2Zr_8Ru_9$-$Nb_{63}V_{18}$	1200 °C 40 h	450 ± 13
$Hf_2Zr_8Ru_9$-$Nb_{63}V_{18}$	1000 °C 200 h	433 ± 16

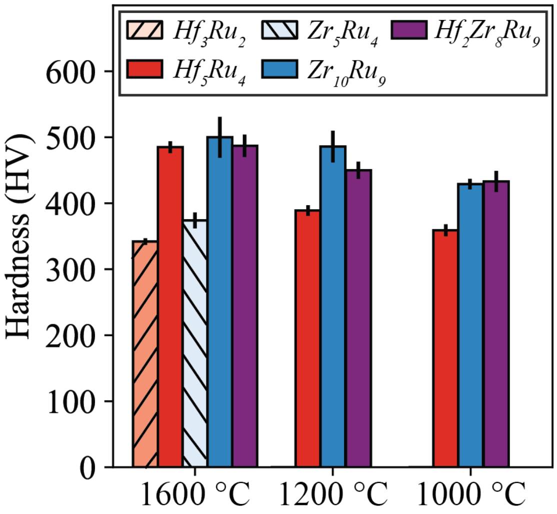

Figure 5.13: Vickers hardness of selected alloys and annealing treatments. Alloys were homogenized at 1600 °C and then subsequently aged at 1000 and 1200 °C. Hardness decreases with decreasing annealing temperature.

tion strategies. In the following sections, the effect of Ru concentration on B2 solvus temperatures, overall tendencies towards deleterious phase formation, and the efficacy of CALPHAD predictions are discussed for each system. Potential design strategies to further develop this alloy system are discussed throughout.

5.5.1 Trends in B2 volume fraction

Ru drives B2 formation in these alloys and increasing the Ru concentration results in an increased B2 volume fraction (Figure 5.7) and $T_{s,B2}$ (Section 5.5.2). However, Ru is a expensive alloying agent[268]. Developing cost effective alloys will require both utilizing the included Ru content efficiently and discovering alloying agents that can substitute for Ru. The latter is not addressed in detail in this article but is an important future avenue of research. For an alloy to be an efficient B2 former, the matrix will need to have a low Ru solubility and the Ru must partition primarily to the B2 phase without being lost to other tertiary phases. To evaluate trends in the B2 volume fraction and determine how effectively the investigated alloys are forming B2, it is helpful to normalize the B2 volume fractions by the Ru content.

Assuming a theoretical B2 phase composed of 50 at% Ru, the normalized B2 volume fraction can be calculated by:

$$v_{f,norm} = \frac{v_{f,B2}}{2 * X_{Ru}} \tag{5.1}$$

where $v_{f,B2}$ is the B2 volume fraction and X_{Ru} is the Ru concentration of the alloy. If $v_{f,norm}$ is equal to 0, the alloy is in a solutioned condition. If $v_{f,norm}$ is equal to 1, all the included Ru is being converted to B2 and the alloy is at a theoretical volume fraction maximum. Experimentally, Ru-B2 phases can contain less than 50 at% Ru (with 40-50 at% Ru being commonly observed throughout this dissertation) and therefore values above 1 are allowed. $v_{f,norm}$ for Hf_5Ru_4, $Zr_{10}Ru_9$, and $Hf_2Zr_8Ru_9$ in all conditions are plotted in Figure 5.14.

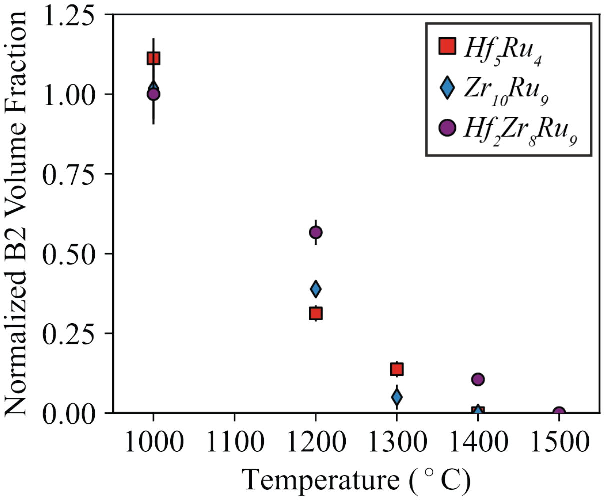

Figure 5.14: Normalized B2 volume fractions for each alloy at each aging temperature. The B2 volume fraction is normalized by dividing by 2*(Ru concentration) and represents how much of the included Ru content has been converted into B2 at each aging temperature. Ratios above 1 are allowed because the B2 phases can contain less than 50 at% Ru.

Despite the differences in thermal stability between HfRu- and ZrRu-B2, the normalized volume fractions for Hf_5Ru_4 and $Zr_{10}Ru_9$ follow each other closely at all annealing temperatures and both alloys are approaching their theoretical volume fraction maximums at 1000 °C. $Zr_{10}Ru_9$ does trail Hf_5Ru_4 slightly at 1000 °C and at 1300 °C, consistent with the higher Ru concentration of the matrix in $Zr_{10}Ru_9$ at 1000 °C and the loss of Ru to tertiary phases at 1300 °C. When ZrRu-B2 is stabilized with additions of Hf, resulting in suppression of the tertiary phases and potentially reducing the Ru solubility of the matrix, this results in higher $v_{f,norm}$'s for $Hf_2Zr_8Ru_9$ from 1200-1400 °C. However, because $Zr_{10}Ru_9$ forms fewer tertiary phases at lower temperatures, the addition of 2 at% Hf does not appear to significantly affect the $v_{f,norm}$ at 1000 °C.

While not investigated here, having a $v_{f,norm} \approx 1$ at 1000 °C indicates there is a plateau in the $v_{f,B2}$ below 1000 °C, unless the composition of the B2 phase changes or other tertiary phases form. This suggests that the most efficient use of Ru requires that alloys are designed such that $\mathrm{v}_{f,norm} = 1$ at their application temperatures. This would stabilize the B2 volume fraction in case of thermal fluctuations and provide maximum strengthening for the chosen Ru concentration. Strategies to increase the plateau temperature (i.e. increase the temperature where $\mathrm{v}_{f,norm} = 1$) would require decreasing the stability of tertiary phases that uptake β' formers and decreasing the solubility of Ru in the matrix at higher temperatures.

5.5.2 Solvus temperature trends of HfRu- and ZrRu-B2

While exact $T_{s,B2}$'s of the HfRu- and ZrRu-B2 were not determined, a solvus temperature window was defined for each alloy and the BCC matrix compositions were measured at each annealing temperature. Therefore, a solvus line from 1000-1400 °C can be constructed for each system (Figure 5.15). Additional values that were reported for $Hf_{11}Ru_9$ are included in the solvus line for the Hf system, extending the defined range up to 1750 °C [?]. Readers should note that an increase in Ru concentration is accompanied by an equivalent increase in Hf or Zr content. Overall, for alloys in X-Ru-Nb-V quaternary systems where coherency is desired (therefore fixing the V concentration), alloys containing ZrRu-B2 precipitates will have lower solvus temperatures than HfRu-B2 alloys for equivalent Ru contents. For Hf-containing alloys with 28 at% V, the solubility limit is close to 2 at% Ru at 1000 °C; for Zr-containing alloys with 18 at% V, the solubility limit is close to 4 at% Ru. With comparison to the binary BCC → BCC + Ru-B2 solvus lines (plotted for reference in Figure 5.15), the thermal stability of the B2 phases was increased in the multi-component systems.

For the Zr-containing alloys, the BCC matrix compositions suggest a solvus curve that is shifted to slightly lower Ru concentrations compared to bulk alloy compositions

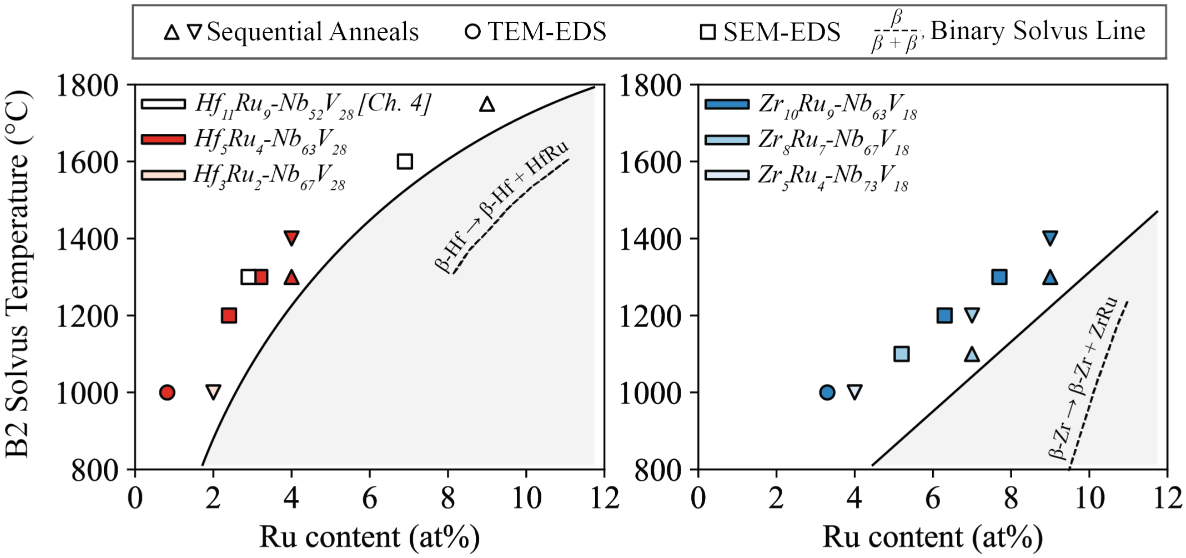

Figure 5.15: Solvus temperatures of the (left) Hf-containing and (right) Zr-containing alloys. The solvus temperature windows determined for each alloy are plotted as a set of triangles representing the lowest solutioning temperature (▽) and highest aging temperature attempted (△). The solvus temperature of the B2 phase must fall within these values. The Ru concentrations of the BCC matrices present at each temperature are also plotted and identified by their method of measurement (○ for STEM-EDS and ☐ for SEM-EDS). The maximum aging temperature and BCC matrix compositions reported for $Hf_{11}Ru_9$-$Nb_{62}V_{28}$ are also included[**?**]. For reference, the solvus lines for each binary system (Hf-Ru and Zr-Ru) are plotted on each respective figure and are reproduced from [187] and [189]. The V content is fixed for each system; increases in Ru content would be accompanied by an equivalent increase in Hf or Zr concentration. The shaded regions denote combinations of Ru content and temperature that would result in a $\beta + \beta'$ microstructure; readers should note that these alloys would also form some quantity of deleterious tertiary phases. A version of this figure with an additional Hf-containing alloy is available as Supplemental Figure 3.

(i.e. the B2 solvus temperature is overestimated). This difference could arise from several factors: (i) in EDS, the Zr and Nb peaks are convoluted, affecting the reliability of the composition measurements compared to Hf-containing alloys where the Hf and Nb peaks are distinct; (ii) the Zr alloys form tertiary phases that contain significant quantities of Ru (10-20 at%), which may deplete the matrix of Ru; and (iii) the experimentally achieved Ru content for some alloys may be lower then the nominal values. From Figure 5.15, it is clear that small variations in Ru concentration can change the $T_{s,B2}$ by 50-100 °C and it should be closely monitored in future investigations.

Many interesting questions remain regarding the effect of mixed Hf and Zr concentrations on the properties of the B2 phase. The addition of 2 at% Hf to $Zr_{10}Ru_9$ increased the solvus temperature range from 1300-1400 °C to 1400-1500 °C, which is consistent with the higher thermal stability of HfRu-B2. At 1400 °C, the B2 phases in $Hf_2Zr_8Ru_9$ are composed of 19.6 at% Hf, which represents 42 % of the combined Hf+Zr content in the B2 phase (Table 5.4). This is disproportionate to the ratio of Hf to Zr in the nominal alloy composition, where Hf is ≈ 20 % of the included B2 formers. A similar bias towards a Hf-rich B2 composition when multiple B2 formers are present has been observed in other alloys with equivalent additions of Hf, Ti, and Zr[190, 243]. Given the low concentration of Hf in this alloy, the composition of the B2 phase could also change with temperature as the B2 volume fraction increases from 1400 to 1000 °C. This leads to the question of whether an incremental transition from Zr to Hf (i.e. from $Zr_{10}Ru_9$-$Nb_{63}V_{18}$ to $Hf_{10}Ru_9$-$Nb_{63}V_{18}$) would demonstrate a linear change in $T_{s,B2}$ and other properties or, instead, distinct behaviors will emerge for Hf-rich and Zr-rich alloys.

5.5.3 Misfit between the BCC and B2 phases

Several factors affect the δ between two phases and the resulting precipitate morphology. As coherent precipitates with cube-cube orientation relationships coarsen, they can evolve from spherical to cuboidal morphologies due to interactions between the interface energy, elastic strain energy, and elastic interaction energy[284, 243, 285]. The critical size at which the spherical to cuboidal transition occurs is typically determined by the degree of misfit in nickel superalloys[286]. With larger misfits, cuboidal precipitates will eventually evolve to globular precipitates as the interface transitions from coherent to semi-coherent [286].

As indicated by the diffraction patterns containing both the BCC and B2 phases, the Ru-B2 precipitates have a cube-cube orientation relationship with the BCC matrix (Figures 5.10G and 5.11C). This is consistent with the orientation relationships observed in (Al,Ti,Zr)-B2 RMPEAs[152] and Cr alloys with NiAl-B2 precipitates[146]. Both Hf_5Ru_4 and $Zr_{10}Ru_9$ have $\delta \approx 0.5$ % after annealing at 1000 °C for 200 h. The misfits are equal in magnitude, but the misfit is positive (the BCC phase is smaller) for Hf_5Ru_4 and negative for $Zr_{10}Ru_9$. Due to likely differences in thermal expansion between the BCC and B2 phases, the misfit at the annealing temperature will be different from the misfit measured from the sample after being cooled to room temperature[287, 288]. However, the spherical morphology of the B2 precipitates and their homogeneous distribution throughout the microstructure indicate that δ is still < 1.0 % at 1000 °C. While not explicitly measured, the similar morphology and distribution of the precipitates after annealing at 1200 °C suggests that the misfits at 1200 °C are also < 1 %.

However, some microstructural evidence for increasing δ and loss of coherency is visible at the highest annealing temperatures. At 1300 °C in Hf_5Ru_4 (Figure 5.5C) and 1400 °C in $Hf_2Zr_8Ru_9$ (Figure 5.5O), the B2 precipitates begin to decorate subgrain boundaries. Further, the morphology of the B2 particles in $Hf_2Zr_8Ru_9$ are more globular and less spherical, indicating a transition to a semi-coherent interface. The coefficients of thermal expansion of the BCC and B2 phases are unknown and could result in a loss of coherency at increasing temperatures[289]. The changing composition of the matrix with changes in B2 volume fraction would also have an effect on the misfit at different annealing temperatures. As the B2 volume fraction increases, the V concentration of the matrix increases and the Hf, Zr, and Ru concentrations decrease. This may have a significant effect on the BCC lattice parameter.

No cuboidal precipitates were observed in samples that were fully homogenized and isothermally aged, even at 1300 °C where precipitate radii exceeded 130 nm. Nickel superalloys with similar misfit typically exhibit cuboidal precipitates at this size[286]. Inconel X-750, with a $\delta = +0.5$ %, forms cuboidal γ' precipitates at $r > 40$ nm[286]. Cuboidal Ru-B2 precipitates have been observed in $Hf_{11}Ru_9$-$Nb_{52}V_{28}$ after slow cooling (seen in Ch. 4) and in partially homogenized samples where the nucleation density is lower (Figure 5.12). Understanding morphological evolution in these materials will require further aging studies and tracking changes in misfit at elevated temperatures[288]. The Ru-B2 precipitate radii in this investigation are comparable in size to NiAl-B2 precipitates in Cr-based alloys (where $\delta < 0.2$ %) that underwent similar aging treatments, suggesting a potentially similar coarsening rate from 1000-1200 °C [146]. Further coarsening studies are necessary to determine this. In particular, coarsening and misfit at temperatures above 1200 °C need to be be investigated, given desired application temperatures at or above 1300 °C.

5.5.4 Formation of deleterious phases

One major obstacle for the continued development of Nb-based alloys with Ru-based B2 precipitates is the formation of grain boundary phases. The formation of tertiary phases at intermediate temperatures is a known issue for RMPEAs and often results in embrittlement when the grain boundaries are covered[91]. A number of tertiary phases form in both the Hf-containing and Zr-containing alloys: HfO_2, ZrO_2, β-Hf, a V-rich C14 Laves, a ternary orthorhomic P phase, a Zr-rich tetragonal $L1_0$ phase, and other Zr- and Hf- rich phases that were not identified (HF2, ZR2, ZR3, and ZR4). These phases are present in small volume fractions on the grain boundaries and need to be mitigated, potentially by small adjustments in composition.

One strategy has already been demonstrated in the present article, which is the addition of small amounts of Hf to Zr-containing alloys. These small additions appreciably suppress the formation of V- and Zr-rich phases by increasing the stability of the B2 phase. Another pathway would be to reduce the Hf and Zr concentrations. An excess percentage of Hf and Zr were included with the hypothesis that this would be beneficial for the $T_{s,B2}$ and $v_{f,B2}$. A question remains whether this did have beneficial impacts or, instead, resulted in a greater quantity of tertiary phases without affecting the properties of the B2 phase. If the latter is true, reducing the Hf and Zr concentrations should reduce the quantity of tertiary phases that form.

The effect of oxygen on the tertiary phase population also needs to be considered: the oxygen content of these alloys, while comparable to typical literature values, is still relatively high (300-500 ppmw). O is known to stabilize the HCP form of Hf and Zr and promote the Zr-Nb miscibility gap[290]. Reducing the bulk oxygen content would likely reduce the grain boundary populations of β-Hf (in Hf-containing alloys) and oxides, and potentially have an impact on ZR4 (in Zr-rich alloys) and the Hf/Zr needles within the grains (in Hf- and Zr-containing alloys).

V is necessary for reducing the lattice parameter of the BCC matrix and reducing the misfit to ≤ 1 %; however, its inclusion is also driving the formation of Laves phases. Other refractory metals can also reduce the BCC lattice parameter, namely Cr, Mo, and W (Table 5.1). Cr is well known to stabilize Laves phases in Nb-based alloys and would not be a good replacement for V[106]. Alternatively, the Mo-and W-containing alloys that have been investigated do not appear to form many tertiary phases, which is promising (Discussed in Chs. 3 and 4). However, the investigated heat treatments had a minimum temperature of 1300 °C and Zr was not included as a B2 former. In their binary phase diagrams, Mo and W can form σ phases with Ru and Laves phases with Hf and Zr at lower temperatures. Further investigation is needed to determine whether those phases would be less stable then those formed by V in a multi-component solution. Mo and W also intrinsically embrittle the BCC matrix, so they cannot wholly substitute for V- however, a small amount could be sufficient to further reduce the Laves phases in combination with other approaches. Further potential benefits of Mo and W additions is an improvement of the creep strength of the BCC matrix and a likely increase of the $T_{s,B2}$ due to the lower solubility of Ru in Mo-containing matrices.

Beyond the direct embrittlement of the grain boundaries due to the presence of deleterious phases, both the Hf-containing and Zr-containing alloys form PFZs when the tertiary phases are present (Figure 5.6, Figure 5.9). In superalloys, PFZs are associated with the diffusion of γ' formers from the γ' precipitates towards phases (i.e. carbides, borides) at the grain boundaries[291, 292]. For the alloys under investigation, the PFZs would be the result of the diffusion of Hf, Ru, and Zr from B2 particles towards the tertiary phases. In Zr-containing alloys, the suppression of the tertiary phases via Hf additions markedly reduced the width of the PFZs, supporting this assumption. PFZs beyond a certain width result in decreased mechanical properties and should be mitigated by controlling the type and density of grain boundary phases through the strategies discussed above[291, 293, 292].

5.5.5 Comparison to CALPHAD

A common tool for alloy design is the CALculations of PHAse Diagram (CALPHAD) method. These methods rely upon assessed phase diagrams to make predictions in unexplored composition spaces. Unfortunately, many of the Ru-containing ternary phase diagrams have not been experimentally investigated. The TCHEA7 database offered by Thermo-Calc® [200] does include Ru as a constituent and has tentatively assessed a number of Ru-containing ternaries. To verify whether the Thermo-Calc® software is currently applicable to Nb-based Ru-B2 alloys, phase stability predictions were made on the Hf_5Ru_4 and $Zr_{10}Ru_9$ compositions.

For both alloys, a disordered BCC and an ordered B2 phase were predicted to be stable until the solidus temperature (Figure 5.16). In Hf_5Ru_4, the B2 volume fraction is approximately constant at 0.10 from 500 to 1000 °C, followed by a more rapid decrease until the solidus temperature where the B2 volume fraction is near zero. In $Zr_{10}Ru_9$, the B2 volume fraction decreases gradually with temperature, with a maximum volume fraction of 0.21 at 500 °C and 0.13 at the solidus temperature. No tertiary phases were predicted.

These predictions are inconsistent with the experimental results. Both alloys are single phase BCC solid solutions at 1400 °C and above and form a number of tertiary phases below 1400 °C. However, the predicted volume fractions are close to the experimental volume fractions at 1000 °C. While lower annealing temperatures were not investigated, the constant B2 volume fractions from 500 to 1000 °C would likely be consistent with

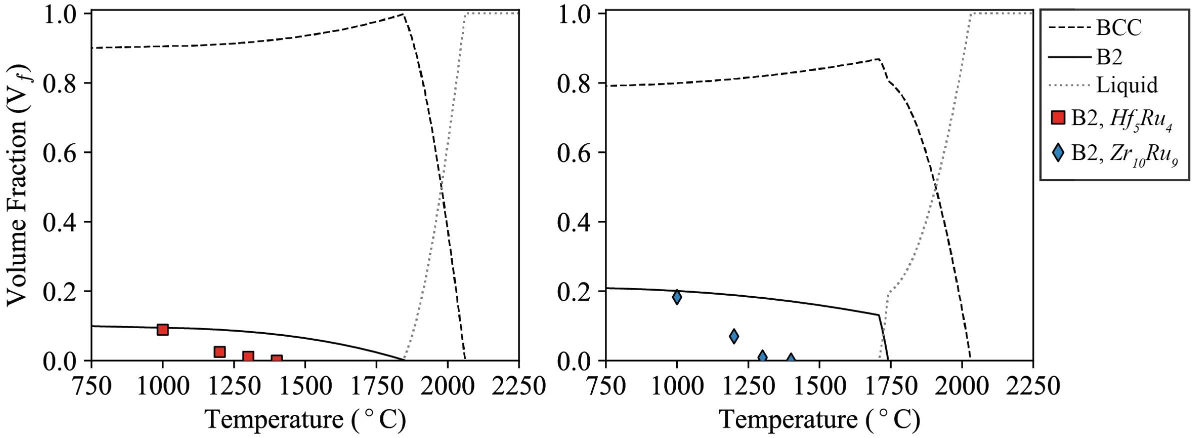

Figure 5.16: Equilibrium CALPHAD predictions for (left) Hf_5Ru_4 and (right) $Zr_{10}Ru_9$. In both cases, CALPHAD predicts that the Ru-B2 phase is stable to the solidus temperature of the alloy. Predictions were made with Thermo-Calc® software and the TCHEA7 database[200]. Experimental B2 volume fractions (symbols) are superimposed on the predictions.

further experiments as both alloys are close to their theoretical maximum B2 volume fraction at 1000 °C (Figure 5.14). Given the lack of accurate $T_{s,B2}$ and tertiary phase formation predictions, additional Thermo-Calc® assessments of Ru-containing systems will be needed to employ it effectively as an alloy design tool.

5.5.6 Precipitation Strengthening

Hardness measurements of selected alloys and annealing conditions are shown in Figure 5.13. Hf_5Ru_4, $Zr_{10}Ru_9$, and $Hf_2Zr_8Ru_9$ are hardest after homogenization at 1600 °C and soften with decreasing annealing temperature. The decreasing strength with decreasing temperature, despite the increasing B2 volume fraction and decreasing precipitate radius, can be related to (i) early stages of phase decomposition in the homogenized samples and (ii) the Ru concentration of the matrix.

There is a high driving force for B2 formation in these alloys. The cooling rate of the vacuum furnace was not sufficient to fully suppress B2 formation after homogenization at

1600 °C. Except for Hf_3Ru_2 and Zr_5Ru_4, all the homogenized samples demonstrate nano-scale features in the matrix that are consistent with the early stages of B2 formation, where Hf, Ru, and Zr are separating from the solid solution (Figure 5.5). These features are significantly smaller than the particles formed after aging, which would result in harder materials if the precipitates are not sheared. Even without the decomposition of the matrix, alloys in the solutioned condition may be harder than aged materials. While hardness data is not available for Nb-Ru alloys, Ru is a potent solid solution hardener in Ta-based alloys (which are closely related to Nb-based alloys) and small increments in Ru content correspond to significant hardening[51]. After homogenization, the Ru concentration of the matrix would be at its highest. The Ru concentration of the matrix continuously decreases as B2 volume fraction increases from 1600 to 1000 °C, resulting in the hardness decreases within each alloy system.

To more accurately assess the impact of the precipitates on hardness, the aged samples should be compared to single phase alloys with compositions equivalent to those of the matrix. While those compositions were not explicitly synthesized, Hf_3Ru_2 and Zr_5Ru_4 can serve as proxy matrix materials for the samples aged at 1000 °C because they did not form B2 and have comparable, though slightly higher, Ru concentrations than the measured matrix compositions. After homogenization, Hf_3Ru_2 had a hardness of 342 ± 5 and Zr_5Ru_4 had a hardness of 374 ± 12, making both of them softer then the equivalent precipitation strengthened alloy. The change in hardness is larger between Zr_5Ru_4 and $Zr_{10}Ru_9$ (ΔHV = 55), consistent with the larger volume fraction of precipitates.

A further estimate of precipitation strengthening can be made by applying the Orowan bowing model:

$$\Delta\tau_b = \frac{Gb}{L - 2r} \tag{5.2}$$

where $\Delta\tau_b$ is the change in shear stress in the material, G is the shear modulus of the matrix, b is the Burgers vector, L is the spacing between precipitates, and r is the average radius of the precipitates. The magnitude of b was calculated from $\frac{a}{2}\langle 111\rangle$, where a is the lattice parameter of the matrix and assumed to be equivalent to the binary B2 lattice parameter of each system (Table 5.1). G was calculated from a weighted average of the matrix composition (Table 5.6) and the shear modulii of the pure elements (Table 5.8). No shear modulus for BCC-Ru was found, so the modulus of HCP-Ru was used[294]. L was assumed to be a square lattice spacing of particles where:

$$L = r\sqrt{\frac{2\pi}{3v_f}} \tag{5.3}$$

and v_f is the volume fraction of the precipitates [4]. $\Delta\tau_b$ can be converted to a change in polycrystalline yield stress by:

$$\Delta\sigma_b = 2.733\Delta\tau_b \tag{5.4}$$

where $\Delta\sigma_b$ is the change in yield strength of the material and 2.733 is the polycrystalline Taylor factor for BCC metals[295].

Table 5.8: Shear modulis (G) of the pure elements and calculated G for Hf_5Ru_4-$Nb_{63}V_{28}$ and $Zr_{10}Ru_9$-$Nb_{63}V_{18}$

Material	G (GPa)	Notes and Source
Hf	24.3	[257], from Table 7.2. G = (C11 - C12 + C44)/3
Nb	31.5	[259]
Ru	169.6	[294]
V	44.3	[259]
Zr	16.3	[257], from Table 7.2. G = (C11 - C12 + C44)/3
Hf_5Ru_4-$Nb_{63}V_{28}$	36.6	
$Zr_{10}Ru_9$-$Nb_{63}V_{18}$	37.6	

Strength estimates for Hf-containing and Zr-containing alloys with theoretical v_f's from 0.01-0.2 are plotted in Figure 5.8B. Curves corresponding to the experimental volume fractions at 1000 and 1200 °C are shown in color and a discrete strength prediction for the measured experimental radii is marked. Precipitation strengthening in Hf_5Ru_4 is predicted to increase the yield strength by $\approx$ 300 MPa at 1000 °C and 57 MPa at 1200 °C. Predicted strength improvements in $Zr_{10}Ru_9$ are larger due to the higher volume fractions, with $\approx$ 500 MPa at 1000 °C and 100 MPa at 1200 °C.

Many commercial refractory alloys have yield strengths of $\leq$ 400 MPa at temperatures between 1000 to 1500 °C[54]. A strength improvement of 100 MPa would be a 25 % increase relative to current alloys. RMPEAs can have higher high temperature yield strengths from 1000 to 1500 °C ($\leq$ 800 MPa) but those strengths are achieved through large additions of Mo or W, which result in dense, brittle alloys[296, 54]. In contrast, the alloys in this work have calculated densities ranging from 8.1-8.4 g/cm^3, lower then the density of pure Nb (Table 5.2). Further, the matrix compositions are consistent with historical alloys that demonstrated appreciable tensile ductility. V, the solute present in the highest quantity, has little effect on the ductility of Nb in Nb-V binary alloys[56]; Hf and Zr have similarly minor effects[56]. Ru is an embrittling element in Ta-based alloys, but alloys with additions of up to 5 at% Ru still demonstrated room temperature elongations to failure of 10 %[51, 297]. The Ru concentrations of the BCC matrices were only 1-3 at% in the Hf-containing alloys, below this limit (Table 5.4). Concentrations were near or beyond 5 at% in the Zr-containing alloys, particularly at higher temperatures and lower B2 volume fractions (Table 5.4). Strategies to reduce the solubility of the Ru in the BCC matrix will need to be developed, which will be concurrently beneficial for increasing overall $T_{s,B2}$ and increasing B2 volume fractions at higher temperatures.

Experimental measurements of high temperature mechanical properties are still needed and the reliability of strength estimates will depend on the deformation mechanisms operating in these alloys. The B2 particles will need to be resistant to shearing to benefit from the Orowan strengthening effect[13]. The post-mortem TEM investigation on compressed micropillars in $Hf_{20}Mo_{20}Nb_{20}Ta_{20}Ru_{20}$ in Ch. 4 observed both paired dislocations (perhaps indicative of precipitate shearing) and dislocations looped around precipitates (indicative of Orowan bowing). Beyond strength predictions, understanding the interactions of dislocations with the B2 precipitates will also be important in understanding whether the ductility of the matrix can be maintained in the two-phase variants.

5.6 Conclusions

A series of Nb-based alloys with coherent HfRu- and ZrRu-B2 precipitates were synthesized by arc melting. Their solvus temperatures were determined via sequential annealing, allowing solvus lines for each system to be determined, and additional aging treatments at 1000 and 1200 °C offer insights into changes in B2 volume fraction and tertiary phase populations with temperature. These results offer guidelines for future alloy design in these systems. In particular, strategies for mitigating tertiary phase formation and increasing B2 solvus temperatures and volume fractions were discussed in detail. The major findings from this investigation are:

1. Misfits between the BCC and B2 phases can be reduced to below 1 % using a weighted average of constituent lattice parameters. This results in a homogeneous distribution of spherical precipitates for all alloys at the investigated temperatures and times.
2. The Ru concentration controls both $T_{s,B2}$ and the maximum B2 volume fractions that can be achieved. By tailoring the Hf:Zr ratio, it may be possible to adjust several properties independently.

3. HfRu-B2 has a higher thermal stability than ZrRu-B2 in the multicomponent alloys investigated. This results both in overall higher solvus temperatures for HfRu-containing alloys at equivalent Ru concentrations and the formation of larger tertiary phase populations in Zr-containing materials.

4. Besides BCC and B2, the following additional phases were identified: HfO_2, ZrO_2, β-Hf, a V-rich C14 Laves, a ternary orthorhombic P phase, and a Zr-rich tetragonal $L1_0$ phase.

5. Increasing the B2 stability is an effective strategy for reducing undesirable tertiary phases that form at grain boundaries.

6. Using the Orowan bowing model, estimated yield strength improvements from the B2 precipitates range from 57-500 MPa. These remain to be validated, but would represent significant strengthening when compared to the current high temperature strengths of commercial refractory alloys.

Chapter 6

Conclusions and Outlook

6.1 Conclusion and design guidelines

Precipitation strengthened Nb-based alloys are candidate high temperature materials for applications with operating temperatures between 1300-1500 °C. The Nb matrix provides ducitlity, toughness, and fabricability, while precipitation strengthening introduces obstacles for dislocation motion, improving strength and creep resistance. This design strategy has been applied both historically, with the investigation of Nb-based alloys strengthened by interstitial compounds, and in the contemporary pursuit of β + β' alloys with intermetallic precipitates. The latter approach seeks to overcome the microstructural instability of the incoherent interstitial compounds by developing alloys with coherent intermetallic precipitates, where the low interfacial energy between the strengthening phase and the matrix reduces the driving force for coarsening. Of the candidate intermetallic phases, Ru-B2 phases are particularly promising due to their high thermal stability and comparable lattice parameters with Nb. Therefore, this dissertation sought to evaluate the potential of using Ru-B2 phases as strengthening precipitates for Nb-based alloys.

The present investigations have demonstrated that Ru is a versatile and robust B2 former in refractory alloys. For Nb-based alloys in particular, additions of Hf and Zr can be used to form coherent HfRu- or ZrRu-B2 phases with tailorable solvus temperatures above 1300 °C. Additionally, Nb-BCC + Ru-B2 alloys can have densities below 9 g/cm^3, can be processed with standard solution and aging pathways, and the resulting matrix compositions are hopeful for achieving sufficient tensile ductility and toughness in future materials, though these properties require further investigation. However, many questions remain regarding dislocation interactions with the precipitates. In the short-term, small-scale testing will be necessary to evaluate if adequate tensile ductility can be achieved in these materials. In the long-term, tailoring the misfit in these materials will require understanding the thermal expansion properties of each phase and development of alloy compositions for specific target temperatures and B2 volume fractions. While many alloys form deleterious tertiary phases on the grain boundaries, there are several potential strategies for mitigating their formation. One strategy, which is is to increase the stability of the B2 phase relative to other deleterious phases with additions of Hf, was successfully demonstrated in Ch. 5.

The pursuit of $\beta + \beta'$ Nb-based alloys still faces significant challenges. The two-phase microstructure theoretically assists with decoupling ductility and strength, but does not solve many of the intrinsic limitations that characterize the refractory metals. Issues such as DBTT, density, cost, and interstitial sensitivity remain to be investigated. This design strategy also does not provide a direct solution to the catastrophic oxidation of refractory metals at high temperature, which has been and remains the Achilles heel of refractory alloys[49, 67, 21]. The challenges faced by $\beta + \beta'$ alloys are multi-faceted and will require leveraging all of the tools of materials science that have been used in service of improving Ni-base superalloys. However, Ru-based B2 phases appear a promising path forward for further development of refractory alloys and, at the very least, provide a model system for investigating the potential of $\beta + \beta'$ alloys overall.

The following design principles can be applied when developing the next generation of Nb-based alloys strengthened by Ru-B2 precipitates. These draw upon both the experimental investigations described in this dissertation and insights from the historical refractory literature.

1. Matrix compositions should be designed such that the intrinsic ductility of Nb is maintained. This favors the use of V as the primary matrix solute, present in the highest concentration after Nb, due to its small lattice parameter and negligible effect on ductility. In small quantities, the following elements could also be beneficial: Al, Mo, Ta, and W.

    - Additions of Mo, Ta, and W can be used improve the creep strength of the matrix. The following additional properties should be considered: Mo and W are detrimental to ductility; Mo, Ta, and W are detrimental to density; and Ta is potentially detrimental, and Mo and W are potentially beneficial, to overall $T_{s,B2}$ and $v_{f,B2}$.
    - Al additions may be introduced to improve oxidation resistance, reduce density, and decrease the lattice parameter of the matrix. The following additional properties should be considered: the formation of deleterious (Al,Zr) and (Al,Nb)-rich tertiary phases; the effect of Al on the lattice parameter of the Ru-B2 phase. It is unlikely that Al can added in sufficient amounts to provide significant oxidation resistance, unless the Al content partitions primarily to the B2 phase.

2. The binary HfRu- and ZrRu-B2 phases have the largest lattice parameters of the known Ru-B2 phases and have the lowest lattice misfit with pure Nb (≤ 3 %). Therefore, Hf and Zr are desirable as the primary B2 forming elements.
    - Alloys based on HfRu allow for higher $T_{s,B2}$ to be achieved with lower Ru concentrations.
    - Alloys based on ZrRu allow for higher $v_{f,B2}$ to be achieved overall.
3. In the presence of a single B2 former, the V concentrations are fixed and the Ru concentration is directly tied to a number of important properties such as cost, $T_{s,B2}$ and $v_{f,B2}$. Utilizing two mutually soluble B2 formers would provide an opportunity to individually tailor properties. Therefore, alloys should be developed with additions of both Hf and Zr to increase design flexibility.
    - The selected Hf and Zr concentrations should be chosen such that the minimum necessary amount are included. Additions of Hf and Zr beyond the concentrations necessary to produce the maximum $v_{f,B2}$ at a specific Ru content will likely contribute to the formation of deleterious grain boundary phases.
    - The Hf and Zr concentrations should also be selected such that gettering of O from the Nb matrix still occurs.
4. Reducing the Ru solubility of the matrix when possible is desirable. Reducing the Ru solubility of the matrix has the potential to improve the tensile ductility and increase overall $T_{s,B2}$ and $v_{f,B2}$ without increasing the Ru concentration.
    - As discussed in Ch. 4. and by Kube *et al.*[261], additions of Mo appear to reduce the solubility of Ru in the matrix. Given the similarities between Cr, Mo, and W, this is likely true of Cr and W as well. These additions would

need to be balanced with their effects on the matrix lattice parameter, density, and tensile ductility.

- The investigated alloys exhibit a rapid raise in Ru solubility at temperatures above 1000 °C. If possible, alloys should be designed such that the solubility of Ru in the matrix does not change significantly above and below the desired application temperature. This provides microstructural stability in the event of temperature fluctuations.

Many interesting and pressing questions remain regarding the fundamental mechanisms that operate in these systems and which, when answered, will arguably change the way these materials are designed. Some of the outstanding questions are discussed in the following sections, hopefully to inspire debate and investigation. In particular, sections 6.2 and 6.3 detail potential investigations into precipitate deformation mechanisms and coarsening behavior, while section 6.4 outlines further questions that are also important for understanding and controlling the behaviors of these alloys.

6.2 Deformation behaviors of the Ru-B2 precipitates

This area of future research would address the following question: *Are Ru-B2 precipitates shearable or unshearable obstacles at ambient and elevated temperatures?*

Interactions between the B2 precipitates and dislocations will dictate the deformation behavior of these alloys. Intermetallic precipitates typically participate in deformation via one of two mechanisms: (i) precipitate shearing and (ii) precipitate bypassing[298, 299]. For precipitate shearing, dislocations will cross from the matrix into the strengthening precipitate during deformation (Figure 6.1d). Due to the ordering in the intermetallic, the passage of a dislocation through the precipitate results in the formation of an anti-phase boundary (APB). The energy associated with the formation of the anti-phase boundary, γ_{APB}, represents a barrier that the dislocations must overcome before they can cut the particles and is a large contributor to the overall precipitation strengthening that occurs in an alloy with shearable obstacles[4]. In the case of precipitate bypassing, dislocations do not cross from the matrix to the precipitate. Instead, dislocations will bow between obstacles and eventually breakaway, leaving a dislocation loop around the obstacle (Figure 6.1a). In the case of BCC alloys, cross-slip may also contribute to the bypass process. The strengthening imparted by these mechanisms is a function of precipitate size and as shearable precipitates coarsen the deformation mechanism may change[13]. This transition occurs in Ni-based superalloys and optimal hardening is observed in the precipitate shearing regime[4]. The interstitial compounds that were used historically to strengthen Nb-based alloys were unshearable obstacles and provided strength through the bypassing mechanism[113]. (Al,Ti,Zr)-B2s in RMPEAs, which are the closest analogous system to Ru-B2 strengthened Nb-based alloys, have demonstrated evidence of precipitate shearing at 600 °C[255].

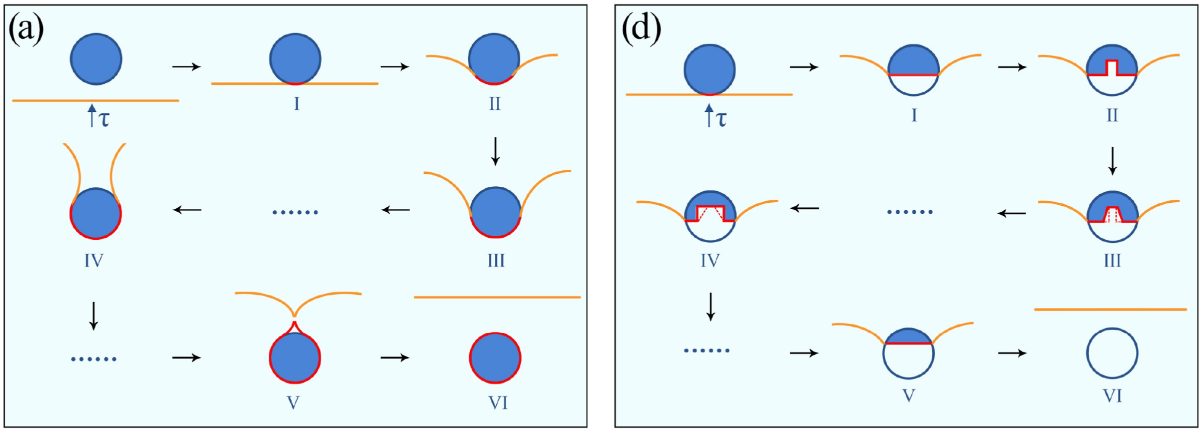

Figure 6.1: (a) Schematic diagram for bypassing of precipitates by dislocations. (d) Schematic diagram for shearing of precipitates by dislocations. Paired dislocations are not represented. Reproduced from Sun *et al.* Thermally-activated precipitation strengthening. J. Mater. Res. Technol. 29, 2131–2141 (2024). Reproduced with permission [13].

Early evidence suggests that the HfRu-B2 and ZrRu-B2 precipitates are shearable, though the calculated anti-phase boundary energy for HfRu (883 mJ/m^2) is high compared to other intermetallics[300, 301]. The APB energy for ZrRu has not yet been reported, but is likely similar in magnitude to that of HfRu. In the room temperature micropillar compression experiments discussed in Ch. 4., with HfRu precipitates in a (Mo, Nb, Ta)-BCC matrix, the microstructure demonstrated evidence of both shearing (suggested by the presence of paired dislocations) and bypassing (suggested by the presence of dislocation loops around precipitates). Given the narrow precipitate size distribution, the presence of both mechanisms is surprising, though the results may be affected by the small size of the micropillars. It is also possible that complex dislocation interactions occur that could also result in paired dislocations, independent of precipitate shearing.

To further investigate whether HfRu and ZrRu are shearable or unshearable obstacles, post-mortem transmission electron microscopy (TEM) investigations of bulk samples could be performed. Room temperature and 1000 °C compression tests on Hf_5Ru_4-$Nb_{63}V_{28}$ and $Hf_2Zr_8Ru_9$-$Nb_{63}V_{18}$ (Ch. 5) would provide a first look at dislocation mechanisms without requiring significant alloy or processing development. While tensile tests are preferred, a viable thermomechanical processing pathway has yet to be developed for these materials. Additionally, the small amount of Hf in $Hf_2Zr_8Ru_9$-$Nb_{63}V_{18}$ would still provide Zr-rich B2 precipitates for comparison while removing grain boundary phases that could cause premature fracture. For further exploration, 20-40g samples could be arc melted, homogenized, and then aged at 1000 °C. This aging temperature currently results in the highest B2 volume fractions and lowest Ru matrix concentrations, improving the likelihood of matrix ductility. Samples with varying aging times of 10, 40, 160, and 640 h would provide insight into changes in deformation mechanism as a function of precipitate radius. Due to the high concentrations of dislocations that occur at large deformation strains, which makes TEM investigations more difficult, the compression tests should be interrupted after the yield point is reached, between 1 and 5% plastic strain.

Post-mortem investigations of the bulk compression specimens could be combined with observations from *in situ* TEM experiments, where dislocation shearing or bypassing of the precipitates could be directly observed in micro-tensile specimens[93]. These experiments utilize tensile loading and can proceed until fracture, which would provide additional insights into the potential tensile ductility of these compositions. Samples for *in situ* TEM experiments could be lifted from within the grains, avoiding the grain boundary precipitates and allowing for pure HfRu and ZrRu precipitates to be compared.

6.3 Coarsening of the Ru-B2 precipitates

This area of future research would address the following question: *What is the coarsening rate of coherent Ru-B2 precipitates at application temperatures?*

The introduction of coherent intermetallic precipitates is meant to overcome the issues of microstructural instability that hindered the development of interstitial strengthened refractory alloys. However, the coarsening rate at desired application temperatures of 1300-1500 °C has yet to be evaluated. Evaluating coarsening would require developing compositions where an appreciable volume fraction of B2 precipitates (≥ 10 %) can be achieved between 1300-1500 °C and the lattice misfit can be reduced to $\leq 0.5\%$ at the testing temperature. Two alloys investigated in this dissertation, $Hf_{11}Ru_9$-$Nb_{52}V_{28}$ (Ch. 4) and $Hf_2Zr_8Ru_9$-$Nb_{63}V_{18}$ (Ch. 5), could be modified for this purpose.

The variations in B2 volume fraction with temperature for $Hf_{11}Ru_9$-$Nb_{52}V_{28}$ and $Hf_2Zr_8Ru_9$-$Nb_{63}V_{18}$ have been reproduced in Figure 6.2 from Chs. 4 and 5. For each composition, the maximum achievable B2 volume fraction is assumed to occur near 1000

°C. With increasing temperature, the solubility of Ru within the (Nb,V)-matrix increases and the B2 volume fractions decrease.

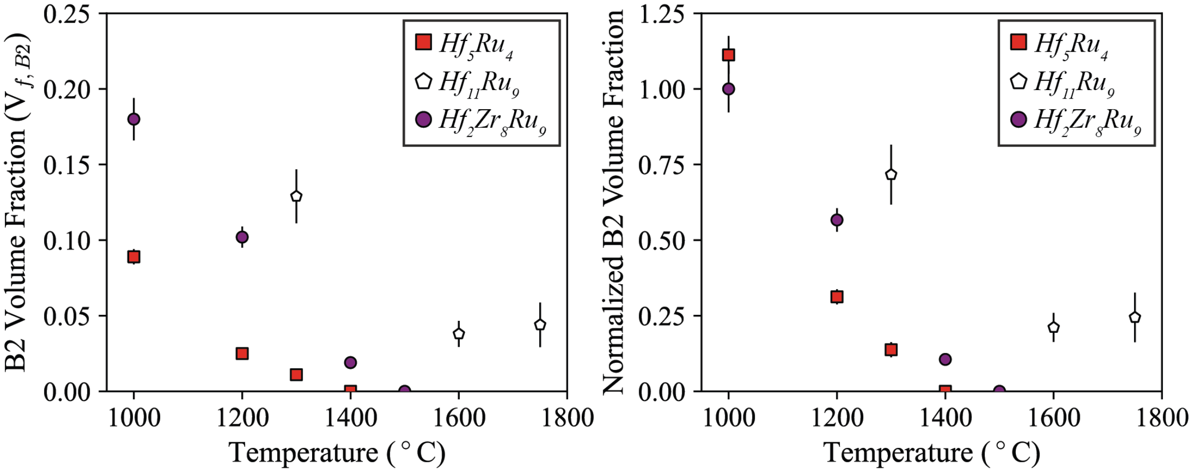

Figure 6.2: (left) Volume fraction of the B2 phase present at each annealing temperature for Hf_5Ru_4-$Nb_{63}V_{28}$, $Hf_{11}Ru_9$-$Nb_{52}V_{28}$, and $Hf_2Zr_8Ru_9$-$Nb_{63}V_{18}$. Volume fractions may be slightly over estimated due to the etching of the BCC matrix during vibratory polishing. (right) Normalized B2 volume fraction for each temperature, where the experimental B2 volume fractions have been divided by 2 * the Ru concentration.

$Hf_{11}Ru_9$-$Nb_{52}V_{28}$ has a solvus temperature between 1750-1830 °C and can achieve a volume fraction of $\approx 13\%$ at 1300 °C. Therefore, this composition could be used nearly unchanged if higher furnace cooling rates could be achieved to suppress precipitate growth on cooling; one suggestion would be to reduce the Hf content to 10 or 9 at% to reduce tertiary phase formation. $Hf_2Zr_8Ru_9$-$Nb_{63}V_{18}$ has a solvus temperature between 1300-1400 °C. The volume fraction at 1300 °C still needs to be evaluated, but is likely $\approx 6\%$ if the volume fractions at 1200 and 1400 °C are interpolated. This is fairly low and the B2 volume fraction and solvus temperature are not directly comparable to $Hf_{11}Ru_9$-$Nb_{52}V_{28}$. Therefore, either the Ru concentration (and accompanying Hf and Zr concentration) or the Hf:Zr ratio would need to be increased. It would preferable to increase the Ru concentration to maintain a Zr-rich B2 phase to compare to the Hf-rich phase in $Hf_{11}Ru_9$-

$Nb_{52}V_{28}$. An increase of 3-4 at% Ru would likely be required to match the B2 volume fraction of $Hf_{11}Ru_9$-$Nb_{52}V_{28}$, assuming each additional 1 at% of Ru results in 2% more B2 once the solubility limit is exceeded. The phase equilibria of $Hf_2Zr_{11}Ru_{13}$-$Nb_{56}V_{18}$ should be evaluated at 1300 °C to determine if the Hf:Zr ratio should be increased to reduce tertiary phase formation and sequential anneals performed to determine the solvus temperature. In both cases, once the initial composition is selected, the V concentration should then be tuned to reduce the lattice misfit between the BCC and B2 phases to $\leq$ 0.5% at 1300 °C. If possible, methods like high temperature x-ray diffraction or neutron diffraction should be used to measure the constrained misfit at 1300 °C[302, 303, 288]; otherwise, preliminary aging treatments at 1300 °C on alloys with varying V content can be used to evaluate the misfit at room temperature and precipitate size[304, 305].

Once compositions are selected, aging treatments at 1300 °C for 1, 4, 16, 64, and 256 h can be performed. From the mean precipitate radii at each condition, a coarsening rate constant, K, can be calculated. The change in precipitate radius with time can be approximated by[146, 306]:

$$r_t^3 - r_0^3 = Kt \tag{6.1}$$

where r_t^3 is the average radius at time t and r_0^3 is the mean radius at the start of coarsening or t = 0. These coarsening rate constants would provide a preliminary evaluation of microstructural stability in these systems and provide insight into next steps for alloy development. Further, K be used to determine the interfacial energies present at the BCC-B2 interfaces[307], which are essential for future modeling efforts. K can be approximated by[146, 306]:

$$K = \frac{8\gamma V_m^{B2}}{9RT \sum_i^N (c_i^{B2} - c_i^{BCC})^2 / D_i^{BCC} c_i^{B2}} \tag{6.2}$$

where γ is the interfacial energy, V_m^{B2} is the molar volume of the B2 phase, R is the ideal gas constant, T is the temperature, and c_i^j and D_i^j are the atomic fractions and diffusion coefficients of solute i in the phase j (BCC and B2). This would also require measurements of the compositions of the BCC and B2 phases, and, if not available in the literature, an evaluation of the diffusion coefficients of the solutes.

After initial coarsening experiments are performed, the effect of Mo or W additions on coarsening rate, which are hypothesised to reduce the solubility of Ru in the BCC matrix and which would likely reduce overall diffusivity, could be investigated. It should also be noted that, due to the high solvus temperatures these alloys possess, these alloys may be difficult to process and would require vacuum furnaces capable of rapid quenching from solution temperatures above 1500 °C.

6.4 Further outstanding questions

1. **Will Nb-BCC + Ru-B2 alloys demonstrate appreciable tensile ductility?** Only a small amount of tensile data is available for refractory alloys containing Ru, with the closest equivalent to Nb being Ta-Ru binary alloys[297, 51]. These results suggest Ru is an embrittling element for the (Nb,V)-matrix and the solubility of Ru in the matrix should to be limited to < 5 at% to maintain appreciable tensile ductility. As discussed in Ch. 5, the equilibrium concentration of Ru in the matrix falls below this threshold for both Hf- and Zr-based alloys when the maximum B2 volume fraction is achieved. This is promising. However, it is unknown whether the Ru ductility limit for a (Nb,V)-based matrix is more or less than in binary Ta-Ru alloys, how the matrix composition will change in light of other alloy design decisions discussed throughout this dissertation, or how dislocation interactions

with the B2 precipitates will impact ductility. While not highlighted in the previous two sections, this is an important avenue of research.

2. **What is a sufficient volume fraction of the B2 precipitates?** V additions are not beneficial for creep resistance in Nb-based alloys dependant on solid solution strengthening[46]. Large amounts of V, such as the quantity necessary to tailor the coherency of the BCC + B2 phases, and the presence of second phases will both have a negative effect on the melting point of the alloy. Therefore, what volume fraction of B2 phases are necessary to overcome the strength debt incurred by decreasing the melting point? How will creep resistance vary as a function of B2 volume fraction and precipitate radius? Preliminary mechanical property investigations of compositions developed in this dissertation suggest that even low volume fractions (≤ 0.2) of B2 can provide substantial short-term strengthening to temperatures up to 1000 °C when tested in compression (Figure 6.3). However, tensile and creep testing at temperatures between 1300-1500 °C are necessary to properly address this question.

3. **Do viable substitutions for Ru exist?** Ru is a platinum group element and cost \$6000-\$9000/kg from 2010 to 2019[308, 309]. Given the amounts of Ru currently required to raise the B2 solvus temperatures above 1300 °C, the investigated compositions are not likely to be adopted commercially. Therefore, do alloying agents exist that can be directly substituted for Ru in HfRu- and ZrRu-B2 alloys? The composition of AlRu-B2 phases, due to the lower thermal stability, can accommodate large amounts of other elements, resulting in significant changes to the B2 composition and lattice parameter[261]. So far, this has not been observed for HfRu and ZrRu, which are the B2 phases with the largest lattice parameters and the most suitable for Nb-based alloys. Further, use of less expensive alternatives,

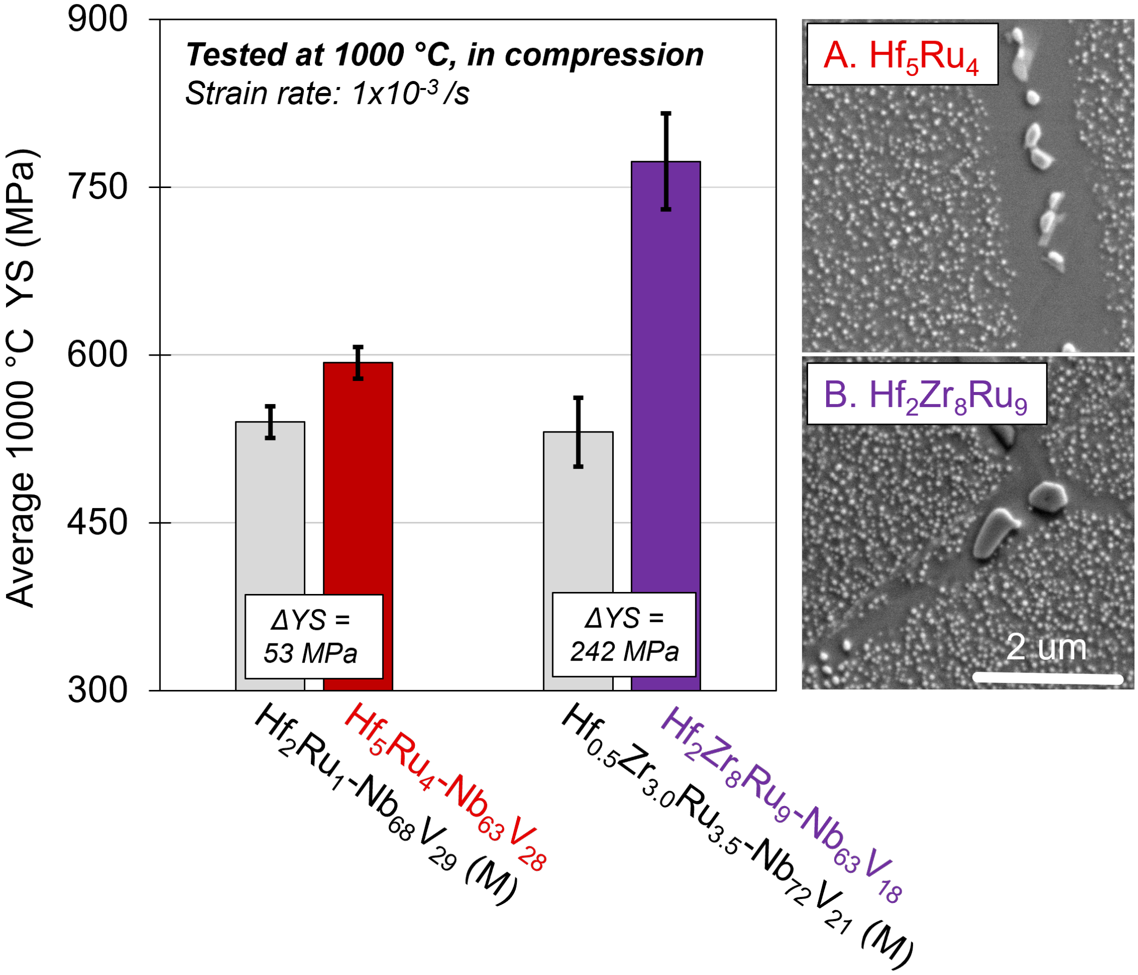

Figure 6.3: Average compressive yield strengths of β + β' and their matrix compositions at 1000 °C. All alloys were homogenized at 1600 °C for 20 h; the β + β' alloys were subsequently aged at 1000 °C for 160 h. The HfRu-B2 precipitates in Hf_5Ru_4-$Nb_{63}V_{28}$ have an average radius ≈ 25 nm and a $v_{f,B2} \leq 0.1$. The (Zr,Hf)Ru-B2 precipitates in $Hf_2Zr_8Ru_4$-$Nb_{63}V_{18}$ have an average radius ≈ 32 nm and a $v_{f,B2} \leq 0.2$. Further characterization of the B2 precipitates is ongoing. The corresponding matrix compositions were derived from the TEM matrix compositions reported in Chapter 5 (Table 5.6). The matrix compositions are plotted in grey, marked with an (M), and plotted adjacent to the corresponding β + β' composition. The compression cylinders were 4 mm in diameter and 6 mm tall; the strain rate was $1x10^{-3}$/s. Significant strengthening is observed in both β + β' alloys compared to their matrices, with increasing $v_{f,B2}$ corresponding to increased strengthening.

such as Fe or Co, are constrained by their negative effect on the melting temperature of Nb and the small lattices parameters of the B2 phases. Unfortunately, computational investigation of sublattice substitutions in binary HfRu[310] and ZrRu[311] indicate Hf and Zr show strong preferences to substitute for the other on their lattice, but the other elements investigated demonstrated no preference for either the Hf/Zr or Ru sublattice. The element with the strongest (but still small) preference for the Ru sublattice was Os. Potential substitutions for Ru are therefore not immediately apparent. An alternative solution to the issue of cost is to develop alternative mineral extraction routes[312].

4. **Once a Ru concentration is selected, are Hf/Zr-poor or Hf/Zr-rich compositions desirable?** Hf and Zr additions are necessary to form the Ru-B2 phases. However, they also form additional phases, as observed in Ch. 5., which can be deleterious for ductility when they form preferentially on the grain boundaries. Therefore, it is important to determine whether excess (Hf + Zr > Ru), equivalent (Hf + Zr = Ru), or deficient (Hf + Zr < Ru) concentrations of Hf and Zr are necessary. Experimentally, the Ru-B2 phases are not composed of 50 at% Ru; instead, the measured Ru concentrations varied from 43-53 at% Ru. Therefore, in alloys with B2 phases that contain < 50 at% Ru, it is possible excess Hf and Zr are necessary to form the maximum possible B2 volume fraction. The inverse is true for alloys where the B2 composition contains > 50 at% Ru. However, the presence of Hf/Ru/Zr-containing tertiary phases (particularly in Zr-rich alloys), the potential effect of O on phase equilibria (addressed in question 5), possible changes in Ru-B2 composition with temperature, and solubility of other alloying elements, such as Nb and V, within the B2 phase complicates this analysis. To address this question, it would be helpful to evaluate the phase diagrams relevant to these systems, both

for direct use and to support the improvement of predictive tools like CALPHAD. Most of the Ru binary and ternary phase diagrams are either unassessed or have not be re-evaluated since the mid-1970's. The Ru-X-Y systems, where X = Hf or Zr and Y = Nb or V, are the most immediately relevant, followed by Mo- and W-containing systems.

5. **What effect does oxygen have on the phase equilibria in these systems?** The O content of the alloys investigated in this dissertation range from 200-600 ppmw and all microstructures contain oxide grains. Therefore, it can be assumed that observed phase equilibria is affected to some degree by the presence of oxygen. The impact of O may be two-fold: (i) through the the promotion of tertiary phases or (ii) by affecting the equilibrium concentration of Hf or Zr that is interacting with the other solutes, such as Ru. For (i), it is known that increasing the O content of refractory alloys promotes the presence of HCP (stemming from the α allotrophs of Hf, Ti, and Zr) and secondary BCC phases (stemming from BCC1 + BCC2 miscibility gaps present within the Nb-Zr and Ta-Zr binary systems)[290]. Beyond the observed β-Hf phase, which is likely promoted by O, it is currently unknown how changes in the O content would affect the other Hf- and Zr-rich tertiary phases observed in Ch. 5. It is possible that reducing the O content could reduce the population of grain boundary phases, improving mechanical properties. For (ii), O can bond with Hf and Zr to form oxide grains. This behavior is used to getter oxygen from the disordered BCC solid solution- small amounts of the reactive elements reduce solubility of oxygen in the disordered BCC phase and trap the oxygen content within oxides phases, improving ductility. Assuming the oxide phases are more stable then the other phases and are present in sufficient amounts to effect the composition, excess Hf and Zr additions above the ideal

(Hf,Zr):Ru ratio may be necessary to compensate for the loss of Hf and Zr to the oxides (or other oxygen-stabilized Hf/Zr-rich phases that form). This assumption is supported by the qualitative observations of phase stability at the edges of annealed samples, where the infiltration of oxygen from the furnace environment results in the replacement of the other phases (including the Ru-B2 phases) with oxides.

6. **What is the oxidation behavior of these systems?** This question is closely related to question 5. Oxidation resistance was not considered as a design criteria but is a critical property for high temperature alloys. While oxidation tests were not performed in this dissertation, the oxidation resistance of the investigated alloys is likely poor. Therefore, consistent with the needs of current commercial refractory alloys, Nb-based alloys with Ru-B2 precipitates will require protective coatings in order to operate in non-inert environments. To increase chances of success, these protective coatings need to be developed concurrently with the development of the underlying $\beta + \beta'$ substrate.

Appendix A

Alloy Compositions

]

Table A.1: Bulk compositions (at%) and interstitial contents (ppmw) of all alloys investigated. Bulk compositions were measured via WDXRF, O and N contents by inert gas fusion, and C contents by combustion analysis. Alloy compositions are standardized to alphabetical ordering for the elements, which may be distinct from the terminology used in a specific chapter. Alloys with "UCSB" as a source were arc melted by Carolina Frey; Alloys from "GE" were arc melted by Scott Oppenheimer.

Alloy	**Source**	**Present in**	**Hf**	**Mo**	**Nb**	**Ru**	**Ta**	**V**	**W**	**Zr**	**O**	**N**	**C**
$Hf_{20}Nb_{20}Ru_{20}Ta_{20}Zr_{20}$	UCSB	Chapter 2	20.9	-	20.0	19.9	19.5			19.7	620	620	75
$Mo_{25}Nb_{25}Ru_{25}Ta_{25}$	GE	Chapter 3	-	24.0	25.9	25.0	25.2	-	-	-	-	-	-
$Mo_{20}Nb_{20}Ru_{20}Ta_{20}W_{20}$	GE	Chapter 3	-	18.5	21.7	21.5	20.1	-	18.2	-	276	30	-
$Hf_{33}Mo_{34}Ru_{33}$	GE	Chapter 3	32.6	35.3	-	32.1	-	-	-	-	1040	30	-
$Hf_{25}Mo_{25}Nb_{25}Ru_{25}$	GE	Chapter 3	25.5	24.7	25.6	24.3	-	-	-	-	858	77	-
$Hf_{25}Mo_{25}Ru_{25}Ta_{25}$	GE	Chapter 3	27.8	23.9	-	23.7	24.7	-	-	-	744	57	-
$Hf_{20}Mo_{20}Nb_{20}Ru_{20}Ta_{20}$	GE	Chapter 3	20.5	19.7	20.6	18.6	20.6	-	-	-	-	-	-
$Hf_{25}Nb_{25}Ru_{25}W_{25}$	GE	Chapter 3	24.8	-	24.0	28.3	-	-	22.9	-	-	-	-
$Hf_{11}Mo_{28}Nb_{22}Ru_{9}Ta_{30}$	UCSB	Chapter 4	11.7	27.8	23.1	8.0	29.5	-	-	-	180	20	-
$Hf_{11}Mo_{28}Nb_{52}Ru_{9}$	UCSB	Chapter 4	11.8	26.8	52.6	8.8	-	-	-	-	170	23	-
$Hf_{11}Nb_{52}Ru_{9}V_{28}$	UCSB	Chapter 4	11.5	-	53.0	8.9	-	26.6	-	-	300	36	-
$Hf_{3}Nb_{67}Ru_{2}V_{28}$	UCSB	Chapter 5	3.0	-	69.0	1.7	-	26.3	-	-	442	22	-
$Hf_{5}Nb_{63}Ru_{4}V_{28}$	UCSB	Chapter 5	5.2	-	64.6	4.2	-	26.1	-	-	360	45	-
$Nb_{73}Ru_{4}V_{18}Zr_{5}$	UCSB	Chapter 5	-	-	74.1	3.9	-	17.4	-	4.6	330	47	-
$Nb_{67}Ru_{7}V_{18}Zr_{8}$	UCSB	Chapter 5	-	-	70.9	6.4	-	16.9	-	5.8	487	21	-
$Nb_{63}Ru_{9}V_{18}Zr_{10}$	UCSB	Chapter 5	-	-	64.6	8.4	-	17.3	-	9.7	380	30	-
$Hf_{2}Nb_{63}Ru_{9}V_{18}Zr_{8}$	UCSB	Chapter 5	2.2	-	64.6	8.5	-	16.8	-	7.9	420	34	-
$Hf_{2}Nb_{63}Ru_{9}V_{18}Zr_{8}$	UCSB	Chapter 6	2.0	-	66.4	8.4	-	16.1	-	7.2	-	-	-
$Hf_{5}Nb_{63}Ru_{4}V_{28}$	UCSB	Chapter 6	5.0	-	64.2	4.4	-	26.4	-	-	-	-	-
$Hf_{0.5}Nb_{72}Ru_{3.5}V_{21}Zr_{3.0}$	UCSB	Chapter 6	0.5	-	74.5	3.5	-	18.8	-	2.7	-	-	-
$Hf_{2}Nb_{68}Ru_{1}V_{29}$	UCSB	Chapter 6	2.0	-	70.0	1.3	-	26.7	-	-	-	-	-

Bibliography

[1] T. M. Pollock, *Alloy design for aircraft engines*, *Nature Materials* **15** (2016), no. 8 809–815.

[2] D. Banerjee and J. C. Williams, *Materials and engineering: An evolving landscape*, *MRS Bulletin* **40** (2015), no. 12 999–1008.

[3] J. Buongiorno, M. Corradini, J. Parsons, and D. Petti, *Nuclear energy in a carbon-constrained world: Big challenges and big opportunities*, *IEEE Power and Energy Magazine* **17** (2019), no. 2 69–77.

[4] R. C. Reed, *The Superalloys: Fundementals and Applications.* Cambridge University Press, New York, 2006.

[5] R. E. Schafrik, *Materials for a Non-Steady-State World*, *Metallurgical and Materials Transactions B: Process Metallurgy and Materials Processing Science* **47** (2016), no. 3 1505–1515.

[6] *Superalloys for gas turbine engines*, in *Introduction to Aerospace Materials* (A. P. Mouritz, ed.), pp. 251–267. Woodhead Publishing Limited, 2012.

[7] C. Sims, *A History of Superalloy Metallurgy for Superalloy Metallurgists*, in *Superalloys 1984 (Fifth International Symposium)* (Maurice Gell, ed.), (Warrendale), pp. 399–419, AIME, 1984.

[8] A. F. Giamei, *Development of single crystal superalloys: a brief history*, *Adv. Mater. Process* **171** (2013), no. 9 26–30.

[9] A. Baldan, *Progress in Ostwald ripening theories and their applications to the γ-precipitates in nickel-base superalloys, Part II: Nickel-base superalloys*, *Journal of Materials Science* **37** (2002), no. 12 2379–2405.

[10] M. Epler, *Structures by Precipitation from Solid Solution*, in *ASM Handbook* (G. F. Vander Voort, ed.), vol. 9, pp. 134–139. ASM International, 2004.

[11] B. Miesenberger, E. Kozeschnik, B. Milkereit, P. Warczok, and E. Povoden-Karadeniz, *Computational analysis of heterogeneous nucleation and*

precipitation in AA6005 Al-alloy during continuous cooling DSC experiments, *Materialia* **25** (2022) 101538.

[12] R. D. Field, T. Pollock, and W. Murphy, *The development of g/g' interfacial dislocation networks during creep in Ni-base superalloys*, in *Superalloys 1992* (S. Antolovich, R. Stusrud, R. MacKay, D. Anton, T. Khan, R. Kissinger, and D. Klarstrom, eds.), (Warrendale), pp. 557–566, TMS (The Minerals, Metals Materials Society), 1992.

[13] G. Sun, L. Zhang, and B. Wen, *Thermally-activated precipitation strengthening*, *Journal of Materials Research and Technology* **29** (2024), no. February 2131–2141.

[14] J. S. Van Sluytman and T. M. Pollock, *Optimal precipitate shapes in nickel-base γ–γ alloys*, *Acta Materialia* **60** (2012), no. 4 1771–1783.

[15] R. Darolia, *Development of strong, oxidation and corrosion resistant nickel-based superalloys: critical review of challenges, progress and prospects*, *International Materials Reviews* **64** (2019), no. 6 355–380.

[16] K. V. Vamsi and S. Karthikeyan, *High-throughput estimation of planar fault energies in A3B compounds with L12 structure*, *Acta Materialia* **145** (2018) 532–542.

[17] J. S. Van Sluytman, A. L. Fontaine, J. M. Cairney, and T. M. Pollock, *Elemental partitioning of platinum group metal containing Ni-base superalloys using electron microprobe analysis and atom probe tomography*, *Acta Materialia* **58** (2010), no. 6 1952–1962.

[18] P. Kontis, H. A. Yusof, S. Pedrazzini, M. Danaie, K. L. Moore, P. A. Bagot, M. P. Moody, C. R. Grovenor, and R. C. Reed, *On the effect of boron on grain boundary character in a new polycrystalline superalloy*, *Acta Materialia* **103** (2016) 688–699.

[19] A. R. Ericks, F. W. Zok, D. L. Poerschke, and C. G. Levi, *Protocol for selecting exemplary silicate deposit compositions for evaluating thermal and environmental barrier coatings*, *Journal of the American Ceramic Society* **105** (2022), no. 6 3665–3688.

[20] F. H. Stott, G. C. Wood, and J. Stringer, *The influence of alloying elements on the development and maintenance of protective scales*, *Oxidation of Metals* **44** (1995), no. 1-2 113–145.

[21] B. Gorr, S. Schellert, F. Müller, H. J. Christ, A. Kauffmann, and M. Heilmaier, *Current Status of Research on the Oxidation Behavior of Refractory High Entropy Alloys*, *Advanced Engineering Materials* **23** (2021), no. 5.

[22] R. T. Wu and R. C. Reed, *On the compatibility of single crystal superalloys with a thermal barrier coating system*, *Acta Materialia* **56** (2008), no. 3 313–323.

[23] I. Barwinska, M. Kopec, D. Kukla, C. Senderowski, and Z. L. Kowalewski, *Thermal Barrier Coatings for High-Temperature Performance of Nickel-Based Superalloys: A Synthetic Review*, *Coatings* **13** (2023), no. 4 1–21.

[24] R. Pyle and B. Aldrin, *Space 2.0: How Private Spaceflight, a Resurgent NASA, and International Partners are Creating a New Space Age*. BenBella Books, 2019.

[25] K. K. Chawla, *Ceramic Matrix Composites*, pp. 251–296. Springer International Publishing, Cham, 2019.

[26] I. Wolff, *Toward a better understanding of Ruthenium Aluminide*, *JOM* **49** (1997) 34–39.

[27] A. Suzuki, H. Inui, and T. M. Pollock, *L1 2 -Strengthened Cobalt-Base Superalloys*, *Annual Review of Materials Research* **45** (jul, 2015) 345–368, [1011.1669].

[28] A. S. B. P. Bewlay S. Nag and M. J. Weimer, *TiAl alloys in commercial aircraft engines*, *Materials at High Temperatures* **33** (2016), no. 4-5 549–559.

[29] N. N. Greenwood, *Vanadium to dubnium: from confusion through clarity to complexity*, *Catalysis Today* **78** (2003), no. 1 5–11.

[30] G. Rayner-Canham and Z. Zheng, *Naming elements after scientists: an account of a controversy*, *Foundations of Chemistry* **10** (2008), no. 1 13–18.

[31] H. Burte, T. Cooper, and J. Elbaum, *Refractory metals - an assessment*. AIAA, 1964.

[32] I. Machlin, *Symposium on metallurgy and technology of refractory metal alloys—A state-of-the-art review*, *JOM* **20** (1968), no. 9 21–25.

[33] J. Cooper R. H. and E. E. Hoffman, *Refractory alloy technology for space nuclear power applications*, (United States), 1984.

[34] E. N. C. Dalder, T. Grobstein, and C. S. Olsen, eds., *Evolution of Refractory Metals and Alloys: A Proceedings of a Symposium Sponsored by the Refractory Metals Committee of the Structural Materials Division Held at the 1993 TMS Annual Meeting, Denver, Colorado, February 21-25, 1993*. TMS (The Minerals, Metals Materials Society), 1994.

[35] G. M. Ault, *A decade of progress in refractory metals [68th astm annual meeting]*, tech. rep., 1965.

[36] H. R. Smith, J. Y. Hum, A. Donlevy, and C. d.A. Hunt, *The mechanical properties of some ductile niobium and tantalum base alloys prepared by electron beam melting*, *Journal of The Less-Common Metals* **2** (1960) 69–75.

[37] J. Wadsworth, T. G. Nieh, and J. J. Stephens, *Recent advances in aerospace refractory metal alloys*, *International Materials Reviews* **33** (1988), no. 1 131–150.

[38] D. L. Anton, D. B. Snow, L. H. Favrow, and A. F. Giamei, *Dispersion Strengthening of High Temperature Niobium Alloys*, tech. rep., United Technologies Research Center, East Hartford, 1989.

[39] V. V. Bukhanovskii, V. A. Borisenko, V. K. Kharchenko, and I. Mamuzic, *High-temperature strength of niobium alloy 5VMTs with a silicide-ceramic coating. Part 2. Characteristics of short-term creep*, *Strength of Materials* **36** (2004), no. 5 504–510.

[40] V. V. Bukhanovskii, V. A. Borisenko, V. K. Kharchenko, and I. Mamuzic, *High-temperature strength of niobium alloy 5VMTs with a silicide-ceramic coating. Part 2. Characteristics of short-term creep*, *Strength of Materials* **36** (2004), no. 5 504–510.

[41] P. I. Glushko, B. M. Shirokov, and A. V. Shiyan, *Effect of silicide coatings on the mechanical properties of alloy 5VMTs*, *Powder Metallurgy and Metal Ceramics* **49** (2011), no. 9-10 616–618.

[42] T. Ronald, *Status and applications of materials developed for NASP [International Aerospace Planes and Hypersonics Technologies].* Chattanooga, TN, 1995.

[43] K. Geelhood and W. Luscher, *Degradation and Failure Phenomena of Accident Tolerant Fuel Concepts. FeCrAl Alloy Cladding/ PNNL-30445*, Tech. Rep. June, Pacific Northwest National Laboratory, Richland, 2019.

[44] R. M. Nekkanti and D. M. Dimiduk, *Ductile-Phase Toughening in Niobium-Niobium Silicide Powder Processed Composites*, *MRS Online Proceedings Library* **194** (1990) 175–182.

[45] B. P. Bewlay, M. R. Jackson, and H. A. Lipsitt, *The balance of mechanical and environmental properties of a multielement niobium-niobium silicide-based in situ composite*, *Metallurgical and Materials Transactions A: Physical Metallurgy and Materials Science* **27** (1996), no. 12 3801–3808.

[46] R. G. Frank, *Recent Advances in Columbium Alloys*, in *Refractory Metal Alloys Metallurgy and Technology* (I. Machlin, R. T. Begley, and E. D. Weisert, eds.), ch. Recent Adv, pp. 325–372. Springer New York, New York, 1 ed., 1968.

[47] L. J. Pionke and J. W. Davis, *Technical assessment of niobium alloys data base for fusion reactor applications*, tech. rep., McDonnell Douglas Astronautics Company, 1979.

[48] C. English, *The physical, mechanical, and irradiation behavior of niobium and niobium-base alloys.* Metallurgical Society of AIME, United States, 1984.

[49] R. A. Perkins and G. H. Meier, *The oxidation behavior and protection of niobium*, *Jom* **42** (1990), no. 8 17–21.

[50] N. R. Philips, M. Carl, and N. J. Cunningham, *New Opportunities in Refractory Alloys*, *Metallurgical and Materials Transactions A* **51** (2020), no. 7 3299–3310.

[51] E. J. Rapperport and A. L. Geary, *Fundamental and applied research and development in metallurgy: High Temperature Properties of Refractory Alloys : Summary Technical Report for the Period July 1, 1961 Through June 30, 1962*, tech. rep., United States Atomic Energy Commission, Office of Technical Information, West Concord, 1963.

[52] R. T. Begley, D. L. Harrod, and R. E. Gold, *High Temperature Creep and Fracture Behavior of the Refractory Metals*, in *Refractory Metal Alloys Metallurgy and Technology* (I. Machlin, R. T. Begley, and E. Weisert, eds.), (Washington, D.C.), American Institute of Mining, Metallurgical, and Petrolium Engineers, Inc., Springer New York, 1968.

[53] T. K. Roche and D. L. Graham, *Development of Oxidation Resistant High-Strength, Columbium-Base Alloys*, tech. rep., Union Carbide Corporation, Kokomo, 1970.

[54] D. B. Miracle, O. N. Senkov, C. Frey, S. Rao, and T. M. Pollock, *Strength vs temperature for refractory complex concentrated alloys (RCCAs): A critical comparison with refractory BCC elements and dilute alloys*, *Acta Materialia* **266** (2024) 119692.

[55] Y.-H. Zhang, E. Ma, J. Sun, and W.-Z. Han, *A unified model for ductile-to-brittle transition in body-centered cubic metals*, *Journal of Materials Science Technology* **141** (2023) 193–198.

[56] R. T. Begley and J. H. Bechtold, *Effect of alloying on the mechanical properties of niobium*, *Journal of The Less-Common Metals* **3** (1961) 1–12.

[57] R. Eck and E. Pink, *Effects of working on strength and ductility of molybdenum and tungsten alloys*, *International Journal of Refractory Metals and Hard Materials* **11** (1992) 337–341.

[58] F. R. Schwartzberg and W. D. Klopp, *Elevated-temperature Mechanical Properties and Oxidation Resistance of Columbium and Its Alloys.* DMIC memorandum. Columbus, Ohio, 1959.

[59] G. Hahn, A. Gilbert, and R. I. Jaffee, *The effects of solutes on the ductile-to-brittle transition in refractory metals*, tech. rep., Battelle Memorial Institute, Columbus, Ohio, 1962.

[60] M. G. Ulitchny and R. Gibala, *The effects of interstitial solute additions on the mechanical properties of niobium and tantalum single crystals*, *Journal of The Less-Common Metals* **33** (1973) 105–116.

[61] M. Sankar, R. G. Baligidad, and A. A. Gokhale, *Effect of oxygen on microstructure and mechanical properties of niobium*, *Materials Science and Engineering: A* **569** (2013) 132–136.

[62] P. Wang and W.-z. Han, *Oxygen solutes-regulated low temperature embrittlement and high temperature toughness in vanadium*, *Acta Materialia* (2024) 119983.

[63] S. T. Wlodek, *Coatings for Columbium*, *Journal of The Electrochemical Society* **108** (1961), no. 2 177.

[64] R. E. Pawel and J. J. Campbell, *The Interaction of Stress and Mechanical Property Effects during Oxidation of Tantalum Base Alloys*, *Journal of The Electrochemical Society* **127** (1980), no. 9 2035–2038.

[65] W. W. Webb, J. T. Norton, and C. Wagner, *Oxidation of Tungsten*, *Journal of The Electrochemical Society* **103** (1956), no. 2 107–111.

[66] D. Nagy and S. A. Humphry-Baker, *An oxidation mechanism map for tungsten*, *Scripta Materialia* **209** (2022) 114373.

[67] A. S. Dorcheh and M. C. Galetz, *Challenges in Developing Oxidation-Resistant Chromium-Based Alloys for Applications Above 900°C*, *Jom* **68** (2016), no. 11 2793–2802.

[68] E. N. Sheftel and O. A. Bannykh, *Niobium–Base Alloys*, *International Journal of Refractory Metals and Hard Materials* **12** (1994) 303–314.

[69] B. Cantor, I. T. Chang, P. Knight, and A. J. Vincent, *Microstructural development in equiatomic multicomponent alloys*, *Materials Science and Engineering A* **375-377** (2004), no. 1-2 SPEC. ISS. 213–218.

[70] J. W. Yeh, S. K. Chen, S. J. Lin, J. Y. Gan, T. S. Chin, T. T. Shun, C. H. Tsau, and S. Y. Chang, *Nanostructured high-entropy alloys with multiple principal elements: Novel alloy design concepts and outcomes*, *Advanced Engineering Materials* **6** (2004), no. 5 299–303+274.

[71] J. W. Yeh, Y. L. Chen, S. J. Lin, and S. K. Chen, *High-Entropy Alloys – A New Era of Exploitation*, *Materials Science Forum* **560** (2007) 1–9.

[72] E. J. Pickering and N. G. Jones, *High-entropy alloys: a critical assessment of their founding principles and future prospects*, *International Materials Reviews* **61** (2016), no. 3 183–202.

[73] P.-K. Huang, J.-W. Yeh, T.-T. Shun, and S.-K. Chen, *Multi-Principal-Element Alloys with Improved Oxidation and Wear Resistance for Thermal Spray Coating*, *Advanced Engineering Materials* **6** (2004), no. 1-2 74–78.

[74] D. B. Miracle and O. N. Senkov, *A critical review of high entropy alloys and related concepts*, *Acta Materialia* **122** (2017) 448–511.

[75] W. Steurer, *Single-phase high-entropy alloys – A critical update*, *Materials Characterization* **162** (2020), no. October 2019 110179.

[76] O. N. Senkov, G. B. Wilks, J. M. Scott, and D. B. Miracle, *Mechanical properties of Nb25Mo25Ta 25W25 and V20Nb20Mo 20Ta20W20 refractory high entropy alloys*, *Intermetallics* **19** (2011), no. 5 698–706.

[77] O. N. Senkov, J. M. Scott, S. V. Senkova, F. Meisenkothen, D. B. Miracle, and C. F. Woodward, *Microstructure and elevated temperature properties of a refractory TaNbHfZrTi alloy*, *Journal of Materials Science* **47** (2012), no. 9 4062–4074.

[78] C. K. Borg, C. Frey, J. Moh, T. M. Pollock, S. Gorsse, D. B. Miracle, O. N. Senkov, B. Meredig, and J. E. Saal, *Expanded dataset of mechanical properties and observed phases of multi-principal element alloys*, *Scientific Data* **7** (2020), no. 1 1–6.

[79] R. Arroyave, *Ultimate: Birdshot. final technical report.*, .

[80] O. N. Senkov, D. B. Miracle, K. J. Chaput, and J.-P. Couzinie, *Development and exploration of refractory high entropy alloys—A review*, *Journal of Materials Research* **33** (2018), no. 19 3092–3128.

[81] G. Hausch, *Comment on the paper "On the formation of hierarchical microstructure in a Mo-doped NiCoCr medium-entropy alloy with enhanced strength-ductility synergy" by J. He, S.Makineni, W.Lu,Y.Shang,Z.Lu,Z.Li,B.Gault, Scripta Mater 175(2020)1-6*, *Scripta Materialia* **187** (2020) 1–3.

[82] J. Dąbrowa, M. Zajusz, W. Kucza, G. Cieślak, K. Berent, T. Czeppe, T. Kulik, and M. Danielewski, *Demystifying the sluggish diffusion effect in high entropy alloys*, *Journal of Alloys and Compounds* **783** (2019) 193–207.

[83] J. Zhang, C. Gadelmeier, S. Sen, R. Wang, X. Zhang, Y. Zhong, U. Glatzel, B. Grabowski, G. Wilde, and S. V. Divinski, *Zr diffusion in BCC refractory high entropy alloys: A case of 'non-sluggish' diffusion behavior*, *Acta Materialia* **233** (2022) 117970.

[84] C. Hsu, J. Yeh, S. Chen, and T. Shun, *Wear resistance and high-temperature compression strength of Fcc CuCoNiCrAl*, *Metallurgical and materials transactions. A, Physical metallurgy and materials science* **35** (2004), no. 5 1465–1469.

[85] P. P. Cao, H. L. Huang, S. H. Jiang, X. J. Liu, H. Wang, Y. Wu, and Z. P. Lu, *Microstructural stability and aging behavior of refractory high entropy alloys at intermediate temperatures*, *Journal of Materials Science Technology* **122** (2022) 243–254.

[86] N. D. Stepanov, N. Y. Yurchenko, S. V. Zherebtsov, M. A. Tikhonovsky, and G. A. Salishchev, *Aging behavior of the HfNbTaTiZr high entropy alloy*, *Materials Letters* **211** (2018) 87–90.

[87] H. Y. Yasuda, Y. Yamada, K. Cho, and T. Nagase, *Deformation behavior of HfNbTaTiZr high entropy alloy singe crystals and polycrystals*, *Materials Science and Engineering A* **809** (2021), no. June 2020.

[88] S. P. Wang, E. Ma, and J. Xu, *New ternary equi-atomic refractory medium-entropy alloys with tensile ductility: Hafnium versus titanium into NbTa-based solution*, *Intermetallics* **107** (2019), no. November 2018 15–23.

[89] C. Gadelmeier, Y. Yang, U. Glatzel, and E. P. George, *Creep strength of refractory high-entropy alloy TiZrHfNbTa and comparison with Ni-base superalloy CMSX-4*, *Cell Reports Physical Science* **3** (2022), no. 8 100991.

[90] G. Sahragard-Monfared, C. H. Belcher, S. Bajpai, M. Wirth, A. Devaraj, D. Apelian, E. J. Lavernia, R. O. Ritchie, A. M. Minor, J. C. Gibeling, C. Zhang, and M. Zhang, *Tensile Creep Behavior of the Nb45Ta25Ti15Hf15 Refractory High Entropy Alloy*, *Acta Materialia* (2024) 119940.

[91] L. H. Mills, M. G. Emigh, C. H. Frey, N. R. Philips, S. P. Murray, J. Shin, D. S. Gianola, and T. M. Pollock, *Temperature-dependent tensile behavior of the HfNbTaTiZr multi-principal element alloy*, *Acta Materialia* **245** (2023), no. June 2022 118618.

[92] C. A. Stewart, S. P. Murray, A. Suzuki, T. M. Pollock, and C. G. Levi, *Accelerated discovery of oxidation resistant CoNi-base γ/γ' alloys with high L12 solvus and low density*, *Materials and Design* **189** (2020) 108445.

[93] J. C. Stinville, M. A. Charpagne, A. Cervellon, S. Hemery, F. Wang, P. G. Callahan, V. Valle, and T. M. Pollock, *On the origins of fatigue strength in crystalline metallic materials*, *Science* **377** (2022), no. 6610 1065–1071.

[94] D. K. Jangid, N. R. Brodnik, M. G. Goebel, A. Khan, S. Majeti, M. P. Echlin, S. H. Daly, T. M. Pollock, and B. S. Manjunath, *Adaptable physics-based super-resolution for electron backscatter diffraction maps*, *npj Computational Materials* **8** (2022), no. 1 255.

[95] K. M. Mullin, C. Frey, J. Lamb, S. K. Wu, M. P. Echlin, and T. M. Pollock, *Rapid screening of single phase refractory alloys under laser melting conditions*, *Materials Design* **238** (2024) 112726.

[96] I. J. Beyerlein, P. Cao, and T. M. Pollock, *Complex concentrated alloys and chemical short-range ordering*, *MRS Bulletin* **48** (2023), no. 7 746–752.

[97] S. Chen, Z. H. Aitken, S. Pattamatta, Z. Wu, Z. G. Yu, D. J. Srolovitz, P. K. Liaw, and Y.-W. Zhang, *Short-range ordering alters the dislocation nucleation and propagation in refractory high-entropy alloys*, *Materials Today* **65** (2023) 14–25.

[98] L. T. W. Fey, S. Xu, Y. Su, A. Hunter, and I. J. Beyerlein, *Transitions in the morphology and critical stresses of gliding dislocations in multiprincipal element alloys*, *Phys. Rev. Mater.* **6** (Jan, 2022) 013605.

[99] X. Wang, F. Maresca, and P. Cao, *The hierarchical energy landscape of screw dislocation motion in refractory high-entropy alloys*, *Acta Materialia* **234** (2022) 118022.

[100] M. R. Jones, L. T. W. Fey, and I. J. Beyerlein, *Phase-field dislocation dynamics simulations of temperature-dependent glide mechanisms in niobium*, *Computational Materials Science* **232** (2024) 112652.

[101] C. Baruffi, F. Maresca, and W. A. Curtin, *Screw vs. edge dislocation strengthening in body-centered-cubic high entropy alloys and implications for guided alloy design*, *MRS Communications* **12** (2022), no. 6 1111–1118.

[102] L. T. W. Fey, C. Reynolds, A. Hunter, and I. J. Beyerlein, *Phase-field modeling of dislocation–interstitial interactions*, *Journal of the Mechanics and Physics of Solids* **179** (2023) 105370.

[103] L. Kaufman and H. Bernstein, *Computer calculation of phase diagrams With special reference to refractory metals.* Academic Press Inc, United States, 1970.

[104] A. K. Mallik, *Computer calculations of phase diagrams*, *Bulletin of Materials Science* **8** (1986), no. 2 107–121.

[105] J. B. Zhang, X. Yu, X. Wu, Y. Q. Zhang, S. B. Pan, S. Y. Yang, C. P. Wang, and X. J. Liu, *Experimental Investigation of Phase Equilibria in the Nb-V-Hf Ternary System*, *Journal of Phase Equilibria and Diffusion* **44** (2023), no. 5 669–678.

[106] Q. X. Long, J. Zhou, J. Yan, Y. Du, J. Deng, Q. Yao, H. Zhou, S. L. Shang, and Z. K. Liu, *Experimental isothermal section of the system Cr-Nb-Ru at 1100 ℃*, *Journal of Alloys and Compounds* **962** (2023), no. June 171090.

[107] F. Maresca and W. A. Curtin, *Mechanistic origin of high strength in refractory BCC high entropy alloys up to 1900K*, *Acta Materialia* **182** (2020) 235–249.

[108] S. I. Rao and B. Akdim, *A simpler technique for determining substitutional solute-screw dislocation interaction energies in BCC structures useful for estimating solid solution screw strengthening*, *Acta Materialia* **269** (2024) 119820.

[109] Y. Rao, C. Baruffi, A. De Luca, C. Leinenbach, and W. A. Curtin, *Theory-guided design of high-strength, high-melting point, ductile, low-density, single-phase BCC high entropy alloys*, *Acta Materialia* **237** (2022) 118132.

[110] P. Kumar, S. J. Kim, Q. Yu, J. Ell, M. Zhang, Y. Yang, J. Y. Kim, H. K. Park, A. M. Minor, E. S. Park, and R. O. Ritchie, *Compressive vs. tensile yield and fracture toughness behavior of a body-centered cubic refractory high-entropy superalloy Al0.5Nb1.25Ta1.25TiZr at temperatures from ambient to 1200°C*, *Acta Materialia* **245** (2023), no. July 2022.

[111] C.-J. Liu, C. Gadelmeier, S.-L. Lu, J.-W. Yeh, H.-W. Yen, S. Gorsse, U. Glatzel, and A.-C. Yeh, *Tensile creep behavior of HfNbTaTiZr refractory high entropy alloy at elevated temperatures*, *Acta Materialia* **237** (2022) 118188.

[112] Q. Wang, Z. Li, S. Pang, X. Li, C. Dong, and P. K. Liaw, *Coherent precipitation and strengthening in compositionally complex alloys: A review*, *Entropy* **20** (2018), no. 11.

[113] E. N. Sheftel, G. S. Usmanova, V. K. Grigorovich, and V. N. Geminov, *Short-Time and Long-Time Strength of Nitrided Niobium Alloys*, *Metallovedenie i Termicheskaya Obrabotka Metallov* (1984), no. 2 48–51.

[114] J. Askill, *Radioactive Tracer Diffusion Data in Metals, Alloys, and Oxides*, pp. 27–29. Springer US, Boston, MA, 1970.

[115] J. Buckman R. William, *Carbide strengthened refractory metals*, in *AIP Conference Proceedings*, vol. 271, (Albuquerque), pp. 93–98, 1993.

[116] J. Williams and D. C. Briggs, *Aging in Niobium-Rich Niobium-Hafnium-Carbon Alloys*, *Journal of the Less-Common Metals* **21** (1970) 255–273.

[117] H. E. McCoy, *Creep properties of the Nb-1*

[118] J. A. Cornie and R. T. Begley, Investigation of the Effects of Thermal Mechanical Variables on the Creep Properties of High Strength Columbium Alloys, tech. rep., Westinghouse Astronuclear Laboratory, Pittsburgh, 1969.

[119] J. A. Cornie, Development of Precipitation Strengthened Columbium Base Alloys, tech. rep., Westinghouse Astronuclear Laboratory, Pittsburgh, 1970.

[120] J. LLorca and V. M. Orera, Directionally solidified eutectic ceramic oxides, Progress in Materials Science **51** *(2006), no. 6 711–809.*

[121] Y. Waku, N. Nakagawa, T. Wakamoto, H. Ohtsubo, K. Shimizu, and Y. Kohtoku, A ductile ceramic eutectic composite with high strength at 1,873 K, Nature **389** *(1997), no. 6646 49–52.*

[122] M. E. Schlesinger, H. Okamoto, A. B. Gokhale, and R. Abbaschian, The Nb-Si (Niobium-Silicon) System, Journal of Phase Equilibria **14** *(1993), no. 4 502–509.*

[123] J. T. McKeown, V. R. Radmilovic, R. Gronsky, and A. M. Glaeser, Silicide characterization at alumina-niobium interfaces, Journal of Materials Science **46** *(2011), no. 11 3969–3981.*

[124] P. Tsakiropoulos, Alloys for application at ultra-high temperatures: Nb-silicide in situ composites: Challenges, breakthroughs and opportunities, Progress in Materials Science **123** *(2022), no. July 2020 100714.*

[125] B. P. Bewlay, M. Jackson, J. C. Zhao, R. Subramanian, M. G. Mendiratta, and J. J. Lewandowski, Ultrahigh- Temperature Nb-Silicide-based Composites, MRS Bulletin *(2003), no. September.*

[126] S. Yuan, L. Jia, L. Ma, H. Jiang, and H. Zhang, Eutectic formation during directional solidification: Effect of the withdrawal rate, Materials Letters **92** *(2013) 317–320.*

[127] C.-L. Ma, Y. Tan, H. Tanaka, A. Kasama, R. Tanaka, S. Miura, Y. Mishima, and S. Hanada, Phase Equilibria in Nb-Mo-Ruch Zone of the Nb-Si-Mo Ternary System, Materials Transactions **41** *(2000), no. 10 1329–1336.*

[128] J. Geng and P. Tsakiropoulos, A study of the microstructures and oxidation of Nb-Si-Cr-Al-Mo in situ composites alloyed with Ti, Hf and Sn, Intermetallics **15** *(2007), no. 3 382–395.*

[129] Y. Li, S. Miura, K. Ohsasa, C. Ma, and H. Zhang, Intermetallics Ultrahigh-temperature Nb ss / Nb 5 Si 3 fully-lamellar microstructure developed by directional solidi fi cation in OFZ furnace, Intermetallics **19** *(2011) 460–469.*

[130] *Y. Lu, J. Zhang, L. Tian, Y. Li, and C. Ma, Microstructural evolution of unidirectionally solidified Nb SS-Nb 5Si 3 eutectic alloy,* Rare Metals **30** *(2011), no. SUPPL.1 335–339.*

[131] *H. S. Guo and X. P. Guo, Microstructure and microhardness of directionally solidified and heat-treated Nb-Ti-Si based ultrahigh temperature alloy,* Transactions of Nonferrous Metals Society of China (English Edition) **21** *(2011), no. 6 1283–1290.*

[132] *E. N. Kablov, I. L. Svetlov, M. I. Karpov, and A. V. Neiman, High-Temperature Composites Based on the Nb – Si System Reinforced with Niobium Silicides,* Inorganic Materials: Applied Research **8** *(2017), no. 4 609–617.*

[133] *W. Liu, S. Huang, C. Ye, L. Jia, Y. Kang, J. Sha, B. Chen, Y. Wu, and H. Xiong, Progress in Nb-Si ultra-high temperature structural materials: A review,* Journal of Materials Science and Technology **149** *(2023) 127–153.*

[134] *F. Gang and M. Heilmaier, Influence of Directional Solidification on the Creep Properties of a Binary NbSi Eutectic Alloy,* Jom **66** *(2014), no. 9 1908–1913.*

[135] *Y. A. Bondarenko, A. B. Echin, M. Y. Kolodyazhnyi, and A. R. Narskii, Directional Solidification, Structure, and Mechanical Properties of a Eutectic Nb–Si Alloy with a Natural Composite Structure for GTE Blades,* Russian Metallurgy (Metally) **2017** *(2017), no. 12 1012–1017.*

[136] *L. Y. Sheng, Y. X. Tian, and J. T. Guo, Microstructural characteristics and Mechanical Properties of a Nb/Nb5Si3 Based Composite With and Without Directional Solidification,* Advanced Composites Letters **27** *(2018), no. 4 168–175.*

[137] *X. Fang, X. Guo, and Y. Qiao, Microstructural characterization of integrally directionally solidified Nb-Si based alloys at high withdrawal rates,* Intermetallics **110** *(2019), no. April 106481.*

[138] *A. Misra, G. Ghosh, and G. B. Olson, Phase relations in the Nb-Pd-Hf-Al system,* Journal of Phase Equilibria and Diffusion **25** *(2004), no. 6 507–514.*

[139] *G. Ghosh and G. B. Olson, Integrated design of Nb-based superalloys: Ab initio calculations, computational thermodynamics and kinetics, and experimental results,* Acta Materialia **55** *(2007), no. 10 3281–3303.*

[140] *A. J. Knowles, D. Dye, R. J. Dodds, A. Watson, C. D. Hardie, and S. A. Humphry-Baker, Tungsten-based bcc-superalloys,* Applied Materials Today **23** *(2021) 101014.*

[141] *N. Yurchenko, E. Panina, L. Rogal, L. Shekhawat, S. Zherebtsov, and N. Stepanov, Unique precipitations in a novel refractory Nb-Mo-Ti-Co high-entropy superalloy,* Materials Research Letters **10** *(2022), no. 2 78–87.*

[142] *E. Panina, N. Yurchenko, A. Tojibaev, M. Mishunin, S. Zherebtsov, and N. Stepanov, Mechanical properties of (HfCo)100x(NbMo)x refractory high-entropy alloys with a dual-phase bcc-B2 structure,* Journal of Alloys and Compounds **927** *(2022) 167013.*

[143] *E. Panina, N. Yurchenko, G. Salishchev, S. Zherebtsov, and N. Stepanov, International Journal of Refractory Metals and Hard Materials Thermal stability of (HfCo) 90 (NbMo) 10 and (HfCo) 75 (NbMo) 25 refractory high entropy alloys with a bcc + B2 structure,* International Journal of Refractory Metals and Hard Materials **115** *(2023), no. April 106297.*

[144] *S. Naidu, A. Sriramamurthy, and P. Rao, The Cr-W (Chromium-Tungsten) System,* Bulletin of Alloy Phase Diagrams **5** *(1984), no. 3 289–292.*

[145] *T. Hughes, E. P. Lautenschlager, J. B. Cohen, and J. O. Brittain, X-ray diffraction investigation of β-NiAl alloys,* Journal of Applied Physics **42** *(1971), no. 10 3705–3716.*

[146] *K. Ma, T. Blackburn, J. P. Magnussen, M. Kerbstadt, P. A. Ferreirós, T. Pinomaa, C. Hofer, D. G. Hopkinson, S. J. Day, P. A. Bagot, M. P. Moody, M. C. Galetz, and A. J. Knowles, Chromium-based bcc-superalloys strengthened by iron supplements,* Acta Materialia **257** *(2023), no. July.*

[147] *Y. F. Gu, H. Harada, and Y. Ro, Chromium and chromium-based alloys: Problems and possibilities for high-temperature service,* Jom **56** *(2004), no. 9 28–33.*

[148] *D. B. Miracle, M. H. Tsai, O. N. Senkov, V. Soni, and R. Banerjee, Refractory high entropy superalloys (RSAs),* Scripta Materialia **187** *(2020) 445–452.*

[149] *S. Naka and T. Khan, Designing novel multiconstituent intermetallics: Contribution of modern alloy theory in developing engineered materials,* Journal of Phase Equilibria **18** *(1997), no. 6 635–649.*

[150] *O. N. Senkov, S. V. Senkova, and C. Woodward, Effect of aluminum on the microstructure and properties of two refractory high-entropy alloys,* Acta Materialia **68** *(2014) 214–228.*

[151] *O. N. Senkov, C. Woodward, and D. B. Miracle, Microstructure and Properties of Aluminum-Containing Refractory High-Entropy Alloys,* Jom **66** *(2014), no. 10 2030–2042.*

[152] *J. K. Jensen, B. A. Welk, R. E. Williams, J. M. Sosa, D. E. Huber, O. N. Senkov, G. B. Viswanathan, and H. L. Fraser, Characterization of the microstructure of the compositionally complex alloy Al1Mo0.5Nb1Ta0.5Ti1Zr1,* Scripta Materialia **121** *(2016) 1–4.*

[153] *O. N. Senkov, D. Isheim, D. N. Seidman, and A. L. Pilchak, Development of a refractory high entropy superalloy,* Entropy **18** *(2016), no. 3 1–13.*

[154] *V. Soni, B. Gwalani, T. Alam, S. Dasari, Y. Zheng, O. N. Senkov, D. Miracle, and R. Banerjee, Phase inversion in a two-phase, BCC+B2, refractory high entropy alloy,* Acta Materialia **185** *(2020) 89–97.*

[155] *N. Yurchenko, E. Panina, A. Tojibaev, S. Zherebtsov, and N. Stepanov, Overcoming the strength-ductility trade-off in refractory medium-entropy alloys via controlled B2 ordering,* Materials Research Letters **10** *(2022), no. 12 813–823.*

[156] *S. Laube, A. Kauffmann, S. Schellert, S. Seils, A. S. Tirunilai, C. Greiner, Y. M. Eggeler, B. Gorr, H. J. Christ, and M. Heilmaier, Formation and thermal stability of two-phase microstructures in Al-containing refractory compositionally complex alloys,* Science and Technology of Advanced Materials **23** *(2022), no. 1 692–706.*

[157] *O. N. Senkov, B. Crossman, S. I. Rao, J. P. Couzinie, D. B. Miracle, T. M. Butler, R. Banerjee, and M. Mills, Mechanical properties of an Al10Nb20Ta15Ti30V5Zr20 A2/B2 refractory superalloy and its constituent phases,* Acta Materialia **254** *(2023), no. May 119017.*

[158] *A. Sharma, S. Dasari, V. Soni, Z. Kloenne, J. P. Couzinié, O. N. Senkov, D. B. Miracle, S. G. Srinivasan, H. Fraser, and R. Banerjee, B2 to ordered omega transformation during isothermal annealing of refractory high entropy alloys: Implications for high temperature phase stability,* Journal of Alloys and Compounds **953** *(2023) 170065.*

[159] *O. N. Senkov, J. K. Jensen, A. L. Pilchak, D. B. Miracle, and H. L. Fraser, Compositional variation effects on the microstructure and properties of a refractory high-entropy superalloy AlMo0.5NbTa0.5TiZr,* Materials and Design **139** *(2018) 498–511.*

[160] *D. Schliephake, A. E. Medvedev, M. K. Imran, S. Obert, D. Fabijanic, M. Heilmaier, A. Molotnikov, and X. Wu, Precipitation behaviour and mechanical properties of a novel Al0.5MoTaTi complex concentrated alloy,* Scripta Materialia **173** *(2019) 16–20.*

[161] *Z. T. Kloenne, J. P. Couzinié, M. Heczko, R. Gröger, G. B. Viswanathan, W. A. Clark, and H. L. Fraser, On the bcc/B2 interface structure in a refractory high entropy alloy,* Scripta Materialia **223** *(2023), no. July 2022 30–33.*

[162] *S. Laube, S. Schellert, A. S. Tirunilai, D. Schliephake, B. Gorr, H.-J. Christ, A. Kauffmann, and M. Heilmaier, Microstructure tailoring of Al-containing compositionally complex alloys by controlling the sequence of precipitation and ordering,* Acta Materialia *(2021) 117217.*

[163] *Z. T. Kloenne, K. Kadirvel, J. P. Couzinie, G. B. Viswanathan, Y. Wang, and H. L. Fraser, High temperature phase stability of the compositionally complex alloy AlMo0.5NbTa0.5TiZr,* Applied Physics Letters **119** *(2021), no. 15 0–6.*

[164] *T. E. Whitfield, G. J. Wise, H. J. Stone, and N. G. Jones, The influence of the Nb:Ta ratio on the microstructural evolution in refractory metal superalloy systems,* Applied Physics Letters **119** *(2021), no. 21.*

[165] *E. A. Lass, On the Thermodynamics and Phase Transformation Pathways in BCC-B2 Refractory Compositionally Complex Superalloys,* Metallurgical and Materials Transactions A: Physical Metallurgy and Materials Science **53** *(2022), no. 12 4481–4498.*

[166] *K. Das and S. Das, Order-disorder transformation of the body centered cubic phase in the Ti-Ai-X(X = Ta, Nb, or Mo) system,* Journal of Materials Science **38** *(2003), no. 19 3995–4002.*

[167] *V. Raghavan, Al-Ta-Ti (Aluminum-Tantalum-Titanium),* Journal of Phase Equilibria Diffusion **26** *(2005), no. 6 629–634.*

[168] *V. Raghavan, Al-Nb-Ti (Aluminum-Niobium-Titanium),* Journal of Phase Equilibria and Diffusion **31** *(2010), no. 1 47–52.*

[169] *V. Raghavan, Al-Ti-V (Aluminum-Titanium-Vanadium),* Journal of Phase Equilibria and Diffusion **33** *(2012), no. 2 151–153.*

[170] *H. Wang, N. Warnken, and R. C. Reed, Thermodynamic assessment of the ordered B2 phase in the Ti-V-Cr-Al quaternary system,* Calphad: Computer Coupling of Phase Diagrams and Thermochemistry **35** *(2011), no. 2 204–208.*

[171] *Z. X. Deng, D. P. Zhao, Y. Y. Huang, L. L. Chen, H. Zou, Y. Jiang, and K. Chang, Ab initio and calphad-type thermodynamic investigation of the Ti-Al-Zr system,* Journal of Mining and Metallurgy, Section B: Metallurgy **55** *(2019), no. 3 427–437.*

[172] *J. Wang, W. Zheng, G. Xu, X. Zeng, and Y. Cui, Thermodynamic assessment of the Ti–Al–Zr system and atomic mobility of its bcc phase,* Calphad: Computer Coupling of Phase Diagrams and Thermochemistry **70** *(2020), no. February.*

[173] *D. A. Abreu, A. A. Silva, J. C. Santos, D. F. Barros, C. S. Barros, N. Chaia, C. A. Nunes, and G. C. Coelho, Liquidus projection of the Al–Ti–Zr system,* Journal of Alloys and Compounds **849** *(2020) 156463.*

[174] *J. Brodie, J. Wang, J. P. Couzinié, M. Heczko, V. Mazánová, M. J. Mills, and M. Ghazisaeidi, Stability of the B2 phase in refractory high entropy alloys containing aluminum,* Acta Materialia **268** *(2024), no. January 119745.*

[175] *Y. L. Müller and A. Raju Natarajan, First-principles thermodynamics of precipitation in aluminum-containing refractory alloys,* Acta Materialia *(2024) 119995.*

[176] *T. E. Whitfield, H. J. Stone, C. N. Jones, and N. G. Jones, Microstructural Degradation of the AlMo0.5NbTa0.5TiZr Refractory Metal High-Entropy Superalloy at Elevated Temperatures,* Entropy **23** *(2021), no. 1 80.*

[177] *T. E. Whitfield, N. L. Church, H. J. Stone, and N. G. Jones, On the rate of microstructural degradation of Al-Ta-Ti-Zr refractory metal high entropy superalloys,* Journal of Alloys and Compounds **939** *(2023) 168369.*

[178] *V. Soni, B. Gwalani, O. N. Senkov, B. Viswanathan, T. Alam, D. B. Miracle, and R. Banerjee, Phase stability as a function of temperature in a refractory high-entropy alloy,* Journal of Materials Research **33** *(2018), no. 19 3235–3246.*

[179] *S. Dasari, A. Sharma, V. Soni, Z. Kloenne, H. Fraser, and R. Banerjee, Crystallographic and Compositional Evolution of Ordered B2 and Disordered BCC Phases During Isothermal Annealing of Refractory High-Entropy Alloys,* Microscopy and Microanalysis *(2022) 1–11.*

[180] *O. N. Senkov, S. A. Kube, J. W. Drazin, V. Soni, D. B. Miracle, T. M. Butler, T. M. Pollock, and R. Banerjee, Thermal and Elastic Properties of an A2/B2 Refractory High Entropy Superalloy and Its Constituent Phases,* Metallurgical and Materials Transactions A *(2024).*

[181] *G. F. Hurley and J. H. Brophy, A constitution diagram for the niobium-ruthenium system above 1100C,* Journal of less-common metals **7** *(1964) 267–277.*

[182] *B. H. Chen and H. F. Franzen, High temperature X-ray diffraction and Landau theory investigation of phase transitions in NbRu1 + x and RhTi,* J. Less-Common Met. **153** *(1989), no. 2 13–19.*

[183] *R. M. Waterstrat and R. C. Manuszewski, The vanadium-ruthenium constitution diagram,* Journal of less-common metals **48** *(1976) 151–158.*

[184] *H. Okamoto, Ru-Ta (Ruthenium-Tantalum),* Journal of Phase Equilibria **12** *(1991), no. 3 395–397.*

[185] *J. L. Murray, The Ru-Ti (Ruthenium-Titanium) system,* Bulletin of Alloy Phase Diagrams **3** *(1982), no. 2 216–221.*

[186] *N. David, T. Benlaharche, J. M. Fiorani, and M. Vilasi, Thermodynamic modeling of Ru-Zr and Hf-Ru systems,* Intermetallics **15** *(2007), no. 12 1632–1637.*

[187] *L. S. Kryklya, K. E. Kornienko, V. G. Khoruzhaya, V. M. Petyukh, L. A. Duma, and V. B. Sobolev, Physicochemical materials research: Alloy constitution and phase equilibria in the Hf-Ru-Rh system. I. solidus surface of the partial Hf–HfRu–HfRh system,* Powder Metallurgy and Metal Ceramics **54** *(2016), no. 9 568–582.*

[188] *H. Okamoto, The Ru-Zr system (Ruthenium-Zirconium),* Journal of Phase Equilibria **14** *(1993), no. 2 225–227.*

[189] *H. Okamoto, Ru-Zr (Ruthenium-Zirconium),* Journal of Phase Equilibria and Diffusion **33** *(2012), no. 1 82.*

[190] *C. Frey, R. Silverstein, and T. M. Pollock, A high stability B2-containing refractory multi-principal element alloy,* Acta Materialia **229** *(2022) 117767.*

[191] *D. O. Hobson, Effect of Alloying Elements on the Strength, Stability, and Corrosion Resistance of Columbium, tech. rep., Atomic Energy Commission, 1962.*

[192] *Z. Li, Z. R. Zeng, R. Tan, M. Taheri, and N. Birbilis, A database of mechanical properties for multi principal element alloys,* Chemical Data Collections **47** *(2023), no. July.*

[193] *K. Kadirvel, Z. Kloenne, J. K. Jensen, H. Fraser, and Y. Wang, Phase-field modelling of transformation pathways and microstructural evolution in multi-principal element alloys,* Applied Physics Letters **119** *(2021), no. 17.*

[194] *X. P. Zhu, N. Gao, Z. C. Bai, K. Wang, J. Q. Yao, Z. T. Fan, Z. D. Wang, and X. W. Liu, Phase stability of a light-weight AlNb2TiV refractory high-entropy alloy at high temperature,* Materials Letters **325** *(2022), no. June 132897.*

[195] *B. Zhao, G. Chen, S. Lv, X. Fu, and W. Zhou, A refractory multi-principal element alloy with superior elevated-temperature strength,* Journal of Alloys and Compounds **896** *(2022) 163129.*

[196] *A. Grytsiv, P. Rogl, H. Schmidt, and G. Giester, Constitution of the Ternary System Al-Ru-Ti (Aluminum-Ruthenium-Titanium),* Journal of Phase Equilibria **24** *(2003), no. 6 511–527.*

[197] *L. Perring, F. Bussy, J. C. Gachon, and P. Feschotte, The Ruthenium-Silicon system,* Journal of Alloys and Compounds **284** *(1999), no. 1-2 198–205.*

[198] J. Schindelin, I. Arganda-Carreras, E. Frise, V. Kaynig, M. Longair, T. Pietzsch, S. Preibisch, C. Rueden, S. Saalfeld, B. Schmid, J.-Y. Tinevez, D. J. White, V. Hartenstein, K. Eliceiri, P. Tomancak, and A. Cardona, Fiji: an open-source platform for biological-image analysis, Nature Methods **9** *(2012), no. 7 676–682.*

[199] B. H. Toby and R. B. Von Dreele, GSAS-II: the genesis of a modern open-source all purpose crystallography software package, Journal of Applied Crystallography **46** *(2013), no. 2 544–549.*

[200] J.-O. Andersson, T. Helander, L. Höglund, P. Shi, and B. Sundman, Thermo-Calc DICTRA, computational tools for materials science, Calphad **26** *(2002), no. 2 273–312.*

[201] M. Y. Benarchid, N. David, J. M. Fiorani, M. Vilasi, and T. Benlaharche, Enthalpies of formation of Nb-Ru and Nb-Ru-Al alloys, Thermochimica Acta **482** *(2009), no. 1-2 39–41.*

[202] J. P. Abriata, J. C. Bolcich, and H. A. Peretti, The Hf-Zr (Hafnium-Zirconium) system, Bulletin of Alloy Phase Diagrams **3** *(1982), no. 1 29–34.*

[203] H. Okamoto, Hf-O (Hafnium-Oxygen), Journal of Phase Equilibria and Diffusion **29** *(2008), no. 1 124–124.*

[204] M. Pang, Y. Peng, P. Zhou, and Y. Du, Thermodynamic modeling of the Hf-N system, Journal of Mining and Metallurgy, Section B: Metallurgy **54** *(2018), no. 1 111–118.*

[205] P. Rodriguez and V. S. Arunachalam, Influence of interstitials on the mechanical properties of group IV b metals, in Symposium on Non-ferrous Metals Technology*, pp. 193–206, 1968.*

[206] O. N. Senkov, J. Gild, and T. M. Butler, Microstructure, mechanical properties and oxidation behavior of NbTaTi and NbTaZr refractory alloys, Journal of Alloys and Compounds **862** *(2021) 158003.*

[207] J. R. Donoso and R. E. Reed-Hill, Slow strain-rate embrittlement of niobium by Oxygen, Metallurgical Transactions A **7** *(1976), no. 7 961–965.*

[208] A. E. Diaz and R. E. Reed-Hill, Evidence for the slow strain-rate embrittlement in tantalum due to oxygen, Scripta Metallurgica **13** *(1979) 491–496.*

[209] J. Braun, L. Kaserer, J. Stajkovic, K. H. Leitz, B. Tabernig, P. Singer, P. Leibenguth, C. Gspan, H. Kestler, and G. Leichtfried, Molybdenum and tungsten manufactured by selective laser melting: Analysis of defect structure and solidification mechanisms, International Journal of Refractory Metals and Hard Materials **84** *(2019), no. June 104999.*

[210] *V. Soni, O. N. Senkov, J. P. Couzinie, Y. Zheng, B. Gwalani, and R. Banerjee, Phase stability and microstructure evolution in a ductile refractory high entropy alloy Al10Nb15Ta5Ti30Zr40,* Materialia **9** *(2020), no. December 2019 100569.*

[211] *F. Findik, Discontinuous (cellular) precipitation,* Journal of Materials Science Letters **17** *(1998), no. 1 79–83.*

[212] *Q. He, S. Yoshida, H. Yasuda, and N. Tsuji, Effect of elemental combination on microstructure and mechanical properties of quaternary refractory medium entropy alloys,* Materials Transactions **61** *(2020), no. 4 577–586.*

[213] *M. A. Gibson and G. W. Delamore, Extended lamellar substructures in lead-cadmium eutectic alloys,* Journal of Materials Science Letters **3** *(1984), no. 11 937–941.*

[214] *G. Faivre, Morphological instabilities of lamellar eutectic growth fronts: A survey of recent experimental and numerical results,* Journal of Crystal Growth **166** *(1996), no. 1-4 29–39.*

[215] *C. Zhang, B. E. MacDonald, F. Guo, H. Wang, C. Zhu, X. Liu, Y. Kang, X. Xie, Y. Zhou, K. S. Vecchio, and E. J. Lavernia, Cold-workable refractory complex concentrated alloys with tunable microstructure and good room-temperature tensile behavior,* Scripta Materialia **188** *(2020) 16–20.*

[216] *K. Gschneidner, A. Russell, A. Pecharsky, J. Morris, Z. Zhang, T. Lograsso, D. Hsu, C. H. Lo, Y. Ye, A. Slager, and D. Kesse, A family of ductile intermetallic compounds,* Nature Materials **2** *(2003), no. 9 587–590.*

[217] *I. Baker and P. R. Munroe, Mechanical properties of FeAl,* International Materials Reviews **42** *(1997), no. 5 181–205.*

[218] *K. Ishida, N. Kainuma, N. Ueno, and T. Nishizawa, Ductility enhancement in NiAl (B2) Base Alloys by microstructural control,* Metallurgical Transactions A **22A** *(1991), no. February 441–446.*

[219] *V. Soni, O. N. Senkov, B. Gwalani, D. B. Miracle, and R. Banerjee, Microstructural Design for Improving Ductility of An Initially Brittle Refractory High Entropy Alloy,* Scientific Reports **8** *(2018), no. 1 1–10.*

[220] *M. A. Charpagne, K. V. Vamsi, Y. M. Eggeler, S. P. Murray, C. Frey, S. K. Kolli, and T. M. Pollock, Design of Nickel-Cobalt-Ruthenium Multi-Principal Element Alloys,* Acta Materialia **194** *(2020) 16013.*

[221] *Z. Guo, A. Zhang, J. Han, and J. Meng, Effect of Si additions on microstructure and mechanical properties of refractory NbTaWMo high-entropy alloys,* Journal of Materials Science **54** *(2019), no. 7 5844–5851.*

[222] *Q. Wei, Q. Shen, J. Zhang, Y. Zhang, G. Luo, and L. Zhang, Microstructure evolution, mechanical properties and strengthening mechanism of refractory high-entropy alloy matrix composites with addition of TaC,* Journal of Alloys and Compounds **777** *(2019) 1168–1175.*

[223] *Y. Cao, Y. Liu, Y. Li, B. Liu, A. Fu, and Y. Nie, Precipitation behavior and mechanical properties of a hot-worked TiNbTa0.5ZrAl0.5 refractory high entropy alloy,* International Journal of Refractory Metals and Hard Materials **86** *(2020), no. July 2019.*

[224] *J. Wen, X. Chu, Y. Cao, and N. Li, Effects of al on precipitation behavior of ti-nb-ta-zr refractory high entropy alloys,* Metals **11** *(2021), no. 3 1–10.*

[225] *Y. Dong, Y. Lu, J. Kong, J. Zhang, and T. Li, Microstructure and mechanical properties of multi-component AlCrFeNiMo x high-entropy alloys,* Journal of Alloys and Compounds **573** *(2013) 96–101.*

[226] *C. Wen, Y. Zhang, C. Wang, D. Xue, Y. Bai, S. Antonov, L. Dai, T. Lookman, and Y. Su, Machine learning assisted design of high entropy alloys with desired property,* Acta Materialia **170** *(2019) 109–117.*

[227] *N. Yurchenko, E. Panina, M. Tikhonovsky, G. Salishchev, S. Zherebtsov, and N. Stepanov, Structure and mechanical properties of an in situ refractory Al20Cr10Nb15Ti20V25Zr10 high entropy alloy composite,* Materials Letters **264** *(2020) 127372.*

[228] *C. Frey, H. You, S. Kube, G. H. Balbus, K. Mullin, S. Oppenheimer, C. Holgate, and T. Pollock, High temperature B2 precipitation in Ru-containing refractory multi-principal element alloys,* Metallurgical and Materials Transactions A *(2024).*

[229] *A. Detor, S. Oppenheimer, R. Casey, and C. Crawford, Refractory high entropy alloy dataset with room temperature ductility screening,* Data in Brief *(2022), no. xxxx 108582.*

[230] *ASTM International, West Conshohocken, PA,* E562-19e1. Standard Test Method for Determining Volume Fraction by Systematic Manual Point Count*, 2020.*

[231] *M. D. Uchic and D. M. Dimiduk, A methodology to investigate size scale effects in crystalline plasticity using uniaxial compression testing,* Mater. Sci. Eng., A **400-401** *(2005) 268–278. Dislocations 2004.*

[232] *G. H. Balbus, S. I. Rao, O. N. Senkov, and E. J. Payton, Orientation dependent plasticity of the refractory multi-principal element alloy MoNbTi investigated via micropillar compression,* Acta Materialia **262** *(2024) 119401.*

[233] D. Norfleet, D. Dimiduk, S. Polasik, M. Uchic, and M. Mills, Dislocation structures and their relationship to strength in deformed nickel microcrystals, Acta Mater. **56** *(2008), no. 13 2988–3001.*

[234] F. Mompiou and R. Xie, pycotem : An open source toolbox for online crystal defect characterization from tem imaging and diffraction, Journal of Microscopy **282** *(2021-04), no. 1.*

[235] H. Okamoto, M. E. Schlesinger, and E. M. Mueller, Mo Binary Alloy Phase Diagrams, in Alloy Phase Diagrams, *vol. 3, ch. Mo (Molybdenum) Binary Alloy Phase Diagrams, pp. 489–498. 2016.*

[236] R. Zhao, J. Wang, H. Yuan, B. Hu, Y. Du, and Z. Tan, Thermodynamic reassessment of the Mo–Hf and Mo–Zr systems supported by first-principles calculations, CALPHAD: Comput. Coupling Phase Diagrams Thermochem. **69** *(2020), no. March 101766.*

[237] H. Okamoto, The Hf-Nb (Hafnium-Niobium) System, Journal of Phase Equilibria **12** *(1991), no. 2 211–214.*

[238] A. Kaufmann, E. J. Rapperport, M. F. Smith, J. Wulff, J. Brophy, N. J. Grant, B. C. Giessen, A. Taylor, and N. Doyle, Refractory Metal Consitution Diagrams, tech. rep., United States Air Force, 1960.

[239] T. A. Parthasarathy, S. I. Rao, D. M. Dimiduk, M. D. Uchic, and D. R. Trinkle, Contribution to size effect of yield strength from the stochastics of dislocation source lengths in finite samples, Scr. Mater. **56** *(2007), no. 4 313–316.*

[240] G. Laplanche, P. Gadaud, L. Perrière, I. Guillot, and J. P. Couzinié, Temperature dependence of elastic moduli in a refractory HfNbTaTiZr high-entropy alloy, J. Alloys Compd. **799** *(2019) 538–545.*

[241] F. H. Featherston and J. R. Neighbours, Elastic constants of tantalum, tungsten, and molybdenum, Phys. Rev. **130** *(May, 1963) 1324–1333.*

[242] C. N. Reid, J. L. Routbort, and R. A. Maynard, Elastic constants of ti–40 at.% nb at 298 °k, J. Appl. Phys. **44** *(1973), no. 3 1398–1399, [https://doi.org/10.1063/1.1662365].*

[243] Y. Yamabe-Mitarai, K. Yanao, Y. Toda, I. Ohnuma, and T. Matsunaga, Phase stability of Ti-containing high-entropy alloys with a bcc or hcp structure, J. Alloys Compd. **911** *(2022) 164849.*

[244] Q. Guo and O. J. Kleppa, The standard enthalpies of formation of the compounds of early transition metals with late transition metals and with noble metals as determined by Kleppa and co-workers at the University of Chicago - A review, J. Alloys Compd. **321** *(2001), no. 2 169–182.*

[245] *R. R. Eleti, N. Stepanov, and S. Zherebtsov, Mechanical behavior and thermal activation analysis of HfNbTaTiZr body-centered cubic high-entropy alloy during tensile deformation at 77 K,* Scr. Mater. **188** *(2020) 118–123.*

[246] *R. R. Eleti, N. Stepanov, N. Yurchenko, D. Klimenko, and S. Zherebtsov, Plastic deformation of solid-solution strengthened hf-nb-ta-ti-zr body-centered cubic medium/high-entropy alloys,* Scr. Mater. **200** *(2021) 113927.*

[247] *S. Rao, B. Akdim, E. Antillon, C. Woodward, T. Parthasarathy, and O. Senkov, Modeling solution hardening in bcc refractory complex concentrated alloys: Nbtizr, nb1.5tizr0.5 and nb0.5tizr1.5,* Acta Mater. **168** *(2019) 222–236.*

[248] *S. Rao, C. Woodward, B. Akdim, O. Senkov, and D. Miracle, Theory of solid solution strengthening of bcc chemically complex alloys,* Acta Mater. **209** *(2021) 116758.*

[249] *R. W. Kozar, A. Suzuki, W. W. Milligan, J. J. Schirra, M. F. Savage, and T. M. Pollock, Strengthening mechanisms in polycrystalline multimodal nickel-base superalloys,* Metall. Mater. Trans. A **40** *(2009), no. 7 1588–1603.*

[250] *D. G. Morris and M. A. Morris, Recrystallization in β brass,* J. Mater. Sci. **26** *(1991), no. 7 1734–1740.*

[251] *M. H. Yoo, T. Takasugi, S. Hanada, and O. Izumi, Slip modes in b2-type intermetallic alloys,* Mater. Trans., JIM **31** *(1990), no. 6 435–442.*

[252] *I. Baker, A review of the mechanical properties of B2 compounds,* Mater. Sci. Eng., A **192-193** *(1995), no. PART 1 1–13.*

[253] *R. Taillard and A. Pineau, Room temperature tensile properties of fe-19wt.%cr alloys precipitation hardened by the intermetallic compound nial,* Mater. Sci. Eng. **56** *(1982), no. 3 219–231.*

[254] *M. C. Ha, J.-M. Koo, J.-K. Lee, S. W. Hwang, and K.-T. Park, Tensile deformation of a low density fe–27mn–12al–0.8c duplex steel in association with ordered phases at ambient temperature,* Mater. Sci. Eng., A **586** *(2013) 276–283.*

[255] *J.-P. Couzinié, M. Heczko, V. Mazánová, O. N. Senkov, M. Ghazisaeidi, R. Banerjee, and M. J. Mills, High-temperature deformation mechanisms in a bcc+b2 refractory complex concentrated alloy,* Acta Mater. **233** *(2022) 117995.*

[256] *R. Farraro and R. B. McLellan, Temperature Dependence of the Young'S Modulus and Shear Modulus of Pure Nickel, Platinum, and Molybdenum.,* Metall Trans A **8 A** *(1977), no. 10 1563–1565.*

[257] A. Ghafarollahi, Strengthening mechanisms in dilute and random solid solution high-entropy BCC alloys. *PhD thesis, Swiss Federal Institute of Technology Lausanne, 2022.*

[258] S. I. Rao, C. Woodward, and B. Akdim, Solid solution softening and hardening in binary BCC alloys, Acta Materialia **243** *(2023), no. April 2022 118440.*

[259] R. J. Farraro and R. B. McLellan, High Temperature Elastic Properties of Polycrystalline Niobium, Tantalum and Vanadium, Metallurgical and Materials Transactions A **10A** *(1979) 1699–1702.*

[260] V. N. Eremenko, L. S. Kriklya, V. G. Khoruzhaya, and T. D. Shtepa, Interaction of Hafnium with Ruthenium and Iridium, Poroshkovaya Metaiiurgiya **19** *(1992), no. 5 463–466.*

[261] S. A. Kube, C. Frey, C. Mcmullin, B. Neuman, K. M. Mullin, and T. M. Pollock, Acta Materialia Navigating the BCC-B2 refractory alloy space: Stability and thermal processing with Ru-B2 precipitates, Acta Materialia **265** *(2024), no. August 2023 119628.*

[262] S. Ge, H. Fu, L. Zhang, H. Mao, H. Li, A. Wang, W. Li, and H. Zhang, Effects of Al addition on the microstructures and properties of MoNbTaTiV refractory high entropy alloy, Mater. Sci. Eng., A **784** *(2020) 139275.*

[263] Z. Q. Xu, Z. L. Ma, M. Wang, Y. W. Chen, Y. D. Tan, and X. W. Cheng, Design of novel low-density refractory high entropy alloys for high-temperature applications, Mater. Sci. Eng., A **755** *(2019), no. March 318–322.*

[264] J. L. Murray, The Mo-Ti (Molybdenum-Titanium) System, Bull. Alloy Phase Diagrams **2** *(1981), no. 2 185–192.*

[265] J. F. Smith, D. M. Bailey, and O. N. Carlson, The Cr-V (Chromium-Vanadium) system, Bull. Alloy Phase Diagrams **2** *(1982), no. 4 469–473.*

[266] A. E. Dwight, CsCl-type equiatomic phases in binary alloys of transition elements., Trans. Inst. Min. Metall., **215** *(1959) 283–286.*

[267] R. A. Ricks, A. J. Porter, and R. C. Ecob, Growth of γ precipitates in nickel-base superalloy, Acta Metallurgica **31** *(1983) 43–53.*

[268] X. Fu, C. A. Schuh, and E. A. Olivetti, Materials selection considerations for high entropy alloys, Scripta Mater. **138** *(2017) 145–150.*

[269] J. L. Murray, A. J. McAlister, and D. J. Kahan, The Al-Hf (aluminum-hafnium) system, Journal of Phase Equilibria **19** *(1998), no. 4 376–379.*

[270] *H. N. Su and P. Nash, Enthalpies of formation in the Al-Ni-Ru system by direct reaction synthesis calorimetry,* Journal of Alloys and Compounds **403** *(2005), no. 1-2 217–222.*

[271] *S. V. Meschel, P. Nash, and X. Q. Chen, The standard enthalpies of formation of binary intermetallic compounds of some late 4d and 5d transition metals by high temperature direct synthesis calorimetry,* Journal of Alloys and Compounds **492** *(2010), no. 1-2 105–115.*

[272] *S. V. Meschel and O. J. Kleppa, Standard Enthalpies of Formation of Some 4d and 5d Transition Metal-Antimony Compounds by High Temperature Direct Synthesis Calorimetry,* Journal of Alloys and Compounds **274** *(1998) 193–200.*

[273] *M. Marezio, P. D. Dernier, and C. W. Chu, Low-Temperature X-Ray Diffraction Studies of Near-Equiatomic VRu Alloys,* Physical Review B **4** *(1971), no. 8 2825–2826.*

[274] *E. Raub and W. Fritzsche, Die ruthenium-vanadium-legierungen,* International Journal of Materials Research **54** *(1963), no. 1 21–23.*

[275] *D. C. Goldberg, G. Dicker, and S. A. Worcester, Niobium and Niobium Alloys in Nuclear Power,* Nuclear Engineering and Design **22** *(1972) 95–123.*

[276] *R. Huang, J. Tan, W. Li, Q. Dong, C. J. Li, X. M. Qin, S. F. Guo, and Y. P. Lu, Effects of V content on the microstructure and mechanical properties of Nb31Ti37-xZr26Al6Vx refractory medium-entropy alloys,* Intermetallics **143** *(2022), no. July 2021.*

[277] *N. Siddique, S. Paheding, C. P. Elkin, and V. Devabhaktuni, U-net and its variants for medical image segmentation: A review of theory and applications,* IEEE Access **9** *(2021) 82031–82057.*

[278] *O. Ronneberger, P. Fischer, and T. Brox,* U-Net: Convolutional Networks for Biomedical Image Segmentation, *p. 234–241. Springer International Publishing, 2015.*

[279] *R. Jacobs, Deep learning object detection in materials science: Current state and future directions,* Computational Materials Science **211** *(Aug., 2022) 111527.*

[280] *A. Genc, L. Kovarik, and H. L. Fraser, A deep learning approach for semantic segmentation of unbalanced data in electron tomography of catalytic materials,* Scientific Reports **12** *(Sept., 2022).*

[281] *T. M. Pollock, The growth and elevated temperature stability of high refractory nickel-base single crystals,* Materials Science and Engineering B **32** *(1995), no. 3 255–266.*

[282] A. Suzuki, N. D. Saddock, J. W. Jones, and T. M. Pollock, Solidification paths and eutectic intermetallic phases in Mg–Al–Ca ternary alloys, Acta Materialia **53** *(2005), no. 9 2823–2834.*

[283] D. B. Williams and C. B. Carter, Transmission Electron Microscopy. *Springer New York, New York, 2 ed., 2009.*

[284] M. Doi, Coarsening Behaviour of Coherent Precipitates in Elastically Constrained Systems—With Particular Emphasis on Gamma-Prime Precipitates in Nickel-Base Alloys—, 1992.

[285] M. Cottura, Y. Le Bouar, B. Appolaire, and A. Finel, Role of elastic inhomogeneity in the development of cuboidal microstructures in Ni-based superalloys, Acta Materialia **94** *(2015) 15–25.*

[286] Y. Yamaguchi, R. Tajima, and Y. Terada, Morphology evolution of gamma' precipitates for wrought ni-based superalloys, Materials Transactions **61** *(2020), no. 11 2185–2194.*

[287] K. Wang and R. R. Reeber, The role of defects on thermophysical properties: Thermal expansion of V, Nb, Ta, Mo and W, Materials Science and Engineering R: Reports **23** *(1998), no. 3 101–137.*

[288] S. Huang, K. An, Y. Gao, and A. Suzuki, Determination of γ/γ Lattice Misfit in Ni-Based Single-Crystal Superalloys at High Temperatures by Neutron Diffraction, Metallurgical and Materials Transactions A **49** *(2018), no. 3 740–751.*

[289] B. Tryon, T. M. Pollock, M. F. X. Gigliotti, and K. Hemker, Thermal expansion behavior of ruthenium aluminides, Scripta Materialia **50** *(2004), no. 6 845–848.*

[290] R. J. Pérez and A. R. Massih, Thermodynamic evaluation of the Nb-O-Zr system, Journal of Nuclear Materials **360** *(2007), no. 3 242–254.*

[291] R. Maldonado and E. Nembach, The formation of precipitate free zones and the growth of grain boundary carbides in the nickel-base superalloy NIMONIC PE16, Acta Materialia **45** *(1997), no. 1 213–224.*

[292] A. Bauer, S. Neumeier, F. Pyczak, R. F. Singer, and M. Göken, Creep properties of different γ'-strengthened Co-base superalloys, Materials Science and Engineering: A **550** *(2012) 333–341.*

[293] T. Krol, D. Baither, and E. Nembach, The formation of precipitate free zones along grain boundaries in a superalloy and the ensuing effects on its plastic deformation, Acta Materialia **52** *(2004), no. 7 2095–2108.*

[294] H. L. Brown, P. E. Armstrong, and C. P. Kempter, Elastic properties of polycrystalline Sc, Re, Ru and Pt-21 Ir, Journal of The Less-Common Metals **11** *(1966), no. 2 135–140.*

[295] J. M. Rosenberg and H. R. Piehler, Calculation of the taylor factor and lattice rotations for bcc metals deforming by pencil glide, Metallurgical Transactions **2** *(1971), no. 1 257–259.*

[296] O. N. Senkov, S. I. Rao, T. M. Butler, and K. J. Chaput, Ductile Nb alloys with reduced density and cost, Journal of Alloys and Compounds **808** *(2019) 151685.*

[297] F. F. Schmidt, E. S. Bartlett, and H. R. Ogden, Tantalum Alloys- Some High- and Low-Temperature Properties, tech. rep., Battelle Memorial Institute, Columbus, 1963.

[298] W. Cai and W. D. Nix, Imperfections in Crystalline Solids. *MRS-Cambridge Materials Fundamentals. Cambridge University Press, 2016.*

[299] E. Nembach, Particle strengthening of metals and alloys. *Wiley, New York.*

[300] J. A. Mayer, T. M. Pollock, K. V. Vamsi, and R. Seshadri, Antiphase boundaries in B2 intermetallics: Proximate structures, formation energies, and chemical stability, Physical Review Materials **8** *(2024), no. 1 1–11.*

[301] M. Dodaran, A. H. Ettefagh, S. M. Guo, M. M. Khonsari, W. J. Meng, N. Shamsaei, and S. Shao, Effect of alloying elements on the γ' antiphase boundary energy in Ni-base superalloys, Intermetallics **117** *(2020) 106670.*

[302] D. M. Collins, L. Yan, E. A. Marquis, L. D. Connor, J. J. Ciardiello, A. D. Evans, and H. J. Stone, Lattice misfit during ageing of a polycrystalline nickel-base superalloy, Acta Materialia **61** *(2013), no. 20 7791–7804.*

[303] L. Luo, Y. Ma, S. Li, Y. Pei, L. Qin, and S. Gong, Evolutions of microstructure and lattice misfit in a γ-rich Ni-based superalloy during ultra-high temperature thermal cycle, Intermetallics **99** *(2018) 18–26.*

[304] W. T. Loomis, J. W. Freeman, and D. L. Sponseller, The influence of molybdenum on the γ/'phase in experimental nickel-base superalloys, Metallurgical Transactions **3** *(1972), no. 4 989–1000.*

[305] M. F. Henry, Y. S. Yoo, D. Y. Yoon, and J. Choi, The Dendritic Growth of γ' Precipitates and Grain Boundary Serration in a Model Nickel-Base Superalloy, Metallurgical and Materials Transactions A **24A** *(1993) 1733–1743.*

[306] T. Philippe and P. W. Voorhees, Ostwald ripening in multicomponent alloys, Acta Materialia **61** *(2013), no. 11 4237–4244.*

[307] S. Meher, M. C. Carroll, T. M. Pollock, and L. J. Carroll, Designing nickel base alloys for microstructural stability through low γ-γ interfacial energy and lattice misfit, Materials Design **140** *(2018) 249–256.*

[308] Metal Prices in the United States Through 2010, tech. rep., U.S. Geological Survey, Reston, VA, 2013.

[309] R. F. Schulte, Platinum-Group Metals [Advanced Release], in Metals and Minerals*. Reston, VA, 2019.*

[310] J. Wu, S. Liu, Y. Zhan, and M. Yu, Ternary addition and site substitution effect on B2 RuHf-based intermetallics: A first-principles study, Materials and Design **108** *(2016) 230–239.*

[311] S. Liu, Y. Zhan, J. Wu, X. Chen, and H. Ye, Site preference of the alloying additions on mechanical and electronic properties of B2 ZrRu-based compounds, Computational Materials Science **117** *(2016) 1–6.*

[312] C. Dahl, B. Gilbert, and I. Lange, Mineral scarcity on Earth: are Asteroids the answer, Mineral Economics **33** *(2020), no. 1 29–41.*